Titre: Title:	Ion bombardment effects in low-pressure plasmas : in situ spectroscopic ellipsometry and Monte-Carlo simulation study
Auteur: Author:	Aram Amassian
Date:	2005
Type:	Mémoire ou thèse / Dissertation or Thesis
Référence: Citation:	Amassian, A. (2005). Ion bombardment effects in low-pressure plasmas : in situ spectroscopic ellipsometry and Monte-Carlo simulation study [Ph.D. thesis, École Polytechnique de Montréal]. PolyPublie. https://publications.polymtl.ca/7544/

UNIVERSITÉ DE MONTRÉAL

ION BOMBARDMENT EFFECTS IN LOW-PRESSURE PLASMAS: *IN SITU* SPECTROSCOPIC ELLIPSOMETRY AND MONTE-CARLO SIMULATION STUDY

ARAM AMASSIAN
DÉPARTEMENT DE GÉNIE PHYSIQUE
ÉCOLE POLYTECHNIQUE DE MONTRÉAL

THÈSE PRÉSENTÉE EN VUE DE L'OBTENTION
DU DIPLÔME DE PHILOSOPHIÆ DOCTOR
(GÉNIE PHYSIQUE)
DÉCEMBRE 2005

Your file Votre référence
ISBN: 978-0-494-16981-0
Our file Notre référence
ISBN: 978-0-494-16981-0

UNIVERSITÉ DE MONTRÉAL

ÉCOLE POLYTECHNIQUE DE MONTRÉAL

Cette thèse intitulée:

ION BOMBARDMENT EFFECTS IN LOW-PRESSURE PLASMAS: *IN SITU* SPECTROSCOPIC ELLIPSOMETRY AND MONTE-CARLO SIMULATION STUDY

présentée par: AMASSIAN Aram

en vue de l'obtention du diplôme de : Philosophiæ Doctor

a été dûment accepté par le jury d'examen constitué de:

M. YELON Arthur, Ph.D., président

M. MARTINU Ludvik, Ph.D., membre et directeur de recherche

M. DESJARDINS Patrick, Ph.D., membre et codirecteur de recherche

M. LEONELLI Richard, Ph.D., membre

M. ASPNES David E., Ph.D., membre

Dedication

I dedicate this thesis, all my past achievements and my future success to my parents Achod and Mona Amassian. They have started over their lives three times after loosing all possessions in the bloody civil war in Lebanon (1975 – 1990), my birthplace. I am eternally indebted for the sacrifices they have made to offer my brothers and myself the best quality of life possible by immigrating to Québec in 1990.

Also, this work is dedicated in memory of courageous intellectuals, journalists, and politicians all over the world, who have suffered and given their lives in peaceful efforts to achieve equality, human rights and self-determination for their fellow citizens.

"Errors, like Straws, upon the surface flow;
He who would search for Pearls must dive below."

- John Dryden (1631-1700), British poet, dramatist and critic

Acknowledgements

This work would not have been possible without the exceptional advisement, training, support, and encouragements by Profs. Ludvik Martinu and Patrick Desjardins. Thank you both for being excellent mentors and examples in my future academic endeavours.

Ludvik, I'm thankful to you for supporting my development and my work for so many years, for encouraging my participation to international conferences, for being so open to scientific collaborations often on divergent subjects, and for allowing me to indulge in teaching and lecturing undergrad and graduate students on a regular basis, which I enjoyed immensely.

Patrick, I'm grateful to you for taking the time to help me fine-tune my writing and presentation skills, and for always being an example of scientific excellence and integrity. I believe that these lessons will take me far in my career. Thank you for showing me the joys of scientific research and discovery. I had a lot of fun working on some challenging and complex problems with you.

I also wish to acknowledge former members of our group, the FCSEL, namely Drs. Daniel Poitras (NRC) and Dan Dalacu (NRC) for training me during my early years at École Polytechnique (and their last years as graduate students) in the design, fabrication and characterization of optical interference filters. This training led to my rapid development and helped me become a contributing member of the FCSEL. Thank you both for being excellent mentors and for your generosity.

Dr. Jolanta Sapieha (FCSEL, Department of Engineering Physics, École Polytechnique de Montréal), you have believed in me from the moment we met in 1998. Your

encouragements and praise in times of crisis or uncertainty have helped invigorate my confidence in myself at crucial times. I thank you for your continued trust and support.

A significant part of the work presented in this thesis has benefited from collaborations with two esteemed colleagues: Martin Svec (Department of Physics, J. E. Purkyne University, Czech Republic) and Richard Vernhes (FCSEL, Department of Engineering Physics, École Polytechnique de Montréal). Martin has contributed his computer programming skills to help adapt the TRIDYN simulation code to the case of a broadband energy ion source within a short span, which then permitted me to perform the simulation studies reported in Chapters 5 and 6. Richard, with whom I have enjoyed collaborating for many years and on a number of papers, has been gracious enough to share with me his unique plasma deposition system. It is in this system that we first manufactured together and engineered interfaces of dense/porous multilayers, which we monitored using *in situ* RTSE (see Chapter 7).

My thanks extend to other members of the FCSEL as well, with whom I had the pleasure to collaborate, namely Stéphane Larouche, Bill Baloukas, Jean-Michel Lamarre, Dr. Oleg Zabeida, and Dr. Pawel Jedrzejowski. We evolved together, and engaged in many fruitful discussions, which often resulted in interesting experiments and collaborative papers over the past five years. Life in the laboratory has been very enjoyable thanks to you.

Over the last four years, I have also collaborated with graduate students, researchers and faculty from outside École Polytechnique, and which have led to numerous publications (refer to section 1.7 for a full list of published, accepted and submitted papers). These collaborations have benefited from the characterization and *in situ* monitoring expertise developed during my thesis, and have contributed immensely to my development. I'd like to acknowledge all my co-authors affiliated to the following groups and institutions: the Tabbal group at the American University of Beirut (AUB, Beirut, Lebanon), the Chaker group at the Institut National de la Recherche Scientifique (INRS)-Énergie, Matériaux et

Télécommunications (Varenne, Québec), the Robbie group at Queens University (Kingston, Ontario), Dr. Kate Kaminska (formerly with Robbie's group) at the NRC (Ottawa, Ontario), and Suzuki's group at the Engineering Kyoto University (Kyoto, Japan).

The VASE and M-2000 ellipsometers, so important to this work and the methodology developed in Chapters 4 to 6, are produced by the J. A. Woollam company. John A. Woollam is thanked for the vision and drive behind this exemplary company. I'd like to extend warm thanks to some of my collaborators at the J. A. Woollam Co. over the years for developing excellent scientific instrumentation, analysis software and for providing timely and extensive support: Blaine Johs, James Hilfiker, Ping He, Tom Tiwald, Craig Herzinger, Mark Brayton, and Ron Synowicki.

I'd also like to acknowledge Prof. Dr. Wolfhard Möller, and Dr. Matthias Posselt of the Institute of Ion Beam Physics and Materials Research at Forschungzentrum Rossendorf (FZR, Dresden, Germany), for accepting to share with me a copy of the TRIDYN simulation code, and for providing timely technical support, as well as constructive criticism.

This work would not have been possible without the expert technical help of Gilles Jalbert (retired), who helped build both plasma reactors used for experiments performed in this thesis.

Members of the jury evaluating this thesis, namely Profs. Arthur Yelon, Richard Leonelli, David E. Aspnes, and Yves Audet, are thanked for accepting to read and to diligently review my work. I thank them all for their comments and their suggestions. I am particularly grateful to Prof. Aspnes for accepting to fly to Montréal from North Carolina to attend the defence.

During my long years at École Polytechnique, my fellow students and myself have benefited from the kind and generous help of Céline Labelle (Department of Engineering Physics, École Polytechnique de Montréal) and her administrative team. Thank you very much for always reaching out to us and helping us whenever the bureaucratic red tape needed to be untangled.

I'm grateful to the Natural Sciences and Engineering Research Council (NSERC) of Canada for honouring me with a two-year Post-Graduate Scholarship, and for continuing to fund my training and development as future scientist and scholar by endowing me with a two-year post-doctoral fellowship. The Fond Québécois de la Recherche sur la Nature et la Technologie (FQRNT) is also thanked for offering me a two-year post-doctorate fellowship, which I had to decline.

The Americal Vacuum Society (AVS), the Optical Society of America (OSA) and the Society of Vacuum Coaters (SVC) are thanked for offering me a total of 6 awards and grants in 5 years, and for allowing me to present my research at international venues.

Throughout the last 9 years, I have studied, then taught and worked in the Department of Engineering Physics at École Polytechnique de Montréal. I have interacted and worked with a large number of undergraduate and graduate students, post-doctorate fellows, researchers, faculty and administrative staff. I keep fond memories of all these years of academic, scientific and personal exchange. I feel pride and a great sense of belonging to the Engineering Physics department and the École Polytechnique community at large. I believe it is a premier institution with a great calling, and widespread contributions to the province of Québec, and to Canada as a whole. I hope to give back to this community in the future, and to make it proud as a token of gratitude to the education and sense of belonging that it has endowed me with.

As student-researcher, I have had the privilege to evolve within a great organisation, the Thin film group or *Groupe en recherche et technologie des couches minces* (GCM), combining faculty, research staff and students from both Université de Montréal and École Polytechnique de Montréal. The vision of the GCM was pioneered by Arthur Yelon, professor, and president of my thesis jury. I feel a great deal of gratitude to him and many other faculty members who share his vision vigorously. I feel a sense of pride for having been a junior member of the GCM throughout the years. Today, I share its vision of collaborative scientific research, and I take with me the lessons of teamwork and multi-scale collaborative research which have allowed me to thrive as a young scientist.

A thesis often becomes a struggle, as intellectual and personal boundaries are pushed continuously, and walls are broken down. In this respect, many friends and family have become over the years a part of my support system, as well as victims of my obsessive drive. I would like to recognize the sustained support by some close friends, such as Johny Sudah, Mike Daniel, Vera Kurkjian, Mira Abd-el Malek, Emna Kooli, Daria Obeka, as well as the Topouzian and Alexandrian families. I'm also grateful to Sabrina Percher, who has become the main pillar of my support system, especially in the final months of my PhD studies.

Résumé

Le dépôt par vapeur chimique assisté par plasma (PECVD) est un procédé très versatile. Il a attiré l'attention de la communauté des couches minces optiques en raison de sa capacité de fabriquer des revêtements ayant une gamme élargie et continue de propriétés optiques. Le contrôle accru des propriétés optiques des matériaux préparés par PECVD s'explique par la capacité de varier le mélange de précurseurs gazeux et les caractéristiques de la décharge. Comme pour la plupart des techniques de dépôt assistées par plasma ou par faisceau d'ions, le PECVD compte sur le bombardement ionique intense pour la fabrication – souvent à la température de la pièce – de revêtements optiques lisses et possédant des propriétés similaires à celles des matériaux massiques. Cependant, il s'agit d'un procédé fort complexe en raison de la gamme étendue d'espèces (neutres, radicaux, ions, électrons et photons) interagissant avec la couche en croissance et parce que le bombardement ionique à l'électrode alimentée par la puissance radio-fréquentielle (RF) est, en soi, complexe, puisqu'il possède une distribution énergétique (IEDF) très large et qu'il est composé à la fois d'ions atomiques et moléculaires (par exemple, O^+ et O_2^+ dans le cas d'une décharge RF dans l'O_2). Par conséquent, il existe un déficit important dans la compréhension détaillée des interactions entre le plasma et la surface aux diverses étapes de la croissance des couches minces dans un environnement plasma.

Dans ce travail, nous examinons les interactions ion-surface dans le cas d'ions hyperthermaux (10^0 eV à 10^3 eV) accélérés à l'électrode RF d'un réacteur PECVD dans le but de comprendre leurs effets sous la surface du substrat, lors de la croissance de couches minces et sur la formation d'interface. Nous utilisons la technique de monitoring *in situ* par ellipsometrie spectroscopique en temps réel (RTSE) :

(1) afin de suivre l'évolution des modifications à la surface de substrats modèles de c-Si(001) exposés au plasma à basse-pression d'O_2 à l'électrode alimenté RF en fonction de la tension d'auto-polarisation du porte-substrat (V_B);

(2) pour caractériser l'élargissement de l'interface lors des étapes initiales de la croissance de TiO_2 sur SiO_2;
(3) pour contrôler le traitement par plasma d'Ar de l'interface rugueuse entre des couches poreuses et denses de Si_3N_4, ce qui permet la croissance de multicouches denses/poreuses de bonne qualité.

Dans ce travail, nous avons également développé la capacité de simuler les interactions ion-surface en modifiant le simulateur de type Monte-Carlo bien connu TRIDYN – conçu pour calculer des modifications d'une cible exposée à une dose importance d'ions énergétiques – pour simuler des interactions dans le cas d'une source d'ions ayant une IEDF élargie. Cette nouvelle capacité a rendu possible l'étude du bombardement ionique à l'électrode RF par des simulations dynamiques quantitatives. Les simulations ont permis l'interprétation des résultats de RTSE *in situ* et la prédiction des effets du bombardement ionique sous la surface du substrat pendant le traitement par plasma et lors des premières étapes de croissance de couches minces.

La première partie de cette thèse traite des modifications d'un substrat de c-Si(001) exposé à l'électrode alimentée RF dans une décharge d'O_2. Les échantillons sont caractérisés *ex situ* par ellipsometrie spectroscopique à angle variable (VASE) après un traitement de 10 minutes à V_B entre -60 V et -600 V. Les résultats montrent l'existence de modifications importantes sous la surface du substrat, y compris la formation d'une couche d'oxyde en surface et d'une couche interfaciale fortement endommagée. La profondeur des modifications croît avec $\sim|V_B|^{1/2}$, augmentant de ~3,4 nm à ~9,6 nm pour la gamme de V_B étudiée. Des simulations Monte-Carlo TRIM statiques ont permis de confirmer que ces modifications peuvent être causées par le transport balistique de l'oxygène par implantation.

Dans la deuxième partie du travail, nous avons étudié les effets dynamiques des interactions plasma-surface en utilisant le diagnostic *in situ* RTSE en combinaison avec des

simulations TRIDYN. Les modifications au c-Si prédites par les simulations TRIDYN (dommage et oxydation) sont en très bon accord avec les résultats expérimentaux. Les dommages sont observés immédiatement après l'allumage du plasma (<1 s) pour une dose de ~5×10^{14} O cm^{-2}; l'oxydation débute à une dose plus élevée d'environ 2×10^{15} O cm^{-2} (~1 s – 2 s). Les modifications stagnent à forte dose (~10^{17} O cm^{-2}) puisque la profondeur des modifications atteint de manière asymptotique celle de pénétration maximale des ions, menant à un comportement autorégulé. L'accumulation d'oxygène et de dommages dans la cible est influencée par l'érosion de la surface (causée par la pulvérisation du Si); les simulations révèlent que l'érosion de la surface fait concurrence au transport balistique et notamment à l'accumulation d'oxygène en profondeur, ce qui mène alors à la formation d'une région pauvre en oxygène et fortement endommagée à l'interface SiO_2-Si.

Ayant examiné et compris le rôle des interactions ion-surface à l'électrode alimentée RF d'un réacteur PECVD et ayant validé les résultats des simulations en les comparant avec des résultats expérimentaux, nous avons étudié l'effet du bombardement ionique pendant le dépôt de couches minces de TiO_2 sur SiO_2 dans des conditions typiques (V_B = -450 V) par une combinaison de RTSE *in situ* et simulations TRIDYN. Dans le cas de la croissance à très faible taux de dépôt (r ~ 0,037 nm/s), l'analyse RTSE a révélé que la croissance survient sous la surface du SiO_2 lors des premiers nanomètres de dépôt et est suivie par la formation d'une interface élargie pendant la croissance subséquente de TiO_2. Les simulations révèlent que les atomes de Ti déposés en surface sont déplacés jusqu'à plusieurs nanomètres sous la surface de croissance sous l'effet de collisions par des ions énergétiques d'oxygène. Lors de la croissance subséquente du TiO_2 à température ambiante, le rapport de flux d'ions à celui de neutres (ϕ_i/ϕ_n) dicte l'élargissement de l'interface. Celui-ci procède principalement par mélange balistique des atomes à l'interface, en faisant abstraction des phénomènes chimiques et thermodynamiques. Des simulations effectuées sur une large gamme de valeurs de ϕ_i/ϕ_n ($0{,}06 \leq \phi_i/\phi_n \leq 6$) indiquent que la largeur d'interface est proportionnelle à $\sim(\phi_i/\phi_n)^{1/2}$. En pratique, nous avons trouvé qu'en

maintenant $r > 1$ nm/s ($\phi_i/\phi_n \sim 0{,}025$ à $V_B = -450$ V) l'interface reste plus étroite que 1 nm. De plus, les simulations révèlent que le taux de dépôt détermine si la croissance sera dominée par le dépôt *sur* ou *sous* la surface. Si $r \leq 0{,}1$ nm/s (à $V_B = -450$ V), tous les atomes déposés en surface sont déplacés en volume au moins une fois par le bombardement ionique.

Finalement, nous avons contrôlé la microstructure des couches minces de Si_3N_4 en les déposant dans des décharges microonde (MW) et RF. L'énergie moyenne des ions (E_m) dans une décharge MW est très faible (< 10 eV), ce qui mène, à température ambiante, à la formation de couches minces poreuses avec une rugosité de surface importante. Au contraire, les couches minces déposées à l'électrode alimentée RF sont bombardées avec $E_m > 100$ eV et sont très denses. La compréhension des interactions plasma-surface à l'électrode alimentée RF développée dans la première partie de cette étude a permis de proposer et de tester une procédure d'ingénierie d'interface. Un traitement par plasma d'argon est employé afin de densifier et de lisser la surface des couches poreuses de Si_3N_4. Ceci permet alors la croissance de couches minces de Si_3N_4 denses, homogènes et lisses, et prévient la propagation de la morphologie rugueuse de la couche précédente.

Condensé en français

Les revêtements optiques sont omniprésents dans plusieurs applications, y compris des applications ophtalmiques, décoratives, de contrôle d'énergie, d'affichage, de dispositifs de sécurité et en particulier des filtres optiques interférentiels (OIFs). Ces derniers sont utilisés en optique, photonique et en télécommunication par fibres optiques. La grande majorité des dispositifs à base de revêtements optiques, y compris les OIFs, sont composés d'un agencement en multicouches de matériaux transparents d'indice de réfraction (n) élevé et faible, ce qui favorise les réflexions d'ondes électromagnétiques aux multiples interfaces. Le dénominateur commun à tous les revêtements optiques multicouches est un besoin inhérent de contrôler leur épaisseur, leur microstructure et leurs propriétés d'interface pour ainsi obtenir la réponse optique désirée. La communauté des revêtements optiques manufacture en général ces couches minces par dépôt par vapeur physique (PVD) et utilise le bombardement ionique à la surface de la couche en croissance afin d'assurer la croissance de revêtements optiques denses et lisses.

Nous avons développé, au Laboratoire des revêtements fonctionnels et ingénierie d'interface (LaRFIS), un procédé de dépôt chimique en phase vapeur assisté par plasma (PECVD) pour la fabrication de revêtements optiques. Ce procédé est versatile grâce à l'utilisation de précurseurs gazeux – plutôt que de cibles solides tel que dans le cas du PVD – et de décharges plasmas variées [par exemple, micro-onde (MW) et radiofréquence (RF)]. Le PECVD permet donc de fabriquer des mélanges chimiques de matériaux, comme des oxydes d'indices élevés et faibles (par exemple, TiO_2 et SiO_2), pour obtenir des indices de réfraction (n) intermédiaires, ainsi que des matériaux microstructurés dont la densité est contrôlée en fonction de l'épaisseur. Les revêtements optiques denses fabriqués par PECVD sont déposés en présence de bombardement ionique dans des conditions similaires à celles des procédés PVD, qui sont déjà étudiés et bien compris. Cependant, la source de la distribution énergétique du bombardement ionique à l'électrode alimentée RF –

Abstract

Plasma-enhanced chemical vapor deposition (PECVD) is a very versatile, yet highly complex process which has attracted the attention of the optical coatings community for its ability to synthesize thin film materials with a wide and continuous range of optical properties. The tunability of materials prepared by PECVD strongly depends on the ability to vary gas-phase precursor mixtures and discharge characteristics. As in the case of most plasma-assisted and ion-assisted deposition techniques, PECVD also relies on intense ion bombardment to manufacture smooth optical coatings with bulk-like optical properties at room temperature. However, the process itself is quite complex, owing to the wide spectrum of species (neutrals, radicals, ions, electrons, and photons) interacting with the growing film, and because ion bombardment is inherently complex at the radiofrequency-(RF) powered electrode as a result of a very broad ion energy distribution function (IEDF), composed of atomic and molecular ions. Consequently, there is still a considerable lack of understanding of the detailed interactions between the plasma and the surface at various stages of thin film growth in the plasma environment.

In this work, we investigate the effects of ion-surface interactions in the case of hyperthermal ions (10^0 to 10^3 eV) accelerated at the RF-biased electrode of a PECVD reactor, in order to better understand their effect beneath the substrate surface, on growing films, and on interface formation. We apply *in situ* real-time spectroscopic ellipsometry (RTSE): (1) to monitor modifications at the surface of model c-Si(001) substrates exposed to low-pressure O_2 plasma at the RF-powered electrode as a function of substrate bias voltage (V_B), (2) to determine interface broadening during the initial stages of TiO_2 deposition on SiO_2, and (3) to monitor the Ar plasma treatment of the interface between porous and dense Si_3N_4 films, and its effect on the growth of multilayer dense/porous stacks.

As part of this work, we have also developed a capability to simulate ion-surface interactions by modifying the well-known Monte-Carlo TRIDYN simulator to work in the case of a broadband energy ion source, such as at the RF-powered electrode in a RF discharge. This has enabled quantitative dynamical simulation studies of the ion bombardment at the RF-powered electrode, which is essential to the interpretation of *in situ* RTSE results and for calculating the effects of plasma-surface interactions on sub-surface modifications during plasma treatment and the early stages of thin film deposition.

The first part of this thesis focuses on the modifications of a c-Si substrate resulting from an exposure to an O_2 plasma at the RF-powered electrode by using *ex situ* variable angle spectroscopic ellipsometry (VASE). The study demonstrates the presence of significant sub-surface modifications, giving rise to a top layer oxide (SiO_2) and an interfacial damage layer on c-Si(001). The depth of modifications was found to scale with $\sim|V_B|^{1/2}$, increasing from ~3.4 nm up to ~9.6 nm for V_B ranging between -60 and -600 V after 10 minutes of plasma exposure. Static Monte-Carlo TRIM simulations confirmed that the modifications and scaling can be explained on the basis of depth-dependent O transport by ion implantation.

In the second part of this work, we studied the dynamical effects of plasma-surface interactions by using *in situ* RTSE in combination with TRIDYN (a dynamical version of TRIM) simulations. TRIDYN simulations without any fitting parameter were found to be in excellent quantitative agreement with RTSE results. The modifications of c-Si are observed immediately following plasma ignition (< 1 s), with significant damage first observed after a fluence of $\sim 5\times10^{14}$ O cm^{-2}; the onset of oxidation is observed at a slightly higher fluence of $\sim 5\times10^{15}$ O cm^{-2}. Modifications saturate at high fluence ($\sim10^{17}$ O cm^{-2}) where the depth of modifications converges towards the maximum ion penetration depth, leading to a steady-state modification structure as a result of the self-limiting oxide growth behavior. The accumulation of O and damage in the target are strongly affected by surface recession (due to sputtering); simulations confirm that the surface recession competes with depth-

dependent ballistic transport of O ions and damage formation at the SiO_2-Si interface to broaden the O-deficient interfacial damage layer at steady-state.

Having investigated and understood the role of ion-surface interactions at the RF-powered electrode of a PECVD reactor, and having corroborated the experimental results with quantitatively accurate dynamical simulations, we have studied the effect of ion bombardment during the deposition of TiO_2 films on SiO_2 at an elevated substrate bias (V_B = -450 V). At very low deposition rate (R), *in situ* RTSE revealed that TiO_2 growth occurs below the SiO_2 surface during the first nanometers of deposition, followed by continued interface broadening during the subsequent growth of TiO_2. Simulations reveal that Ti atoms deposited at the surface are in fact subplanted as a result of intense oxygen ion bombardment, which displaces a large fraction of the deposited atoms many nanometers below the growth surface. During the subsequent TiO_2 deposition at low temperature, the ion-to-neutral arrival rate ratio (ϕ_i/ϕ_n) dictates the interfacial broadening, that predominantly proceeds by ballistic mixing, with minimal effects by chemical driving forces. Simulations performed over a broad range of ϕ_i/ϕ_n values ($0.06 \leq \phi_i/\phi_n \leq 6$) indicate that the interface width scales as $\sim(\phi_i/\phi_n)^{1/2}$. In practical terms, we find that keeping $R > 1$ nm/s ($\phi_i/\phi_n \leq 0.025$ at V_B = -450 V) limits interface thickness to below ~1 nm. The deposition rate also determines whether the growth is dominated by surface or sub-surface growth; simulations reveal that for $R \leq 0.1$ nm/s (at V_B = -450 V), all deposited atoms are displaced into the bulk at least once by impinging ions.

Finally, we have used ion bombardment to tailor the microstructure of Si_3N_4 thin films by depositing them in microwave (MW) and RF discharges. Mean ion energy (E_m) in a MW plasma is very low (< 10 eV), leading to the formation of underdense films with high surface roughness at room temperature, whereas RF-deposited films are bombarded at $E_m >$ 100 eV, and are very dense. The understanding of plasma-surface interactions at the RF-powered electrode has permitted the development of an interface engineering procedure, where Ar plasma treatment is used to densify and smoothen the surface of porous Si_3N_4

thin films used. This in turn permits the growth of dense, homogeneous and smooth $SiN_{1.3}$ films on porous films, by inhibiting the propagation of the underdense morphology, and makes interface engineering essential for the manufacture of "single-material" multilayer optical interference filters.

typiquement utilisée pour la fabrication de couches de qualité optique par PECVD – est très large. Ses caractéristiques, telles la largeur de la distribution énergétique (IEDF), l'énergie moyenne (E_m) et le flux (ϕ_i) dépendent de paramètres externes, dont la pression (p) et le potentiel d'autopolarisation (V_B). Ceci complique le comportement du bombardement ionique dans le milieu PECVD et rend difficile d'étendre les leçons acquises du PVD à ce procédé. Outre le bombardement ionique, les interactions plasma-surface sont multiples et complexes. Elles incluent des neutres, des radicaux chimiques, des électrons (primaires et secondaires) et des photons. Les réactions chimiques en surface sont fort complexes, ce qui constitue un obstacle important au développement d'une compréhension quantitative du rôle du bombardement ionique dans le procédé PECVD.

Il existe donc un réel besoin de développer une compréhension approfondie et quantitative de l'influence du bombardement ionique dans le procédé PECVD. Le but de cette thèse est de contribuer à répondre à ce besoin, en se concentrant plus spécifiquement sur l'effet des ions sous la surface. Les objectifs de la thèse sont :

(1) de développer une méthodologie expérimentale qui permette de diagnostiquer les interactions ion-surface à l'électrode alimentée RF;

(2) d'étudier l'effet de ces interactions *in situ* et en temps réel sur une échelle de temps pertinente aux procédés plasma;

(3) de combiner la méthodologie expérimentale et des simulations permettant de calculer les interactions ion-surface dans le cas d'une source RF ayant un IEDF large et de prédire correctement l'influence du bombardement ionique;

(4) d'utiliser la combinaison du diagnostic *in situ* et des simulations pour étudier les effets des interactions ion-surface lors des étapes initiales de la croissance de couches minces, y compris sur l'élargissement de l'interface et sur le dépôt sous la surface;

(5) d'améliorer les propriétés microstructurales, optiques et d'interfaces de couches minces microstructurées denses/poreuses utilisées dans des OIFs.

Nous utilisons le monitoring *in situ* par ellipsométrie spectroscopique en temps réel (RTSE) pour suivre l'évolution des modifications à la surface de substrats modèles de c-Si(001), exposés au plasma à basse-pression d'O_2 à l'électrode alimenté RF en fonction de V_B. Nous utilisons des conditions typiques pour le dépôt de revêtements optiques, c'est-à-dire V_B entre -60 V et -600 V et p = 20 mTorr. Par la suite, nous employons TRIDYN afin de simuler par la méthode Monte-Carlo les interactions ion-surface dans le cas d'une source ayant une IEDF élargie. Nous pouvons ainsi interpréter les résultats RTSE et contribuer à élucider les mécanismes d'interaction ion-surface au niveau de processus atomiques.

L'ellipsométrie spectroscopique est une technique de caractérisation optique mesurant le changement de l'état de polarisation de la lumière lors de la réflexion à la surface de l'échantillon. Elle est sensible à toute modification de la surface de l'échantillon – avec une précision de l'ordre d'une sous-monocouche atomique – qui mène à des changements caractéristiques de la réponse optique. La modélisation optique permet de quantifier les modifications proches de la surface au niveau structurel et chimique. L'ellipsométrie spectroscopique est utilisée depuis des décennies par l'industrie de la micro-électronique pour déterminer le profil d'endommagement et d'oxydation de cibles monocrystallines, telles le c-Si, suite à une exposition à un faisceau d'ions d'énergie entre plusieurs keV à plusieurs centaines de keV.

Nous avons donc décidé d'étudier les interactions plasma-surface dans le cas d'un substrat modèle de c-Si(001) pour une panoplie de raisons dont les deux principales sont que (1) son comportement d'endommagement et d'oxydation sont bien connus et compris en présence d'un faisceau d'ions et (2) que la réponse optique du Si varie fortement selon la phase et l'environnement chimique. Ainsi, n et k (le coefficient d'extinction) du c-Si, du Si amorphe (a-Si) et du SiO_2 sont très différents dans l'ultraviolet (UV), le visible et le proche infrarouge (NIR), ce qui favorise la détection des modifications par l'ellipsométrie spectroscopique.

Le simulateur TRIDYN calcule les changements dynamiques de l'épaisseur et des profils de composition d'une cible ayant plusieurs composants atomiques lors de l'implantation d'ions mono-énergétiques à dose élevée. Ce simulateur est une version dynamique du logiciel très populaire TRIM, fondé sur l'approximation de collisions binaires (BCA). TRIDYN calcule les profils en profondeur des espèces atomiques, le taux de pulvérisation, la densité surfacique des espèces, ainsi que l'érosion et les changements d'épaisseur de la cible en fonction de la dose implantée.

Nous avons développé une nouvelle capacité de simuler les interactions ion-surface en modifiant le logiciel TRIDYN pour calculer des modifications d'une cible exposée à une dose importance d'ions énergétiques possédant une IEDF élargie. Cet outil a permis l'étude du bombardement ionique à l'électrode RF par des simulations dynamiques quantitatives. Celle-ci est essentielle à l'interprétation des résultats de RTSE *in situ* et pour calculer et prédire les effets du bombardement ionique sous la surface d'un substrat ou d'une couche mince pendant le traitement par plasma et lors des premières étapes de croissance d'une couche mince.

La première partie de cette thèse traite des modifications d'un substrat de c-Si(001) résultant d'une exposition à l'électrode alimentée RF dans une décharge en O_2, en utilisant l'ellipsométrie spectroscopique à angle variable (VASE). En particulier, nous avons développé un modèle optique suffisamment flexible et robuste pour décrire quantitativement les changements de la réponse optique suite aux modifications de la surface de c-Si. Les résultats démontrent la présence de modifications significatives sous la surface du substrat : la formation d'une couche d'oxyde (SiO_2) en surface et d'une couche interfaciale fortement endommagée. Cette couche peut-être modélisée optiquement par un mélange de c-Si, a-Si et SiO_2, qu'on peut représenter par l'approximation du milieu effectif de Bruggeman (BEMA). Après 10 minutes d'exposition au plasma RF d'O_2, la profondeur des modifications croît avec $\sim|V_B|^{½}$, passant de ~3.4 nm lorsque V_B = -60 V à ~9.6 nm lorsque V_B = -600 V; l'épaisseur de la couche interfaciale augmente de ~1.4 nm à ~3.5 nm

dans ces mêmes conditions. Cette relation est consistante avec un transport balistique limité par des intéractions nucléaires entre les ions et les atomes de la cible. Des simulations TRIM de type Monte-Carlo statique ont permis de confirmer que les modifications sont causées principalement par le transport balistique de l'oxygène par implantation.

Dans la seconde partie de ce travail, nous avons étudié la dynamique des interactions plasma-surface en utilisant le diagnostique *in situ* RTSE en combinaison avec les simulations TRIDYN modifiées décrites ci-haut. L'analyse *in situ* a permis de vérifier la validité du modèle ellipsométrique *ex situ* et de révéler la dynamique de formation des modifications sous la surface. Les simulations TRIDYN – basées uniquement sur l'interaction ions-surface – ont réussi à prédire toutes ces modifications et montrent un accord exceptionnel avec les résultats expérimentaux. L'endommagement du c-Si est observé immédiatement après l'allumage du plasma (<1 s) pour une dose de ~5×10^{14} O cm^{-2} alors que l'oxydation est initiée à partir d'une dose un peu plus élevée de ~2×10^{15} O cm^{-2} (~1 – 2 s). L'oxyde croît pendant près d'une minute et atteint asymptotiquement une épaisseur limite, égale à la profondeur maximale de pénétration des ions sous la surface. Les modifications stagnent à haute dose (~10^{17} O cm^{-2}) et le gonflement du volume implanté de la cible est remplacé par l'érosion de la surface par pulvérisation du Si. Les simulations TRIDYN révèlent que le profil d'implantation d'oxygène et de formation de dommage dépend du IEDF de la source plasma. Elles démontrent également que l'accumulation d'oxygène et de dommage est inhibée dans le régime dominé par l'érosion de surface (>10^{17} O cm^{-2}), menant ainsi à la formation d'une zone interfaciale élargie, partiellement endommagée et pauvre en oxygène.

Ayant examiné et compris le rôle des interactions ion-surface à l'électrode alimenté RF d'un réacteur PECVD, et ayant confirmé l'exactitude des simulations en effectuant une comparaison systématique avec les résultats expérimentaux, nous avons étudié l'effet du bombardement ionique lors du dépôt de couches minces de TiO_2 sur SiO_2. Après avoir

obtenu la couche de SiO_2 par oxydation plasma de c-Si, nous avons déposé le TiO_2 dans des conditions typiques, i.e. V_B = -450 V et p = 20 mTorr à la température de la pièce. Lorsque le taux de dépôt est très faible ($r \sim 0.037$ nm/s), l'analyse RTSE *in situ* révèle que la croissance des premiers nanomètres de TiO_2 survient sous la surface de SiO_2, menant à la formation d'une interface élargie entre le TiO_2 et le SiO_2. L'élargissement se déroule principalement au début de la croissance, mais les simulations révèlent que des ions énergétiques du IEDF (notamment les ions O^+) continuent de pénétrer jusqu'à la profondeur de l'interface et d'y mélanger les atomes de Ti et Si pendant le dépôt subséquent du TiO_2. Les effets du mélange ionique se font surtout sentir lorsque r est faible ($r < 0.1$ nm/s) et ϕ_i/ϕ_n est élevé. Les simulations révèlent également que les atomes de Ti normalement adsorbés ou chimisorbés en surface sont aussitôt déplacés par le bombardement ionique à plusieurs nanomètres sous la surface de la couche croissante.

Les simulations de la croissance révèlent que le rapport entre le flux d'ions à celui des neutres (ϕ_i/ϕ_n) dicte l'élargissement de l'interface. Des simulations effectuées sur une large gamme de valeurs de ϕ_i/ϕ_n ($0{,}06 \leq \phi_i/\phi_n \leq 6$) indiquent que la largeur d'interface est proportionnelle à $\sim(\phi_i/\phi_n)^{1/2}$, évoluant de ~0,7 nm à ~7 nm pour la gamme de ϕ_i/ϕ_n étudiée. En pratique, nous avons trouvé qu'en maintenant $r > 1$ nm/s ($\phi_i/\phi_n \sim< 0{,}025$) à V_B = -450 V, l'élargissement d'interface par mélange balistique reste à en deçà de ~1 nm.

Les simulations ont également révélé que r détermine si la croissance est en fait dominée par le dépôt en surface ou au-dessous de celle-ci. Si $r \leq 0{,}1$ nm/s (à V_B = -450 V), presque tous les atomes déposés en surface sont déplacés en volume au moins une fois par le mélange balistique des atomes, ce qui mène à un mécanisme de croissance en volume, mettant en doute les modèles de croissance en surface dans ce cas. Le mécanisme de croissance est dominé par les processus surfaciques lorsque le taux de croissance est accru (en diminuant ϕ_i/ϕ_n). Ces conclusions sont d'autant plus significatives que les conditions de

bombardement ionique (ϕ_i/ϕ_n et E_m) dans ce travail sont similaires à celles utilisées par la communauté des revêtements optique dans les procédés PVD assistés par ions.

Dans la troisième et dernière partie de ce travail, nous avons employé le bombardement ionique pour modifier la morphologie de couches minces denses de Si_3N_4 déposées sur des couches poreuses et rugueuses de Si_3N_4. À l'origine, la morphologie et la densité des couches minces dépend du bombardement ionique. Dans le procédé PECVD, nous avons la possibilité de contrôler le bombardement ionique en alternant ou en combinant des décharges MW et RF. Une décharge MW est caractérisée par un E_m très faible ($E_m < 10$ eV), plus petit que E_D, seuil énergétique de déplacement d'un atome en volume, situé en général entre 12 et 80 eV. En l'absence de déplacements atomiques en volume, les couches sont poreuses et développent une rugosité de surface importante. En comparaison, les couches minces déposées à l'électrode alimentée RF sont bombardées par $E_m \sim 100$ eV $>> E_D$ et sont par conséquent très denses. Le problème survient lorsque l'on tente de déposer les couches denses sur les couches poreuses. Les couches denses ont alors un n inférieur à la valeur massique, sont inhomogènes en profondeur et sont très rugueuses (encore plus que la couche poreuse d'origine).

La compréhension des interactions plasma-surface à l'électrode alimentée RF développée dans la première partie de cette étude a permis de développer une procédure d'ingénierie d'interface, par laquelle un traitement par plasma d'Ar (V_B = -580 V) est employé pour densifier et lisser la surface de couches minces poreuses de Si_3N_4 et ainsi les préparer pour le dépôt de couches denses. La préparation de la surface par plasma d'Ar favorise la croissance de couches minces denses, homogènes et lisses de Si_3N_4, en empêchant la propagation de la morphologie rugueuse de la couche précédente. Ceci fait de l'ingénierie d'interface une étape indispensable à la fabrication de filtres interférentiels multicouches à base de matériaux microstructurés denses et poreux.

Le message principal qui ressort de cette étude est que *bien des choses se produisent sous la surface* d'un substrat ou d'une couche mince en croissance à l'électrode alimentée RF. Ainsi, cette étude a démontré que le bombardement ionique mène *inévitablement* à des modifications significatives sous la surface sur une échelle de temps très courte (< 1 à 2 s), à un changement du mécanisme de croissance et de la microstructure des couches minces en raison du mélange balistique d'atomes déposés et à l'élargissement de l'interface dans le cas de multicouches en raison du mélange balistique d'atomes à l'interface.

Nous avons œuvré à étudier et à comprendre l'effet du transport balistique sous la surface de croissance sur l'endommagement, le changement de composition, ainsi que l'élargissement et le contrôle d'interfaces. Notre étude a permis d'adapter un outil de simulation Monte-Carlo pour prédire quantitativement l'influence d'interactions ion-surface dans des procédés de dépôt par plasma. Cependant, il reste à développer une compréhension plus poussée et détaillée de la formation de couches minces lorsqu'elles croissent en présence de bombardement ionique intense, comme nous l'avons étudié et simulé jusqu'ici. Dans ce sens, nous suggérons une étude poussée de la germination, de la coalescence et de la croissance massique – par exemple par une combinaison de microscopie à force atomique (AFM) et par microscopie électronique à transmission (TEM) – serait prescrite afin de comprendre comment les étapes de la croissance sont influencées par le bombardement ionique intense.

La similitude de certaines caractéristiques de base du bombardement ionique, telles l'E_m et le ϕ_i/ϕ_n, entre les procédés PECVD et PVD assistés par plasma ou par faisceau d'ions suggère que les conclusions de cette étude pourraient être étendues à ce dernier, suggérant ainsi que les mécanismes de croissance de revêtements optiques, souvent axés sur les processus de transport en surface dans ces deux procédés, méritent d'être révisées.

Table of Contents

List of Tables

List of Figures

List of Symbols and Abbreviations

$\langle\varepsilon\rangle$	Complex pseudo-dielectric function
δ	Dirac delta
Δ	Ellipsometric angle, delta
$\Delta\varepsilon_2$	Differential peak height of the imaginary part of the dielectric function
Δ_i^{exp}	i^{th} delta measurement
Δn	Birefringence
Δ_i^{mod}	i^{th} delta calculation
Δ_{off}	Delta offset
ΔR_p	Straggle
$\Delta\Phi$	Differential fluence
Δx^0	Initial slab thickness
ε	Complex dielectric function
ε_0	Permittivity of vacuum
ε_1	Real part of the dielectric function
ε_2	Imaginary part of the dielectric function
ε_a	Dielectric function of material a
ε_b	Dielectric function of material b
ε_{eff}	Effective dielectric function
θ	Angle of incidence
λ	Wavelength
λ_0	Interatomic distance
Φ	Ion fluence
ϕ_i	Ion flux
ϕ_n	Neutral flux

ϕ_i/ϕ_n	Ion-to-neutral arrival rate ratio
ρ	Mass density
$\widetilde{\rho}$	Ellipsometric ratio
Ψ	Ellipsometric angle, psi
Ψ_i^{exp}	i^{th} psi measurement
Ψ_i^{mod}	i^{th} psi calculation
σ_a	Amorphization cross-section
σ_s	Cross-section for stimlated amorphization
χ	Chi
D	Atomic density
dpa	Displacement per atom
$d\sigma$	Interaction cross-section
e	Electron charge
E	Photon energy
E'	Integration variable of photon energy
E_a	Energy density in units of eV per atom
E_C	Conduction band energy
E_{CV}	Energy separation between valence and conduction bands
E_D	Bulk displacement energy
E_i	Ion energy
E_m	Mean ion ernergy
E_{max}	Maximum ion energy
E_s	Surface binding energy
E_V	Valance band energy
f_a	Calculated amorphization fraction
$f_{a\text{-}Si}$	a-Si fraction in DL
$f_{c\text{-}Si}$	c-Si fraction in DL

f_{SiO2}	SiO_2 fraction in DL
g_C	Conduction band DOS
g_i	JDOS
g_V	Valance band DOS
$\hbar$	Plank constant
k	Extinction coefficient
$\vec{k}$	Electron wavevector
K	Proportionality constant
M_i	Atomic weight of the i^{th} element
n	refractive index
$\tilde{n}$	complex n
N	Total number of spectral pairs
n_1	n of material 1
n_2	n of material 2
n_{550}	n at $\lambda = 550$ nm
n_{bulk}	n of bulk $\lambda = 550$ nm
n_e	Extraordinary n
N_H	Number of projectiles
N_i	Number of ions
N_{IV}	Number of IV pairs
n_o	Ordinary n
n_{OL}	n of the OL $\lambda = 550$ nm
n_{SiO2}	n of SiO_2 $\lambda = 550$ nm
n_{TiO2}	n of TiO_2 at $\lambda = 550$ nm
n_{void}	n of void
$n(z)$	n depth profile
p	pressure
P	Number of fit parameters

	Cauchy principal value of the integral
p_1	Fraction of component 1
p_2	Fraction of component 2
P_a	Production term for direct amorphization
	Fraction of component a
P_{CV}	Momentum matrix element of the electronic transition from valence to conduction bands
P_i	Amorphous production term for the i^{th} process
p_{O2}	O_2 partial pressure
P_s	Production term for stimulated amorphization
p_{TiCl4}	$TiCl_4$ partial pressure
r	Deposition rate
R	RMA surface roughness
R_i	Range of an individual atom
$\tilde{r}_p$	Complex Fresnel reflection coefficient of the p-polarization
R_p	Range of ions
$\tilde{r}_s$	Complex Fresnel reflection coefficient of the s-polarization
R_S	Sputtering rate
S_e	Electronic cross-section
S_E	Constant-energy surface of an electronic band
S_n	Nuclear cross-section
t	Thickness
	Time
T	Kinetic energy
$t_{interface}$	Interface thickness
t_{IL}	Interfacial layer thickness
t_{DL}	Damage layer thickness
T_m	Melting temperature

T_s/T_m	Reduced temperature
T_{max}	Maximum kinetic energy
t_{OL}	OL thickness
t_{OL1}	OL thickness in state 1
t_{OL2}	OL thickness in state 2
t_p	Porous film thickness
T_s	Substrate temperature
t_{TL}	Top layer thickness
t_{TiO2}	TiO_2 thickness
V_B	Substrate self-bias
V_p	Plasma potential
Y_{Si}	Si sputtering yield
x	Ti molar fraction
z	Depth

AFM	Atomic force microscopy
BCA	Binary collision approximation
BEMA	Bruggeman effective medium approximation
CAD	Computer assisted design
c/a	Crystalline/amorphous
CCD	Charge coupled device
CFI	Canadian Foundation for Innovation
d-	Dense-
DF	Damage fraction
D-I/D-S	Direct-impact and defect-stimulated
DL	Damage layer
DLC	Diamond-like carbon
DOS	Density of states
DWDM	Dense wavelength division multiplexer

EDIP	Environment-dependent interatomic potential
EELS	Electron energy loss spectroscopy
EM	Electromagnetic
EMA	Effective medium approximation
FCSEL	Functional Coatings and Surface Engineering Laboratory
FQRNT	Fond Québécois de la Recherche sur la Nature et la Technologie
FZR	Forschungszentrum Rossendorf
GFF	Gain flattening filter
GLAD	Glancing angle deposition
HF	Hydrofluoric acid
IB	Ion bombardment
IBAD	Ion beam assisted deposition
IBO	Ion beam oxidation
IEDF	Ion energy distribution function
IL	Interfacial layer
INRS	Institut National de la Recherche Scientifique
IP	Ion plating
IR	Infrared
ITO	Indium-doped tin oxide
IV	Interstitial-vacancy
JDOS	Joint density of states
K-K	Kramers-Kronig
KMC	Kinetic Monte-Carlo
KP	Kinchin-Pease
LaRFIS	Laboratoire de revêtements fonctionnels et ingénierie de surface
LEED	Low-energy electron diffraction
MC	Monte-Carlo
MD	Molecular dynamics
MW	Microwave

NIR	Near infrared
NRC	National Research Council
NSERC	Natural Sciences and Engineering Research Council
OE	Oxidation efficiency
OEDF	Oxygen energy distribution function
OIF	Optical interference filter
OL	Overlayer
OSA	Optical Society of America
OT	Optical thickness
p-	Porous-
PECVD	Plasma-enhanced chemical vapor deposition
PIII	Plasma immersion ion implantation
PLZT	Lanthanum-modified lead zirconium titanate
PVD	Physical vapor deposition
RF	Radiofrequency
RTSE	Real-time spectroscopic ellipsometry
R&D	Research and development
RAE	Rotating analyzer ellipsometer
RBS	Rutherford backscattering spectroscopy
RCE	Rotating compensator ellipsometer
RIE	Reactive ion etching
RMS	Root mean square
RQMP	Regroupement québécois sur les matériaux de pointe
T-III	Tersoff-III
TL	Top layer
UV	Ultraviolet
SE	Spectroscopic ellipsometry
SIMS	Secondary ion mass spectroscopy
SRIM	Stopping and range of ions in matter

STO	Strontium titanate
SW	Stillinger-Weber
SZM	Structure zone model
TEM	Transmission electron microscopy
TRIDYN	Dynamic TRIM
TRIM	Transport and range of ions in matter
UHV	Ultra-high vacuum
UMS	Unbalanced magnetron sputtering
VASE	Variable angle spectroscopic ellipsometry
XPS	X-ray photoelectron spectroscopy
XTEM	Cross-section TEM
ZBL	Ziegler-Biersack-Littmark

Chapter 1. Introduction

1.1 Importance of Optical Coatings

Thin films are the basic building blocks of devices and systems such as integrated circuits, micro- and nano-electromechanical systems, optical filters, anti-counterfeiting color-shifting security devices, wear- and corrosion-resistant coatings, hard coatings, and thermal barrier coatings. As such, they have become critical components of modern information technologies, and they have led to the success of many current industries.

Optical network applications which enable digital transmission of voice, video and data across the internet, have been one of the markets with the highest margins and fastest growth for thin film technology. Ground-based telecommunication networks are essential to the day-to-day connectivity of most businesses, institutions, and billions of consumers worldwide. They require complex filters for long-range transmission of multi-channel signals along optical fibres.

The push toward global connectivity has driven an upsurge in thin film-based optical interference filter (OIF) demand, and fuelled a worldwide research and development (R&D) effort. In Canada, technology firms such as Nortel and JDS-Uniphase have played a leading role in these R&D efforts and, as a result, they have successfully acquired a large market share in the global telecom components sector. OIFs [1, 2, 3] have been the technology of choice, because of their unparalleled filtering capability; with devices such as dense wavelength division multiplexers (DWDM) [4] and gain flattening filters (GFF) [5] contributing to the steady increase of bandwidth and range of fibre-based data transmission.

The OIF device is placed in the pathway of electromagnetic (EM) radiation (e.g. between two optical fibres) in order to alter its spectral, polarization and phase characteristics upon reflection off – or transmission through – the device. An OIF is constructed by stacking

transparent thin films, which are typically oxides and sometimes nitrides and fluorides of semi-conducting elements and transition metals. Alternating high- and low-refractive index (n) coatings in a multilayer stack produces multiple internal reflections of the EM radiation, which can interfere constructively or destructively depending on the phase conditions. The interference conditions can be shaped to be constructive and/or destructive in a spectrum-dependent manner by tailoring the thickness of individual layers of the stack to be quarter wave or half wave optical thickness.

Despite a slowing down of the telecom sector in recent years, optical coatings and OIFs still enjoy a great deal of interest, especially due to the emergence of new markets, such as in the biomedical, astronomical, energy control, display, and security sectors [6].

1.2 Challenges for the 21st Century

The R&D efforts over the past decade have led to new developments at all levels of OIF technology, including computer assisted design (CAD) tools, new materials and fabrication processes, *in situ* monitoring and process control.

Traditional quarter-wave design methods have evolved towards computer-based numerical synthesis techniques, such as Flip-Flop [7] and Needle [8, 9], that can numerically build an OIF with almost any desired optical response. These numerical syntheses methods are quite powerful as they have been instrumental in the production of so-called "perfect antireflection coatings", which transmit light at a wide range of angles and over a broad wavelength spectrum [10]. Naturally, this requires that a large range of materials with tailored optical properties be available for deposition [11], and that fabrication processes enable their controlled deposition over a wide range of thicknesses [from nanometer (ultra-thin films, < 10 nm) to micrometer scales] with minimal interface broadening and constant refractive index (n) with depth. Figure 1.1 illustrates some of the requirements in the design of a numerically synthesised broad-band anti-reflective OIF. The filter incorporates four

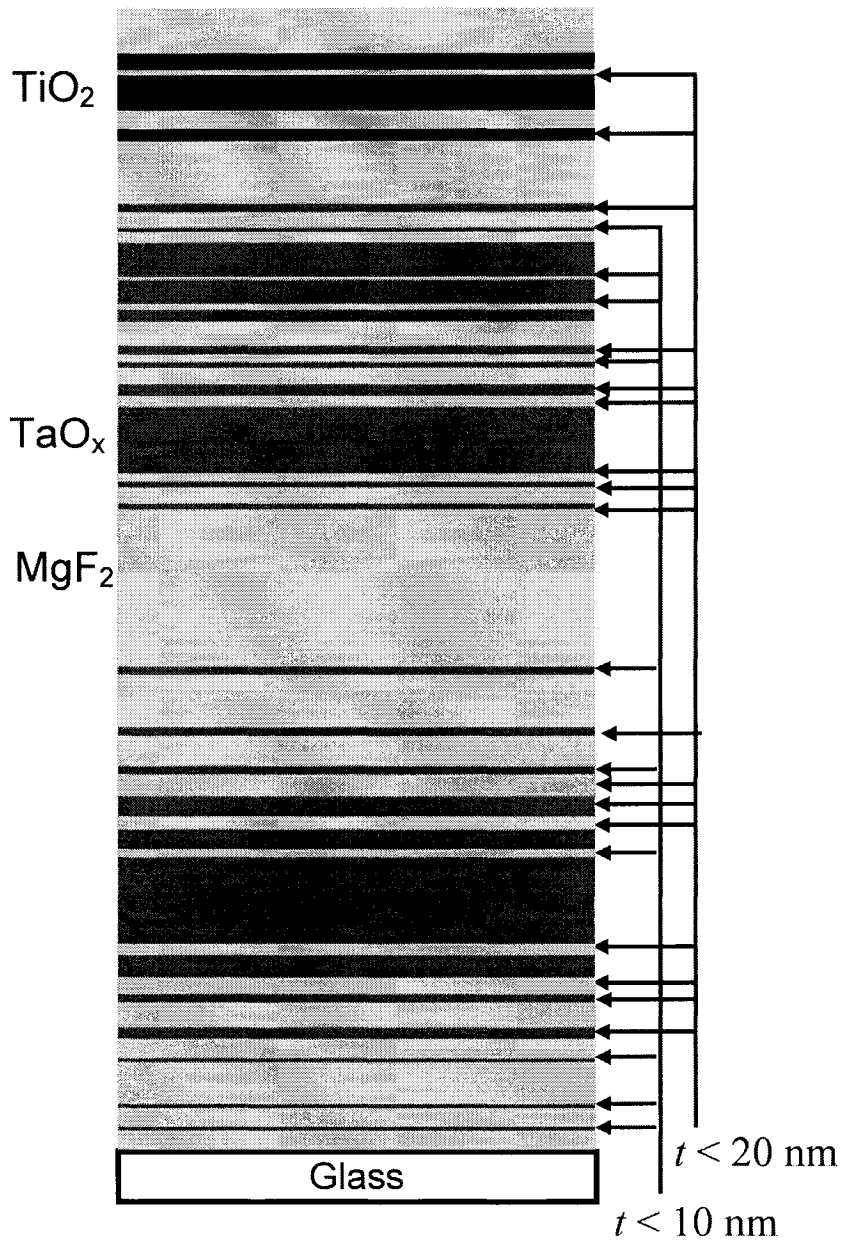

Figure 1.1. *Schematic view of a 53 layer wide-band AR coating for photographic lens synthesized by the Flip-Flop method. Winner of the 1991 Berlin design contest, by W. H. Southwell [7].*

different materials and has a complex non-quarterwave design. A survey of layer thicknesses reveals that close to ~25% of all layers are ultra-thin, i.e. less than 10 nm-thick. These films obviously require great care during deposition to obtain laterally uniform films

with bulk-like density, abrupt interfaces, a constant n depth-profile, and controlled average thickness to within a fraction of a nanometer.

In its recent tri-annual meeting [12], the optical coatings community has identified numerous challenges that need to be addressed, and proposed a "roadmap", to permit the widespread manufacture of OIFs such as the one shown in Fig. 1.1. The challenges include (but are not limited to): (1) the deposition of multiple materials or mixed oxides so that different optical constants may be obtained in any order in the same chamber or in an integrated process (useful for multilayer, graded index, and hybrid homogeneous/inhomogeneous OIFs); (2) the ability to maintain thin film composition, microstructure and density constant with depth, in order to keep the refractive index variations (Δn) very low ($\Delta n \leq 0.001$) [related to (1)]; (3) the ability to vary n in a continuous way so as to allow index matching (broad spectrum optical impedance matching [13]) between an OIF and another device or a specific environment [14, 15]; (4) the control of thicknesses with sub-nanometer precision and accuracy (down to 0.1 nm), possibly with the help of *in situ* broadband optical monitoring (photometric [16] or ellipsometric [17]); (5) minimal interface thickness, especially for ultra-thin films [related to (4)]; (6) enhanced tribo-mechanical properties in terms of stress control in thin films, and of wear-, scratch- and abrasion-resistance [18].

Traditionally, optical filters have been fabricated by physical vapor deposition (PVD) techniques such as evaporation and sputtering, frequently assisted by ion bombardment [ion beam assisted deposition (IBAD), unbalanced magnetron sputtering (UMS), ion plating (IP), and their variants], as described in earlier reviews [19, 20]. Today, PVD technology is quite mature; it can produce good quality transparent amorphous oxides adequate for most OIFs currently in use [6]. The range of materials that can be fabricated by PVD techniques, although impressive, remains limited by the availability of evaporation and sputtering target materials. Figure 1.2a shows the gamut of refractive index values accessible by typical PVD materials. The range from low- to high-n is interspersed with many gaps, and

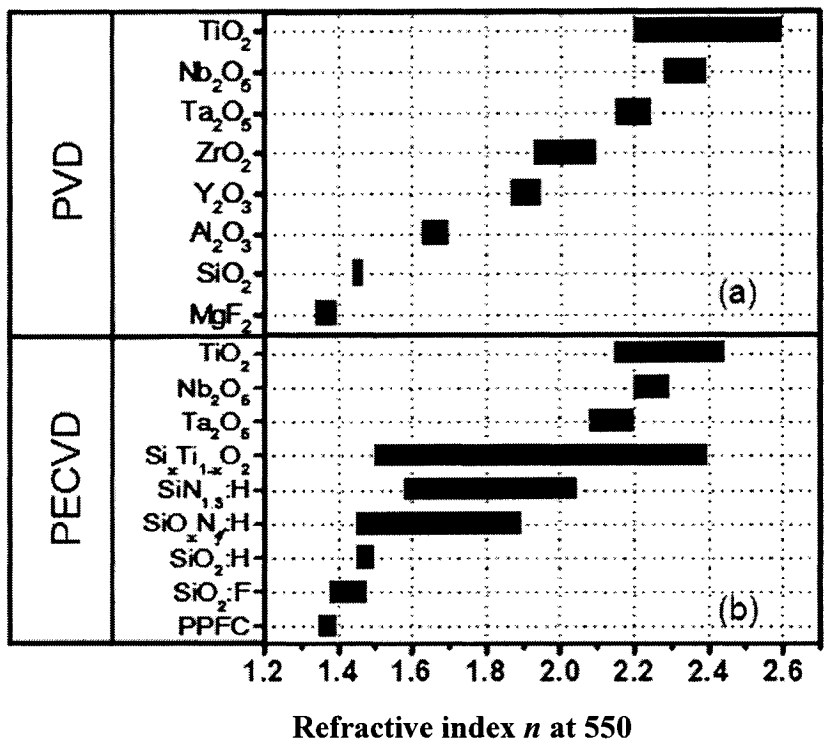

Figure 1.2. *Refractive index (at λ = 550 nm) of different (a) PVD and (b) PECVD optical coating materials. Data from references [21, 23, 28].*

most processes are limited to the use of two materials, traditionally possessing the lowest- and highest-*n* materials available.

Traditional PVD techniques now appear to lack the versatility required to achieve the level of control of film composition, microstructure, and porosity increasingly required to meet the broad *n*-range demanded by novel OIF applications. Looking to the future, we contend that the success of the optical coatings industry hinges on its ability to develop and integrate new processes that allow tunability of optical, micro- and nano-structural, and mechanical properties over a wide range, as well as lend themselves well to the tailoring of interfaces so critical to the optical performance of OIFs. Research is therefore moving towards the exploration and development of new and more sophisticated deposition

processes to synthesize materials with fine tuned optical properties, composition, microstructure, and nanostructure by means of control of process parameters and thin film growth characteristics at an atomistic level.

1.3 Plasma-Enhanced Chemical Vapor Deposition of Optical Coatings

The research in our Functional Coating and Surface Engineering Laboratory (FCSEL) has particularly focused on developing and exploring plasma-enhanced chemical vapour deposition (PECVD) to fabricate good quality optical coatings that possess a broad range of optical and mechanical properties.

PECVD has been shown to fabricate films with controlled chemical composition [21, 22], microstructure, and porosity [23, 24], as well as nanocomposite films [25, 26, 27], with interesting nonlinear optical properties, color, electrical conductivity and other functional characteristics. PECVD is increasingly recognized by the optical coatings community as versatile and flexible [6, 28]. Most notably, Angus Macleod (Thin Film Center) and George Dobrowolski (NRC-Ottawa), two of the pioneers of the field of optical coatings, have referred to the flexibility of the PECVD process as one of its most promising features, making it an important tool to develop in the 21st century [29]. The optical properties of selected PECVD materials are plotted in Fig. 1.2b. They demonstrate the special ability of this process to synthesize a wide range of low-, intermediate- and high-n materials with full coverage of the n range.

The tunability of optical properties in the PECVD process is facilitated by (1) the availability of many gas phase precursors, which may also be mixed in the deposition chamber [21, 22] to control plasma chemistry, and are not as limiting as solid-state targets; (2) the range of discharges available, such as microwave (MW), radiofrequency (RF), and dual-mode MW/RF combined [28, 30, 31, 32] to enhance the control of ion bombardment characteristics. A survey of different types of PECVD processes available to the optical

coatings community was recently completed by Martinu and Poitras [28].

1.4 Complex Problems and Strategies to Resolve Them

The exceptional flexibility and versatility of PECVD comes at the expense of increased complexity. This is primarily attributed to the existence of a wide spectrum of species in the gas phase during a glow discharge, namely neutrals, atomic and molecular ions, electrons, radicals, and energetic photons [33], which tend to interact with the substrate or film surface. Compounding this problem is the fact that the abundance, energy and other properties associated to the various species – and by extension their interactions with the substrate or thin film – are often interdependent and indirectly controlled by external process parameters, such as working pressure (p), gas phase composition, plasma power, and substrate biasing (V_B). This complexity has greatly hampered the development of an atomistic understanding of thin film growth in the PECVD process.

An important part of our vision at the FCSEL has been to develop strategies which can bridge the knowledge gap between the bulk properties of the plasma, plasma-surface interactions, and their effects in terms of surface-, interface- and thin film-modifications. In the recent past, we have investigated plasma emission [34, 35] and chemistry [36], ion bombardment characteristics, such as ion energy distribution function (IEDF) [31, 37], ion flux (ϕ_i) [32], in relation to external process parameters, such as plasma power, V_B, p, gas-phase precursor mixtures, substrate temperature (T_s), and pulsing characteristics [38, 39]. Film properties were also extensively analysed in terms of micro- and nano-structural, optical, electrical and mechanical properties [28, 39, 40], usually as a function of the process parameters enumerated above. However, studies of direct correlation between detailed plasma characteristics, and surface, interface and thin film processes in the PECVD environment are hard to come by [23, 33, 41, 42]. It is our firm belief at the FCSEL that a great deal of information can be gained by monitoring the substrate/thin film modifications *in situ* and *during-processing* in well characterized plasma conditions. We

can then bridge the knowledge gap by explaining the modifications – and even accurately predicting them with the help of simulation tools – in terms of the multiple plasma-surface interactions.

The effort to perform *in situ* dynamic monitoring of the substrate/thin film surface during plasma exposure or thin film deposition is hampered by the "hostility" of the low-pressure ($20 < p < 200$ mTorr) PECVD environment towards electron- and ion-based probes. However, optical probes do not appear to suffer from the same shortcomings, because they hardly interact with the electrically and chemically active environment. They are also non-destructive and non-invasive vis-à-vis the target. Consequently, optical probes appear to be the most promising diagnostic tools to study the effects of plasma-surface interactions on surfaces, interfaces and thin films during processing.

Real-time spectroscopic ellipsometry (RTSE) based on the rotating compensator design (RCE, see section 3.2) [43, 44] is one of the most powerful and capable optical monitoring tools currently available for the investigation of surfaces and film deposition. *In situ* RTSE has previously been used to successfully study thin film growth, including surface and interface properties in a plasma environment [45, 46, 47, 48]. Ellipsometry measures the change in amplitude ratio and phase difference of polarized light upon reflection from a sample [49]. It is a highly surface-sensitive technique, with sub-monolayer sensitivity and precision [50]. A wealth of depth-dependent information can be extracted about the optical properties, microstructure and composition of the substrate and/or growing thin film [51]. This is possible because optical probes – usually from the ultraviolet (UV) to near infrared (NIR) – interact with bound and unbound electrons according to the material's band structure. The theoretical basis for using ellipsometry to study the modifications resulting from ion-surface interactions will be given in section 2.3.3.

Among the multiple plasma-surface interactions present in the PECVD environment, there are strong indications that ion-surface interactions dominate the near-surface modifications

of the target [52] and the growth mechanism of thin films [53]. Numerous reports also point to ion-surface interactions in the hyperthermal range (1 to 10^3 eV) to explain the dense and amorphous microstructure of optical coatings fabricated by low-pressure plasma processing [19, 20, 24, 28, 31, 39, 41, 42, 54, 55], including PECVD.

The importance of investigating ion-surface interactions leading to interface broadening in a PECVD environment is further emphasized by the fact that ion bombardment can have a negative effect on the spectral performance of OIFs [56]. Interface broadening is the result of IB-induced mixing of atoms at the interface between two thin films [57, 58], and must be controlled and reduced in the context of OIF fabrication. It depends strongly upon IB characteristics (ion energy and mass), thin film properties (atomic numbers and density), and growth dynamics (ion-to-neutral arrival rate ratio) [59, 60]. Consequently, it appears rather difficult to predict or control interface broadening without performing detailed *in situ* studies and simulating the effects of ion-surface interactions in a plasma environment, and especially during thin film growth.

Simulation tools, such as the Monte-Carlo (MC) based TRIM [61, 62] and TRIDYN [63, 64] codes, can accurately calculate the transport of ions and atoms in any given solid-state target, and can be very useful in interpreting *in situ* dynamic results by calculating the effect of ion-surface interactions. Benefiting from the existing knowledge base about IB characteristics in specific plasma conditions, and the current understanding of ion-surface interactions [65, 66], TRIM and TRIDYN can be used to predict the effects of ion bombardment, including damage and amorphization, composition changes, and interface broadening. In addition, TRIDYN is a dynamical version of TRIM, and therefore allows one to calculate depth-dependent modifications on time and fluence scales of interest for thin film deposition processes ($\sim 10^{-1}$ s < time < 10^3 s), making it a powerful tool for interpreting experimental results, and even predicting how specific processing conditions will affect surface, interface and thin film growth. However, its predictive capability must be tested by confronting it to experimental results.

1.5 Objectives of the Present Work

The motivation of this work is to gain in-depth understanding of the role of ion-surface interactions in the PECVD environment, by performing *in situ* RTSE studies and TRIM/TRIDYN simulations of surface modifications and thin film growth. This in turn will permit process optimization in terms of interface and thin film properties, and fine-tuning of ion bombardment characteristics. In the extreme case of the novel dense-porous multilayer OIFs, we will show that IB-control of interfacial properties can dramatically enhance the microstructural and optical properties of thin films.

Based on these goals, the objectives of this thesis are the following:

a. To develop a methodology for measuring and quantifying the depth of ion-surface interactions in model substrate and thin film materials systems.
b. To study these modifications *in situ* and in real-time, on a time scale pertinent to low-pressure plasma processing.
c. To simulate ion-surface interactions – using TRIM and TRIDYN – by taking into consideration the broad IEDF common to low-pressure plasmas, such as in the bias-controlled radiofrequency discharges common to PECVD.
d. To use a combination of *in situ* diagnostics and TRIDYN simulations to study the effects of ion-surface interactions responsible for subplantation and interface broadening during the initial moments of thin film deposition by PECVD.
e. To improve the optical, structural and interfacial properties of dense-porous multilayer OIFs by engineering the interfaces with the help of IB characteristics.

Throughout this work, we shall use *ex situ* variable angle spectroscopic ellipsometry (VASE) and *in situ* RTSE to gain insight into ion-surface interactions in the PECVD environment by monitoring the plasma exposure of c-Si and the initial growth of TiO_2 on SiO_2. We will modify TRIDYN to make it a reliable tool for predicting IB effects below

target surfaces in the context of ion sources with arbitrary complexity. TRIM and TRIDYN simulations will help in the interpretation of RTSE results, and reveal the dynamics of ion bombardment effects at high fluence. The extensive knowledge-base about ion-beam implantation, damage and amorphization, and oxidation of c-Si will help us to interpret our results and to assess the effects of IB induced by the plasma source. Finally, we will use this understanding to demonstrate how IB-induced interface engineering can be used to control and enhance the microstructure of thin films in a multilayer dense-porous $SiN_{1.3}$-based OIF.

1.6 Organization of the Thesis

This work is presented in 8 chapters. Chapter 2 gives a brief overview of the basic concepts and theory of ion-surface interactions, along with a brief review of well known effects of IB on substrate, and thin film surfaces and interfaces, including damage and amorphization, composition changes, and ion mixing. This chapter also sets the theoretical basis for the sensitivity of optical probes to structural and compositional changes in crystalline targets. Chapter 3 describes the methodology of plasma-based surface treatments and thin film deposition, presents the IB characteristics in RF and MW discharges, and describes the MC-based simulation tools (TRIM and TRIDYN) used throughout this work.

The main body of the thesis is presented as four articles in Chapters 4-7. We study and model the effects of ion bombardment at the RF-powered electrode by *ex situ* variable angle spectroscopic ellipsometry (VASE) in Chapter 4 ("Ion-Surface Interactions on c-Si(001) at the Radiofrequency-Powered Electrode in Low-Pressure Plasmas: *Ex Situ* Spectroscopic Ellipsometry and Monte-Carlo Study"), then we develop in Chapter 5 ("Dynamics of Ion Bombardment-Induced Modifications of Si(001) at the Radiofrequency-Biased Electrode in Low-Pressure Oxygen Plasmas: *In Situ* Spectroscopic Ellipsometry and Monte-Carlo Study") a novel methodology which consists in monitoring *in situ* and in real-time the effects of ion-surface interactions on model c-Si(001) substrate at the RF-powered

electrode, combined with TRIDYN simulations of the ion bombardment effects of a broadband energy ion source. The insight we gain into IB-related processes at the RF-electrode is the basis for thin film growth and interface control studies in Chapters 6 and 7. We study subplantation and interface broadening during TiO_2 deposition on SiO_2 at the RF-electrode in Chapter 6 ("Interface Broadening Due to Ion Mixing During Thin Film Growth at the Radiofrequency-Powered Electrode in a Plasma-Enhanced Chemical Vapor Deposition"), and the effect of surface and interface smoothening by RF plasma treatment on the microstructural control of dense/porous multilayer stacks of Si_3N_4 fabricated in RF and MW plasmas in Chapter 7 ("Interface Engineering During Plasma-Enhanced Chemical Vapor Deposition of Porous/Dense $SiN_{1.3}$ Optical Multilayers").

The conclusions, a general discussion, and future perspectives are presented in Chapter 8.

1.7 Additional Publications by this Candidate

In addition to the four articles forming the heart of this thesis, this candidate has been involved in several other investigations during his PhD studies. His involvement was based on the expertise and knowledge he developed on *ex situ* and *in situ* SE analyses and TRIDYN simulations. This led to additional journal publications and conference proceedings summarized below.

a) *In situ* RTSE investigation of the dynamics of plasma-surface interactions and TiO_2 deposition by PECVD; TRIM and TRIDYN simulations of ion-surface interactions:
   - **A. Amassian**, P. Desjardins, and L. Martinu, "Study of TiO_2 Film Growth Mechanisms in Low-Pressure Plasma by *In Situ* Real-Time Spectroscopic Ellipsometry", *Thin Solid Films*, 447-448 (2004) 40.
   - **A. Amassian**, P. Desjardins, and L. Martinu, "Influence of Low Ion Bombardment Energy on Interface Formation and Thin Film Growth in a Plasma-CVD Environment", *Proc. 48th Ann. Tech. Conf., Society of Vacuum Coaters* (2005) 410.

- **A. Amassian**, P. Desjardins, and L. Martinu, "Dynamics of Surface Modifications During Optical Coating Deposition in Plasma-Assisted Processes", in *Optical Interference Coatings on CD-ROM* (The Optical Society of America, Washington, DC) TuE9 (2004) (3 pages).
- **A. Amassian**, S. Larouche, J. E. Klemberg-Sapieha, P. Desjardins, and L. Martinu, "*In situ* Ellipsometric Study of the Initial Growth of a-TiO_2 Deposited by PECVD", *Proc. 45th Ann. Tech. Conf., Society of Vacuum Coaters* (2002) 250.
- **A. Amassian**, S. Larouche, R. Vernhes, J. E. Paultre, J. E. Klemberg-Sapieha, P. Desjardins, and L. Martinu, "Analysis and Control of Optical Film Growth by *In Situ* Real-Time Spectroscopic Ellipsometry" in *SPIE Regional Meeting on Optoelectronics, Photonics, and Imaging,* SPIE Vol. TD01 (2002) 493.

b) *In situ* RTSE investigation of the growth of dense/porous $SiN_{1.3}$ thin films and the ion bombardment-control of interfaces and thin film properties:

- R. Vernhes, **A. Amassian**, J. E. Klemberg-Sapieha, and L. Martinu, "Plasma treatment of porous SiN_x:H films for the fabrication of porous-dense multilayer optical filters with tailored interfaces", *J. Appl. Phys.* (submitted).
- **A. Amassian**, R. Vernhes, J. E. Klemberg-Sapieha, P. Desjardins, and L. Martinu, "Interface Engineering of Porous/Dense Multilayers of $SiN_{1.3}$: *In Situ* Real-Time Spectroscopic Ellipsometry Study", *Proc. 47th Ann. Tech. Conf., Society of Vacuum Coaters* (2004) 86.
- **A. Amassian**, R. Vernhes, J. E. Klemberg-Sapieha, P. Desjardins, and L. Martinu, "Study of the Growth and Interface Engineering of Dense/Porous $SiN_{1.3}$ Optical Coatings by Real-Time Spectroscopic Ellipsometry", in *Optical Interference Coatings on CD-ROM* (The Optical Society of America, Washington, DC). MF3 (2004) (3 pages).

c) *Ex situ* VASE analysis and novel optical modeling strategies for $SrTiO_3$ (STO) and electro-optic lanthanum-modified lead zirconium titanate (PLZT) thin films deposited on c-Si(001) and ITO-coated glass substrates:

- **A. Amassian**, M. Gaidi, M. Chaker, and L. Martinu, "Optical Depth Profiling of Strontium Titanate and Electro-Optic Lanthanum-Modified Lead Zirconium Titanate Multilayer Structures For Active Waveguide Applications" *J. Vac. Sci. Technol.* **A24** (2005) 55.
- M. Gaidi, **A. Amassian**, M. Kulishov, L. Martinu, and M. Chaker, "PLZT Pulsed Laser Deposition: Structural and Optical Characterization". *Appl. Surf. Sci.*, 226 (2004) 347.
- M. Gaidi, L. Stafford, **A. Amassian**, M. Chaker, J. Margot, L. Martinu, and V. Kulishov, "Influence of the Microstructure on the Optical Properties of $SrTiO_3$ Thin Films", *J. Mat. Res.* 20 (2005) 68.

d) *Ex situ* VASE and *in situ* SE characterization of glancing angle deposited (GLAD) nanoporous a-Si thin films used for photonics applications:

- K. Kaminska, **A. Amassian**, L. Martinu, and K. Robbie, "Growth of Vacuum Evaporated Ultra-Porous Silicon Studied With Spectroscopic Ellipsometry and Scanning Electron Microscopy", *J. Appl. Phys.* 97 (2005) 13511.
- K. Kaminska, **A. Amassian**, N. Davis, L. Martinu, and K. Robbie, "Ellipsometric Analysis of High Temperature Glancing Angle Deposited Amorphous Silicon Films", *Thin Solid Films* (submitted).
- K. Kaminska, **A. Amassian**, L. Martinu, and K. Robbie, "Growth Study of Ultra-Porous Silicon Photonic Interference Filters", in Optical Interference Coatings on CD-ROM (The Optical Society of America, Washington, DC), MF4 (2004) (3 pages).

e) *Ex situ* VASE and *in situ* RTSE characterization and growth study of nanocomposite hard coatings manufactured by PECVD, and TRIM/TRIDYN simulations of IB-induced transport:

- P. Jedrzejowski, **A. Amassian**, E. Bousser, J. E. Klemberg-Sapieha, and L. Martinu, "Real-Time *In Situ* Growth Study of TiN - and TiC_xN_y - Based Superhard Nanocomposite Coatings Using Spectroscopic Ellipsometry", *Appl. Phys. Lett.* (in press).
- P. Jedrzejowski, J. Cizek, **A. Amassian**, J. E. Klemberg-Sapieha, J. Vlcek, and L. Martinu, "Mechanical and Optical Properties of Hard SiCN Coatings Prepared by PECVD", *Thin Solid Films*, 447-448 (2004) 201.
- P. Jedrzejowski, **A. Amassian**, E. Bousser, L. Martinu, and J. E. Klemberg-Sapieha, "Real-Time *In Situ* Growth Study of TiN and TiC_xN_y – Based Superhard Nanocomposite Coatings Using Spectroscopic Ellipsometry", *Proc. 48th Ann. Tech. Conf., Society of Vacuum Coaters* (2005) 68.
- P. Jedrzejowski, J. Cizek, **A. Amassian**, J. E. Klemberg-Sapieha, J. Vlcek, and L. Martinu, "Mechanical Properties of Hard SiCN Coatings Prepared by PECVD", *Proc. 46th Ann. Tech. Conf., Society of Vacuum Coaters*, (2003) 530.

f) *Ex situ* VASE study and *in situ* monitoring/control of multilayer and graded-index TiO_2/SiO_2 optical interference filters fabricated by PECVD:

- S. Larouche, **A. Amassian**, B. Baloukas, and L. Martinu, "Turning-Point Monitoring is Not Simply Optical Thickness Compensation", in *Optical Interference Coatings on CD-ROM* (The Optical Society of America, Washington, DC). TuE8 (2004) (3 pages).
- S. Larouche, **A. Amassian**, J. E. Klemberg-Sapieha, and L. Martinu, "Plasma-Deposited Inhomogeneous Optical Filters", in *SPIE Regional Meeting on Optoelectronics, Photonics, and Imaging*, SPIE Vol. TD01: (2002) 488.
- S. Larouche, **A. Amassian**, S. C. Gujrathi, J. E. Klemberg-Sapieha, and L. Martinu, "Multilayer and Inhomogeneous Optical Filters Deposited by PECVD Using

Titanium Dioxide and Silicon Dioxide", *Proc. 44th Ann. Tech. Conf., Society of Vacuum Coaters* (2001) 277.

- S. Larouche, H. Szymanowski, **A. Amassian**, J. E. Klemberg-Sapieha, and L. Martinu, "Microstructure of SiO_2/TiO_2 Coatings and Their Use in Graded-Index Optical Filters", *Proc. 46th Ann. Tech. Conf., Society of Vacuum Coaters*, (2003) 334.

g) Design, fabrication and characterization of two- and four-layer broadband antireflective coatings on spherical lenses:

- O. Zabeida, **A. Amassian**, S. Larouche, C. Lavigne, J. E. Klemberg-Sapieha, L. Martinu, D. E. Morton, and F. Zimone, "Plasma Deposition of Anti-Reflective Coatings on Spherical Lenses", in *Optical Interference Coatings, OSA Technical Digest*, WA7 (2001) (3 pages).

h) *Ex situ* VASE characterization and interface modeling of Ta_2O_5 and Nb_2O_5 films submitted to annealing:

- J. P. Masse, H. Szymanowski, O. Zabeida, **A. Amassian**, J. E. Klemberg-Sapieha, and L. Martinu, "Effect of Annealing on the Optical Properties of Plasma-Deposited Ta_2O_5 and Nb_2O_5 Films", *Thin Solid Films* (in press).

i) *Ex situ* VASE characterization of the optical and band gap properties of nanostructured CN_x coatings deposited by post-discharge assisted pulsed laser deposition:

- M. Tabbal, T. Christidis, S. Isber, P. Mérel, M. A. El Khakani, M. Chaker, **A. Amassian**, and L. Martinu, "Correlation Between the sp^2-Phase Nanostructure and the Physical Properties of Unhydrogenated Carbon Nitride" *J. Appl. Phys.* **98** (2005) 044310.

Chapter 2. Ion-Surface Interactions

The interaction of hyperthermal ions with a solid-state target in a low-pressure PECVD environment is the main focus of this thesis. Since the main results of this work are presented in a concise format in 4 articles (Chapters 4 to 7), each one containing a brief review of the pertinent literature, there is no necessity here to be repetitive. Instead, we will present the theoretical and experimental background which can be helpful at various stages of the reading. Our presentation will therefore be limited to a summary of essential concepts and relevant results taken from the literature.

The first part of this chapter describes the fundamental interactions which influence the transport and range of ions in solid-state targets (section 2.2). We also present ion implantation-induced damage and amorphization of c-Si (section 2.3), followed by composition changes, such as oxidation, which occur in high fluence implantation (section 2.4). Next, the theoretical basis for optical probing of damage, amorphization and composition changes is presented (section 2.5), backed up by supporting examples from the literature. This is followed by a discussion of ion mixing (section 2.6) and thin film deposition in the presence of ion bombardment (section 2.7).

2.1 Background

A low-pressure plasma environment is characterized by a large spectrum of species, including neutrals, atomic and molecular ions, radicals, electrons and energetic photons interacting with the target surface. In typical low-temperature discharges, these species possess energy in the range of a meV to a few eV. However, in the presence of a powered substrate holder, such as at the RF-biased electrode, negative biasing leads to the acceleration of positive ions toward the substrate/film surface. Under the conditions most suitable for optical coating deposition, biasing is in the range of tens to hundreds of volts,

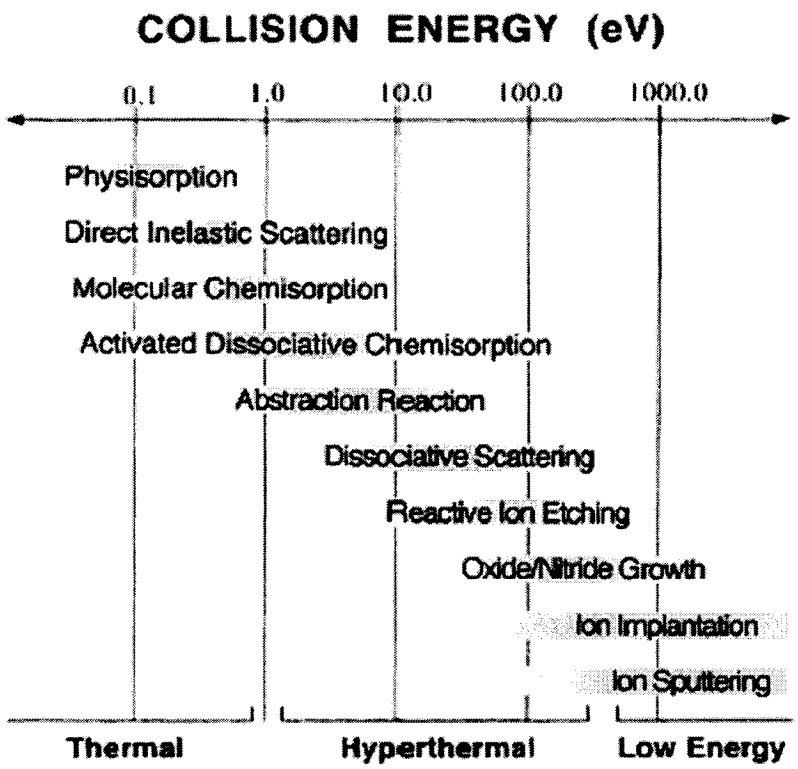

Figure 2.1. *Energetic range associated with various processes that can be observed during ion-surface interactions. Reproduced from [66].*

and the ensuing ion energy increases up to ~10^3 eV, far exceeding the energy (and momentum) of all other particles (neutrals, radicals, electrons, and photons) incident on the target. As a result, ion bombardment is believed to dominate the plasma-surface interactions in the PECVD environment. Ion bombardment effects are generally limited to near-surface regions of the target, typically a few nanometers to tens of nanometers for hyperthermal ions (10^0 to 10^3 eV), hence they reasonably qualify as ion-surface interactions.

Figure 2.1 summarizes the kinetic energy-dependent processes resulting from collisions in thermal (< 1 eV), hyperthermal (1 to 10^3 eV), and so-called low-energy (> 10^3 eV) regimes. Hyperthermal ions, especially those with a kinetic energy of ~10^2 eV, play an important

role during the deposition of dense oxide and nitride films [66, 67], and are also involved in subplantation and atomic relocations, responsible for thin film densification.

2.2 Transport of Ions in Solids

Energetic particles can penetrate the target surface, and are continuously slowed down through interactions with target nuclei and electrons. In the coming paragraphs, we briefly describe ion-surface interactions and ion penetration depth, within the framework of the binary collision approximation (BCA) [61].

2.2.1 Energy Loss of Ions in Solids

The kinetic energy of incident energetic particles is dissipated in the target via two main mechanisms, namely nuclear (n) and electronic (e) interactions. Nuclear interactions are elastic, and are responsible for atomic relocations, as illustrated in Figure 2.2. Each incident ion displaces target atoms (one at a time via binary collisions) within the target, and can produce collision cascades [68], i.e. multiple displacements per incident ion. An atomic displacement in the bulk can form an interstitial (I) and a vacancy (V), also called an IV pair (a Frenkel pair, or a defect bond), or can cause a replacement collision, even an ejection from the target surface, known as sputtering. Electronic interactions, on the other hand, are inelastic, and responsible for the gradual slowing of ions and recoils between two nuclear interactions. Electronic interactions mainly cause ionization and point defects (only at very high energy).

The stopping power of a target layer with thickness dt can be expressed as the sum of the nuclear and electronic contributions [69]:

$$\frac{dE_i}{dt} = \left(\frac{dE_i}{dt}\right)_n + \left(\frac{dE_i}{dt}\right)_e = -N\left[S_n(E_i) + S_e(E_i)\right], \tag{2.1}$$

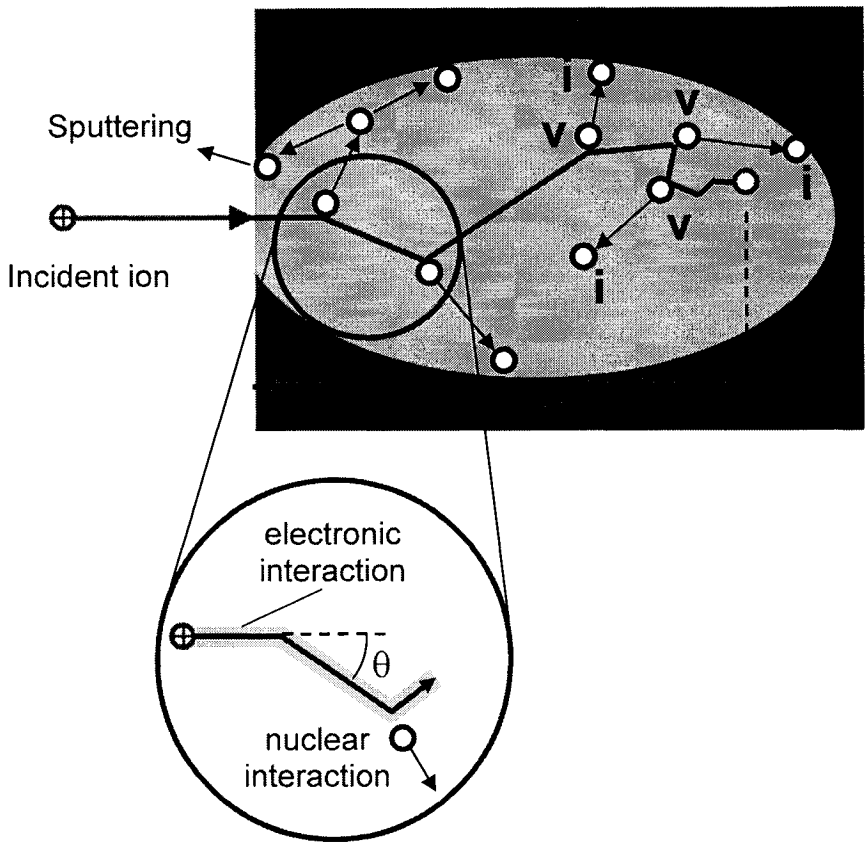

Figure 2.2. *Schematic representation of nuclear and electronic interactions of incident ions with the target.*

where E_i is ion energy, N is the atomic density of the target, and $S_n(E_i)$ and $S_e(E_i)$ are nuclear and electronic cross sections, respectively. The nuclear stopping cross section is defined by the integral [70]:

$$S_n(E_i) = \int_0^{T_{max}} T d\sigma(E_i, T), \tag{2.2}$$

where $d\sigma$ is the interaction cross-section, T is the kinetic energy transferred to the recoil, and T_{max} is the maximum energy transfered in a head-on collision between incoming and target atoms with masses M_1 and M_2. T_{max} is given by [61]

$$T_{max} = \frac{4M_1M_2}{(M_1 + M_2)^2} E_i . \tag{2.3}$$

The probability distribution for the energy transfer T is given by the scattering cross-section $d\sigma(E_i, T)$. Without getting into details, we note that the Coulomb interaction is essential to describe the screening of repulsive forces of the nuclei by surrounding electrons [62]. Variations on this potential (e.g. Tersoff III, Molière, Zeigler-Biersack, etc.) are used to describe interactions in different ion energy ranges [61].

In general, $S_n(E_i)$ increases approximately as $\sim E_i^n$ in the hyperthermal range, with $n < 1/2$, then reaches a plateau at intermediate energies, and decreases at higher energy. This is illustrated in Fig. 2.3a, where $S_n(E_i)$ is plotted in the case of O ion implantation in SiO_2. At high energy, the energy loss mechanism is dominated by electronic excitation. $S_n(E_i)$ is proportional to ion velocity, hence it scales with the square root of the kinetic energy [71]:

$$S_e(E) \approx KE^{1/2}, \tag{2.4}$$

K is a proportionality constant which depends on ion and target characteristics. Figure 2.3a plots the total stopping power of O ions in a SiO_2 target [75], demonstrating the E_i-dependence of the stopping power of ions by the target. Generally speaking, nuclear interactions dominate mainly for hyperthermal and low-E_i ions, while electronic loss is mostly felt at high energy.

2.2.2 Range of Ions in Solids

The loss of ion energy to target nuclei and electrons eventually leads to the stopping of ions at a characteristic depth inside the target. The implantation depth profile in a homogeneous target resembles a Gaussian distribution (Fig. 2.4), because of the stochastic nature of binary – elastic nuclear – collisions. While the range of an individual atom, defined as R_i, is completely random, statistically speaking, the distribution depth profile for a large number of ions is characterized by the mean projected range (R_p), the straggle (or standard deviation, ΔR_p), skewness and kurtosis [62]. R_p and ΔR_p are defined by the following equations:

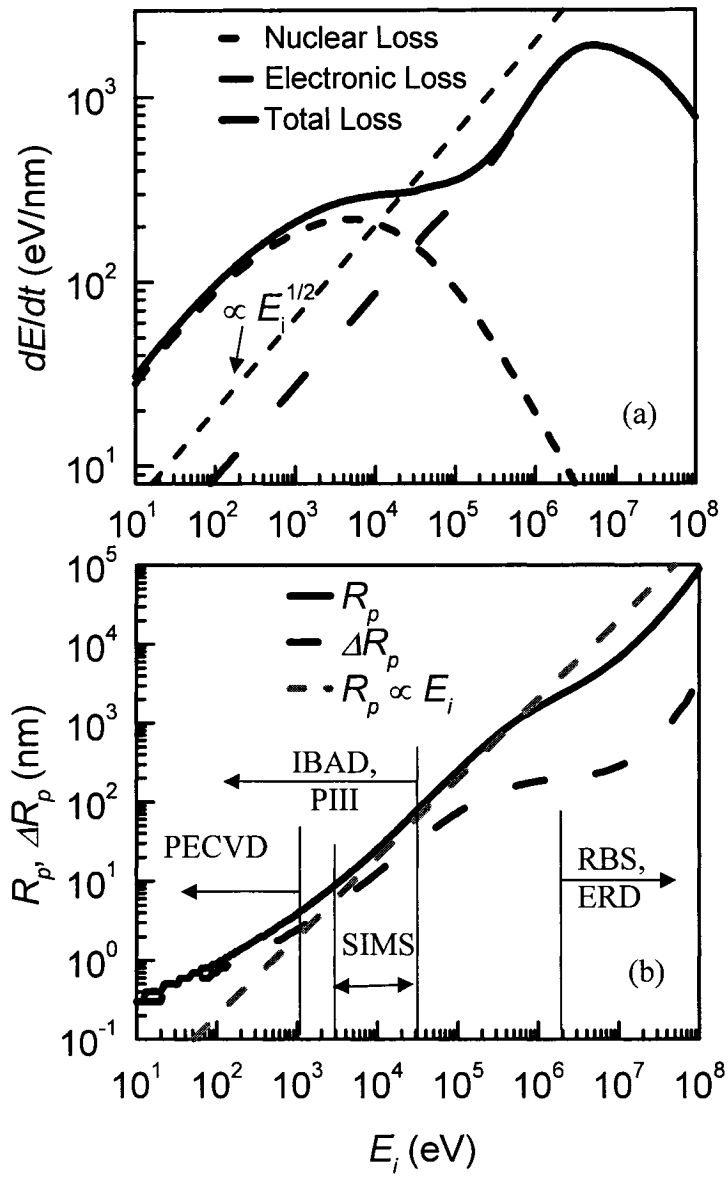

Figure 2.3. *Energy dependence of (a) the stopping power (dE/dt) and (b) the range (R_p) and straggle (ΔR_p) of O ions implanted in a SiO_2 target. The nuclear and electronic stopping powers in (a) are obtained from databases in SRIM 2003 [72]; range and straggle calculations in (b) are based on the Ziegler-Biersack-Littmark (ZBL) method [62] also found in the SRIM simulation package [62]. Process energy ranges are indicated in (b) for PECVD, ion-beam assisted deposition (IBAD), plasma immersion ion implantation (PIII), secondary ion mass spectroscopy (SIMS), Rutherford backscattering spectroscopy (RBS), and elastic recoil detection technique (ERD).*

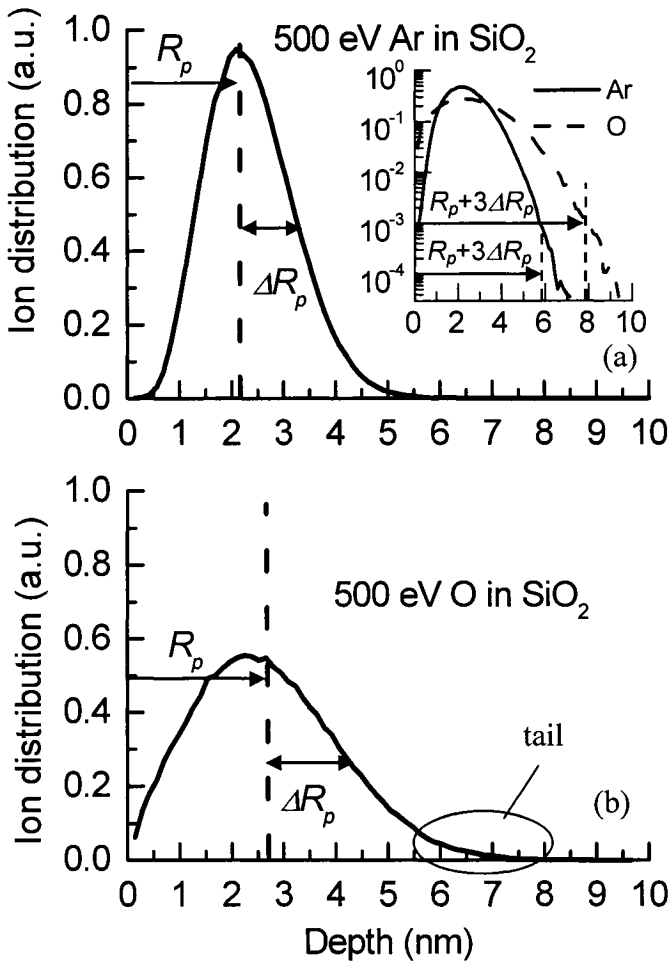

Figure 2.4. *Ar (a) and O (b) ion distribution depth profiles after 500 eV implantation in SiO_2 at normal incidence. Inset shows depth profiles in semi-logarithmic plot; calculations were made using SRIM 2003 [72].*

$$R_P = \frac{1}{N_i}\sum_{i=1}^{N_i} R_i \tag{2.5}$$

$$\Delta R_P = \sqrt{\frac{1}{N_i}\sum_{i=1}^{N_i} R_i^2 - R_p^2} \tag{2.6}$$

where, N_i is the number of ions. The skewness shows whether the peak is skewed towards the surface or away from it, while kurtosis is a measure of the intensity of the distribution

tail (see Fig. 2.4b) with relation to a Gaussian tail (i.e. broader or more abbreviated end-tail).

Figs. 2.4a and 2.4b show the simulated implantation depth profiles of 10^5 Ar and O ions incident on an SiO_2 target at 500 eV. The results were obtained using the Monte-Carlo TRIM code as part of the SRIM 2003 software package [72]. Ion distributions suggest that most hyperthermal Ar and O ions are subplanted to a depth of up to ~5 and ~7 nm, respectively. In addition, the inset of Fig. 2.4a (plotted on a semi-logarithmic scale) suggests that the effects of ion bombardment, so far as ion implantation and atomic displacements are concerned, may be felt at greater depths at high fluence exposures.

TRIM is known to predict R_p and ΔR_p values in excellent agreement with experimental results [73, 74] even for ultra-low energy implantation [e. g. ^{4}He in Si ($1 < E_i < 100$ eV, see Fig. 3.5b], however the computation time required to obtain statistically good results of R_p and ΔR_p may be high. So, to decrease the computation time, we have used the semi-analytical method developed by Ziegler, Biersack and Littmark (ZBL) [62] to determine R_P and ΔR_p. The ZBL method solves the transport problem of energetic ions in a given target, based on two uncorrelated ion-target interactions and their respective energy-dependent stopping cross-sections: (1) binary elastic collisions with target nuclei, and (2) continuous slowing by electronic interactions. The ZBL method is attractive because it is orders of magnitude faster than TRIM simulations, and has been shown to accurately calculate R_P and ΔR_p (within 5% of SRIM results) for ion beams over a wide E_i range.

We used the ZBL method to calculate the E_i-dependence ($E_i \sim 10^1$ to 10^8 eV) of R_p and ΔR_p for O beams incident on SiO_2 (Fig. 2.3b). The logarithmic plot shows that ΔR_p scales with E_i^n, where $n \sim 1$ in the low- to medium-E_i range, and $n \sim 1/2$ in the hyperthermal range. This is in direct consequence of the stopping powers of the target (see Fig. 2.3a), which are plotted in Fig. 2.3b.

It is useful to note that while the peak of the ion distribution is located near R_p, the effect of ions may be felt beyond a depth of $\sim R_p + 2\Delta R_p$ and $\sim R_p + 3\Delta R_p$, where, respectively, ~5% and ~0.5% of incident ions come to a stop in the target.

2.3 Damage and Amorphization by Ion Bombardment

This section presents a selection of results from recently published work on the atomistic understanding of ion-beam damage and amorphization of c-Si. Its goal is simply to acquaint the reader with information that is deemed helpful for the understanding of Chapters 4 and 5 of the thesis.

An incident ion can create multiple IV pairs in a solid-state target. Kinchin and Pease [75] first estimated the number of IV pairs (N_{IV}) created per incident ion according to the following simplistic relationship:

$$N_{IV} \cong \begin{cases} 0 & E_i < E_D \\ E_i / 2E_D & E_i \geq E_D \end{cases}, \qquad (2.7)$$

where E_D is the bulk displacement energy threshold of target atoms. E_D in most materials is between 10 and 40 eV; $E_D \approx 12$ eV in c-Si, and so a 500 eV ion can theoretically produce up to ~20 Frenkel pairs in Si.

An IV pair is a local rearrangement of bonds without excess or deficit atoms; hence it is also known as a bond defect. It introduces in the c-Si lattice the five- and seven-membered rings typically found in amorphous Si (a-Si) [76]. Isolated IV pairs are known to spontaneously recombine at room temperature, as Marqués et al. [77] have recently demonstrated. The activation energy for that recombination process is 0.43 eV, implying that average lifetimes at room temperature are in the range of microseconds. This means that the IV pair formation alone is not sufficiently stable to justify damage accumulation.

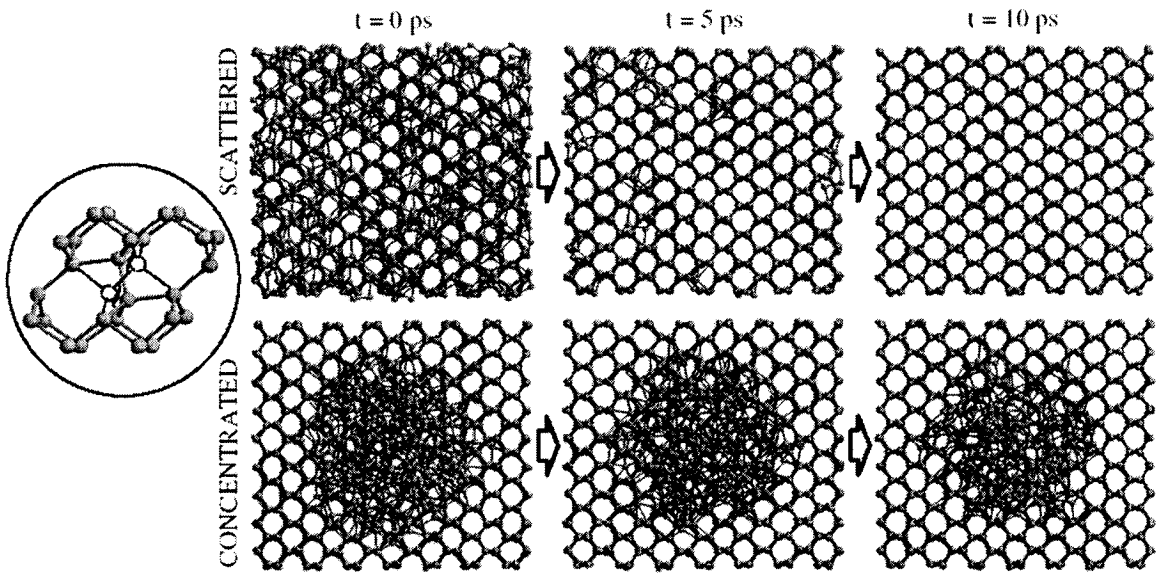

Figure 2.5. *Annealing at 1200 K of samples with the same number of IV pairs (8%), scattered in one case and concentrated in the other. Each pair is introduced in the lattice by randomly choosing two neighboring atoms and displacing them as shown in the inset. Reproduced from [77].*

However, it was later demonstrated that the stability of IV pairs is greatly enhanced by the presence of additional pairs in close proximity, as illustrated by MD simulations of the annealing behavior at 1200 K of the same number of IV pairs scattered in one case and concentrated in the other (Fig. 2.5).

Marqués et al. further represented the recrystallization velocities for the scattered and concentrated damage in an Arrhenius plot (Fig. 2.6), along with a crystal/amorphous (c/a) Si(001) interface. The calculated activation energies for the scattered damage was found to be 0.44 eV, while in the case of the concentrated damage, the activation energy is higher, 0.89 eV, and the recrystallization velocity lower. The activation energy for recrystallization at the c/a interface is 2.44 eV, in agreement with experiment [78]. The energy required to nucleate an IV pair in a purely amorphous matrix is 5 eV [79].

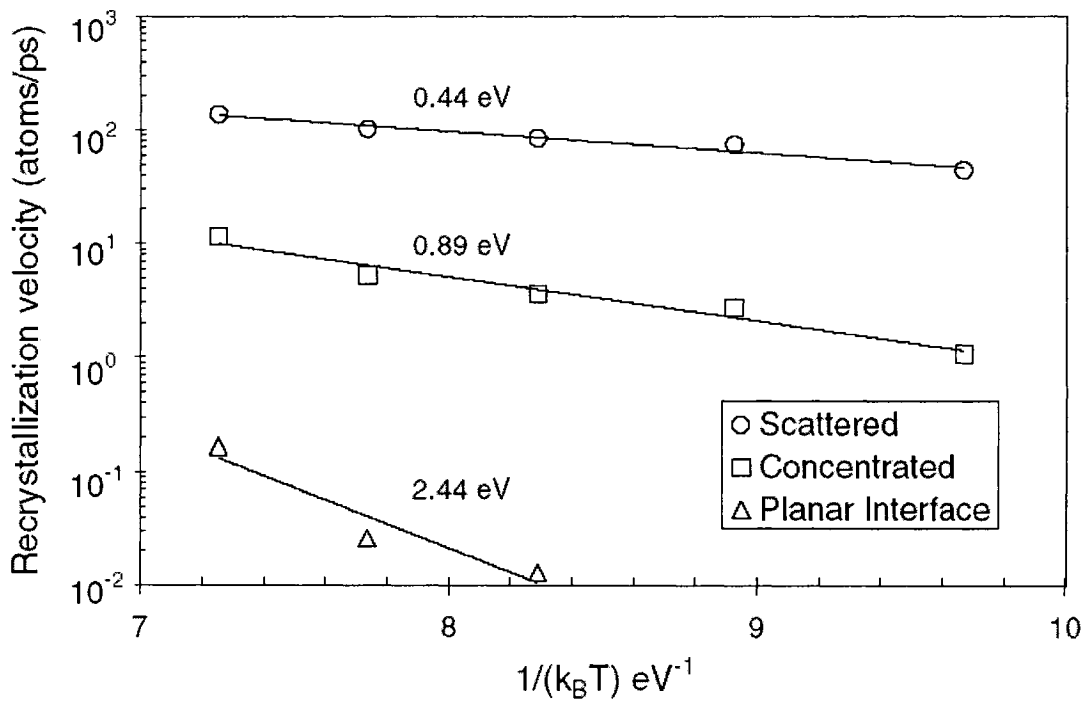

Figure 2.6. *Arrhenius plot of the recrystallization velocity in samples with scattered, concentrated and c/a planar interface. Lines are best fits to each data set, allowing to calculate the activation energy. Reproduced from [77].*

To extend simulations of damage formation and accumulation to time and dimensional scales comparable to experiments, Marqués et al. have incorporated the pertinent information gained from MD simulations in a kinetic Monte-Carlo (KMC) code [77]. The KMC simulator has produced results which agree remarkably well with experimental observations. For instance, the superlinear damage accumulation behavior vs. ion fluence is captured by simulations, as seen in Fig. 2.7. This happens because damage is dilute at low fluence, but as the concentration of IV pairs increases, they start interacting and become more stable and a larger proportion of the damage survives. This explains the superlinear increase of damage.

Pelaz et al. [76] have also demonstrated that the KMC simulator reproduces the equilibrium between amorphization and recrystallization processes in Si, which is one of the most

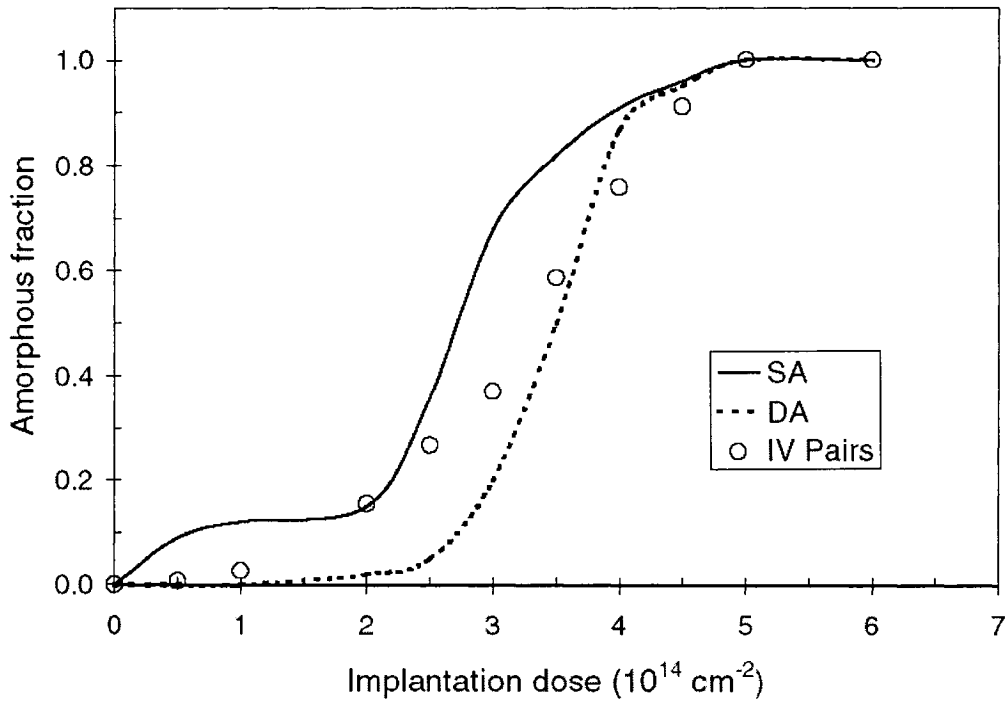

Figure 2.7. *Fluence dependence of the damage produced by 100 keV Si^+ ions at room temperature. Solid and dashed lines correspond to the single-aligned (SA) and double-aligned (DA) RBS spectra. The amorphous fraction is obtained as the ratio of the maximum IV pair concentration to that corresponding to a pure amorphous Si matrix (25 % of IV pairs). Reproduced from [77].*

complex phenomena to model. Ion mass, target temperature, ion fluence, and flux all interact to yield the competition behavior between damage formation and dynamic annealing. Fig. 2.8 shows the IV peak concentration as a function of concentration and fluence rate for an 80 keV Si^+ implantation to a fluence of 10^{15} cm^{-2}. At low temperatures, there is little dynamic annealing and most damage survives, independent of ion flux. At higher temperature, the lattice recovers quickly and it becomes more difficult to start nucleating sufficiently stable amorphous pockets with enough IV pairs, even at relatively high flux.

While dynamic annealing plays a significant role in room temperature Si, and especially for low damage concentrations, it is even more important and in some cases a dominant

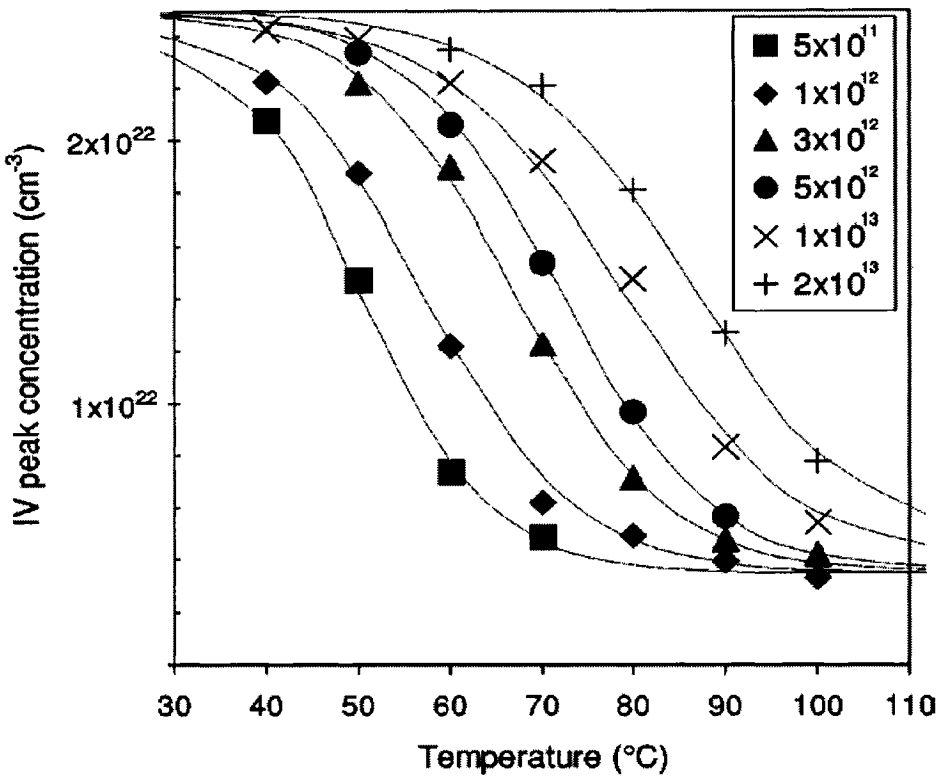

Figure 2.8. *Maximum IV pair concentration vs temperature for several fluxes (in $cm^{-2}s^{-1}$) in 80 keV Si implants to a fluence of 10^{15} cm^{-2}. Reproduced from reference [76].*

process in other ceramics. Dynamic annealing is shown in Fig. 2.9 to be very important for AlAs, GaN and AlN semiconductors [80], indicating that these crystals are very difficult to damage and amorphize. This has been explained with the help of thermodynamic arguments, according to which the activation energy of IV pair annihilation is so low or even nil (such as in metals), that damage formation in some ceramics may require higher ion fluence than chemical composition changes.

A crystalline material is considered fully amorphized when there is complete loss of the long-range structural order in the material. In ion beam processing, amorphization may be accomplished by damaging the crystalline structure (e.g., displacing atoms and forming IV pairs) at increasing ion fluence, until there is complete loss of the long-range structural

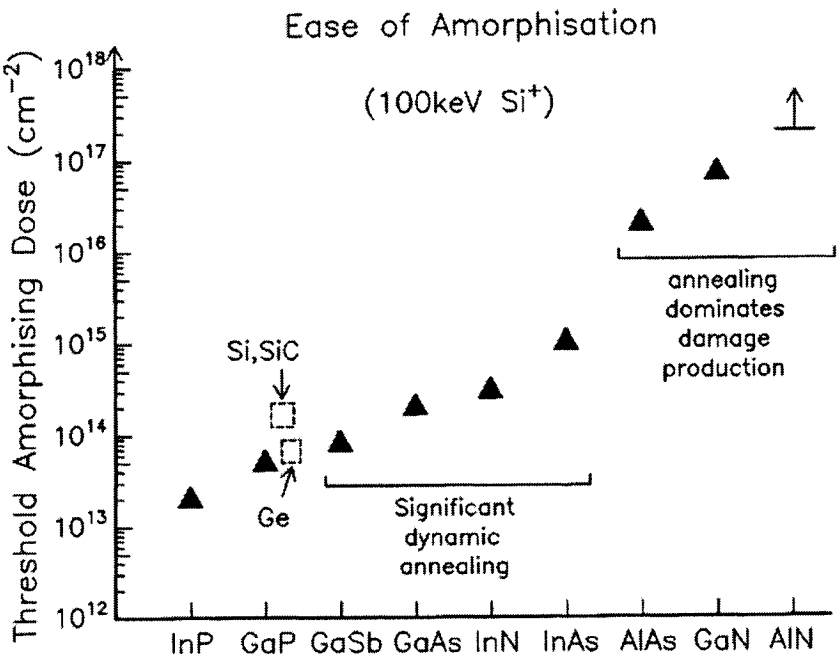

Figure 2.9. *Ease of amorphization of various crystalline targets at room temperature. Reproduced from reference [80].*

order. Most simulation and experimental studies of Si damage are carried out by low- to intermediate-E_i ion beams in the tens to hundreds of keV range, while we are mainly interested here by the damage behavior of c-Si in the presence of hyperthermal ions. We can cite the study by Bock et al. [81], which showed, using a combination of *in situ* low energy electron diffraction (LEED) and electron energy loss spectroscopy (EELS), that c-Si (111) becomes fully amorphized by an Ar^+ beam at a critical fluence of ~$5 \cdot 10^{14}$, $3 \cdot 10^{14}$ and $2.5 \cdot 10^{14}$ cm^{-2}, at 100, 250 and 750 eV, respectively. The ion beam energy dependence of critical dose was explained by the increasing penetration depth of energetic ions. They have also calculated the defect and energy density required to amorphize c-Si (to extinguish the LEED image) based on a procedure outlined by Brice et al. [82]. They found that the critical energy density (E_a) is $E_a = 12.6 \pm 3.8$ eV/atom at room temperature, which is in line with other amorphization studies [83, 84, 85, 86] of Si by low- and medium-E_i beams, which show that $E_a \sim 10 - 11$ eV/atom.

Some MD simulations have been carried out extensively in the hyperthermal range, and have shown similar damage and amorphization to low- and medium-energy ion-beam damage studies. Hensel and Urbassek [87] have studied damage of c-Si [(100), (110) and (111)] under 100 eV Si self-bombardment, where they found comparable ion ranges below all surfaces. They showed that in contrast to elemental metals, Si does not produce many point defects, instead forming amorphous nanoclusters, as revealed in low- to high-E_i damage and amorphization studies of c-Si [86, 88].

Nord, Norlund and Keinonen [65] have recently performed damage and amorphization simulations by MD, in which they also included all recoils with energy down to 3 eV (recoils with energy below 15 eV are usually ignored, because they are so abundant that the computation time is substantially increased), to show that these recoils play a critical role in damage formation. Such low-energy recoils contribute to the dynamic annealing and recrystallization of the target during implantation.

In general, amorphization in ceramics occurs either homogeneously or heterogeneously. Homogeneous amorphization proceeds by progressive accumulation of point defects or a specific type of defect in the bulk, as in the case of quartz [89]. Here, amorphization is observed in the target only after a critical defect concentration is exceeded. In most ceramics, however, amorphization is a heterogeneous process, leading to the gradual nucleation and growth of damaged or amorphous nanoclusters in an otherwise crystalline matrix, and has been described by several mechanisms, including (1) the direct-impact amorphization within individual cascades, (2) the local accumulation of high defect concentrations due to overlap of collision cascades, (3) the nucleation and growth process [90, 91], or a combination of these processes, such as (4) direct-impact combined with cascade-overlap amorphization [92], or (5) direct-impact in combination with stimulated amorphization at c/a interfaces (D-I/D-S) [93].

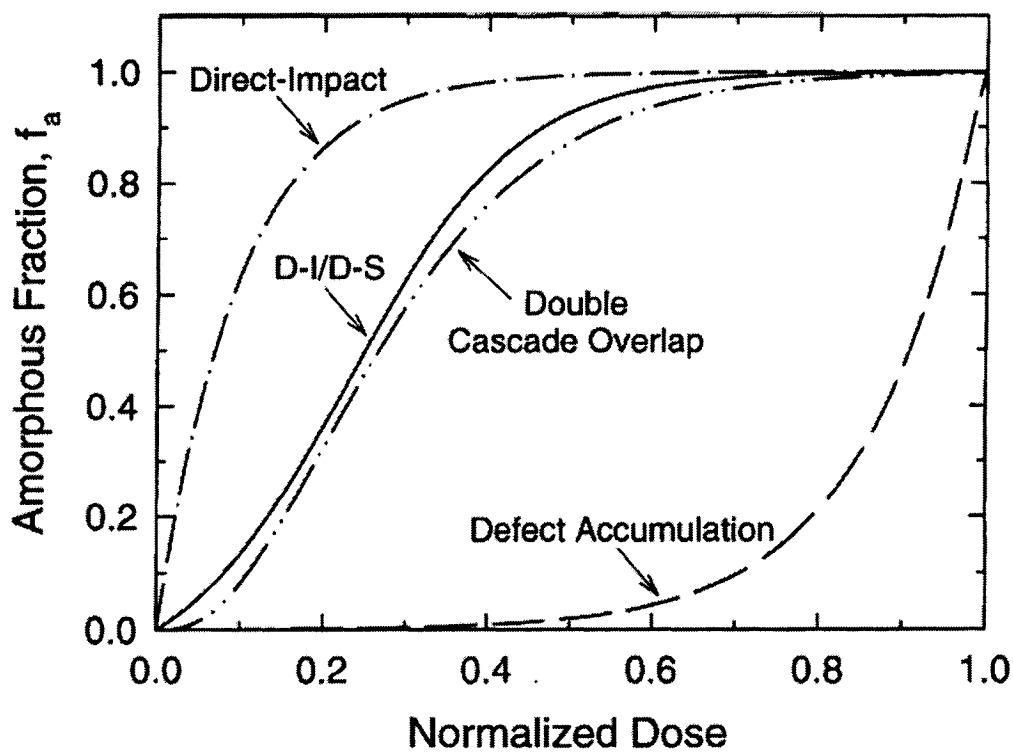

Figure 2.10. *Amorphous fraction as a function of normalized fluence according to defect accumulation, direct-impact, double-cascade-overlap, and direct-impact/defect-stimulated (D-I/D-S) processes. Reproduced from [98].*

Fig. 2.10 illustrates the amorphous fraction (f_a) as a function of normalized fluence for the five amorphization mechanisms described in the previous paragraph. Among these models, studies have shown that the last (D-I/D-S) successfully describes the amorphization of Si [65, 93, 94, 95], $Si_{1-x}Ge_x$ [96] and SiC [97]. The analytical relationship between ion fluence and the amorphization fraction in the target can be obtained by considering the rate of amorphization, expressed as follows:

$$\frac{df_a}{dt} = \sum_i P_i \times g_i(f_a), \tag{2.8}$$

where P_i is the amorphous production term for the i^{th} process and $g_i(f_a)$ is the probability associated to that process given the value of f_a. In direct impact amorphization, P_a is the product of amorphization cross-section (σ_a) and the ion flux (ϕ_i), while the probability

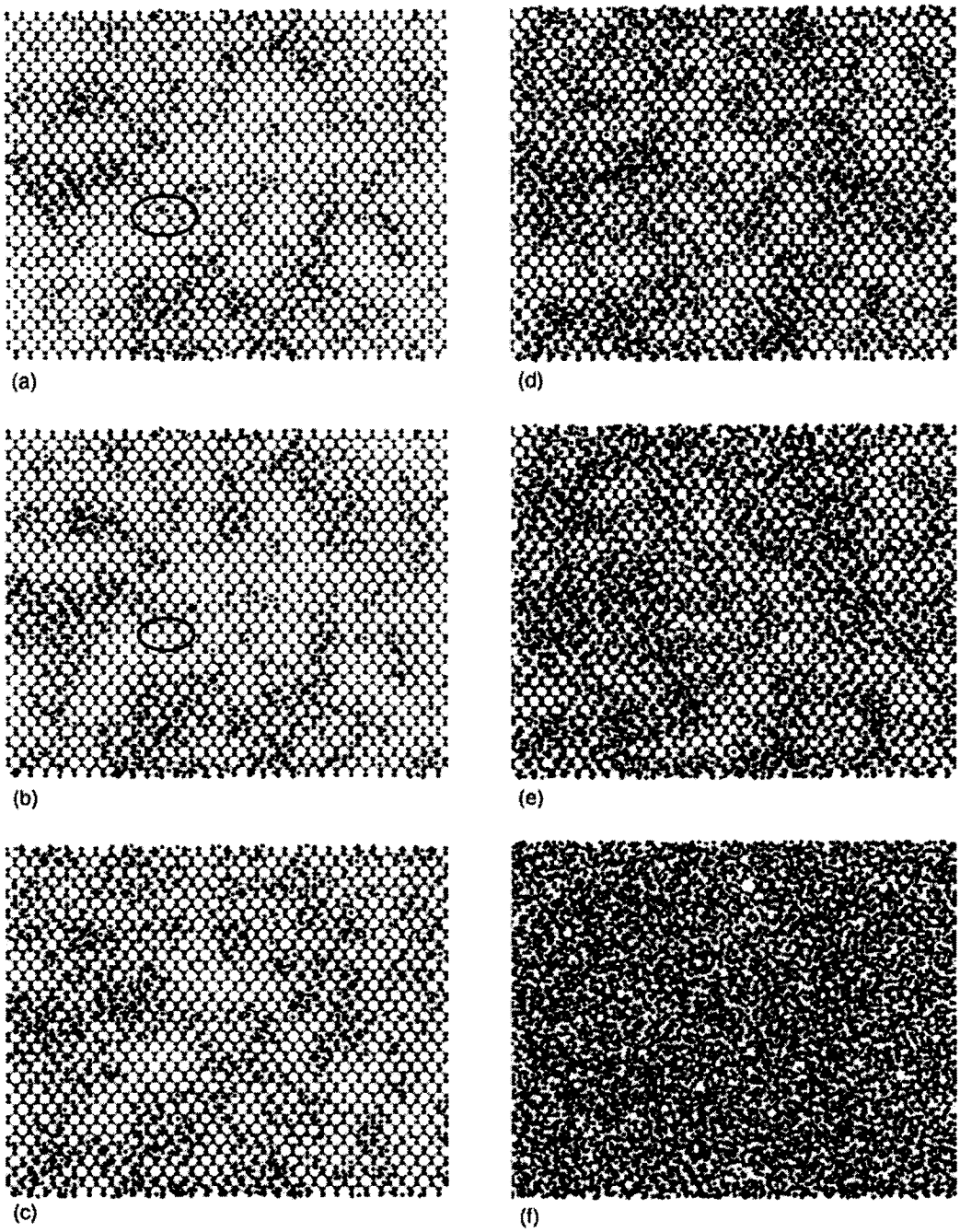

Figure 2.11. *Cross-section view of a MD simulation cell of c-Si (110) plane calculated for increasing deposited energy density (a) 1.1 eV/atom, (b) 1.5 eV/atom, (c) 2.8 eV/atom, (d) 4.2 eV/atom, (e) 5.6 eV/atom, and (f) 14 eV/atom. The defect circled in (a) is dynamically annealed, as seen in (b). Reproduced from [65].*

function $g_a(f_a)$ is given by $(1 - f_a)$. The probability $g_s(f_a)$ associated to interface stimulated production (P_s) is taken to be $f_a(1 - f_a)$, which is proportional to the amount of c/a

interfaces. The model is therefore expressed as follows:

$$\frac{df_a}{dt} = P_a(1-f_a) + P_s f_a(1-f_a). \tag{2.9}$$

The analytical solution to eq. (2.9) is known as the Hecking model [93, 98], and is expressed as follows:

$$f_a = 1 - \frac{\sigma_a+\sigma_s}{\sigma_a+\sigma_s e^{(\sigma_a+\sigma_s)\Phi}}, \tag{2.10}$$

where Φ is ion fluence ($\Phi = \phi_i \times$ time) and σ_s is the effective cross-section for stimulated amorphization.

Nord et al. [65] have used MD to study the c-Si damage and amorphization process by a spectrum of Si recoils (3 eV to 2 keV) and as a function of deposited energy doses (E_a, in units of eV per atom). One of the particularities of this work is that the authors used a very large sample size, composed of 40000 atoms, and calculated amorphization using a range of different semiempirical interatomic potentials: the Tersoff III (T-III), the environment-dependent interatomic potential (EDIP), and the Stillinger-Weber (SW) potential. The reliability of the results for the potentials was determined by comparing experimental values for an amorphization fluence and density with the simulated ones; the T-III potential was found to predict experimental results the best, and was subsequently used for detailed amorphization studies reported in their paper.

The authors verified that amorphization proceeds by a combination of direct-impact and defect-stimulated processes, and fitted a version of eq. (2.10) where Φ is replaced by E_a and obtained numerical values for both cross-sections ($\sigma_a = 0.0553\pm0.0003$ eV^{-1} and $\sigma_s = 0.447\pm0.002$ eV^{-1}). Figure 2.11 illustrates a four-unit-cell-thick cross section of the simulation cell in the (110) plane during ion irradiation of Si. The evolution of damage accumulation into clusters, and dynamic annealing (encircled in Figs. 2.11a and 2.11b) are observed with increasing E_a. Full amorphization leads to complete loss of long range order

in the crystal for E_a > 10 to 11 eV/atom. What is most notable about amorphization simulation studies with recoils is that they dissociate the amorphization process from the implanted ions and IEDF by linking f_a directly to recoils in the target. In this sense, eq. (2.10) can be used to calculate $f_{a\text{-}Si}$ in c-Si based on E_a depth profiles obtained for any hyperthermal or low-E_i ion source. Eq. 2.10 will be used extensively in Chapter 5 to calculate the damage and amorphization of c-Si exposed to ion bombardment at the RF-powered electrode of a PECVD reactor.

The authors state that their simulations are quantitatively accurate and reliable for damage and amorphization studies carried out at 150 K or below, because defects become increasingly mobile above this temperature. However, we believe that eq. 2.10 can still be used at slightly higher temperatures (such as 300 to 400 K) in the case of high ϕ_i experiments, such as at the RF-powered electrode, because increasing the ϕ_i can significantly inhibit the dynamic annealing [76, 77]. For instance, we observed in Fig. 2.8 that increasing ϕ_i from 5×10^{11} to 2×10^{13} $cm^{-2}s^{-1}$ reduced the dynamic annealing at 90°C to the level observed at 40°C. The reason behind this is that IV pairs do not have sufficient time to recombine when they are quickly surrounded by many other IV pairs. We therefore believe that an additional increase of ϕ_i to values exceeding ~10^{14} and ~10^{15} $cm^{-2}s^{-1}$, will likely further inhibit dynamic annealing, which then likely increases the temperature range of validity of eq. 2.10 closer to room temperature. This is supported by the good agreement we report in Chapter 5 between experiment and simulations using eq. 2.10.

2.4 Ion Beam- and Plasma-Induced Composition Changes

In the event of high fluence implantation of reactive species, such as oxygen ions, significant composition changes take place as a result of implantation and chemical reactions to a depth characterized by the ion range and straggle. As an example, Williams et al. [74] have implanted Si with low-energy oxygen ions (3 to 40 keV) at high fluence (up to

10^{18} cm^{-2}), and demonstrated that an oxide layer is formed (after ~10^{17} cm^{-2}) between the surface and a depth of $R_p + 2\Delta R_p$.

Similar ion beam oxidation (IBO) experiments have been performed using hyperthermal O^+ ions. Vancauwenberghe et al. [99, 100] and Todorov et al. [101] have extensively studied IBO in the sub-keV range, and both have successfully predicted the oxide thickness with the help of Monte-Carlo based ion implantation codes, demonstrating that oxidation is supply-limited, rather than reaction-limited, and self-limiting, owing to the depth-dependent transport of O ions.

When a target (e.g. Si, Ge or GaAs) is placed at a floating potential in a low-pressure O_2 plasma discharge, the process is generally called plasma-assisted oxidation or anodization (positive bias) [102]. Such processes have been used to perform low-temperature (<600°C) oxidation in order to reduce the thermal budget of microelectronics processes [103]. The plasma oxidation processes use very low energy hyperthermal ion bombardment, typically less than 50 eV [104, 105], and rely in good part on the field enhanced transport (Cabrera-Mott model) of negatively charged atomic O ions (O^-) inside SiO_2 to the SiO_2-Si interface [106, 107, 108, 109] to produce high quality oxides with low defect concentration. Irene's group [110] has shown that negative biasing is not conducive to field-enhanced transport. It was suggested that O_2^- ions dissociate easily into O^- and O, while the rate of O_2^+ dissociation is low.

Capacitively coupled RF plasmas [111, 112, 113], similar to what we use for plasma oxidation in this study, have also been shown to oxidize Si (when it is placed at the anode). In the case of negative substrate biasing, the oxidation behavior is self-limiting and is so far believed to be limited by the ion penetration depth [110]. Detailed information about ion bombardment characteristics of RF plasmas are provided in Section 3.4.

2.5 Optical Probe of Damage and Oxidation in c-Si

Most analytical techniques used to characterize damage formation and amorphization are either destructive (TEM), highly invasive (RBS channeling) or simply inoperable during plasma processing (LEED, XPS). Optical probes have emerged as a nondestructive and non-invasive way to extract a great deal of depth-dependent information *in situ* and during processing.

To understand the sensitivity of optical probes to structural changes in materials, we recall that optical properties are directly linked to electronic band structure. The functional form for the energy dependence of the complex refractive index $\tilde{n}(E) = n(E) - ik(E)$ – where $n(E)$ and $k(E)$ are the photon energy-dependent refractive index and extinction coefficient – can be found by calculating the real and imaginary parts of the dielectric function [$\varepsilon(E) = \varepsilon_1(E) - i\varepsilon_2(E)$] based on the electronic band structure. The relationship between $\tilde{n}(E)$ and $\varepsilon(E)$ is

$$n(E) - ik(E) = \sqrt{\varepsilon_1(E) - i\varepsilon_2(E)}\,, \tag{2.11}$$

which implies that

$$\varepsilon_1 = n^2 - k^2 \tag{2.12a}$$

and

$$\varepsilon_2 = 2nk\,. \tag{2.12b}$$

Conversely,

$$n = \sqrt{\frac{\varepsilon_1 + \sqrt{\varepsilon_1^2 + \varepsilon_2^2}}{2}} \tag{2.13a}$$

and

$$k = \sqrt{\frac{\sqrt{\varepsilon_1^2 + \varepsilon_2^2} - \varepsilon_1}{2}}\,. \tag{2.13b}$$

For direct interband transitions in monocrystalline semiconductors,

$$\varepsilon_2(E) = \frac{\hbar \pi e^2}{m_e^2 E \varepsilon_0} \sum_k |P_{cv}|^2 \, \delta\left[E_c(\vec{k}) - E_v(\vec{k}) - E\right], \tag{2.14}$$

where P_{cv} is the momentum matrix element of the transition between the valence and conduction bands, E_c and E_v are the energy of the conduction and valence bands, respectively, as a function of wavevector ($\vec{k}$), $\hbar$ is Plank's constant, e is the electronic charge, m_e is the free electron mass, and ε_0 is the permittivity of vacuum. The real part of the dielectric constant, $\varepsilon_1(E)$, is related to eq. (2.14) by the Kramers-Kronig (K-K) transformation:

$$\varepsilon_1(E) = 1 + \frac{2}{\pi} P \int_0^\infty \frac{E' \varepsilon_2(E')}{E'^2 - E^2} dE' \tag{2.15}$$

where P represents the Cauchy principal value of the integral. The summation of the delta functions over $\vec{k}$ in eq. (2.14) can be replaced by an integration over energy of the joint density of states (JDOS) $g_j(E)$, the density of pairs of states in two bands, namely the valence and the conduction bands, with energy separation $E_{cv}(\vec{k}) = E_c(\vec{k}) - E_v(\vec{k})$ at the same $\vec{k}$-value. The JDOS is defined as:

$$g_j(E) = \frac{2}{(2\pi)^3} \int \frac{dS_E}{|\nabla_k (E_{cv})|}. \tag{2.16}$$

It is obtained from the band structure energy separation [$E_{cv}(\vec{k})$] via an integration in $\vec{k}$-space over the Brillouin zone of a constant-energy surface (S_E) of the band structure. Thus, flat bands in $\vec{k}$-space give rise to sharp features in the JDOS, called van Hove singularities, because $\nabla_k E_{cv} = 0$. This condition is satisfied for transitions between band extrema, and also for transitions between two states for which the local gradients are equal, i.e. $\nabla_k E_c(\vec{k}) = \nabla_k E_v(\vec{k})$.

Van Hove singularities in the JDOS give rise to peaks in the $\varepsilon_2(E)$ spectrum, which also lead to characteristic spectral features in $\varepsilon_1(E)$ too, according to the K-K relation, as we

shall see shortly. In the case of disordered materials (e.g. a-Si), the loss of translational periodicity means that electron wavevectors ($\vec{k}$) are ill-defined and electron states cannot be described in terms of a band structure. The $\vec{k}$-selection rule for optical transitions is relaxed, meaning that the optical spectra are much simpler than for crystals. There are no sharp features in $\varepsilon_2(E)$ corresponding to van Hove singularities. For the interband transition in amorphous solids, it makes no sense to discuss the optical properties in terms of *joint* density of states. However, the density of states (DOS) is still a valid description. Hence, $\varepsilon_2(E)$ is taken to be proportional to an integral of the *product* of the valence- and conduction-band DOS (g_V and g_C, respectively):

$$\varepsilon_2(E) \propto \frac{|P_{CV}|^2}{E^2} \int_0^E g_V(-E')g_c(E-E')dE', \tag{2.17}$$

where the zero of energy is fixed at the top of the valence band. The approach is generally similar in the case of indirect gap materials, but is not illustrated here so as to avoid repetition.

Fig. 2.12 shows the DOS of c-Si and a-Si calculated using the tight-binding approximation [114]. While the DOS are qualitatively similar, van Hove singularities are smeared out in the case of an amorphous solid, owing to the absence of translational periodicity. The changes in the DOS directly affect the optical response of Si and are responsible for the dramatic difference between the dielectric functions of c-Si, a-Si, and a-SiO_2 as seen in Figs. 2.13a and 2.13b. We have also plotted the corresponding n and k spectra in Figs. 2.13c and 2.13d for c-Si [115], a-Si [116], a-SiO [117] and a-SiO_2 [118]. We see that O incorporation greatly reduces both n and k, and leads to $k \sim 0$ in the case of stoichiometric SiO_2 in the spectrum of interest.

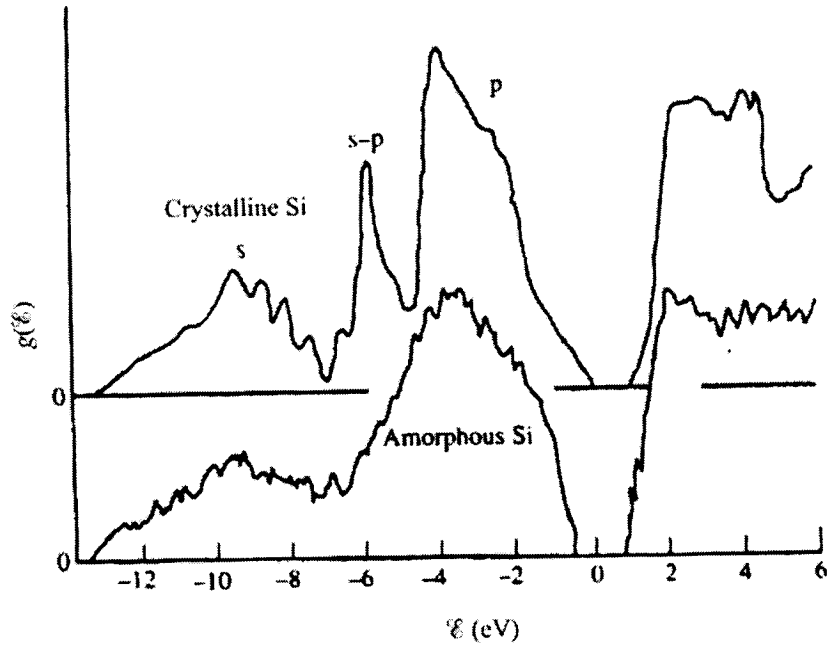

Figure 2.12. *Calculated density of states (DOS) for a-Si and c-Si according to the tight-binding approximation. From reference [114].*

To describe the effective optical response of a heterogeneous mixture, such as that of a crystalline matrix with amorphous inclusions, we calculate the combined optical responses of the two phases according to the effective medium approximation (EMA) [119]. A number of studies have demonstrated that the isotropic Bruggeman EMA (BEMA) model works best in the case of Si damage [51, 120, 121]. According to the BEMA model, the effective dielectric function ε of a two-component mixture (e.g. c-Si, a-Si), where inclusions are much smaller than the wavelength of light, may be calculated according to the following equation which (can be easily generalized to three or more components):

$$P_a \frac{\varepsilon_a - \varepsilon_{eff}}{\varepsilon_a + 2\varepsilon_{eff}} + (1 - P_a) \frac{\varepsilon_b - \varepsilon_{eff}}{\varepsilon_b + 2\varepsilon_{eff}} = 0, \qquad (2.18)$$

where ε_a and ε_b are the dielectric functions of components a and b, and P_a is the fraction of component a. We have used the BEMA model to calculate the effective dielectric function and optical properties of a 1:1 mixture of a-Si and c-Si in Fig. 2.13. We see that the optical

response of the mixed-phase material changes dramatically from c-Si optical response towards that of a-Si, hence making optical probes in the spectral region rather sensitive to structural changes. The EMA method does not accurately model chemical mixtures, such as the optical properties of $Si_xTi_{1-x}O_2$ by combining the optical properties of TiO_2 and SiO_2 [22], because the alloy or solid-state solution has a different electronic band structure, and therefore optical response, than a heterogeneous mixture. The EMA model works better for physical mixtures where inclusions have dimensions much smaller than the wavelength of light. At the lower end, small dimensions can lead to quantum confinement effects too, which cannot be described by the EMA model.

Spectroscopic ellipsometry (SE) (described in detail in section 3.3) is one of the most powerful optical diagnostic tools because of its excellent sensitivity to near-surface structural and composition changes, which permits us to perform depth-profiling of damage formation and amorphization in crystalline materials [122]. Damage study by SE was first proposed in the 1970s and 1980s by a number of works [123, 124, 125, 126], where it was shown that optical modeling can provide quantitative depth-dependent information about damage formation.

The ability of SE to provide quantitatively accurate data about the depth and extent of modifications has been systematically tested and verified [51]. Numerous comparative studies have validated ellipsometric models and results, with the help of more direct, but destructive tools such as cross-section transmission electron microscopy (XTEM, see Fig. 2.14) [124], RBS channeling [127], and secondary ion mass spectroscopy (SIMS) depth profiling [120]. In general, it has been found that SE can yield depth-dependent results with sub-nanometer precision and accuracy. Fig. 2.14 shows a comparison of damage depth profiles in c-Si determined by XTEM and SE for a 80 keV Si^+ beam with 10^{16} cm^{-2} fluence. The comparison points to the excellent depth-profiling capability of SE analysis, as well as its unique capability to quantify the level of damage in the target.

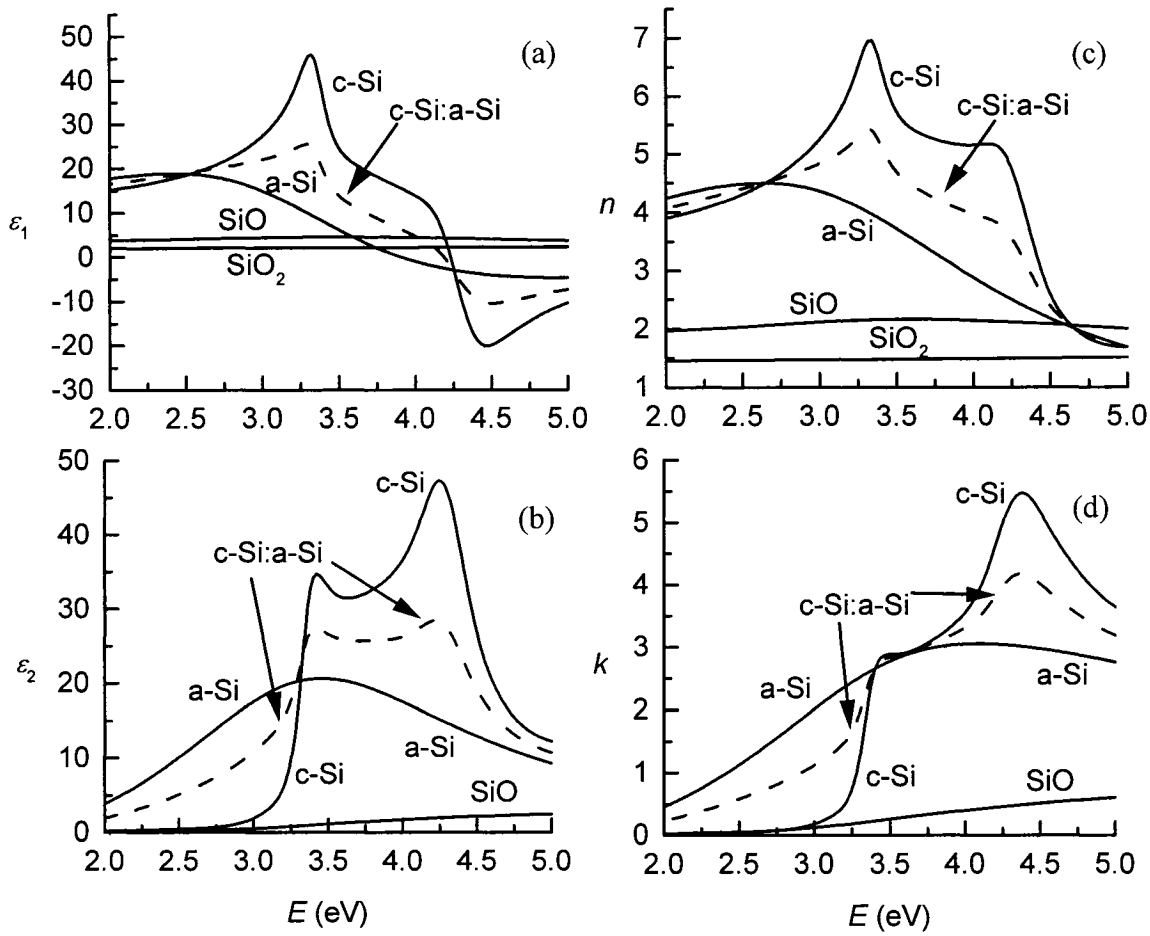

Figure 2.13. *(a) Real and (b) imaginary parts of the dielectric function, and corresponding (c) refractive index and (d) extinction coefficients of c-Si, a-Si, SiO and SiO_2, as well as an isotropic BEMA mixture of c-Si and a-Si (c-Si:a-Si = 1:1) calculated using Eq.(2.18).*

Expanding on this capability, Giri et al. [128] have used SE to study crystalline-to-amorphous phase transition and band structure evolution of Ar^+-beam (120 keV) damaged Si. The authors used BEMA to extract the optical constants of ion-damaged Si (Fig. 2.15a). They also plotted the evolution of the differential peak height of the imaginary part of the dielectric function ($\Delta\varepsilon_2$) at E_1 and E_2 transitions [129] as a function of Ar^+ fluence (Fig. 2.15b). Both plots show the transition at ~$5 \cdot 10^{14}$ cm^{-2}, between a damage accumulation regime (Fig. 2.15a, 1 – 4), characterized by reduction in E_1 and E_2 transition peaks, and an

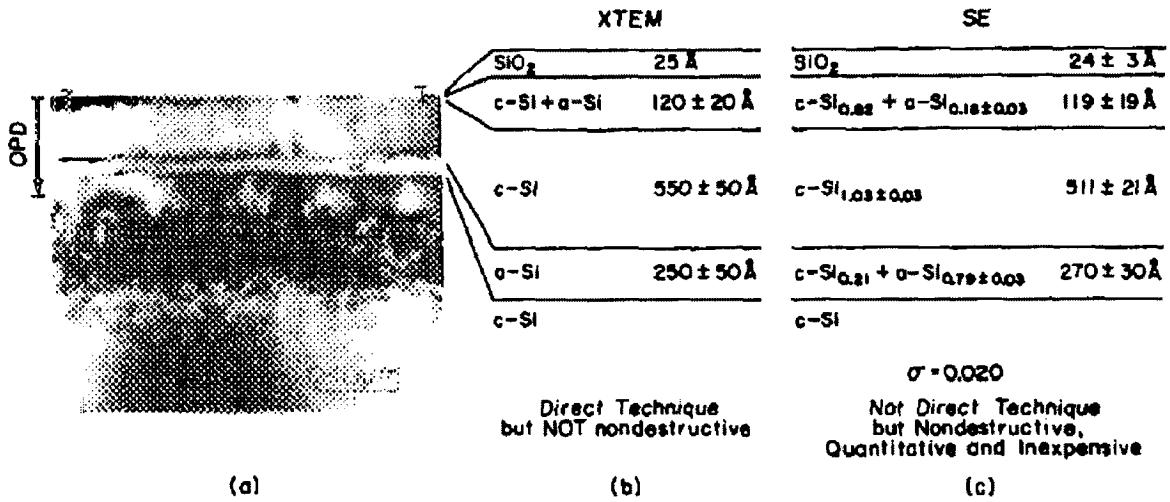

Figure 2.14. *Comparison of (a-b) cross-sectional transmission electron microscopy and (c) spectroscopic ellipsometry characterization of c-Si irradiated by 80 keV Si^+ with 10^{16} cm^{-2} total fluence. SE analysis was performed prior to XTEM. From reference [51]. OPD: optical penetration depth.*

amorphization regime, characterized by smoothening out of characteristic peaks of ε_2 (Fig. 2.15a, 5 – 9).

This ability of SE to quantify and depth-profile the near-surface damage is especially valuable, since it can be used *in situ* and in real-time (RTSE) to perform rapid, non-destructive and non-invasive measurements during plasma processing (Chapters 5 to 7). A detailed description of SE analysis is given in section 3.2.

2.6 Ion Bombardment During Thin Film Deposition

So far, in this chapter we have presented the basic principles of ion-surface interactions, including implantation, sputtering, damage formation and composition changes. These effects are also expected to play a significant role during thin film growth by PECVD. In this section, we briefly discuss the effects of these basic physical processes on the growth of thin films on amorphous substrates, and we discuss the microstructure of thin films as a function of substrate temperature. We then present two important phenomena involving the

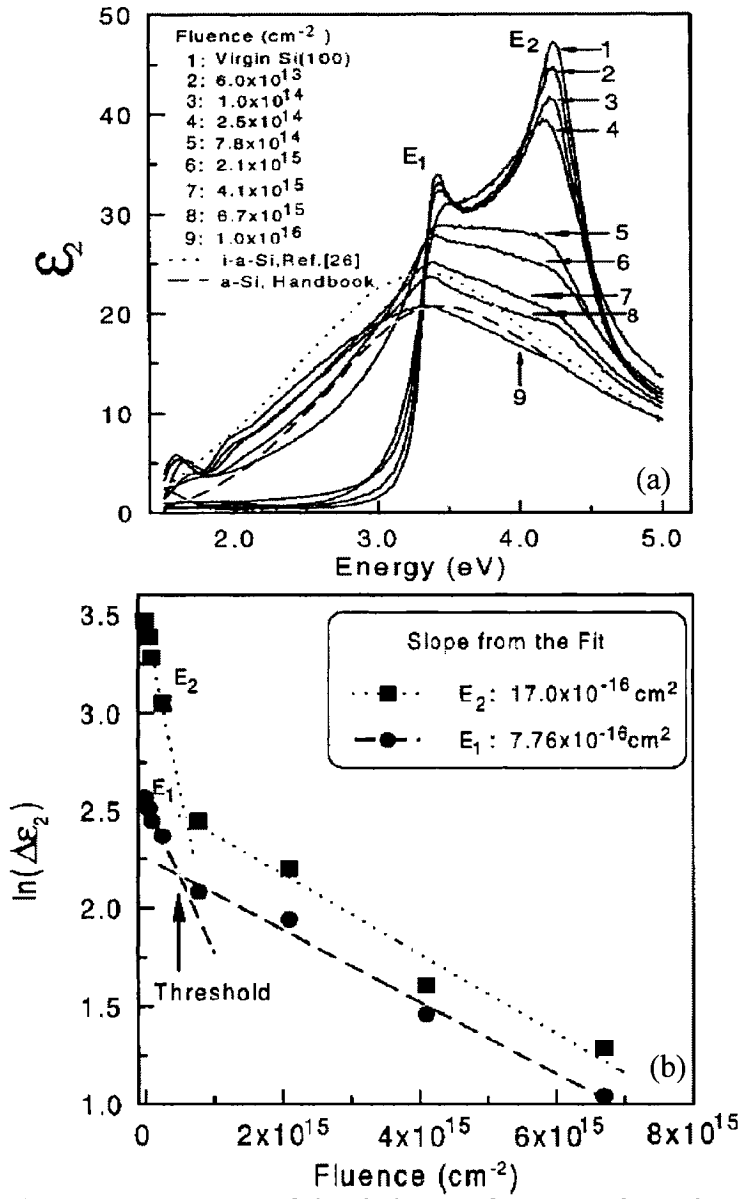

Figure 2.15. *(a) Imaginary part of the dielectric function of ion-damaged Si exposed to 100 keV Ar^+ beam; (b) semilogarithmic plot of differential peak heights as a function of fluence for two major transitions E_1 and E_2. From reference [128].*

role of hyperthermal ion bombardment during thin film growth, subplantation and densification.

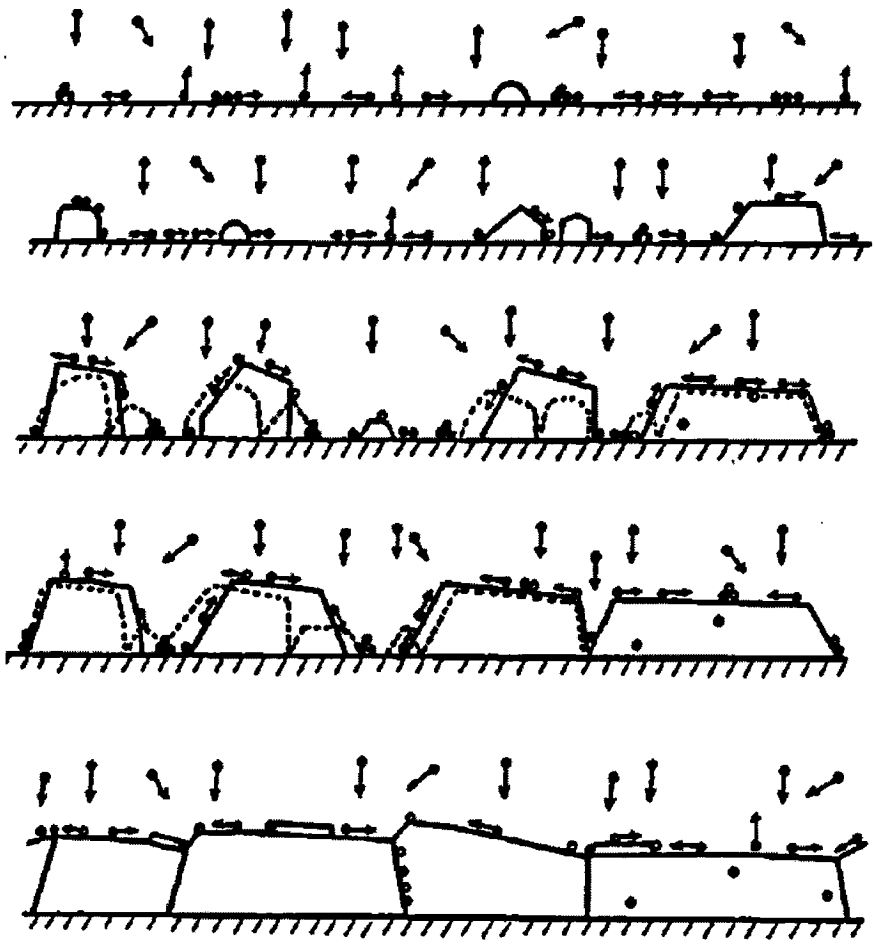

Figure 2.16. *Schematic diagram illustrating fundamental growth processes controlling the microstructural evolution of thin films: nucleation, island growth, impingement and coalescence of islands, grain coarsening, formation of polycrystalline islands and channels, development of a continuous structure, and film growth. From reference [130].*

2.6.1 Thin Film Microstructure and Structure Zone Models

Films used in industrial applications are often deposited at relatively low processing temperatures (T_s), which are less than 0.2-0.3 of the melting point T_m (in Kelvin). Film fabrication thus takes place far from thermodynamic equilibrium. As a consequence, their microstructure is different from that of bulk material, and it typically evolves in a competitive fashion as a result of kinetic limitations during low-temperature processing,

thus enabling the controlled growth of metastable phases.

Among the atomic processes controlling the evolution of the microstructure during film deposition are surface and bulk diffusion. These processes are naturally affected by T_s, but also by (1) the presence of energetic particles, which can enhance adatom mobility and nucleation, and by (2) the presence of impurity elements and their segregation to surfaces and grain boundaries. Geometric shadowing also controls film microstructure by promoting the capture of off-normal flux by protruding surfaces.

The use of amorphous substrates at low temperature allows one to isolate the effects of individual deposition variables on texture development. On such substrates, film growth often proceeds via a three-dimensional or Volmer-Weber mode. The growth processes controlling microstructural evolution are presented schematically in Fig. 2.16; they include nucleation, growth, impingement and coalescence of islands, formation of polycrystalline islands and channels, development of a continuous structure, and bulk-like growth [130]. If surface diffusion is very high, then bulk-like growth proceeds via local epitaxy on individual grains. Grain coarsening (recrystallization through grain boundary migration) can proceed during the early stages of growth and later, during bulk-like growth.

Generally, for $T_s/T_m < 0.4\text{-}0.5$, nucleation proceeds by solid-phase island formation with random orientation in the plane of the surface [131, 132]. During island coalescence, there is a strong driving force for coarsening via surface atom diffusion and grain boundary motion, as the system attempts to minimize the overall surface and interface energy. Coalescence also results in new open substrate area for secondary nucleation. Grain coarsening during coalescence proceeds until local grain sizes become sufficiently large that grain boundaries are immobile.

In 1969, Movchan and Demchishin [133] observed that the microstructural evolution of evaporated pure elemental films, such as Ni, Ti, and W, as well as some oxide coatings

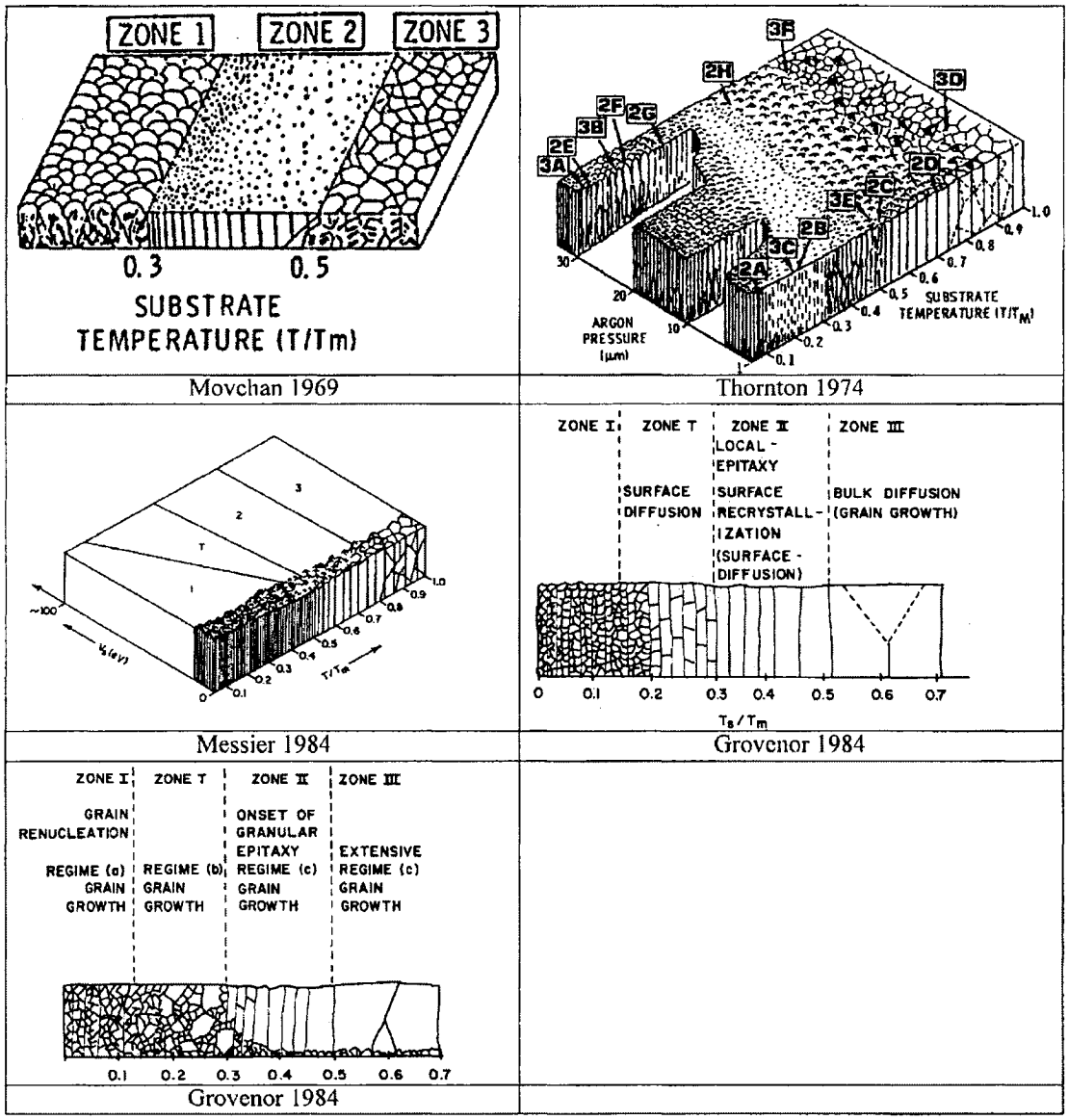

Figure 2.17 *Summary view of structure zone models proposed by Movchan [133], Thornton [142], Messier et al. [143] and Grovenor et al. [144]. Reproduced from reference [137].*

(Al_2O_3 and ZrO_2) can be systematically represented by a single structure zone model (SZM) diagram plotted versus homologous temperature (T_s/T_m, see top-left panel of Fig. 2.17), consisting of three regimes: Zone 1 corresponds to very low deposition temperature, and is characterized by negligible adatom diffusion; in Zone 2 (often called Zone T, for

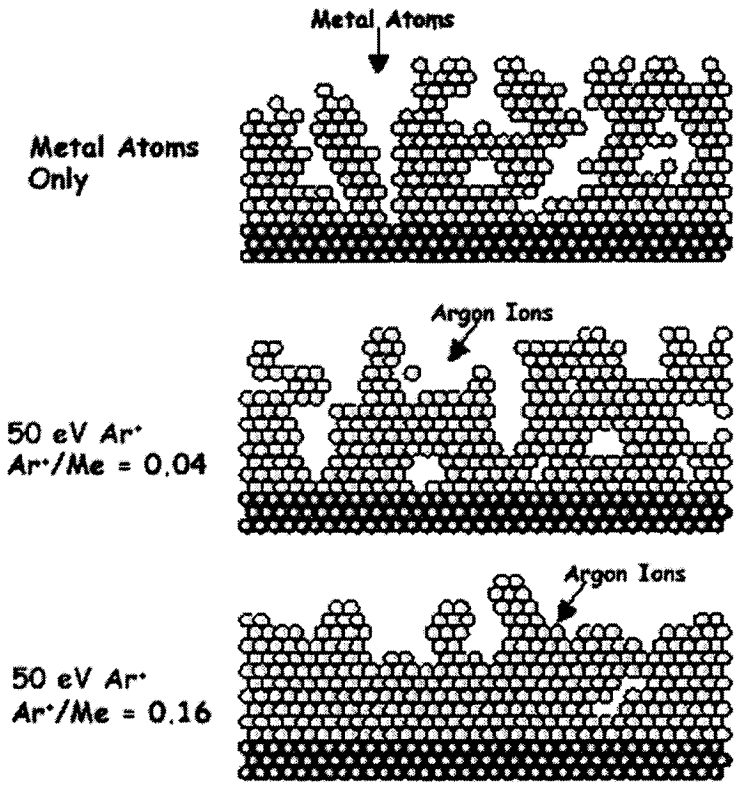

Figure 2.18. *MD simulations of the effect of increasing ion bombardment on the density and roughness of metal thin films. Modified from [145].*

transition), surface diffusion becomes significant; and both surface and bulk diffusion mechanisms contribute to film growth in Zone 3.

Films grown in the low-T_s Zone 1 regime are underdense with a fine fibrous structure. Adatom mobility at the surface is low and nuclei form into columns with random orientation [53], which can be composed of small equiaxed grains, or can be completely amorphous. Surface roughness develops in a fractal geometry [134, 135], due, in good part, to self-shadowing and the inability of surface diffusivity to overcome it.

At higher temperature (Zone 2), grain coarsening occurs during coalescence, and leads to the formation of denser films. However, grain boundaries become immobile when a continuous film is formed. Crystallites, if formed, are nearly random in orientation. In this

T_s/T_m range, adatom diffusion is significant, and can lead to local epitaxial growth taking place in individual grains, and more so on planes with low surface diffusivity, as high diffusivity planes grow slowly and may become trapped on adjacent grains. Consequently, competitive growth can lead to a continuous change of morphology, texture and surface roughness with film thickness, which in fact lead to changes of film properties too.

Films grown at high-T_s in Zone 3 are dense and significantly textured, with mobile grain boundaries even after continuous film formation, as a result of significant bulk diffusion.

2.6.2 Ion Bombardment-Induced Densification

Low-energy ion bombardment during thin film growth is used extensively to overcome or control the characteristic rough and underdense microstructures of materials in Zones 1 and 2 ($T_s/T_m < 0.25$) [136, 137, 138, 139, 140, 141], and can control the nucleation rate and density of growing films, by inhibiting grain growth and columnar microstructure associated to high surface roughness.

The role of IB on thin film microstructure is summarized in the SZMs of Thornton [142] and Messier [143] presented in Fig. 2.17. Thornton's SZM deals with the effect of ion bombardment by reflected and sputtered atoms from the target, and demonstrates that increasing ion bombardment (by reducing Ar pressure) leads to a reduction of T_s/T_m required to form Zone 2-type films. Messier's SZM reveals a similar tendency in the case of ion-assisted depositions. In addition, Fig. 2.17 shows Grovenor's [144] proposed SZMs, which take the influence of substrate morphology into consideration.

Collisions and enhanced surface mobility of adatoms during ion bombardment lead to the formation of densely packed coatings. The atomistic role of ion bombardment on film densification and microstructure was first illustrated with the help of MD simulations by Muller [145] who showed how ions are capable of displacing atoms and entire clusters into forming a densely packed thin film. Fig. 2.18 illustrates that in the absence of ion

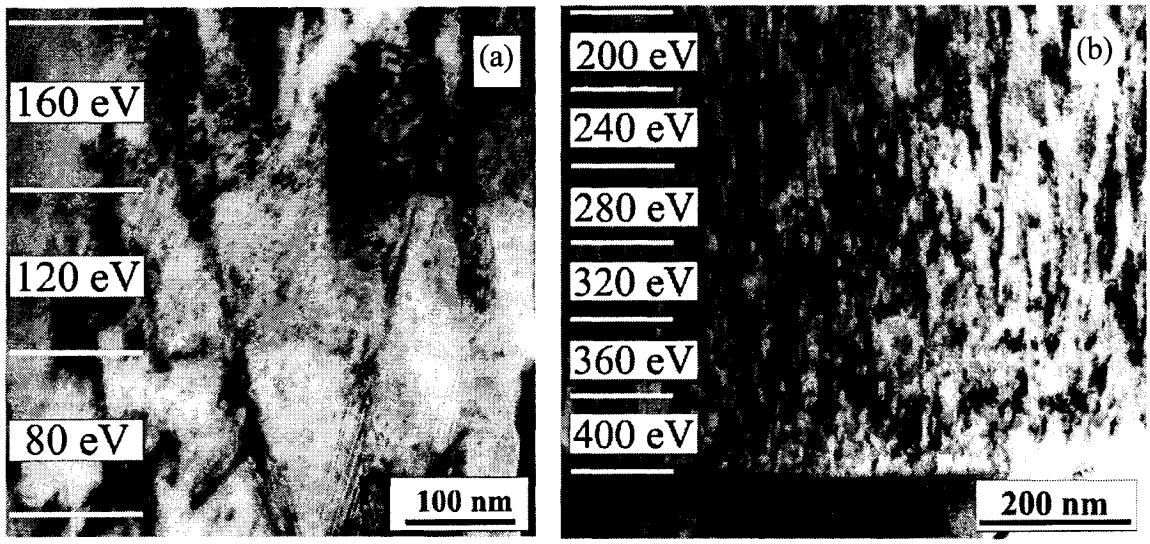

Figure 2.19. *Bright-field micrographs obtained from a 3.5 μm-thick TiN layer grown by reactive magnetron sputtering on steel at 300°C with a total pressure of 5.6 mTorr. (a) middle and (b) bottom portions of the same film, where E_i was varied by 40 eV increments between 40 and 400 eV. Reproduced from [136].*

bombardment during thin film deposition tends to form a porous structure, and that the addition of ion bombardment in the low hyperthermal energy range is sufficient to enhance the density of the growing film and decrease surface roughness.

Increasing the ion energy, while maintaining the ion-to-neutral arrival rate ratio constant, affects the film microstructure primarily through collision cascade effects. For instance, in the case of TiN thin films deposited by magnetron sputtering (T_s = 300°C, pressure = 5.6 mTorr) with ion-to-neutral flux ratio kept below one, and E_i < 80 eV (Fig. 2.19a), the microstructure consists of dense columns with open boundaries [136]. When E_i ~ 120 eV, the voids along column boundaries disappear and the film becomes fully dense. This is accompanied by incorporation of intragranular damage, whose concentration increases at even higher E_i (>200 eV, see Fig. 2.19b), leading to disrupted column growth, and repeated nucleation events.

2.6.3 Subplantation

Lifshitz, Kasi and Rabalais [41, 42] were the first to bridge the gap between surface deposition and shallow implantation, which they aptly called subplantation. The authors proposed that the growth of diamond-like carbon (DLC) coatings in the presence of incident hyperthermal C^+ particles progresses along the following path. Energetic species penetrate below the surface to a depth which depends on the characteristics of the incident species (energy, mass) and the target (composition, density, etc.) (see Fig. 2.20). The range of energetic C (10^3 eV) in the hyperthermal range varies from 1 to 10 nm (Fig. 2.20a), depending on target mass density (Au to Li, respectively). The stopping of these species proceeds by two mechanisms, namely atomic displacements and electron excitation (as discussed earlier), and it also leads to phonon excitation by recoils with kinetic energy below E_D. Atomic displacements lead to damage (Fig. 2.20e), whereas phonons and electronic excitations are responsible for thermal spikes, which can enhance transient diffusion and reordering locally. Energetic species occupy predominantly interstitial sites inside the film or substrate. This can lead to formation of inclusions and clusters, which possibly lead to the growth of a new phase. In the case of DLC coatings, the authors proposed that stress accumulation from the formation of inclusions favors the growth of sp^3 bonds, which is desired to obtain nearly bulk-like properties (see Fig. 2.21). Fig. 2.21 also shows that as the fluence of energetic C^+ increases, the structure and composition of the metal substrate evolves from pure metal, to a carbide mixture, and finally to the formation of an sp^3 carbon coating, with a transitional interface with the metal substrate. The structure of the evolving film is then determined by crystallographic effects (or mold effect), by preferential displacement of atoms (which tends to leave high-E_D atoms in place) (see Fig. 2.22) and by the ability of defects (including IV pairs) to accumulate (leading to the formation of another crystallographic phase, including an amorphous one).

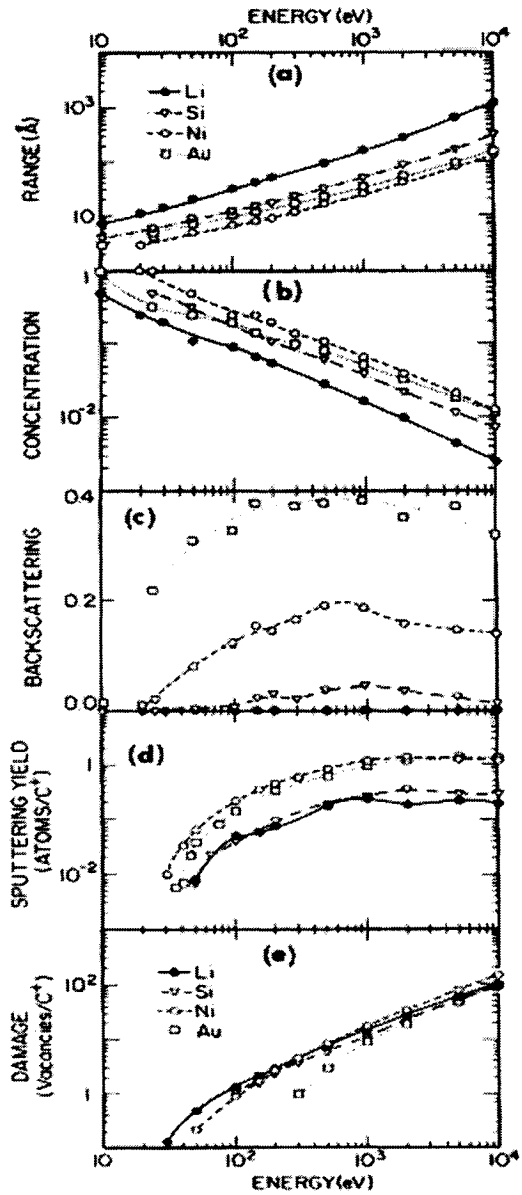

Figure 2.20 *TRIM calculations of C bombardment of Li, Si, Ni and Au. (a) Range (R_p) of C, (b) local concentration ($1/\Delta R_p$) of C, (c) backscattering, (d) sputtering yield of target atoms, and (e) damage; notice the significant mass effects on (a) and (c). Reproduced from reference [42].*

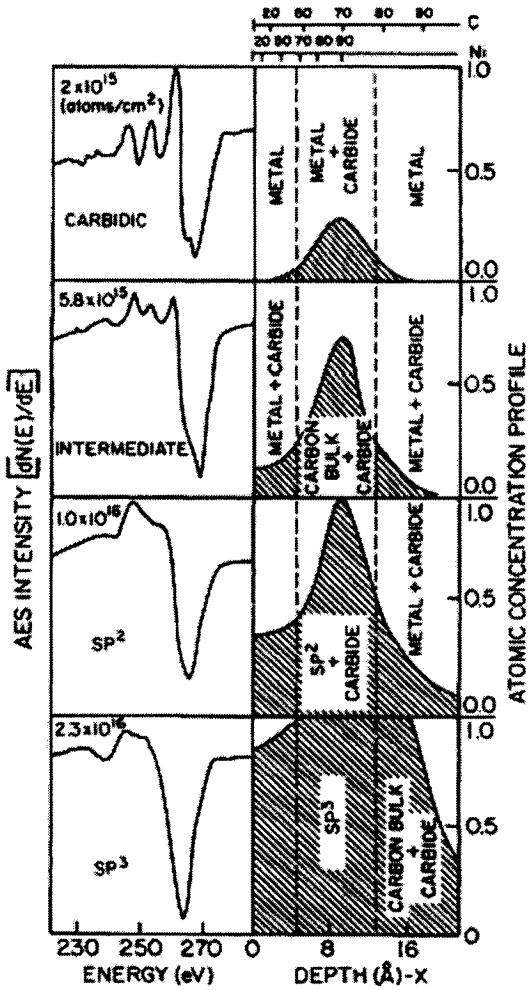

Figure 2.21 *Stages of subplantation growth demonstrating sub-surface deposition. Left column: C KLL Auger electron spectroscopy (AES) line shapes for different C^+ fluences for 150 eV C^+ ions on Ni(111). Right column: subsurface entrapment of energetic carbon and buildup of carbon deposits. The top scale indicates the relative contribution to the AES intensity (%) derived from a layer of depth x (lower scale). Reproduced from reference [42].*

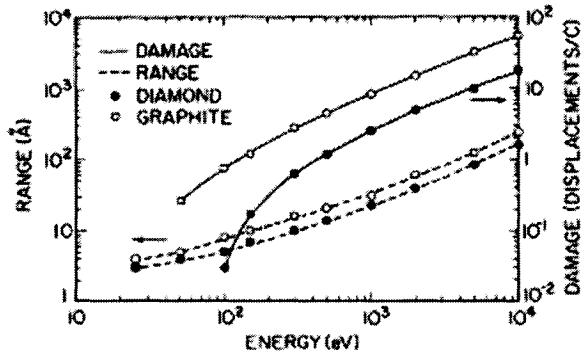

Figure 2.22 *TRIM calculations of R_p and damage for C^+ ions with energy ranging from 10 eV up to 10 keV impinging on graphite (E_d = 25 eV, density = 2.26 g/cm3) and diamond (E_d = 80 eV, density = 3.5 g/cm3). Note preferential displacement of graphite compared to diamond, especially between 100 and 200 eV, where damage in diamond is negligible compared to graphite. Reproduced from reference [42].*

Chapter 3. Experimental Methodology and Simulation Tools

In this chapter we describe the PECVD reactor, the substrate preparation method, and the ion bombardment characteristics of RF and MW plasmas employed in this work. We also introduce the principles of ellipsometry and ellipsometric analysis, and briefly describe *ex situ* VASE characterization and *in situ* RTSE monitoring. Finally, we describe the BCA-based Monte-Carlo TRIM [62] and TRIDYN (dynamic TRIM) [63, 64] simulation programs used to calculate the effects ion-surface interactions.

3.1 Plasma Deposition Systems

3.1.1 RF Plasma Reactor for Plasma Oxidation and TiO_2 Deposition

O_2 plasma treatments (presented in Chapters 4, 5 and 6) and TiO_2 depositions (see Chapter 6) were performed at room-temperature in the capacitively coupled RF plasma (13.56 MHz) system schematically shown in Fig. 3.1 [146, 147]. It consists of a 30 liter capacity stainless steel vacuum chamber (30 cm in diameter), and a pumping system with mechanical (roughing) and turbomolecular pumps equipped for corrosive gases. The gas distribution system introduces O_2 and $TiCl_4$ separately, to avoid gas-phase oxidation. The working pressure (p) is measured by a capacitance gauge, the pumping speed is regulated by a butterfly valve, and RF power is supplied to the substrate holder-electrode (15 cm in diameter) through a matching unit. A negative self-bias (V_B) develops on the RF-powered substrate holder, and is regulated by the power supply and matching unit.

In this work, all experiments (unless stated otherwise) were performed on standard c-Si (001) substrates, that were degreased in acetone, isopropanol and DI water, cleaned in a Piranha solution (H_2SO_4 :H_2O :H_2O_2 = 4 :1 :1) for 5 minutes, rinsed in DI water, blow-dried with N_2, and immediately inserted in the vacuum chamber, which was then pumped down to $<10^{-5}$ torr.

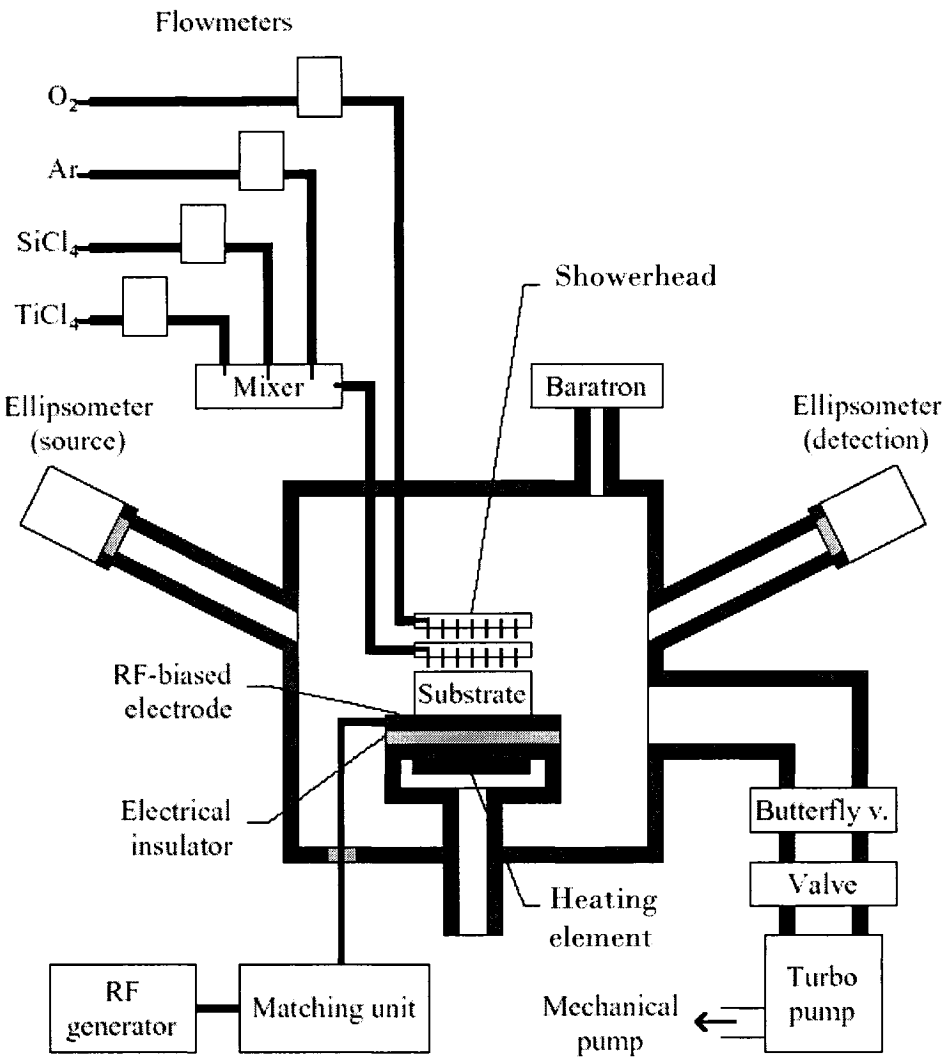

Figure 3.1. *Schematic view of the plasma reactor used for surface treatment and deposition experiments; in situ spectroscopic ellipsometer is also shown. Reproduced with permission from [147].*

The c-Si substrate is pretreated prior to thin film deposition; this is the subject of a detailed study by *ex situ* and *in situ* SE, together with Monte-Carlo simulations. The pretreatment consists of exposure to an RF discharge in O_2 at the RF-powered electrode. O_2 is first introduced into the chamber at a flowrate of 60 sccm and the working pressure is set at p =

20 mTorr. The plasma is ignited at a power level corresponding to V_B conditions specifically selected to emulate ion bombardment conditions typical for PECVD deposition of optical coatings (V_B = -60 to -600 V), and pretreatment is performed for a few minutes.

TiO_2 thin film deposition is initiated by introducing $TiCl_4$ into the plasma reactor after a 10 minute pretreatment at V_B = -600 V. V_B is adjusted prior to TiO_2 deposition and reduced to the desired deposition value, -450 V. $TiCl_4$ is introduced without stopping the O_2 RF plasma (after adjusting V_B), using a computer-controlled flowmeter, while the O_2 flow and the total pressure (20 mTorr) is kept constant. The $TiCl_4$ flowrate is adjusted to control TiO_2 growth rate, while keeping the ion flux approximately constant (by maintaining V_B and p constant). The initial stages of TiO_2 growth and the ion-surface interactions leading to interface broadening are the subject of *in situ* RTSE and TRIDYN simulation studies in Chapter 6.

There are many advantages to performing a plasma pretreatment prior to thin film deposition (versus depositing on virgin c-Si), and to switching from pretreatment to deposition without extinguishing the plasma. First, we avoid the problem of non-reproducibility of the plasma ignition process which is usually accompanied by instabilities sometimes lasting up to a few seconds. Second, we avoid the problem of $TiCl_4$ – and other contaminant – adsorption on the native oxide surface prior to deposition. Because of its low vapor pressure, $TiCl_4$ is notorious for adsorbing at the surface [148], thereby potentially modifying the surface chemistry, energetic conditions and even the initial growth of TiO_2.

In addition, this methodology ensures that TiO_2 deposition is initiated on a highly-reproducible and well-characterized 6 nm-thick SiO_2 layer formed during the O_2 plasma pretreatment (see chapters 5 and 6). The oxide formation also ensures that TiO_2 deposition is initiated on SiO_2 instead of c-Si, which allows us to investigate interface broadening pertinent to the deposition of optical coatings, such as TiO_2 on SiO_2.

3.1.2 *Dual-Mode MW/RF Plasma Reactor Used for Microstructured $SiN_{1.3}$ Deposition with Plasma-Engineered Interfaces*

Chapter 7 of this work features microstructured $SiN_{1.3}$ deposition in both MW and RF plasmas. Fabrication of porous and dense $SiN_{1.3}$ was pioneered by Martinu et al. [54], explored by Poitras for optical films [149], and by Vernhes et al. [23], who used a combination of MW (mean energy, $E_m \sim 8$ eV [31]), and RF discharges ($E_m \sim 100$ eV at the RF-powered electrode) for the fabrication of porous/dense multilayer OIFs.

This work was carried out in a dual-mode RF/MW PECVD reactor shown in Fig. 3.2 [23]. The MW discharge (2.45 GHz) is excited by a power supply with a fixed pulse frequency of 60 Hz and a duty cycle of 0.1. The MW power is coupled to the chamber through a fused-silica window by use of a slotted silica waveguide applicator. The RF powered substrate holder is equipped with a rotating carousel, allowing subsequent deposition of four samples that were introduced to the chamber via a load-lock system. In this work, the system is operated in two modes, namely pure MW and RF, although it can also be operated in a dual-mode regime. $SiN_{1.3}$ films are deposited at $p = 40$ mTorr from a SiH_4 and N_2 mixture, with respective flows of 5 sccm and 20 sccm. Films are grown with different density and microstructure, benefiting from large differences in ion energy and IEDF (see next section for details about the IEDF of incident ions in a MW discharge and at the RF-powered electrode in a RF discharge).

RF plasma treatment of MW-deposited $SiN_{1.3}$ films was carried out in Ar at $p = 40$ mTorr, in order to modify surface roughness of porous films, and to enable the growth of good quality dense-porous multilayers. Both the thin film depositions and the plasma treatment were monitored by *in situ* RTSE.

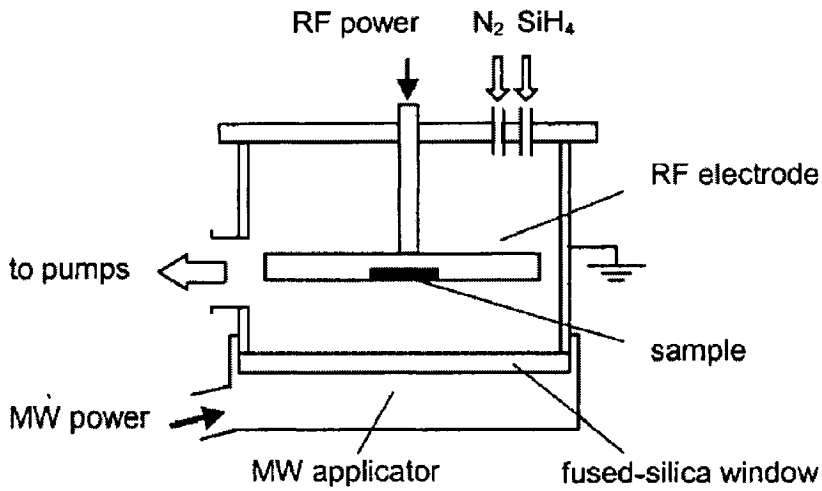

Figure 3.2. *Schematic illustration of the dual-mode MW-RF plasma reactor [23].*

3.2 Ion Energy Distribution Function in RF and MW Plasmas

In this section, we briefly present the IB characteristics of both RF and MW plasmas. Fig. 3.3 shows the IEDF measured at the grounded and RF-powered electrodes of RF, MW and dual-mode RF/MW discharges in Ar at p = 60 mTorr measured by an electrostatic ion energy analyzer coupled to a quadrupole mass spectrometer [28, 31]. The comparison of left- and right-hand panels in Fig. 3.3 illustrates the differences between a MW discharge at the grounded electrode (Fig. 3.3b) and an RF-discharge at the RF-powered electrode (Fig. 3.3d) in terms of ion energy and relative ion flux. The IEDF at the RF-powered electrode is much broader and reaches much higher energies than at the grounded electrode in MW discharge. The relative ion flux is greater in a MW discharge than at the RF-powered electrode in an RF discharge by as much as an order of magnitude.

3.2.1 Radiofrequency Plasma

In a capacitively coupled RF plasma reactor, such as the one shown in Fig. 3.1, a strong negative self-bias V_B develops at the RF-powered substrate-holder/electrode, hence positively charged ions are accelerated in the plasma sheath and bombard the substrate

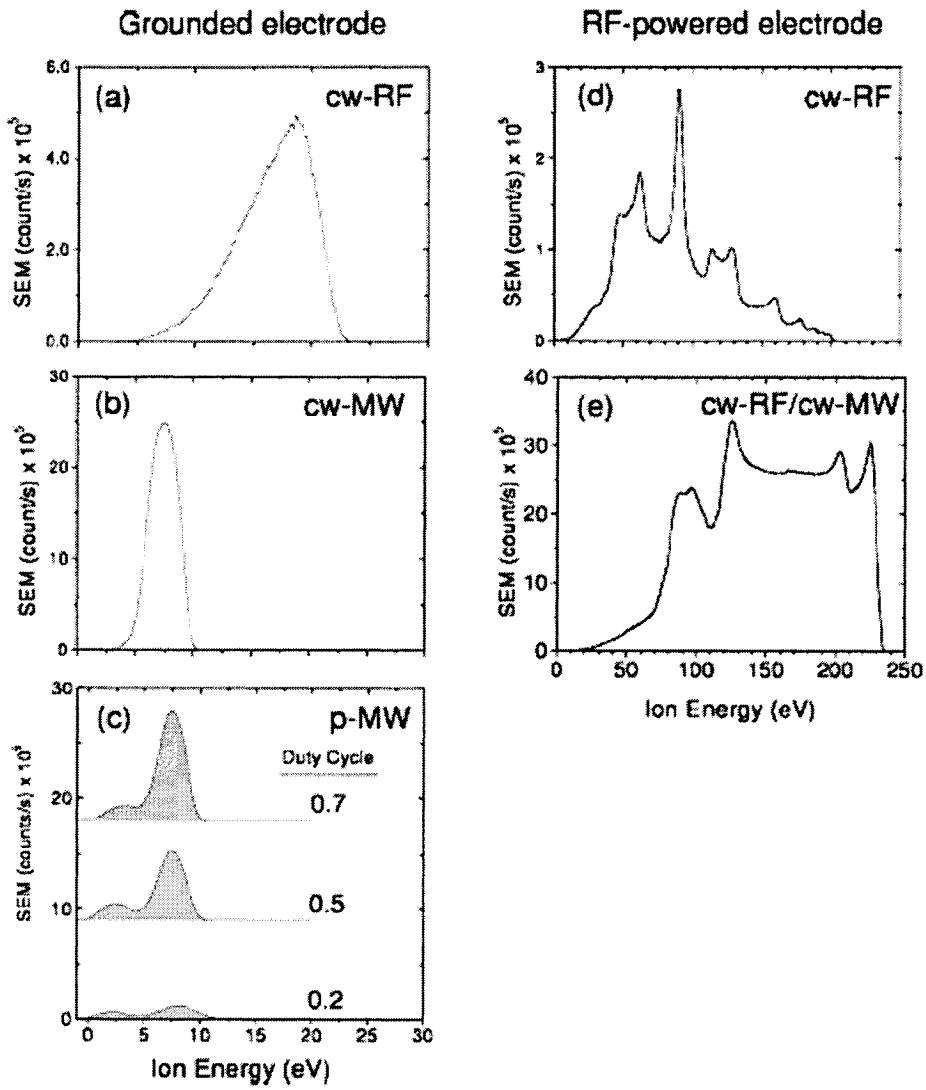

Figure 3.3. *Ion energy distribution function (IEDF) of an Ar plasma at p = 60 mTorr measured in the following configurations: (a) grounded electrode in continuous wave (cw) RF discharge at V_B = -150 V; (b) grounded electrode in cw-MW discharge at a power level (P_{MW}) of 300 W; (c) grounded electrode in a pulsed (p-) MW discharge (P_{MW} = 300 W); (d) RF-powered electrode in a cw-RF discharge (V_B = -150 V); (e) RF-powered electrode in a dual-mode cw-RF/cw-MW discharge (V_B = -150 V, P_{MW} = 300 W). Reproduced from reference [28].*

placed at the cathode. It is essential to investigate the ion bombardment characteristics in order to understand their effects and simulate ion-surface interactions by MC-based simulation programs, such as SRIM and TRIDYN (see section 3.4).

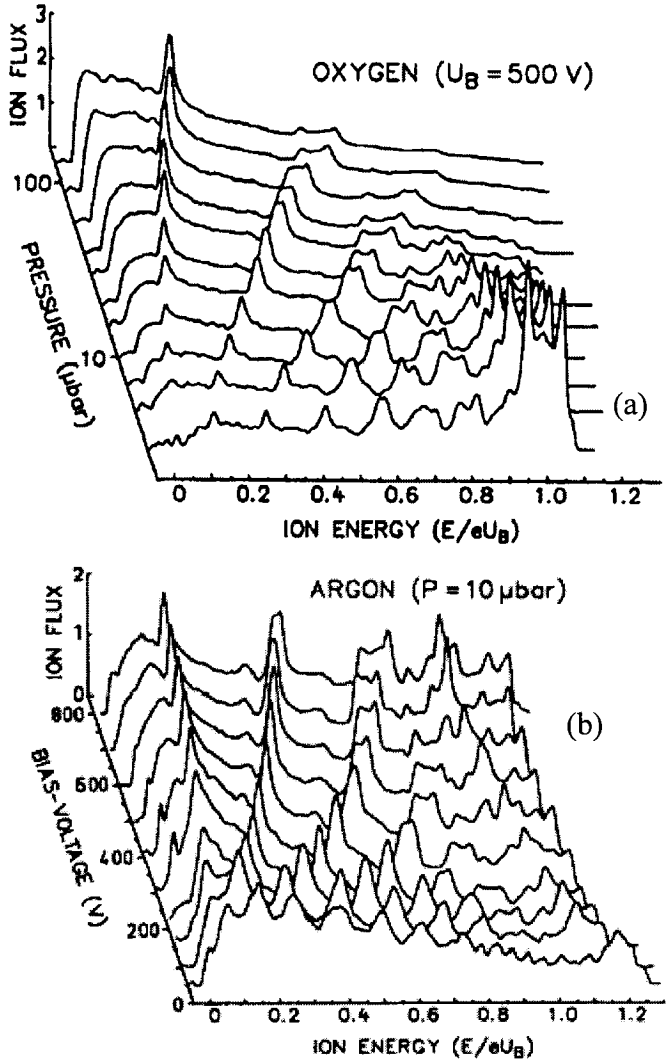

Figure 3.4. *Ion energy distribution function (IEDF) of (a) O_2 plasma at the RF-powered electrode as a function of working pressure, and (b) Ar plasma as a function of V_B (U_B in the figure). Ion flux is expressed in arbitrary units. From reference [8].*

The measured IEDF at the RF-powered electrode in pure O_2 by a standard retarding grid method is shown in Figs. 3.4a and 3.4b as a function of p and V_B, respectively [37]. The multiple resonance peaks observed in the IEDF are formed as a result of (1) charge exchange collisions between O_2 neutrals and O_2^+ molecular ions, and (2) extended residence time of some ions in the sheath. Long residency time of ions may be equivalent to multiple RF cycles, during which ions are accelerated and decelerated as they pass through

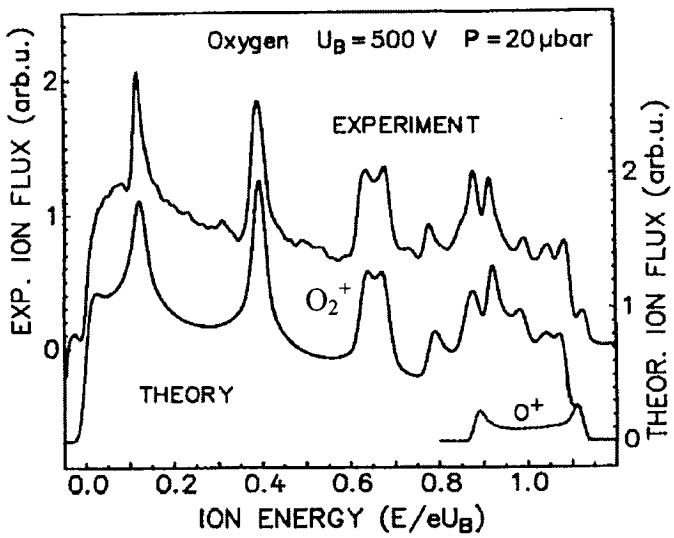

Figure 3.5. *Measured and theoretical IEDF of O_2 plasma at the RF-powered electrode in pressure and bias conditions similar to what is used in this work (see Chapters 4 to 6) (U_B is identical to V_B). The saddle-like structure associated to O^+ is theoretically calculated. From reference [8].*

the plasma sheath. Resonance peaks in the IEDF are shifted with increasing p: high-E_i peaks gradually decrease in intensity until they disappear, as low-E_i peaks shift toward higher energy. As a result, the IEDF becomes skewed towards lower energy as p increases, and the mean ion energy also decreases. The effect of increasing V_B (Fig. 3.4b) is seen to contribute slightly to increasing the relative abundance of high energy ions in the IEDF. The maximum ion energy (E_{max}) at the RF-powered electrode is given by $E_{max} = e(V_p - V_B)$ $\approx 1.15e|V_B|$, where V_p is the plasma potential.

O_2 plasma pretreatment is carried out at p = 20 mTorr and V_B between -60 and -600 V, whereas TiO_2 depositions are performed at V_B = -450 V. In these conditions, the IEDF is very broad and only slightly skewed toward low energies. This is seen in Fig. 3.5, where measured and calculated IEDF are plotted for p = 15 mTorr and V_B = -500 V [37]. Theoretical predictions of the IEDF made by a parametric model of the ion transport through the sheath agree very well with experimental results [37] (Fig. 3.5), and suggest that the IEDF is made up of a majority of O_2^+ ions and a saddle-like distribution at high

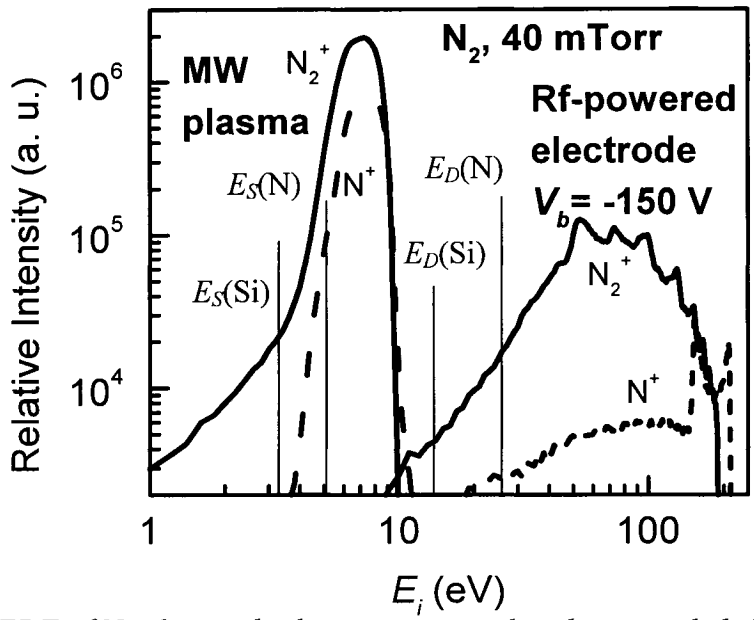

Figure 3.6. *IEDF of N_2 plasma discharges measured at the grounded electrode in a 300 W MW discharge and at the RF-electrode in a RF discharge for V_B = -150 V. E_s and E_D (the surface and bulk displacement energies) of Si and N in Si_3N_4 are also shown for reference. Modified after reference [31].*

energy associated to O^+ ions. Mass spectrometry measurements of the IEDF at the RF powered-electrode were carried out in our laboratory, and confirmed that the saddle-like structure at high energy is in fact associated with atomic ions [31]. This information is essential to the understanding of ion-surface interactions in a PECVD environment, and should be used to simulate ion sources in MC-based calculations of ion bombardment effects in a PECVD environment (see Chapters 4 to 6).

3.2.2 MW and RF Discharges in N_2

The IEDF of MW and RF discharges in N_2 at p = 40 mTorr [31] are shown in Fig. 3.6. MW discharges are characterized by very low-E_i (<10 eV), while E_i in RF plasmas can range up to hundreds of eV, depending on the applied bias. The ion flux in the MW discharge is about an order of magnitude higher than in RF, but most MW-generated ions do not participate in the displacement of bulk target atoms, which typically requires tens of eV of

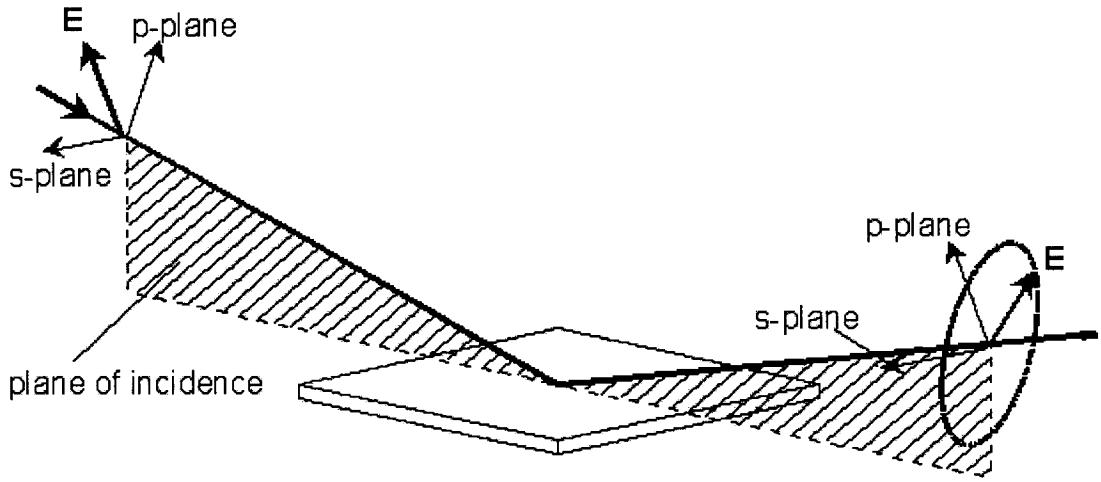

Figure 3.7. *Illustration of polarization change during specular reflection off a sample from linearly- to elliptically-polarized.*

energy. We have included markers to indicate the typical bulk (E_D) and surface (E_S) displacement energies of Si and N assuming E_s ~$0.25E_D$. Clearly, MW plasmas cannot produce $SiN_{1.3}$ films as dense as RF, because E_i(MW) < E_D(Si) < E_D(N) < E_i(RF); however ion bombardment in MW plasma can significantly enhance surface processes.

3.3 Spectroscopic Ellipsometry

3.3.1 Basic Principles

Spectroscopic ellipsometry [49] is a highly versatile and very sensitive optical metrology tool typically used to probe specular-reflecting surfaces. Ellipsometry measures the change in the polarization state of light upon reflection off a sample (Fig. 3.7). This change in polarization has traditionally been expressed in terms of the well-known ellipsometric ratio ($\tilde{\rho}$) of complex Fresnel reflection coefficients for *s*– and *p*– polarizations, respectively $\tilde{r}_p$ and $\tilde{r}_s$:

$$\tilde{\rho} = \frac{\tilde{r}_p}{\tilde{r}_s} = \tan(\Psi)e^{i\Delta}. \tag{3.1}$$

Here Ψ and Δ are ellipsometric angles, $\tan(\Psi)$ is defined as the amplitude ratio of Fresnel coefficients, and $\Delta = \delta_p - \delta_s$ is the difference between the phase change upon reflection of *s*– and *p*–polarizations. Ellipsometry is highly surface-sensitive with sub-monolayer precision because of its ability to sensitively measure Δ. In addition, ellipsometry measures the amplitude ratio and phase difference between p- and s- polarizations, hence it is not handicapped by intensity instabilities of the light source, contrary to photometric measurements. In studies of near-surface effects on bulk-like materials (optically semi-infinite sample, e.g. c-Si substrate in the UV-visible), it is useful to present results in terms of the pseudo-dielectric function of the material, $\langle\varepsilon\rangle = \langle\varepsilon_1\rangle - i\langle\varepsilon_2\rangle$, where $\langle\varepsilon\rangle$ is directly obtained from $\tilde{\rho}$ and the angle of incidence (θ, defined with respect to surface normal) as follows:

$$\langle \varepsilon \rangle = \sin^2\theta\left[1+\tan^2\theta\left(\frac{1-\tilde{\rho}}{1+\tilde{\rho}}\right)^2\right] \tag{3.2}$$

In the case of an optically semi-infinite medium with atomically smooth surface in vacuum (or air), we have

$$\langle\varepsilon\rangle = \varepsilon, \tag{3.3}$$

where ε is the dielectric function of the bulk material. Any deviation from the ideal single-interface model can lead to considerable changes in measured spectra, owing to the extreme surface-sensitivity of Δ. These deviations often sensitively depend upon structural and composition variations, such as oxidation, surface roughening, damage of the crystalline structure, thin film deposition, etc. In addition, different spectral regions permit to detect different aspects of variations (structural and composition changes may result in changes to electronic band structure, which produce changes of *n* and *k* in the ultraviolet (UV), visible and near infrared (NIR) parts of the electromagnetic spectrum; chemical changes associated with molecular dipole excitations are active at lower frequency and may change *n* and *k* in the IR). Thus, acquiring data in appropriate spectral regions, such as VUV, UV, visible, NIR and IR, may provide us with enough structural and composition information about the

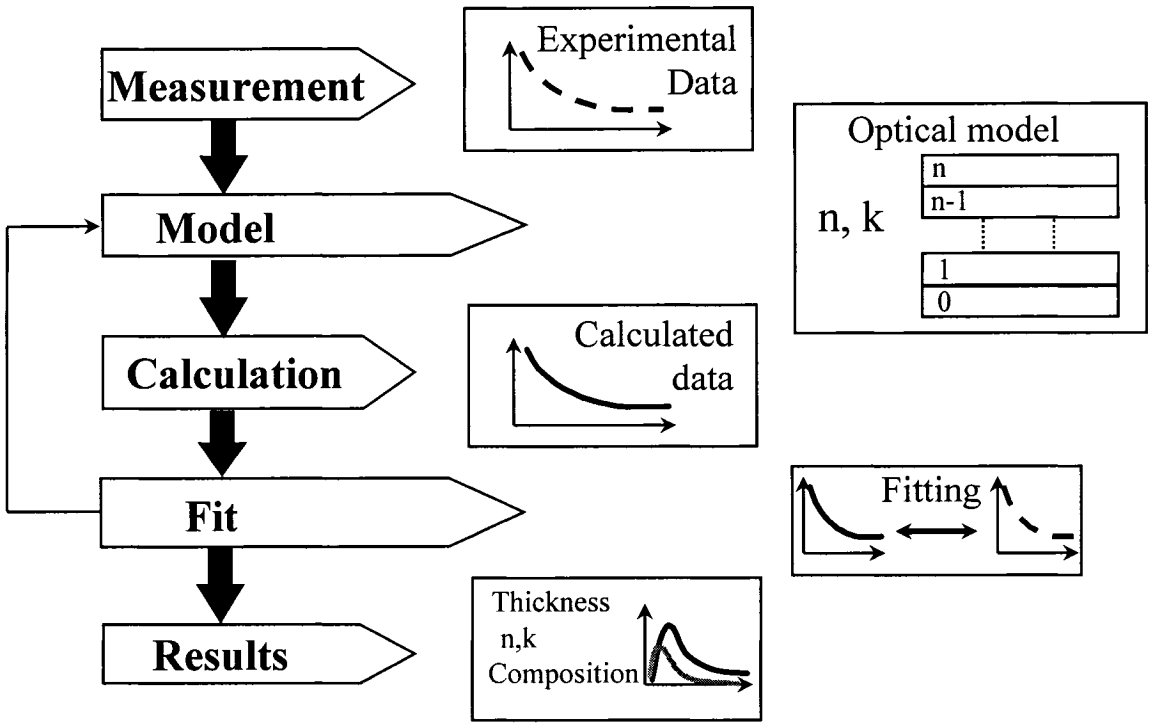

Figure 3.8. *Description of the reverse engineering process used in SE characterization of thin films, surfaces and interfaces.*

sample to quantitatively and accurately "reverse engineer" the layered structure formed on (or beneath) the surface.

The reverse engineering methodology used in SE characterization is schematically represented in Fig. 3.8. An optical model is constructed, which consists of thin stratified layers on a substrate. Each layer is assigned a nominal thickness and optical constants (n and k). The Abelès matrix formalism [150] is then used to calculate $\tilde{\rho}$ [eq. (3.1)] and the pseudo-dielectric function [eq. (3.2)] of the optical model. An excellent overview of the matrix formulation and its derivation from Maxwell's equations is given by Macleod [151]. The agreement between the simulated and measured $\langle\varepsilon\rangle$ is both visually and numerically evaluated by using a merit function. The Levenberg-Marquardt numerical fitting procedure [152, 153, 154] is used to vary the film thickness and optical properties, when the

agreement between the calculated and measured spectra is close enough to obtain convergence of the simulated spectra towards the measurements.

3.3.2 Ex situ Variable Angle Spectroscopic Ellipsometry

Variable angle SE (VASE [155], J. A. Woollam Co.) is used for *ex situ* optical characterization of plasma pretreated c-Si samples. The VASE system used (Fig. 3.9) is a rotating analyzer ellipsometer (RAE) especially equipped with an AutoRetarder® [156], a computer-controlled compensating element. The RAE suffers from the following limitations: (1) it cannot determine the "handedness" of the phase term Δ, i.e. they measure from 0° to 180° when in reality it varies from 0° to 360°, and (2) precision and accuracy are poor when Δ is near 0° or 180°. These limitations are inconsequential for many applications. However, accurate Δ values near 0° and 180° are essential for thin layers or index matched layers on transparent substrates. Compensators are used in ellipsometry to enhance measurement accuracy by changing the phase of an incident wave, delaying one of the two orthogonal light constituents. This delay occurs because of optical anisotropy ($n_o \neq n_e$) in the compensator, which causes the two orthogonal electric fields see a different index, thus producing a different phase velocity for each. The use of the Autoretarder therefore enhances the accuracy of SE measurements over the entire Δ range from 0 to 360°.

VASE measurements were made on c-Si after plasma treatment in the following conditions: spectral range from 4.40 eV to 1.25 eV by 0.025 eV steps, and θ from 70° to 80° by 1° steps. Using a large number of incidence angles increases the amount of information about the sample, can maximize sensitivity to all model parameters, and can help uniquely determine multiple unknowns. Acquiring data at multiple angles also ensures optimum sensitivity to a wide range of surface modifications. Data analysis and fitting were performed using commercially available WVASE32 software [157]. Kindly refer to

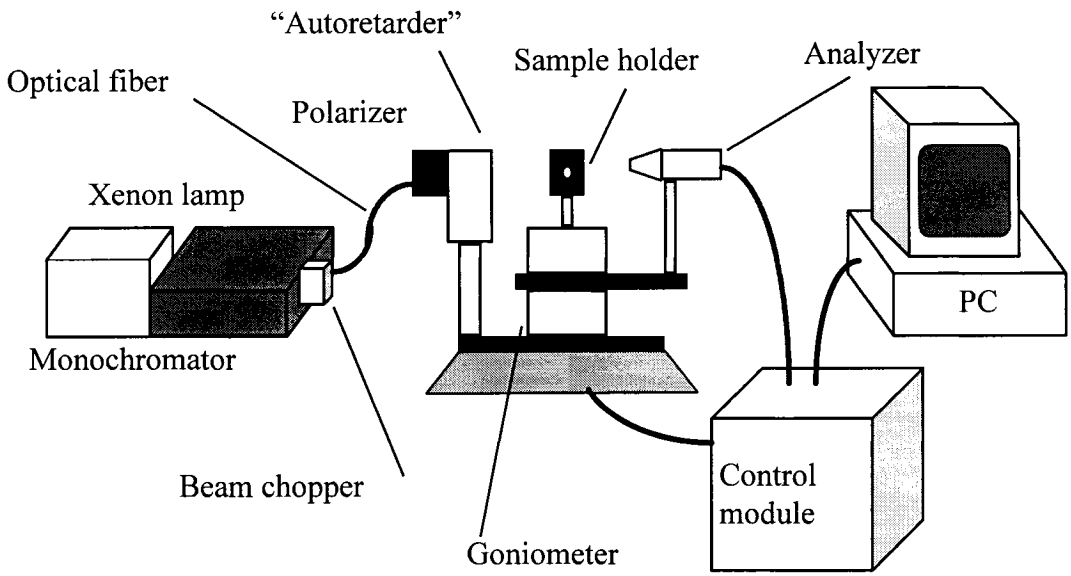

Figure 3.9. *Schematic illustration of the VASE® system with Autoretarder ® produced by the J. A. Woollam Co.*

Chapter 4, section 4.2 for modeling and analysis details.

3.3.3 In situ Real-Time Spectroscopic Ellipsometry

Many key experimental results presented in this work were acquired by *in situ* RTSE (see Fig. 3.1). We used an M-2000FI (J. A. Woollam Co.) rotating compensator ellipsometer (RCE). The RCE configuration compensates for most of the disadvantages of the RAE [43, 158, 159]. The advantages of RCE include: (1) accurate measurements of the ellipsometric Ψ and Δ parameters over the complete measurement range (Ψ= 0-90°, Δ = 0-360°), (2) no residual input or output polarizations sensitivity (due to a fixed polarizer on the input and a fixed analyzer on the output), and (3) the capability to directly measure depolarization effects. In addition, commercial RCE systems employ a CCD array detector making simultaneous acquisition of spectroscopic ellipsometric data possible. The RCE design gives it other distinct advantages over RAE, such as (4) lower sensitivity to the angle of incidence (θ) and (5) ease of calibration for window effects [160, 161]. The RCE design

also has (6) additional measurement capabilities, such as depolarization, anisotropy and Mueller matrix measurements [44, 162]. We have not used these capabilities in this work.

The M-2000 used at the FCSEL can measure 690 wavelengths simultaneously over the spectral range from 245 to 1700 nm (5.04 to 0.73 eV) at a rate of up to 20 Hz. The choice of the acquisition rate used in our experiments was dictated by many factors: (1) the dynamic study of near surface effects by RTSE requires good signal-to-noise ratio, as well as (2) minimum systematic errors, and (3) adequate time resolution. A good compromise was to perform analyzer two-zone averaging, while using 500 ms integration time at each zone. This resulted in an interval close to 2 s between two successive spectra. Analysis of the ellipsometric data was performed using EASE [163] and WVASE32 software packages (J. A. Woollam Co., Inc.), and it will be described in more details in Chapters 5 to 7. In cases where dynamic modifications are rapid, time resolution was substantially increased by carrying out measurements without two-zone averaging.

3.4 Monte-Carlo Simulations of Ion Bombardment Effects

A considerable number of simulation programs are capable of calculating ion range and straggle, as well as other characteristics of ion distribution in the target (see Ref. [61] for an excellent review). The most widespread program is TRIM [62, 61, 164] (available in SRIM 2003 software package [62, 72]). In this section, the TRIM code and its dynamic counterpart TRIDYN, are described in general terms, with special emphasis on their limitations. Specific simulation setups and parameters are described in Chapters 4 to 6.

3.4.1 Static TRIM Simulations

TRIM (*Transport and Range of Ions in Solids*) is a three-dimensional program which considers projectiles and recoils in its calculations based on the BCA approach. TRIM assumes the target structure to be randomized (amorphous), so the next collision partner is

found by a random selection process. For this reason, TRIM and similar simulation tools are called Monte-Carlo programs. They are known to be the simplest ones, and they require short computing time. For programs which assume crystalline targets (e.g. MARLOWE [165]), the procedure to find subsequent collisions (after the first randomly selected collision) is completely deterministic.

TRIM is only valid for low fluence or equilibrium cases, where the target is not significantly modified by ion bombardment. The mean free path, λ_0, (interatomic distance) is defined as a function of the atomic density D:

$$\lambda_0 = D^{-1/3}. \tag{3.1}$$

Additional details about the features, computational methods, limitations for TRIM and many other programs are described and discussed at length in an excellent review by Eckstein [61]. Given the severe limitations of TRIM in dealing with intermediate to high fluence ion bombardment effects, we will use the TRIM program only (1) to calculate the sputtering rate in the case where target composition has reached a steady state; (2) to determine ion and recoil distributions for a given target structure and composition; (3) and to calculate the range of ions and recoils in the target. In all these cases, TRIM is known to provide adequate results, as documented in the next paragraphs.

Figure 3.10a shows modeling results for physical sputtering (full curves) and experimental results (points) for the interaction of hydrogen, deuterium, helium and carbon ions with graphite. Excellent agreement is observed for energies in excess of 40 to 50 eV, where physical sputtering dominates. In fact, some [33, 61, 165] have argued that since the necessary energy transfer to a surface atom in a collision cascade leading to physical sputtering is in the range of few eV, the TRIM code has to be able to model the trajectory of the projectile in the solid down to this kinetic energy. In fact, excellent agreement between modeled and experimental results of ion range and straggle in Fig. 10b justifies this, and implies that TRIM should be valid down to the 10 eV energy range. Thus, the only

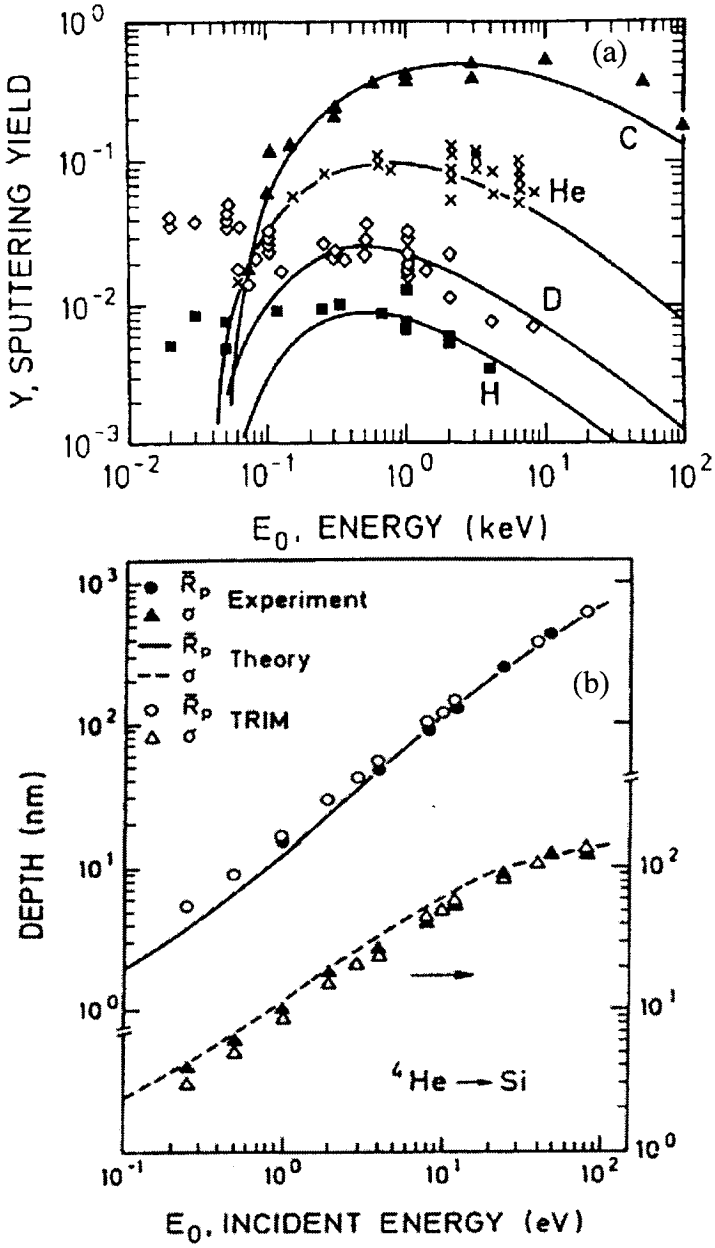

Figure 3.10. *(a) Calculated (full curves) and experimental (data points) sputtering yield for hydrogen (H), deuterium (D), helium (He) and carbon (C) in graphite. Reproduced from reference [33]; (b) ultra-low energy ^{4}He range and straggle in Si; E_0 is ion energy, E_i. Reproduced from reference [61].*

limitation is that at low energies chemical sputtering (due to surface bond breaking effects, etc. [61]) may affect the overall sputtering yield. In his review, Eckstein concluded that the BCA model fails in the eV range, that this "failure is gradual, starting at several tens of eV,

and becomes serious somewhere in the eV range". This seems to be confirmed by experimental sputtering data, which do not show a dramatic breakdown of the BCA. Robinson [165] has also compared BCA and MD simulations at low energy, and concluded that the former is not on solid ground at energies below about 10 eV.

Ion range can also be determined accurately from TRIM simulations. Robinson [165] has not found any limitations of the BCA to determine ion ranges at low energy. Here too, some breakdown is expected in the eV range. Figure 3.10b shows the exceptional agreement between the Ziebler-Biersack-Littmark (ZBL) analytical method (full curves), TRIM simulations (open symbols) and experimental (solid symbols) results for ^{4}He range and straggle in a c-Si target for energies ranging from ~1 eV up to ~100 eV [61].

The TRIM program also allows us to take ion energy distributions into account, which will be essential for the calculation of sputtering and range of a broad IEDF source such as the RF plasma sources. See Chapter 5 for more details.

3.4.2 Dynamic Simulations Using Modified TRIDYN: Description and Limitations

Targets with multiple elements complicate interactions of ions with solids, especially at high fluence, because elemental depth profiles are modified due to ion bombardment. TRIDYN [63, 64] is based on the TRIM program using the BCA model for ballistic transport, and allows dynamical changes of multi-component target thickness and composition to be accounted for during high fluence ion implantation and ion-beam-assisted deposition.

Ballistic effects such as projectile deposition and reflection, sputtering, and ion mixing are computed for a target at zero-temperature. TRIDYN covers only non-thermal processes. Due to the binary collision approximation, its lower energy limit is in the order of 10 eV. Nevertheless, experience shows that also collisional processes with slightly lower

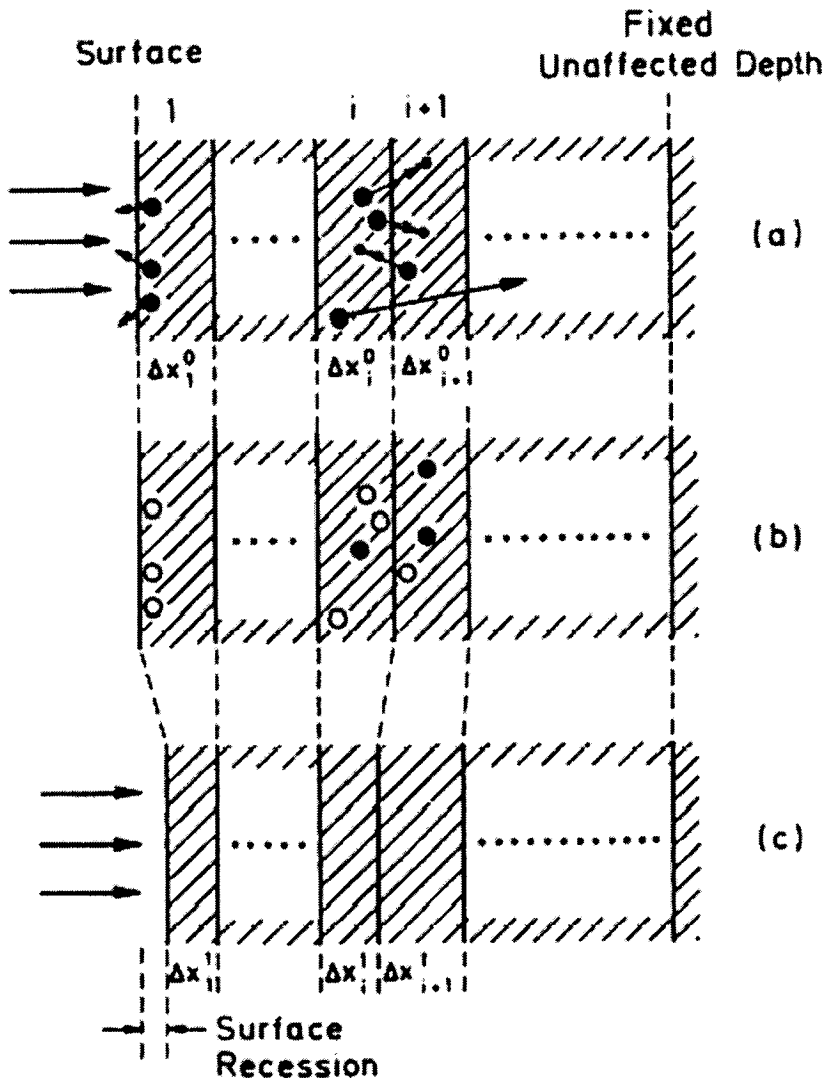

Figure 3.11. *Schematic representation of ion and recoil transport and dynamic relaxation. (a) Sputtering and displacement of atoms lead to (b) vacancies (open circles) and interstitial atoms (solid circles). (c) According to the net change in the number of atoms in each slab, the depth interval is allowed to relax. From reference [61].*

characteristic energies, such as sputtering, are predicted quite accurately. The upper energy limit is given by feasible times of computation. The target and the grown layers are assumed to be amorphous. Each simulated projectile ("pseudoprojectile") represents a physical increment of incident fluence (incident particles per unit area). Up to 5 different atomic species in the target and/or in the beam may be considered, with different energies

and angles of incidence for the beam components. TRIDYN allows to calculate the depth profiles of all atomic species in the target as a function of the incident fluence, as well as sputtering yields, total areal densities, surface concentrations, re-emitted amounts and surface swelling and erosion.

In TRIDYN, the target is subdivided into slabs of initially constant thickness Δx^0 (see Fig. 3.11). Depth intervals can change during the course of a simulation; however, all outputs are calculated by interpolation for equidistant intervals. Instead of individual atoms, pseudoparticles representing differential fluence $\Delta\Phi$ are used, determined by the total fluence, Φ, and the number of projectiles, N_H:

$$\Delta\Phi = \Phi / N_H . \tag{3.2}$$

During ion bombardment, the processes of implantation and atomic relocation and sputtering cause removal or addition of pseudoprojectiles (ions and target atoms) in different slabs (see Fig. 3.11). Based on the change of the number of pseudoparticles, one can calculate the new atomic surface densities of real atoms, fractional compositions, and atomic density in each layer. The local depletion or excess densities are allowed to relax by adjustment of interval thickness, which results in either surface recession or thickness increase by swelling. Additional details about the calculation procedures are also summarized in Refs. [61, 63, 64] and will not be repeated here.

In simulations performed in this thesis, we have set $\Delta x^0 = 0.1$ nm for all targets, given the shallow penetration of ions on nanometer-scale depths, and limited the maximum concentration of O in both Si and Ti to 66.667%. Excess O is allowed to hop to the adjacent layer for relaxation, and is reemitted if these are saturated, in conformity with previous simulation studies using TRIDYN [101].

It is important to mention here that there will be no fitting of simulation parameters in any of the simulations reported in this work. Simulation parameters have been selected based

on their wide acceptance by the scientific community, or taken as the default values proposed by the simulation program. In the case of oxides, the limit of solubility of O was set in the target to be given by the stoichiometry of the oxide (e.g. a maximum of 66.667% O is allowed to remain in SiO_2 and TiO_2); excess O is allowed to hop instantaneously to the adjacent slab, and is reemitted by the target if the latter is saturated.

In addition, a novel strategy was developed to perform TRIDYN simulations in a way to consider the broad energy ion source typically observed at the RF-powered electrode in a RF discharge. The procedures and calculation parameters used in the modified TRIDYN program are described in dedicated sections in Chapters 5 and 6.

Chapter 4. Article 1: Ion-Surface Interactions on c-Si (001) at the Radiofrequency-Powered Electrode in Low-Pressure Plasmas : *Ex Situ* Spectroscopic Ellipsometry and Monte-Carlo Simulation Study

A. Amassian, P. Desjardins, and L. Martinu

Regroupement québécois sur les matériaux de pointe (RQMP) and Department of Engineering Physics,
École Polytechnique de Montréal, P. O. Box 6079,
Station Centre-ville, Montréal, Québec, H3C 3A7, Canada

Article published: *Journal of Vacuum Science and Technology* **A24** (2006) 45-54.

4.1 Abstract

We use variable-angle spectroscopic ellipsometry (VASE) to investigate oxide and interface formation during plasma-oxidation of monocrystalline Si(001) at the radiofrequency (RF) powered electrode of a plasma-enhanced chemical vapor deposition reactor. HF-etched c-Si(001) wafers were exposed to an oxygen plasma under conditions similar to those used in optical coatings deposition in order to ascertain the effects of plasma-bulk interactions, and to gauge to what depth O_2^+ and O^+ ions interact with and alter the structure and composition of the target in the presence of negative self-bias, V_B. From VASE analyses, modifications are best described using a two-layer model: a top layer consisting of SiO_2 and a defective interfacial layer (DL) composed of a mixture of c-Si, a-Si, and SiO_2. The saturation value of the modification depth (oxide and DL thickness) increases from 3.4±0.4 to 9.6±0.4 nm, for V_B ranging from -60 to -600 V, respectively, and scales with $E_{max}^{1/2}$, where E_{max} is the maximum energy of ions from an RF discharge. These results are in agreement with nuclear ion-bulk interactions leading to atomic displacements and defect accumulation. The interfacial layer broadens with increasing $|V_B|$ while the fraction of a-Si detected increases from ~1% up to ~55% over the investigated V_B range, indicative of ballistic and thus depth-dependent oxygen transport to the SiO_2-Si interface. Monte-Carlo simulations in the binary collision approximation predict significant surface recession due to sputtering, therefore resulting in an apparent self-limiting oxidation mechanism. The surface layers reach their steady-state thicknesses within the first 2 minutes of plasma exposure and subsequently move into the bulk of the c-Si substrate as a result of oxide sputtering and oxygen transport.

4.2 Introduction

Understanding and controlling atomistic processes at surfaces and interfaces are important prerequisites to obtain high quality optical films. Most of such coatings are based on oxides grown under intense ion bombardment [6]. This has typically been accomplished by ion assisted physical vapor deposition and, more recently, by plasma-enhanced chemical vapor deposition (PECVD) techniques. PECVD is a very promising process for optical coatings deposition [28] due to its flexibility and ability to tune optical and mechanical properties of films deposited at room temperature. In PECVD, film property adjustment is achieved by controlling plasma parameters, including the mean ion energy (E_m), ion energy distribution function (IEDF), and the ion-to-neutral arrival ratio (ϕ_i/ϕ_n). In order to manufacture thin films suitable for optical coatings applications, substrates are typically placed at the radiofrequency (RF) powered electrode of the PECVD reactor, where negative biasing in the range of tens to hundreds of volts ensures desired film properties [28].

The nature of plasma-induced modifications at the RF-powered electrode in PECVD are qualitatively understood [30, 32, 67, 146] and are thought to be predominantly associated with bombardment by molecular and atomic ions [37, 31] similar to ion-beam experiments [33, 74]. As such, ions are expected to be implanted to some depth below the surface, creating multiple defects, and eventually stopping to form chemical bonds [145]. Another important effect of ion bombardment is sputtering [62].

In a low-pressure RF plasma the situation is complex. The IEDF is very broad and can span from few eV up to ~1 keV, depending primarily on substrate bias (V_B) and reactor pressure (p). Furthermore, ion bombardment is accompanied by energetic photons, neutrals, and chemically active radicals arriving at the surface [33]. The ion flux is typically between ~10^{14} and ~10^{16} $cm^{-2}\cdot s^{-1}$ and is therefore sufficiently high to cause almost instantaneous and permanent modifications to the substrate structure and composition, including defect

accumulation and chemical changes [80]. The overall sputtering rate is also expected to be a function of the IEDF [166].

Given the complexity of the processes involved in RF plasmas, little is known about the extent of structural modifications during the initial moments of thin film deposition in a RF-PECVD environment. Furthermore, direct observation of ion bombardment effects from an RF plasma below the surface of an amorphous oxide film is close to impossible to accomplish with sufficient temporal and depth resolution using conventional techniques. However, we have recently demonstrated, using *in situ* real-time spectroscopic ellipsometry (RTSE) analyses, that significant, quantifiable, and reproducible modifications of the monocrystalline Si [c-Si (001)] substrate [167] occur during the initial stages of TiO_2 deposition by PECVD. We have linked these modifications to ion bombardment, but have not studied them in detail until now. An in-depth investigation of these plasma-induced modifications in the absence of film deposition is, in our opinion, a crucial step in the assessment of the role of ion-surface and ion-bulk interactions at the RF-powered electrode during film growth.

In this article, we focus on studying the modifications of a c-Si(001) surface induced by an oxygen plasma at the RF-powered electrode as a function of V_B. We use *ex situ* variable angle spectroscopic ellipsometry (VASE) to determine oxide and interface characteristics after 10 minutes of plasma exposure, where modifications are known to have reached saturation [167]. Monte-Carlo simulations of O ion bombardment in Si and SiO_2 are used to gain insight into the nature of plasma-surface interactions, to quantify the modifications and, to some extent, to substantiate the ellipsometric analysis. We propose a growth model where oxidation is self-limited, since it appears to be driven by oxygen ballistic transport to the SiO_2-Si interface, competing with RF sputtering of the oxidized surface.

4.3 Experimental Methodology

c-Si (001) wafers (10 Ω·cm) were cleaned in a piranha solution (H_2SO_4:H_2O: H_2O_2 = 4:1:1) for 5 minutes, rinsed in de-ionized water, followed by native oxide removal for 60 s in 49% water-diluted HF. Samples were then dipped in de-ionized water and dried using N_2. Substrates were then immediately loaded into a 13.56 MHz capacitively coupled RF plasma reactor and placed on a RF-powered substrate holder-electrode. The system was then pumped down to 10^{-6} torr using a turbomolecular pump. *Ex situ* VASE and X-ray photoelectron spectroscopy (XPS) measurements performed within minutes of oxide removal revealed a residual oxide of ~0.6±0.2 nm, where the uncertainty shows run to run reproducibility of surface etching.

After pumpdown, O_2 was introduced into the reactor chamber, and plasma conditions similar to those typical of oxide deposition by PECVD were adjusted [28, 67]. O_2 flowrate was set at 60 sccm, and the total pressure was adjusted at p = 20 mTorr. Plasma was initiated at room temperature using an RF power varying from 7 to 110 W, resulting in a self-bias voltage, V_B, varying between –60 and –600 V. The exposure time was set to 10 minutes (see below).

Ex situ characterization was performed by VASE (J.A. Woollam Co.). The data acquisition procedure, as well as the regression method used are similar to those applied by Herzinger *et al.* [115]. Measurements were made from 4.40 to 1.25 eV by 0.025 eV steps, and from 70° to 80° by 1° steps. While the larger number of incidence angles is not essential, it does improve the data analysis by increasing the sensitivity of VASE to ultra-thin film thickness and composition, and helps confirm the uniqueness of the parametric fit. Straight-through measurements in air yielded Ψ within 0.02° of 45° and Δ within 0.3° of 0° over the entire measurement spectrum.

For convenience, all ellipsometric data are presented in the form of the pseudo-dielectric

function, $\langle\varepsilon\rangle = \langle\varepsilon_1\rangle - i\langle\varepsilon_2\rangle$, computed from:

$$\langle \varepsilon \rangle = \sin^2\theta\left[1+\tan^2\theta\left(\frac{1-\tilde{\rho}}{1+\tilde{\rho}}\right)^2\right] \tag{4.1}$$

Here, $\tilde{\rho}$ is the Fresnel ratio defining the ellipsometric angles Ψ and Δ in terms of the s- and p- polarized complex Fresnel reflection coefficients, $\tilde{r}_s$ and $\tilde{r}_p$:

$$\tilde{\rho} = \frac{\tilde{r}_p}{\tilde{r}_s} = \tan\Psi e^{i\Delta} \tag{4.2}$$

In the case of a perfectly abrupt interface between two semi-infinite media (e.g. optically opaque c-Si (001) with atomically smooth surface in air), a direct inversion of $\tilde{\rho}$ to $\langle\varepsilon\rangle$ provides the exact dielectric function of the bulk, and $\langle\varepsilon\rangle = \varepsilon$ is exact. Any departure from the abrupt interface model, such as oxidation, amorphization, or roughening, will result in characteristic spectral shifts of $\langle\varepsilon\rangle$ away from ε.

Ellipsometric models are proposed in the next section based on realistic physical assumptions, such as (1) the presence of a surface oxide and (2) a transitional layer between the SiO_2 surface layer and the c-Si substrate with partial amorphization and oxidation. Ψ and Δ are then calculated using the Abelès formalism [150] and are compared to measured changes in $\langle\varepsilon\rangle$ to conclude which model can best emulate them. The quality of the fit is quantitatively evaluated with the unbiased estimator, σ:

$$\sigma = \frac{1}{2N-P}\chi^2 \tag{4.3}$$

Here, N is the total number of spectral pairs, P is the number of fit parameters, and χ^2 is the chi-square. The Levenberg-Marquardt algorithm is used for fast convergence. In order to verify the reproducibility and uniqueness of each fit, a number of starting solutions were proposed and used. The cross-correlation matrix was then calculated and off-diagonal terms were used to detect excessive parameter correlation (> 0.8). All error bars reported are taken as two standard deviations given by the fit. Error bars are also weighted by the cross-

correlation parameters, and are thus larger for cases where parameters are more strongly correlated.

4.4 Results

We have carried out a series of oxygen plasma exposure experiments to investigate plasma-bulk interactions. As a first step, we establish, based on *ex situ* VASE measurements, an ellipsometric model that accurately describes variations of SE spectra of c-Si (001) due to modifications by oxygen plasma exposure after 10 minutes. Based on the previous *in situ* RTSE studies mentioned above, modifications are time-dependent, and characterized by the saturation of the measured optical signal after 1 to 2 minutes of plasma exposure. In the present work, we focus on the saturated modifications.

4.4.1 Ex Situ Variable Angle Spectroscopic Ellipsometry

Ex situ spectroscopic ellipsometry data from untreated and O_2 plasma-treated c-Si(001) samples are shown in Figure 4.1. For convenience, the spectra pertain to a single angle, $\theta =$ 78°, and the dielectric function of atomically smooth c-Si(001) [115] is also plotted for comparison. Based on calculations [157] for a simple optical model composed of SiO_2 or surface roughness (50% void + 50% c-Si) on c-Si, we estimate that the height of the interband direct transition peak in $\langle\varepsilon_2\rangle$ at 4.25 eV should decrease by 6.4/nm for a thin oxide layer or by 9.2/nm for surface roughness, from its value of $\langle\varepsilon_2\rangle$ = 48.3 for an atomically smooth bulk sample. For the HF-cleaned c-Si sample, the departure from this number indicates that a surface layer corresponding to either ~0.7 nm of oxide or ~0.5 nm of roughness are present.

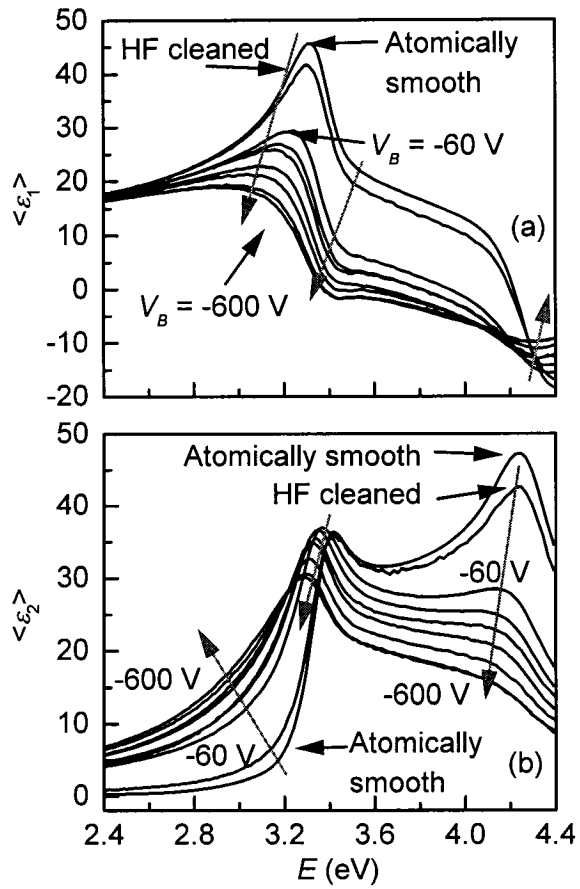

Figure 4.1. *Pseudo-dielectric function* $<\varepsilon>=<\varepsilon_1>-i<\varepsilon_2>$ *measured by ex situ VASE for c-Si(100) samples exposed to an* O_2 *plasma for 10 minutes at bias values* V_B *ranging from -60 to -600 V: (a) real part* $<\varepsilon_1>$*; (b) imaginary part* $<\varepsilon_2>$.

4.4.2 Ellipsometric Models

In order to accurately describe the spectral variations observed in Figure 4.1, we propose three possible surface modification models of increasing complexity and realism [51, 107, 168, 169] (Figure 4.2). We then compare their best fit to the VASE experimental data as explained in section 4.3. Detailed fitting results including deviation curves (i.e. the arithmetic difference between the measured and the modeled spectra) at θ = 78° are

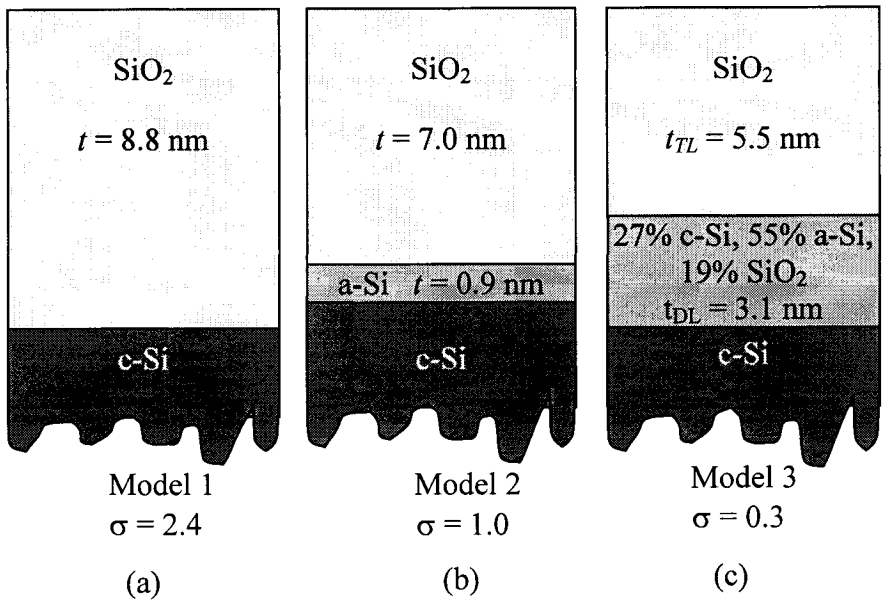

Figure 4.2. *Three ellipsometric models proposed to describe the modifications of c-Si(100): (a) a single layer SiO_2 film on c-Si (model 1), (b) a two-layer system with SiO_2 on an a-Si interfacial layer (model 2), and (c) a two layer system with a SiO_2 top layer (TL) on a BEMA mixed phase interfacial damage layer (DL) (model 3). The best fit to the ellipsometric data is obtained using model 3. All data refer to V_B = -600 V.*

presented in Fig. 4.3 for V_B = -500 V. The best-fit values along with σ for each model are reported in Fig. 4.2 for V_B = -500 V.

The optical properties of the materials (SiO_2 [118], c-Si [115], a-Si [116]) considered in the models were taken from the literature. Model 1 is a single-layer SiO_2 film on c-Si(001), with the SiO_2 thickness being the only fitting parameter. Model 2 consists of two layers, namely SiO_2 on top of a-Si on the c-Si(001) substrate; both thicknesses can be adjusted to fit the experimental data. Finally, model 3 consists of two layers as well, namely a pure SiO_2 top layer (TL) and an interfacial damage layer (DL). The latter is assumed to be a Bruggeman effective medium approximation [119] (BEMA) of a three-phase a-Si, c-Si and SiO_2 isotropic mixture; the depolarization factor was set to 1/3, representing spherical clusters. The two layer thicknesses, t_{TL} and t_{IL}, as well as the DL composition are adjustable parameters. $f_{a\text{-}Si}$, $f_{c\text{-}Si}$ and f_{SiO2} are the volume fractions of a-Si, c-Si and SiO_2, respectively.

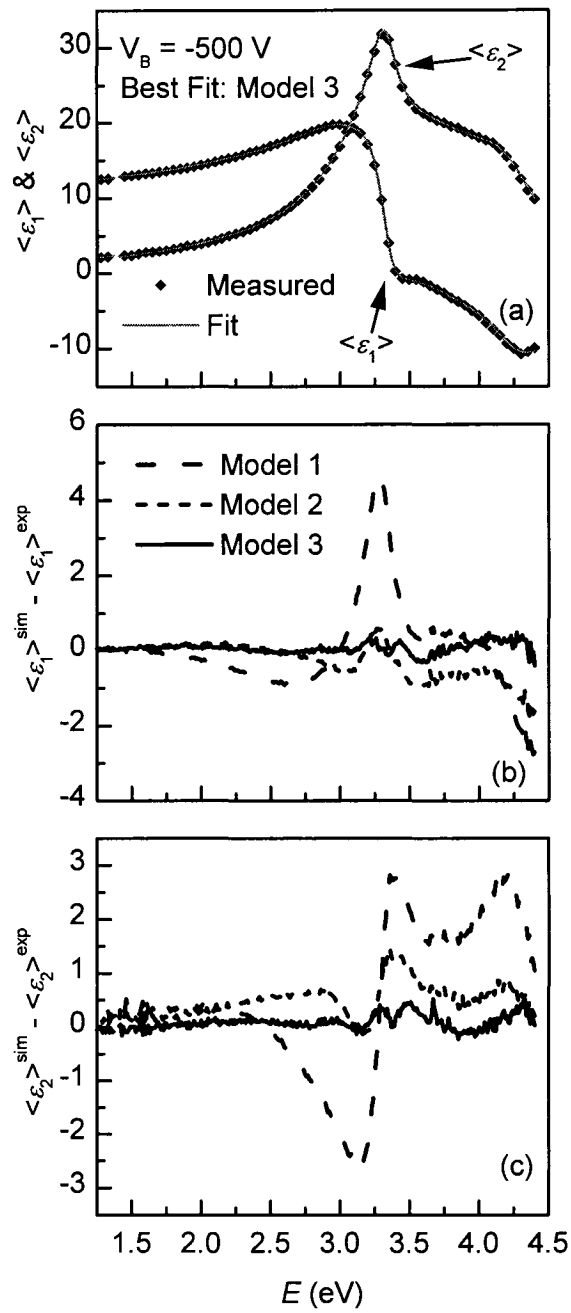

Figure 4.3. *Experimental and fitted ellipsometric signals as a function of photon energy E for a sample with V_B = -500 V: (a) Best fit using model 3. Deviation between experimental and fitted values for the three models are presented in (b) and (c) for the real and imaginary parts, respectively. For clarity, only data for $\theta = 78^o$ are shown.*

Each of the three models was fitted to the VASE data. As an example, Figure 4.3 illustrates the best fit to the data at V_B = - 500 V for the three models. This bias was selected because it corresponds to typical conditions used for PECVD of optical coatings [28]. Figure 4.3a features the SE data points (for clarity most data points were skipped) as well as the fitted curve that minimizes σ for model 3. The agreement between the experimental and calculated curves is remarkable for both $<\varepsilon_1>$ and $<\varepsilon_2>$ over the whole spectral range. In order to reveal the quality of the fit and to discriminate the three proposed models, we plot in Figs. 4.3b and 4.3c the deviation curves between the experimental and the simulated data for the best fits using each model. Such curves enable us to easily identify the parts of the spectrum that are more sensitive to certain types of surface modifications, such as oxidation, interface formation and composition (optical properties), and to verify the ability of a given model to describe subtle spectral changes.

For the V_B = -500 V sample, the best fit using model 1 is obtained with a 8.8 nm-thick SiO_2 layer, yielding an error of σ = 2.4. The deviation curves in Figs. 4.3b and 4.3c show the discrepancy between simulated and SE data to be the most important. The single-layer model totally fails to reproduce spectral features in $<\varepsilon_1>$ for $3.0 < E < 3.5$ eV, and those in $<\varepsilon_2>$ for $E > 2.5$ eV. The addition of an amorphous Si intermediate layer in model 2 improves considerably the fit over the full spectrum (σ = 1.0). This simplified two-layer model yields a 7.0 nm oxide and a 0.9 nm interface. The decrease of σ (Fig. 4.2b) is reflected in an improvement of the spectral fit at high photon energies (Figs. 4.3b and 4.3c) for both $<\varepsilon_1>$ and $<\varepsilon_2>$, as deviations decrease from as high as 5 (model 1) to below 2 (model 2) for $<\varepsilon_1>$, and from as much as 3 (model 1) to less than 1.5 (model 2) for $<\varepsilon_2>$. In model 3, the interfacial damage layer is more complex, its composition further improves the fit (σ = 0.3), and both $<\varepsilon_1>$ and $<\varepsilon_2>$ deviations are completely flattened, nowhere exceeding a value of 0.5. The best result is therefore a 5.5 nm SiO_2 TL and a 3.1 nm DL having a composition of 55% a-Si, 27% c-Si, and 19% SiO_2.

Additional numerical testing was done to verify the uniqueness of the fit using model 3. First, it was fitted to spectra from different V_B conditions and it performed just as well. Second, alternate starting thickness and composition solutions were tested; the fit converged consistently to the same solution. The fitting did not improve significantly by adding additional degrees of freedom, such as a-Si and SiO_2 in the TL, or when SiO_2 in the DL was replaced by SiO. Parameterization of the DL optical constants was also attempted using the Tauc-Lorentz oscillator [170], but failed owing to the presence of some c-Si (see section 4.4.3), which indicates incomplete amorphization [128]. Based on the above discussion, we conclude that model 3 is the most capable to describe the optical response, measured by VASE[1], of the plasma-induced modifications of c-Si (001). We will therefore use this model for the analysis of all O_2 plasma treated samples.

4.4.3 Bias-Dependent Ex Situ Results

Figure 4.4 shows thickness and composition as a function of V_B for both TL and DL following a 10 minute-long oxygen plasma exposure. Both t_{TL} (Fig. 4.4a) and t_{DL} (Fig. 4.4b) increase notably with $|V_B|$. t_{TL} increases from 2.1±0.1 to 6.1±0.2 nm over the

[1] There is strong evidence in the scientific literature that model 3 can yield accurate thickness values and good assessment of overall damage in c-Si. SE is also known to yield accurate thicknesses for ultra-thin films (< 10 nm), such as gate oxides [168], and it has also been extensively used for ion-beam damage studies, showing the ability to depth profile complex structures and to provide useful insights about structural modifications [51, 121]. McMarr, Vedam and Narayan [51] were among the firsts to demonstrate the ability of SE to analyze multilayer surface structures formed in c-Si by 80 to 200 keV Si^+ ion-beam damage with a resolution of 0.1 to 0.2 nm. They have performed extensive comparative testing with cross-section transmission electron microscopy (XTEM) to demonstrate sub-nanometer thickness accuracy and excellent correlation with the extent of the a-Si fraction in damaged layers.

investigated $|V_B|$ range. A similar increase is observed for the DL (Fig. 4.4b) as t_{DL} varies from 1.3±0.3 to 3.5±0.2 nm. The total modification depth (t_{TL} + t_{DL}) almost triples from 3.4±0.4 to 9.6±0.4 nm when V_B changes by a factor of 10, from -60 to -600 V. Increasing $|V_B|$ also leads to the observation of significant changes in DL composition (Fig. 4.4c-e), namely variations of $f_{a\text{-}Si}$ and $f_{c\text{-}Si}$. At low $|V_B|$ values, the DL is predominantly made up of c-Si (71%) and SiO_2 (28%) (Fig. 4.4e) with only traces of a-Si (~1%), while at intermediate bias $f_{a\text{-}Si}$ (44%) increases considerably at the expense of $f_{c\text{-}Si}$ (31%), as seen for V_B = -200 V in Fig. 4.4. This trend continues at higher biases ($|V_B| \geq 200$ V), where $f_{a\text{-}Si}$ becomes greater than 50%. As a rule, the increase of $f_{a\text{-}Si}$ occurs at the expense of $f_{c\text{-}Si}$ in the DL, while f_{SiO2} decreases only slightly (from 28±4% to 18±3% over the entire V_B range investigated).

4.5 Monte-Carlo Simulations of Ion Bombardment

4.5.1 Modeling of Broad RF-Plasma Ion Source

As mentioned in the Introduction, a RF plasma is composed of ions, neutrals, photons, chemically active radicals, and primary and secondary electrons. The kinetic energy distribution of molecular O_2 neutrals has not been measured in a RF-PECVD environment. Although they are known to outnumber ion species by ~ 3-4 orders of magnitude [171], we do not expect to see any significant bulk effect associated with neutrals, especially at relatively low working pressure where the plasma sheath is rather collisionless. Chemically active molecular radicals are also known to mainly react with the surface and do not contribute to bulk modifications deeper than 2-3 nm [172]. Photons, which range in energy from a few meV to tens of eV and can carry very little momentum and tend to interact with bonded electrons of the target rather than nuclei. Based on these assumptions, we have opted to neglect the effect of neutrals, photons, chemically active radicals, as well as primary and secondary electron generation in simulations of plasma-surface interactions for c-Si targets and focus on ion bombardment effects.

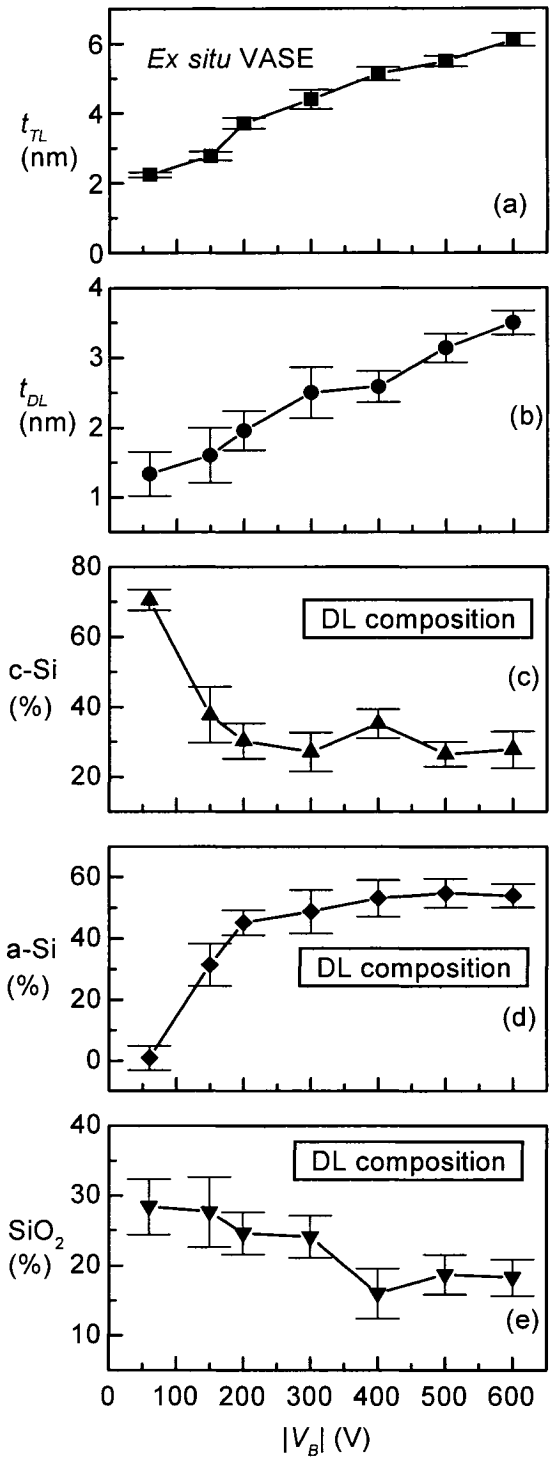

Figure 4.4 *Evolution of the surface modifications according to model 3 extracted from ex situ VASE data: (a) TL thickness, (b) DL thickness, and (c-e) DL composition as a function of* V_B.

We carry out a series of Monte-Carlo simulations, based on the binary collision approximation (BCA), using the SRIM software [72]. We are primarily interested in simulating the maximum depth of oxidation and damage, and calculating the sputtering yield of the oxidized surface. The simulations are fully static and cannot explicitly take into consideration chemical changes at high fluence, including volume swelling or recession of the target surface due to sputtering, and so we have to be mindful of these limitations in the interpretation of results. Maximum ion range from the RF plasma source depends on the maximum ion energy, E_{max}, of the plasma which is directly related to V_B and to the plasma potential, V_p, and may be estimated as follows [67]:

$$E_{max} = e|V_P - V_B| \approx 1.15e|V_B| \qquad (4.4)$$

In contrast, the sputtering of the target surface depends on the average energy of impinging ions, not E_{max}, and so the sputtering rate, R_s, may be well approximated assuming a single-energy source E_m in SRIM simulations.

A typical IEDF is schematically shown in Fig. 4.5a. It is inspired from previous IEDF measurements at the RF powered electrode for both O_2 [37] and N_2 [31] plasmas with conditions very similar to ours. Ignoring the peaks, the O_2^+ IEDF may be reasonably represented by a rectangular function with E_i ranging from a few eV up to ~$1.1e|V_B|$, while the saddle-like O^+ distribution may be represented by a small rectangle centered at around $E_i \sim e|V_B|$ and ranging in energy from ~$0.85e|V_B|$ to ~$1.15e|V_B|$. The relative area of the main peak vs. the saddle-like structure indicates that O^+ ions represent at most 5% of the total IEDF. Considering this rectangular approximation, we can dissociate all molecular ions (>~95% of all ions [37]) into atomic species having half the energy and double the flux (Fig. 4.5b), since the dissociation energy of molecules is much smaller than the ion energy [74] used in the present experiments. The resulting IEDF (Fig. 4.5b) is therefore made up of low- and high-energy atomic oxygen contributions, respectively 97.5% and 2.5% of the total number of O atoms. As a result, the O flux is 1.95 times greater than the measured ion

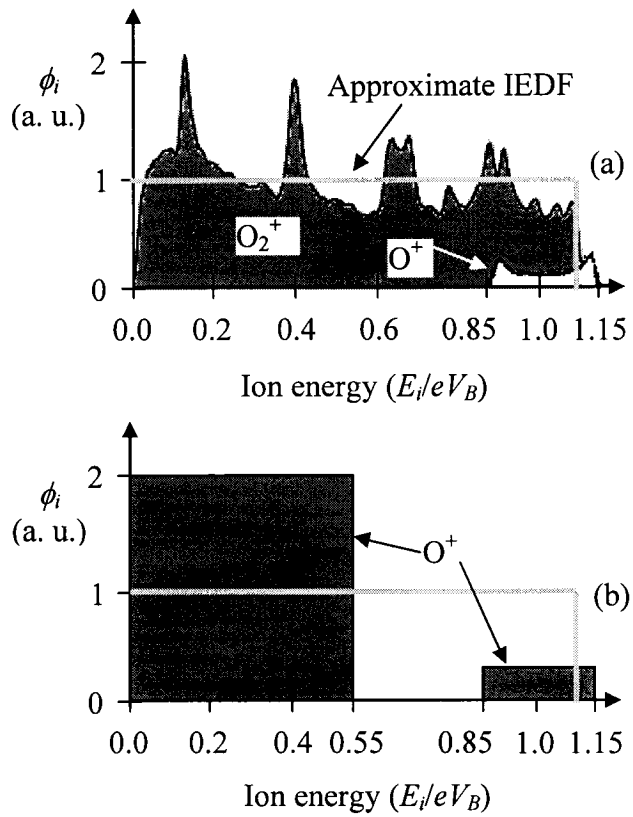

Figure 4.5 *Schematic representation of (a) the ion energy distribution function of O_2 plasma at the RF-powered electrode and (b) the oxygen atom energy distribution function after dissociating O_2^+ molecules. (a) is modified after [37].*

flux reported in Table 4.1. We can now estimate E_m for atomic O species with the following weighted average

$$E_m \approx e\,|V_B|\left(0.975\frac{0.55}{2}+0.025\frac{1.15+0.85}{2}\right)\approx 0.293e\,|V_B| \qquad (4.5)$$

4.5.2 Static Monte-Carlo Simulations of Ion-Surface Interactions

SRIM Monte-Carlo (MC) calculations were performed with full damage cascades using 100,000 O ions at normal incidence on a 50 nm slab of Si with mass density (ρ) of 2.32 g/cm^3. Thin SiO_2 layers of 0.8, 3, and 6 nm with $\rho = 2.2$ g/cm^3 were placed on top of Si to

approximate oxide formation at various stages; this target was then bombarded with 100,000 O ions at E_{max} = 230 eV and 690 eV for V_B = -200 V and -600 V, respectively.

Semi-logarithmic plots of O ion as well as Si and O atomic recoil depth profiles are shown in Figure 4.6 for E_{max} = 690 eV (Figs. 4.6a to 4.6c) and 230 eV (Figs. 4.6d to 4.6f). The vertical black solid line in each figure designates the position of the SiO_2/Si interface used in the simulation runs. The ion implantation distribution is almost Gaussian in shape (on a linear scale) and slightly skewed toward the surface, indicating that the most probable depth for ion range (peak position) is greater than the mean depth. This also implies that ion transport into the target is depth-dependent, as is the case for Si and O recoils.

Figure 4.6 also shows that O target atoms are displaced from their site within the oxide layer in significant numbers, and are preferentially transported as recoils towards the bulk, even exceeding the O implantation profile just below the SiO_2-Si interface. This is not surprising since the kinetic energy of ions exceeds by far the bulk displacement energy threshold, E_D, of O and Si in SiO_2 {E_D(O) ≈ 20 eV, E_D(Si) ≈ 12 eV [62]}, and is mainly lost via elastic collisions with target nuclei. Such collisions lead to the creation of multiple recoils and recoil cascades along the ion path. We conclude from these simulations that oxidation progresses by depth-dependent ballistic transport of O below the oxide surface by a combination of direct O implantation and indirect O displacement from the SiO_2 layer into the bulk.

The depth of the O penetration determines the oxide thickness, and is therefore responsible for the self-limiting growth behavior. As the oxide thickness increases, the driving forces gradually subside, because very few implantations and recoils are transported to the SiO_2-Si interface. Because most notable (and optically detectable) modifications can only occur where Si is not yet transformed into damaged Si or SiO_2, the ever-decreasing fraction of

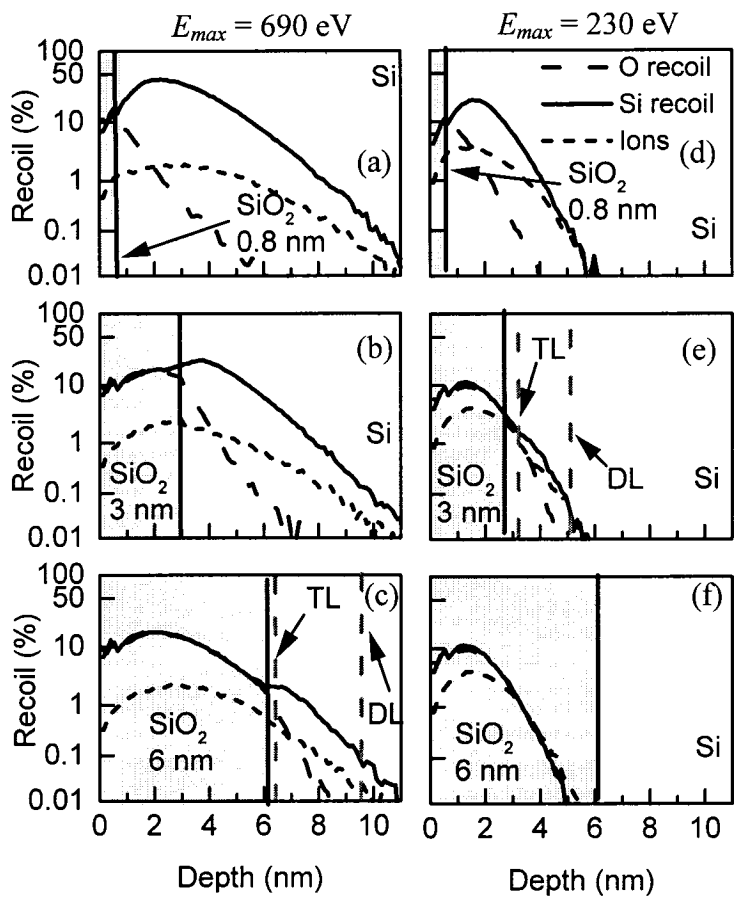

Figure 4.6. *Monte-Carlo SRIM simulations of O ion bombardment in SiO_2 on Si. E_i = 690 eV and the SiO_2 thickness is (a) 0.8 nm, (b) 3 nm, (c) and 6 nm; E_i = 230 eV and the SiO_2 thickness is (d) 0.8 nm, (e) 3 nm, (f) and 6 nm. Markers in (c) and (e) limit the TL and DL layers determined by VASE analysis, for V_B = -600 V and -200 V, respectively.*

ions and recoils that can reach the c-Si results in a slowdown of the oxidation process. This is displayed in the 690 eV simulation, where the maximum O fraction reaching the non-oxidized region decreases by an order of magnitude from as much as ~10 % for 0.8 nm (Fig. 4.6a), to ~1% at 6 nm (Fig. 4.6c), thereby decreasing the rate of oxidation. Similar observations can be made about the 230 eV simulation, where E_{max} and E_m are lower by a factor of 3. In this case, total modification depth after 10 minutes is smaller ($t_{TL} + t_{DL} \approx 5.8$ nm), owing to shallower O implantation. The simulation in Fig. 4.6f is a 6 nm oxide on Si exposed to a 230 eV O plasma. Such a thick oxide cannot form under these conditions as

the penetration depth clearly is smaller than the SiO_2 layer thickness, thereby illustrating the self-limiting oxidation behavior.

The ballistic transport of Si recoils (see Fig. 4.6) plays a critical role in the interfacial damage (DL) formation detected by VASE analysis. Si recoils are formed by elastic nuclear collisions inside the target where they tend to accumulate. Point defects [87, 173] interstitial and vacancy pairs – also called Frenkel pairs [59, 173], as well as amorphous nanoclusters [65, 87, 173] form where collision cascades are located. At high fluence the crystallinity is degraded and long range order is lost. This leads to effective amorphization [98] of the crystalline target, which is supported by experimental results in Figs. 4.4b and 4.4c.

The SRIM simulated O transport depth profiles shown in Fig. 4.6 suggest that oxygen can accumulate in the DL region with increasing fluence, since the DL is within range of O ions. We estimate that no more than ~4% of implanted and recoiled O can penetrate below the 6 nm-thick TL (Fig. 4.6c, 690 eV). A supply of $\sim 1.6 \cdot 10^{16}$ O cm^{-2} is necessary to form a 3 nm-thick SiO_2 layer below the TL, which requires a total fluence of $\sim 3.3 \cdot 10^{17}$ O cm^{-2}. At V_B = -600 V, this may be accomplished within ~130 s for an O flux of $\sim 2.5 \cdot 10^{15}$ $cm^{-2}s^{-1}$ (Table 4.1). The fact that DL remains so oxygen-deficient, even after a fluence $>10^{18}$ O cm^{-2}, may be explained in the context of continuous surface recession due to RF sputtering of SiO_2. Surface recession is expected to compete with oxygen accumulation in the target, and may explain DL formation at high fluence, as we will discuss in section 4.6.2.

4.5.3 Oxidation-Induced Swelling and RF Sputtering

We have shown that VASE is very sensitive to near surface modifications, including slight structural and composition changes in silicon. However, it cannot detect surface motion,

namely volume swelling and sputtering of the surface, because as with most other interference-based optical techniques, VASE is not sensitive to the thickness changes of bulk substrates. Nevertheless, surface motion dynamics are important to consider because they may influence the ability of the ions to subplant (shallow implantation), to form defects, to mix atoms, and to alter near-surface and in-depth composition.

Volume swelling results from the incorporation of atoms into the target. It was calculated by assuming that the SiO_2 TL and the SiO_2 fraction in the DL are both stoichiometric, and that the ratio of SiO_2 to Si volume is ~ 2.2. Swelling data, directly calculated from t_{TL}, t_{DL} and f_{SiO2} (Fig. 4.4), are reported in Table 4.1. As expected, swelling increases with V_B, as the number of O atoms incorporated in the target increases. The estimated O surface density (calculated from t_{TL} and f_{SiO2} in DL, and using $\rho \approx 2.2$ g/cm^3) in the target is also reported in Table 4.1.

The sputtering yield of Si, Y_{Si} (Table 4.1), in the SiO_2 target was calculated using the SRIM simulation program (surface binding energies, E_S: E_S(Si) = 4.7 eV, E_S(O) = 2 eV) by approximating the plasma as a single-energy source E_m (eq. 4.4). E_m is the mean ion energy of the plasma source, therefore it is expected to yield a reasonably good approximation of Y_{Si}. The calculated sputtering rates (Table 4.1) vary by at least two orders of magnitude over the investigated V_B range, and signify that surface recession is very much V_B-dependent. Following a 600 s plasma irradiation, the approximate sputtered thickness for V_B = -60 V is less than the swelling volume (<<0.1 nm), and it increases to 1.3 and 9.5 nm when V_B = -200 and -600 V, respectively.

The calculated sputtering rates, R_S, indicate that surface motion is always present, even after steady-state values are obtained by VASE and *in situ* RTSE analyses [167]. It should be noted that SRIM calculations of the sputtering yield neglect chemical etching effects at

very low E_i [33], and possible molecular effects in the energy transfer between the projectiles and target atoms [174]. The latter one has been shown to enhance the sputtering yield of a gold target for O_2^+ over O^+, but only for kinetic energies below 100 eV per incident atom. The enhancement factor was found to be ~1.7 at 50 eV, and suggests that SRIM calculations underestimate R_s at $|V_B|$ conditions for which $E_m < 100$ eV. For the ion bombardment conditions used in this work, such effects will in general be small and are not expected to affect our calculations and general conclusions. We discuss the impact of surface motion on DL formation in the next section.

Table 4.1. *Estimation of sputtering rate, swelling and O surface density. See text for details.*

V_B (V)	E_{max} (eV)	E_m (eV)	Y_{Si} in SiO_2 @ E_m	ϕ_i ($\times 10^{15}$ ions/cm^2)	R_S (nm/s)	Total etched thickness (nm)	Swelling (nm)	O surface density (10^{15} cm^{-2})
-60	69	18	0.0003	0.13	$2 \cdot 10^{-5}$	0.01	1.1	2.8
-150	173	44	0.0008	0.31	0.0012	0.7	1.4	3.5
-200	230	59	0.0015	0.41	0.0022	1.3	1.9	4.7
-300	345	88	0.0032	0.65	0.0047	2.8	2.2	5.5
-400	460	117	0.005	0.87	0.0080	4.8	2.4	6.1
-500	575	147	0.006	1.10	0.0120	7.2	2.7	7.1
-600	690	176	0.008	1.33	0.0159	9.5	3.0	7.5

4.6 Discussion

The results presented in the previous section indicate that near-surface modifications in c-Si (001) can be measured very sensitively using VASE. The analyses revealed that ion

bombardment from the plasma leads to notable modifications to a V_B-dependent depth below the surface, including oxidation near the surface, and formation of a relatively thick interfacial layer between the oxide and c-Si. The depth of these modifications and their dependence with V_B were explained with the help of SRIM Monte-Carlo simulations. The transport of O ions and Si and O recoils was shown to be depth-dependent, ballistic, and mainly responsible for damage formation at the interface. We invoked surface motion to explain the low concentration of O in the DL at high fluence.

In this section, we will focus on two important topics that require further discussion, namely (1) on the nature of ion-surface interactions, to understand the modifications below the surface, and (2) on the role of surface motion in the formation of a broad V_B-dependent interface.

4.6.1 Depth and Nature of Plasma-Bulk Interactions at the RF Electrode

It has been established for some time that the transport and range of ions and recoils in solid-state matter is dependent on ion energy and mass, as well as target elements and density. These combine to determine the primary stopping power of the target, i.e. nuclear, electronic or a mix of both. Nuclear stopping is prevalent at low ion energies (< keV), while electronic stopping peaks in the MeV range [75]. Based on the distinct E_i-dependence and scaling of target stopping powers, it is clear that the scaling of ion penetration depth with E_i^n depends squarely on the type of ion-bulk interactions.

The exponent value n may be obtained by performing a large number of SRIM simulations over a wide energy range. From these simulations we would obtain ion range, R_p, and straggle, ΔR_P (half-width at half maximum), both taken in the direction perpendicular to the surface. To decrease the computation time, we have used the transport equation approach developed by Ziegler, Biersack and Littmark (ZBL) [62] to calculate R_P and ΔR_p. This

semi-analytical method calculates R_P and ΔR_p by solving the transport problem of energetic ions in a given target, based on two uncorrelated ion-target interactions and their respective energy-dependent stopping cross-sections (see next paragraphs): (1) binary elastic collisions with target nuclei, and (2) continuous slowing by electronic interactions. The ZBL method is attractive because it is orders of magnitude faster than SRIM simulations, and is known to be quite accurate (within 5% of SRIM results) over a wide range of ion energies for single energy beams [62]. In the case of a plasma source with broad IEDF, the range and distribution is more complex, but highest energy ions determine the maximum penetration depth. Therefore, we use the ZBL method to estimate R_P and ΔR_p at E_{max}. The oxide thickness (t_{TL}) and maximum modification depth ($t_{TL} + t_{DL}$) can be estimated to be $\sim R_p + 2\Delta R_p$ and $\sim R_p + 3\Delta R_p$, respectively, as shown in Figure 4.7a on a logarithmic scale. We find excellent agreement between ZBL predictions and experiment, and observe scaling of the depths with $E_{max}^{1/2}$.

A similar approach had been used in the past by Williams et al. [74] to compare oxide thickness from ion-beam oxidation (IBO) in the range from 3 to 40 keV (O fluence of $\sim 5 \cdot 10^{17}$ cm^{-2}), with $\sim R_p + 2\Delta R_p$ obtained from SRIM. We have plotted Williams' data in Fig. 4.7a to show the continuity with our plasma-oxidation results in the sub-keV energy range. We have also added SRIM-simulated data points (solid diamonds) of the damage depth at energies where IBO experiments were performed, to compare with $\sim R_p + 3\Delta R_p$. The damage depth was estimated by setting a threshold of 0.1 displacement per atom (dpa) calculated from an exposure to a fluence of $5 \cdot 10^{17}$ O cm^{-2}. Williams observed a linear scaling of the oxide thickness with E_i, in agreement with ZBL (see Fig. 4.7a, *linear regime*).

In order to identify the mechanism responsible for the scaling change we plotted the nuclear and electronic stopping powers of SiO_2 implanted by O in Fig. 4.7b [75]. The

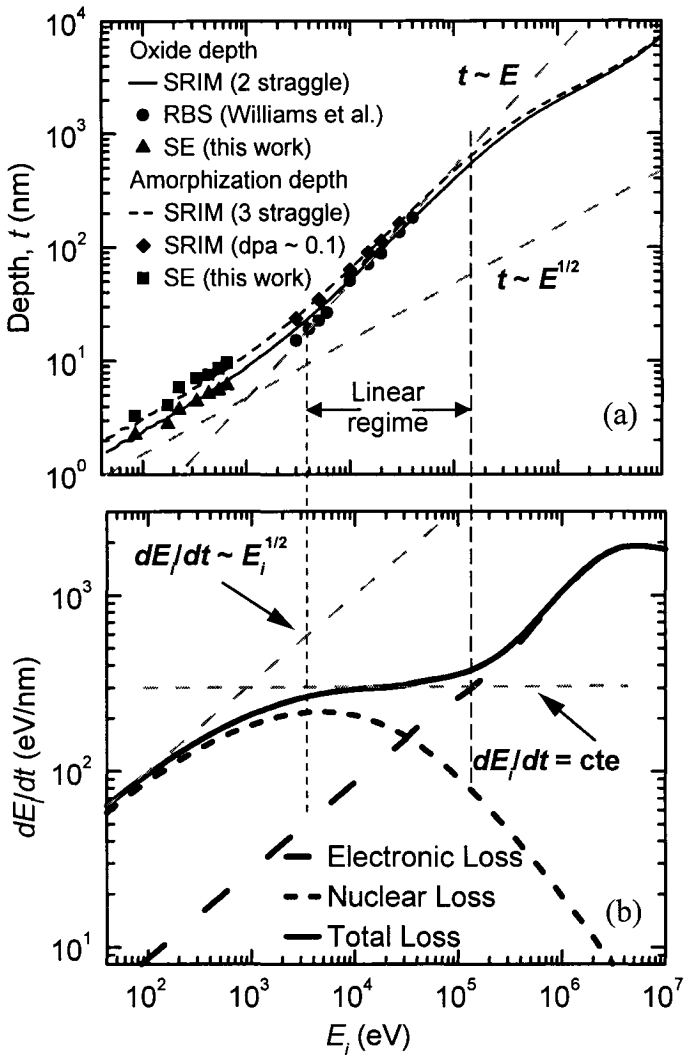

Figure 4.7. *Logarithmic plots of (a) theoretical and measured depth of modification as a function of E_i from this work and from Williams et al. [74], and (b) energy loss per unit depth of O^+ ions in SiO_2 as a function E_i.*

nuclear and electronic stopping powers of SiO_2 vary by orders of magnitude over the E_i range shown. Nuclear losses dominate in low-energy regions (below few keV), while electronic losses are prevalent at high energy (above few hundred keV). A transition region exists between 3 and 100 keV (Fig. 4.7b), where the total energy loss per traveled thickness, dE_i/dt, is quasi-constant. It is therefore expected that ion penetration in this energy range scales approximately linearly with E_i. For $E_i < 1$ keV, nuclear loss is by far

the dominant loss mechanism (Fig. 4.7b) and it scales as E_i^n, where $n < ½$ and continues to decrease with increasing E_i. This scaling behavior is therefore responsible for the square-root ($n \sim ½$) dependence of ion range on E_i.

The excellent agreement between experimental results and theoretical predictions reinforces the fact that O transport is ballistic and dominated by elastic interactions with target nuclei, leading to atomic displacements. Such interactions are directly responsible for the large number of recoils generated in SRIM simulations (Fig. 4.6), and explain the damage formation observed in the DL (Fig. 4.4) at high $|V_B|$. More importantly, the dominance of nuclear interactions at low energies is pertinent to all deposition technologies involving ion bombardment, such as plasma-assisted and ion-assisted techniques.

4.6.2 Effect of Surface Motion on Oxide and Interface Formation

As introduced in section 4.5.2, two competing mechanisms can lead to surface motion during plasma exposure: (1) oxidation-induced volume swelling and (2) surface recession due to SiO_2 sputtering. The evolution of the total surface swelling and recession as a function of V_B after 10 minutes of plasma exposure are reported in Table 4.1. Both effects become more significant at high $|V_B|$, but swelling saturates early on, while surface recession continues unabated.

Based on VASE results, and SRIM calculations (Table 4.1), we propose a qualitative model which explains the formation of a thick interfacial damage layer. During the initial seconds of plasma exposure, O ions are implanted into c-Si and form multiple Si recoils according to the distribution profiles shown in Fig. 4.6. Accumulation of defects leads to significant damage [65, 80] and amorphous cluster formation [65, 87, 173]. This is consistent with *in situ* low energy electron diffraction (LEED) and electron energy loss spectroscopy (EELS) studies [81] of ion-beam amorphization of c-Si by low energy (250 eV) Ar^+ ions, which

show full amorphization of the top few monolayers for an ion fluence of ~2-3·10^{14} cm^{-2}. The low amorphization fluence suggests that this threshold is attained very early during plasma exposure, owing to its high flux (Table 4.1). Therefore damage precedes the onset of oxidation and swelling. This is schematically illustrated in Fig. 4.8a, where we show damage accumulated along the O ion distribution profile in the target. As O fluence increases, O accumulates in the target, forming SiO_2. Volume swelling that accompanies O implantation and oxidation pushes the ion penetration front away from the bulk (Fig. 4.8b), which can reduce the supply of O to the pre-swelling damaged area (Fig. 4.8a). As SiO_2 formation nears completion, surface recession becomes more important, and takes control of surface motion.

The slow recession of the surface forces the movement of the ion distribution profile into the target at the same rate, leading to the establishment of an equilibrium between the supply of O to the SiO_2-Si interface, and the removal of SiO_2 from the surface (Fig. 4.8c). Oxygen is supplied according to the ion implantation depth profile, and contributes to the shape and composition of the interface at steady-state. The pre-swelling damage is eventually consumed, and disappears when surface recession exceeds swelling (Fig. 4.8d). After 10 minutes of exposure, we expect that all samples, except V_B = -60 V, are in the steady-state regime shown in Fig. 4.8d; VASE results in Fig. 4.4 can therefore be considered as steady-state values. At V_B = -60 V surface recession is negligible and the structure formed may be similar to that in Fig. 4.8b. In this case, however, VASE indicates a c-Si fraction as high as 70% and almost no a-Si in the DL, suggesting that O accumulation may have partly oxidized the pre-swelling damage owing to the very slow surface recession. Since the ion energy is very small, with E_m ~ 18 eV and E_{max} ~ 69 eV, most ions cannot displace bulk atoms. In the steady-state regime, the composition of the DL (Fig. 4.4) reflects the amount of O, and the proportion of damaged versus crystalline Si remaining in the DL.

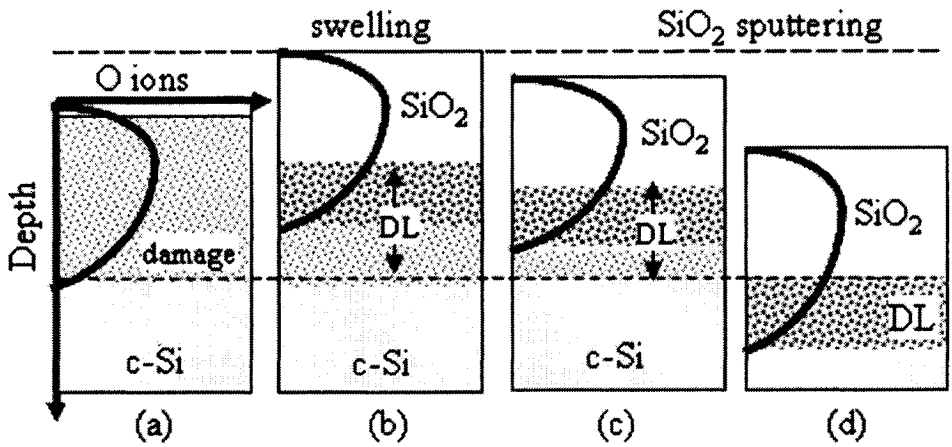

Figure 4.8. *Schematic representation of ion distribution in Si at specific times during O_2 plasma treatment of c-Si (001): (a) before oxidation, (b) during surface swelling, and (c, d) after surface recession by sputtering. At first, surface swelling may lead to thicker DL formation, but as surface recession by sputtering overtakes swelling, a steady state DL (constant thickness and composition) is reached.*

To shed some light on the V_B-dependence of the steady-state DL composition, we consider the energy dependences of ion range and damage formation ($f_{a\text{-}Si}$). Both are expected to increase with E_i. Ion range scales with $\sim E_i^{1/2}$, while the number of defects created per ion scales with $\sim E_i$ [175]. Assuming, for example, that E_i is quadrupled, then the maximum range of ions is expected to double, the number of defects *per* O should then quadruple, and the defect concentration in the new (doubled) volume should double. Such a behavior is observed in Fig. 4.4. For instance, when comparing results at V_B = -200 V with V_B = -600 V (factor of 3, $3^{1/2} \approx 1.7$), we find that t_{DL} increases by a factor ~1.8, while a-Si fraction increases by a factor of ~1.2, in good agreement with the expected changes of 1.7 for thickness and 1.2 for a-Si fraction. The latter value (1.2) has been corrected from 1.7 (by dividing with 1.4) owing to the fact that there is ~40% more O subplanted in the DL at -200 V than at -600 V (Fig. 4.4e).

4.7 Conclusion

We have shown that ion bombardment in a typical PECVD process can lead to important modifications of the substrate. In the case of O_2 plasma on c-Si, modifications include damage of the crystalline structure and near-surface oxidation. Monte-Carlo simulations support the view that oxide and damage formation are due to subplantation and atomic displacements. The depth of oxidation (t_{TL}) depends directly on maximum ion energy and scales with $(E_{max})^{1/2}$, in agreement with the ZBL method and in continuation of ion beam oxidation data at higher energy. These results also suggest that nuclear interactions dominate ion-bulk effects. Therefore, the transport of O ions and recoils (O and Si) is ballistic and depth-dependent.

The broad interface detected by VASE could not be explained without invoking the surface motion dynamics, which are mainly the result of swelling and surface sputtering. At high fluence, surface recession dominates the motion, and O supply to the SiO_2-Si interface becomes limited by the ability of the plasma to subplant O while sputtering SiO_2 from the surface. Under these circumstances energetic O^+ ions which can penetrate below the oxide, displace Si atoms and damage the crystalline structure. The abundance and preferential displacement of Si contribute to accumulation of defects below the oxide, especially at high V_B, which leads to the formation of the DL.

For typical PECVD conditions, such as those used for the fabrication of optical coatings, the ion penetration below growth surfaces scales as $E_i^{1/2}$. The significant O subplantation implies that continuous atomic mixing occurs during film deposition, as energy is transferred to surface and bulk atoms. For film growth under intense ion bombardment, the effect of surface motion is therefore very important: it controls the rate of incorporation of hyperthermal species [41, 42], leading to densification [23, 24, 54], to stress release [176, 177], and, as we have shown in another work, to considerable interface mixing [178].

This work has lead to other noteworthy outcomes: (i) oxidation and interface formation may be tuned by altering the O transport depth profile, for instance, by modifying the IEDF; particularly, by increasing the proportion of energetic O^+, one can enhance the transport of O to the DL; (ii) adjusting the deposition rate (or ion-to-neutral arrival rate ratio) for a given V_B value can be used for interface control during thin film deposition.

4.8 Acknowledgements

The authors thank Mr. Stéphane Larouche and Dr. Oleg Zabeida (Ecole Polytechnique), and Mr. Blaine Johs (J.A. Woollam Co., Inc.) for fruitful discussions, and Mr. Gilles Jalbert for expert technical assistance. This work was supported by the Natural Sciences and Engineering Research Council (NSERC) of Canada. PD acknowledges support from the Canada Research Chair program. AA acknowledges the support from the NSERC Post-Graduate program.

Chapter 5. Article 2: "Dynamics of Ion Bombardment-Induced Modifications of Si(001) at the Radiofrequency-Biased Electrode in Low-Pressure Oxygen Plasmas: *In Situ* Spectroscopic Ellipsometry and Monte-Carlo Study"

A. Amassian[1], M. Svec[2], P. Desjardins[1] and L. Martinu[1]

[1]Regroupement québécois sur les matériaux de pointe (RQMP) and Department of Engineering Physics, École Polytechnique de Montréal, Montréal, Québec, Canada

[2]Department of Physics, J. E. Purkyne University, Usti Nad Labem, Czech Republic

Submitted for publication: *Journal of Applied Physics* (November 2005)

5.1 Abstract

Low pressure O_2 plasma exposures were performed on c-Si (001) at a radiofrequency (RF)-powered electrode in the presence of substrate self-biasing (V_B) from V_B = -60 to -600 V, under conditions suitable for the fabrication of optical interference filters. The plasma-surface interactions were monitored *in situ* using real-time spectroscopic ellipsometry (RTSE), which reveals time- and ion fluence-resolved information about depth-dependent modifications. RTSE analysis also indicates almost immediate damage formation (< 1 s) to a depth of a few nanometers below the surface after exposure to a low oxygen ion fluence (~5×10^{14} O cm^{-2}). Oxide growth is detected at intermediate fluence (~10^{15} to 10^{16} O cm^{-2}); it forms near the surface of the target on top of an O-deficient interfacial damage layer (DL). Both layers experience a self-limiting growth behavior at high fluence (> 10^{17} cm^{-2}) as oxide and DL thicknesses reach V_B-dependent steady-state values. At steady-state, the silicon oxide thicknesses reach ~3 and ~6 nm, while the DL thicknesses are ~1.2 and 3.5 nm at V_B = -150 and -600 V, respectively. The *in situ* experimental study was complemented by Monte-Carlo TRIDYN simulations based on the binary collision approximation, which were adapted to calculate dynamic changes of target composition exposed to a broad-energy ion source (RF plasma source) at high fluence. Simulation results are found to agree exceptionally well with experiment. In addition, they reveal that the 1.2 to 3.5 nm-thick O-deficient interfacial layer formed in the steady state regime is a result of damage formation due to (1) a small number of high energy O^+ ions in the plasma source, capable of penetrating and damaging up to 3 nm deeper than other ions, and (2) because of important surface motion resulting from oxidation-induced swelling and sputtering-induced recession. Surface recession observed at high fluence (>10^{18} O cm^{-2}) for $|V_B| \geq 300$ V inhibits oxygen accumulation at high depth in the target, thus forming the DL.

5.2 Introduction

Low-pressure plasma processes (< 100 mTorr) have been gaining in importance in recent

years for a variety of applications, ranging from surface treatment [103, 107, 179, 180, 181, 182, 183] and thin film deposition [6, 19, 20] to reactive ion etching (RIE) [184, 185, 186, 187], ion-cutting [188, 189], and plasma immersion ion implantation (PIII) [190, 191, 192]. As such, they are used in a wide range of ion energy, E_i (E_i ~10^0 to ~10^4 eV), and flux, ϕ_i, (ϕ_i ~10^{14} to ~10^{16} $cm^{-2}s^{-1}$) conditions with a variety of gas phase species. In most low-pressure plasma processes, ion bombardment (IB) plays a central role at the exposed surface and even below it, especially when $E_i > 10$ eV. Impinging ions transfer their kinetic energy and momentum to target nuclei, and lead to significant atomic relocations (displacements), which can result in damage formation and amorphization, atomic mixing, sputtering, and composition changes below the surface. The range and effect of ions depends on ion and target characteristics, namely the ion mass, energy, target composition and density [62].

Some of these effects have been exploited for the fabrication of dense dielectric optical coatings. In particular, hyperthermal ions with energies E_i ~ 1 to 10^3 eV, play an important role on the novel low-pressure plasma-enhanced chemical vapor deposition (PECVD) processes used for the deposition of optical films [67], while having been traditionally used for the fabrication of hydrogenated amorphous Si (a-Si:H) [114, 193] and amorphous carbon (a-C:H) [41, 42] coatings. These include oxides, such as SiO_2, TiO_2, Ta_2O_5, and Nb_2O_5 [28], and $SiN_{1.3}$ [23, 67].

In addition, the demonstrated versatility and flexibility of PECVD have enabled the tuning of the optical and mechanical properties of thin films [28], a task that was regarded as nearly impossible by traditional physical vapor deposition (PVD) technologies [19, 20]. The tunability of optical properties in the PECVD process is facilitated by the availability of a wide range of gas phase precursors, which may be mixed to control plasma and surface chemistry, in order to tailor thin film compositional [21, 22, 149] and nanostructural [25, 26, 27] properties.

Furthermore, combining discharges, such as microwave (MW, E_i < 10 eV) and radiofrequency (RF, 10 < E_i < 10^3 eV), in dual-mode MW/RF plasmas [31, 32] enables one to vary the IB characteristics, including the mean ion energy (E_m), the maximum ion energy (E_{max}), the ion energy distribution function (IEDF), ϕ_i, and the ion-to-neutral arrival rate ratio, ϕ_i/ϕ_n. For example, a pure MW discharge produces porous $SiN_{1.3}$ coatings with a refractive index of $n \sim 1.6$ ($\lambda \sim 550$ nm), while a RF discharge yields dense films with $n \sim 1.9$ [23]. A combination of MW and RF discharges in a single process enables the fabrication of multilayer or continuously graded dense/porous optical interference filters (OIFs) [23, 24, 194].

On the other hand, the flexibility of PECVD processes is a source of great complexity owing to the spectrum of species arriving at the surface, including neutrals, atomic and molecular ions, electrons, radicals, and energetic photons, which all together define the plasma-surface interactions. Furthermore, the indirect dependence and interdependence of important IB characteristics (E_m, E_{max}, ϕ_i, etc.) on external process parameters such as the RF self-bias (V_B) and working pressure (p) result in complex relationships between target or thin film microstructure and ion-surface interactions.

In a previous article [195], we contributed to the understanding of the effect of plasma-surface interactions at the RF-biased electrode by performing 10-minute long plasma exposures on c-Si (001) in V_B conditions suitable for optical coating fabrication (V_B = -60 to -600 V). *Ex situ* spectroscopic ellipsometry (SE) analysis revealed that modifications, which include near-surface oxidation and interfacial damage, occurred at depths of up to ~3.5 and 10 nm for V_B = -60 and -600 V, respectively. Long exposure times enabled to determine that the near-surface modifications are self-limiting. From the knowledge of the IB characteristics as a function of V_B (E_m, E_{max} and ϕ_i [32]), we established that these modifications can be accounted for by IB effects, and showed that their maximum depth can be predicted by binary collision calculations of O ion transport.

In situ experiments are now required to obtain a dynamic insight into the effects of ion-surface interactions in a PECVD environment and specifically in conditions and on time scales (seconds) relevant for optical coatings fabrication. Such experiments can reveal the characteristic time scales associated with the self-limiting oxidation behavior, including the onset and dynamics of target damage and oxidation – expected to occur at different characteristic fluences [80, 167].

Given the complexity of ion-surface interactions (implantation, displacements, sputtering, composition changes, etc.), the use of simulation tools is required for an in-depth analysis of the results of *in situ* monitoring. Simulations enable to break down phenomena involving multiple – and sometimes competing – processes. For instance, they can reveal how modification dynamics are affected by the presence of molecular and atomic ions in the broad IEDF of the negatively biased RF plasma source. They are essential to identify surface swelling (from O incorporation) and recession (from Si sputtering) during target modifications.

Molecular dynamics (MD) simulations of ion beam damage and amorphization of c-Si have been extensively reported in the literature, because they provide an insight into atomistic processes [65, 76, 77, 87, 173]. The results of MD studies suggest that damage of Si begins with individual defect formation, which agglomerate into thermodynamically metastable amorphous nanoclusters in an otherwise crystalline matrix, and grow until the Si matrix is fully amorphized. Interstitial and vacancy (IV) pairs (also known as Frenkel pairs or bond defects) formed by IB-induced atomic displacements [175, 196] have been identified as the primary defects involved in Si damage and amorphization. MD simulation work by Marqués et al. [77] has shown that while isolated IV pairs in Si annihilate within microseconds at room temperature, IV pair clustering increases their thermodynamic stability.

By simulating the ion beam exposure of Si by MD until complete amorphization was achieved, Nord et al. [65] provided a quantitative relationship between the amorphization fraction in bulk c-Si and the energy dose deposited in the target. The relationship confirmed that a combination of direct-impact and amorphous/crystalline (a/c) interface-stimulated processes are involved in Si amorphization, for which an analytical expression was derived [98]. As a result, we can now use significantly less time consuming simulators – such as the Monte-Carlo-based TRIDYN code – to predict the dynamical evolution of amorphization depth profiles in Si (and other materials) over time (fluence) scales ranging from << 1s of up to a few minutes with sufficient accuracy.

The TRIDYN [63, 64] simulator is a powerful TRIM-based program capable of addressing dynamic alterations of the target's composition (in addition to volume and surface position) during high fluence implantation by a single-energy ion beam. TRIDYN has been used to study sub-keV ion beam oxidation of Si, where it accurately predicted the oxide formation thickness and dynamics at room temperature [101]. Deposition processes, such as sputtering [197, 198], ion beam assisted deposition (IBAD), [192] and cathodic arc deposition [199], have also benefited from the capability of TRIDYN to calculate ion and recoil transport effects, including defect formation, sputtering, and ion mixing (during thin film growth) on time and length scales relevant to these processes. Consequently, it appears that the study of plasma-surface interactions at the RF-powered electrode can greatly benefit from TRIDYN simulations of IB effects in well-characterized IB conditions.

In the present work, we focus on investigating the dynamics of sub-surface modifications in c-Si(001) during O_2 RF-plasma exposure, using a combination of *in situ* real-time spectroscopic ellipsometry (RTSE) measurements and TRIDYN simulations. c-Si (001) was used as a model system because its optical response changes sensitively and reliably in the presence of near surface modifications, and because these are well detected by SE [128]. The TRIDYN simulator was modified to make possible the simulation of IB sources with a very broad energy range, such as at the RF-biased electrode [37]. We show that this

combination enables unprecedented capabilities for monitoring and simulating near-surface modifications for plasma exposure times ranging from ~0.1 s up to a few minutes, corresponding to ion fluence ranging between ~10^{14} and 10^{18} cm^{-2}. Our analysis reveals that damage formation in the Si matrix precedes all other effects, and is observed as early as ~2×10^{14} cm^{-2}, corresponding to < 1 s of exposure time. Oxidation is detected after a few seconds of exposure, and is accompanied by volume swelling until the oxygen concentration in the target saturates in the depth accessible to ions. Swelling is then overcome by surface recession as a result of Si and O sputtering, which in turn inhibits O accumulation in the target, because of continuous motion of the implantation profile into the bulk. TRIDYN simulations demonstrated that high energy O^+ ions (<5% of all ions) combined with surface recession at high fluence are responsible for the growth of a permanently O-deficient and highly damaged interfacial layer between the near-surface oxide and c-Si.

5.3 Experimental Methodology

c-Si (001) wafers (10 Ω·cm) were cleaned in a piranha solution (H_2SO_4:H_2O:H_2O_2 = 4:1:1) for 5 minutes, rinsed in de-ionized water, followed by native oxide removal for 60 s in 49% water-diluted HF. Substrates were then dipped in de-ionized water, dried using N_2, and then immediately loaded on the RF-powered substrate holder-electrode of a 13.56 MHz capacitively coupled plasma reactor [146]. The system was then pumped to ~10^{-6} torr.

After pumpdown, O_2 was introduced into the reactor chamber and conditions were adjusted similar to those of typical oxide deposition by PECVD [22]: O_2 flowrate was set at 60 sccm, and the total pressure was fixed at p = 20 mTorr. Plasma was initiated using an RF power varying from 7 to 110 W, resulting in a self-bias voltage (V_B) between –60 and –600 V, respectively.

An M-2000 (J. A. Woollam Co.) rotating compensator ellipsometer was mounted on the

reactor on a pair of flanges with a nominal incidence angle $\theta = 78^{o}$ from the normal to the substrate holder. The ellipsometer measures the complex ratio ($\tilde{\rho}$) of p– to s– polarizations of the reflected light:

$$\tilde{\rho} = \frac{\tilde{r}_p}{\tilde{r}_s} = \tan\Psi e^{i\Delta}, \qquad (5.1)$$

where $\tilde{r}_p$ and $\tilde{r}_s$ are the complex Fresnel reflection coefficients, and Ψ and Δ are ellipsometric angles.

In the present study, a number of photon energies between 2.5 and 5.0 eV (247 - 490 nm) were recorded simultaneously, when performing analyzer two-zone averaging with 500 ms integration time per zone with a 2.3 s interval between consecutive spectra. Two-zone averaging automatically corrects for out-of-plane window birefringence effects in Ψ, and for potential misalignments of the plane of incidence [49]. Strain-free fused silica windows (2 cm-thick) were used to keep in- and out-of-plane birefringence effects to a minimum. In-plane birefringence (Δ_{off}) was determined in vacuum using a pre-run *in situ* calibration process allowing one to determine both Δ_{off} (which offsets Δ as $1/\lambda$) and θ. In some instances an order of magnitude faster but also noisier measurements were performed without two zone-averaging, with the goal of improving the time resolution of RTSE dynamical analysis.

RTSE data acquisition was initiated at least one minute prior to plasma ignition and was stopped after the substrate was cooled down. Analysis of the pre-ignition data allows to verify that θ and Δ_{off} have not changed since the calibration run, to detect any residual surface layer following HF cleaning, and to determine the substrate temperature with the help of an optical model (see below).

For convenience all ellipsometric data are presented in the form of the pseudo-dielectric function ($\langle\varepsilon\rangle = \langle\varepsilon_1\rangle - i\langle\varepsilon_2\rangle$) computed from the following expression:

$$< \varepsilon >= \sin^2\theta\left[1+\tan^2\theta\left(\frac{1-\tilde{\rho}}{1+\tilde{\rho}}\right)^2\right]. \qquad (5.2)$$

In the case of a perfectly abrupt interface between two semi-infinite media (e.g. optically thick c-Si with atomically smooth surface in air), direct inversion of $\tilde{\rho}$ to $<\varepsilon>$ provides the exact dielectric function of the bulk material, i.e. $<\varepsilon> = \varepsilon$. Any departure from the abrupt interface model, such as oxidation, damage accumulation, amorphization, or roughening, will result in spectral modifications of $<\varepsilon>$.

Based on our *ex situ* study [195] of plasma-surface interactions, we consider three ellipsometric models to describe the real-time modifications of c-Si (section 5.5.1.2). The optical properties of the materials considered in the models are taken from the literature, hence they are not fitted. Model 1 is a single-layer SiO_2 [118] film on c-Si(001) [115], with the SiO_2 thickness being the only fitted parameter. Model 2 is formed by two layers, namely SiO_2 on top of amorphous Si (a-Si) [116] on the c-Si(001) substrate; both layer thicknesses can be adjusted to fit the experimental data. Finally, model 3 consists of two layers as well, a pure SiO_2 top layer (TL) and an interfacial damage layer (DL), assumed to be a Bruggeman effective medium approximation (BEMA) [119] of an isotropic mixture of a-Si, c-Si and SiO_2. In this case, the two layers thicknesses and the DL composition are adjustable parameters.

The quality of the fit is quantitatively evaluated with the unbiased estimator (σ) :

$$\sigma = \frac{1}{2N-M}\sum_{i=1}^{N}\left[\left(\Psi_i^{\exp}-\Psi_i^{\mathrm{mod}}\right)^2+\left(\Delta_i^{\exp}-\Delta_i^{\mathrm{mod}}\right)^2\right], \qquad (5.3)$$

where N is the total number of spectral pairs, M is the number of fit parameters, and superscripts "exp" and "mod" refer to experimentally measured and ellipsometric model values, respectively. The fit uses the Levenberg-Marquardt algorithm for fast convergence.

The analysis of *in situ* optical data requires the use of an additional parameter: the substrate temperature (T_s). Thermocouple measurements show that T_s can increase by as much as ~100°C during plasma exposure, thereby shifting the optical properties of c-Si quite significantly [200] and leading to systematic errors in RTSE data analysis. To correct for heating and cooling effects, we incorporate experimentally determined T_s-dependent c-Si optical constants [167, 200]. The T_s-dependence of SiO_2 optical constants was ignored, since the oxide's refractive index (n) variations with T_s are negligible compared to n and k (extinction coefficient) variations expected for c-Si [201]. The optical constants of a-Si are also expected to be T_s-dependent [202]. However, a-Si inclusions in a mixed-phase layer (DL) are not expected to behave in the same way as an a-Si thin film [202, 203]. Consequently, we bypassed this difficulty by simply assuming fixed a-Si optical constants. We show in sections 5.5.1.1 and 5.5.1.2 that this approach yields acceptable results.

5.4 TRIDYN Simulations of Ion Bombardment by a Broadband Ion Source

The TRIDYN simulation code, developed by Moeller and Eckstein [63, 64], accounts for dynamic target modifications during ion bombardment at high fluence. It has been previously used to simulate low energy ion beam oxidation of Si [101], and more recently, to study target surface modifications during magnetron sputtering [197]. These simulations were performed for single-energy ion sources and cannot properly describe the effects of broad-band sources similar to those observed at the RF-powered electrode in a PECVD process [37].

We have developed a simple procedure to take into account the IEDF of a broad-energy ion source within TRIDYN simulations. A typical IEDF at the RF-powered electrode in O_2 plasma (p = 20 mTorr) is schematically represented in Fig. 5.1a [37, 31]. Ignoring the resonance peaks, the IEDF may be approximated by a rectangular function with E_i ranging

from few eV up to E_{max}, while the O^+ distribution is a saddle-like structure, centered at around $E_i \sim e|V_B|$, with energy ranging from ~$0.85e|V_B|$ to ~$1.15e|V_B|$. Working with the rectangular distribution, we first dissociate all molecular ions (≥95% of all ions [37]) into atomic species, owing to the fact that the dissociation energy of O_2^+ molecules is much smaller than E_i. Thus, molecular ions dissociate into atomic oxygen with half the energy and double the fluence. We have plotted in Figure 5.1b the calculated atomic O energy distribution function (OEDF). The OEDF is made up of low- and high-energy atomic oxygen contributions, representing respectively 97.5% and 2.5% of the ion population: we use this ion source for all TRIDYN and SRIM [62, 72] simulations presented in this work, unless stated otherwise. In the remainder of this paper, we refer to the broad energy OEDF simulation method as the IEDF method.

The IEDF in Fig. 5.1b was split into 10 discrete energy channels (Fig. 5.1b, see large dots) and simulations were performed at each energy channel using 10 pseudoparticles (or packets) of 10^{11} O cm^{-2} fluence each, for a total O fluence of 10^{12} cm^{-2} per E_i. The overall impact of the broadband plasma source on the target was calculated by weighted averaging simulation results (such as elemental depth profiles, surface densities, sputtering yield, surface recession, etc.) from 10 different E_i according to the IEDF shown in Fig 5.1b. The results of the weighted averaging after a fluence increment of 10^{12} O cm^{-2} are taken as the starting point for the next incremental exposure to 10 pseudoparticles at each of the 10 E_i. This procedure is repeated until a total fluence of 10^{18} O cm^{-2} is reached, equivalent to a plasma exposure time of a few minutes.

The number of energy channels is a compromise solution that allows to emulate the IEDF in Fig. 5.1b as closely as possible, while minimizing computational time. Increasing the number of channels to 20 yielded very similar quantitative results compared to 10 channel calculations. Reducing the number of channels to two (E_m and E_{max}, defined below) led to systematic discrepancies and significant noise increase compared to 10 or 20 channel calculations.

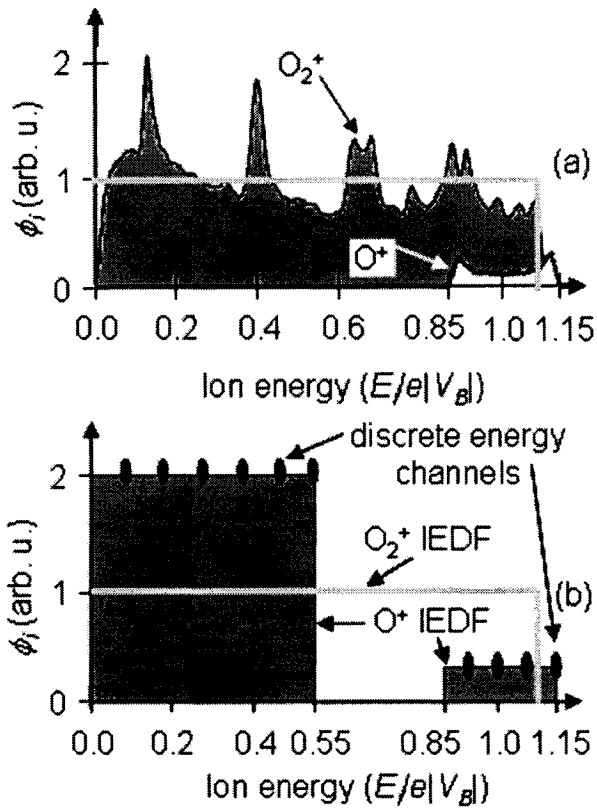

Figure 5.1. *Schematic representation of (a) the ion energy distribution function in an O_2 plasma at the RF-powered electrode inspired from reference [37], and (b) the oxygen atom energy distribution function after dissociating O_2^+ molecules and splitting into 10 discrete energy channels for TRIDYN simulations.*

The choice of 10^{11} O ions/pseudoparticle is about an order of magnitude lower than what has been reported by other TRIDYN users for monoenergetic beams [101, 197, 198]. One must bear in mind, however, that the best accuracy is achieved only when the IEDF method emulates the quasi-simultaneous exposure of the target to all energies of the IEDF. This is only achieved by weighted-averaging the simulation results at all 10 channels after very small fluence increments (10^{12} cm^{-2}, equivalent to ~10^{-4} to 10^{-3} s of plasma exposure). This ensures that very small – almost negligible – incremental modifications occur with increasing fluence, as if they were produced by various components of a broad energy source (most modifications are detected for fluence above ~10^{14} cm^{-2}, see next section).

Therefore, the use of 10 pseudoparticles per E_i (10^{11} O ions/pseudoparticle) is required to improve the statistical quality and to reduce the noise of individual energy channels. Additional testing was also performed with 10^{10} cm^{-2}/pseudoparticle and 10^{11} cm^{-2}/E_i, without noticeable improvements or changes in the simulation results.

The IEDF presented in Fig. 5.1b can be used to define the mean ion energy, E_m, by the following weighted average:

$$E_m \approx e\,|\,V_B\,|\left(0.975\frac{0.55}{2}+0.025\frac{1.15+0.85}{2}\right)=0.293e\,|\,V_B\,|\approx 0.3e\,|\,V_B\,|, \qquad (5.4)$$

while the maximum ion energy, E_{max}, is related to plasma potential, V_p as follows:

$$E_{max} = e|V_p - V_B| \approx 1.15e|V_B| \qquad (5.5)$$

In addition, the total atomic O flux, ϕ_O, is estimated to be $\phi_O \sim 1.95\cdot\phi_i$, as calculated by splitting molecular ions. Ion flux was estimated from measurements performed earlier [32]: ϕ_i ~0.13×10^{15}, ~0.31×10^{15}, ~0.65×10^{15}, ~0.87×10^{15}, ~1.10×10^{15}, and ~1.33×10^{15} $cm^{-2}s^{-1}$ for V_B = -60, -150, -300, -400, -500, and -600 V, respectively. Dynamic data presented in this paper (except Figure 5.4), is reported as a function of O fluence, Φ_O, calculated as $\Phi_O = 1.95\cdot\phi_i\cdot$time, where the plasma exposure time is taken in seconds.

5.5 Results

5.5.1 Plasma Exposure of c-Si(001) at the RF-Powered Electrode: In Situ RTSE Study

We monitored a series of oxygen plasma treatments of c-Si(001) substrates using *in situ* RTSE. Ellipsometric spectra taken before and after plasma ignition at V_B = -600 V are plotted in Fig. 5.2. The real and imaginary parts of the dielectric function of atomically flat c-Si(001) are also shown for comparison [115]. Our experimental SE data for $<\varepsilon_1>$ and

$<\varepsilon_2>$ at t = 0 s reveal the presence of a 0.5 to 0.8 nm-thick residual oxide which is confirmed by X-ray photoelectron spectroscopy (XPS).

Significant changes in the ellipsometric spectra are detected immediately after plasma ignition at V_B = -600 V and continue to increase with time, until they eventually saturate. The variations of $<\varepsilon_1>$ and $<\varepsilon_2>$ spectra are very significant, with largest changes observed in $<\varepsilon_2>$ near the direct transition peak at 4.25 eV. This peak is expected to decrease by 6.4 per nanometer of SiO_2 [157] suggesting that important near-surface modifications of c-Si occur within the initial seconds of oxygen plasma exposure (see Fig. 5.2b).

The time-evolutions of $<\varepsilon_1>$ and $<\varepsilon_2>$ vary sensitively with plasma exposure time. $<\varepsilon_1>$ decreases with exposure time in the range E < 4.3 eV, and increases elsewhere, whereas $<\varepsilon_2>$ decreases when E > 3.4 eV, and increases elsewhere. Special markers are placed at E_1 = 3.2 eV and E_2 = 3.65 eV to enable the visual tracking of $<\varepsilon_1>$ and $<\varepsilon_2>$ variations. Measured values of $<\varepsilon_1>$ and $<\varepsilon_2>$ decrease together at E_2, while they move in opposite directions at E_1.

In the next section, we establish an ellipsometric model that accurately emulates *all* real-time spectral modifications of $<\varepsilon_1>$ and $<\varepsilon_2>$. The model can then be used to quantitatively analyze damage and oxide formation dynamics.

5.5.1.1 Optical Modeling of Plasma-Induced Modifications and Heating

The ellipsometric models proposed to fit the *in situ* RTSE data are illustrated in Fig. 5.3a. We have previously demonstrated that model 3 describes best the *ex situ* VASE spectra after 10-minute long O_2 plasma exposures for V_B ranging from -60 to -600 V [195]. Here,

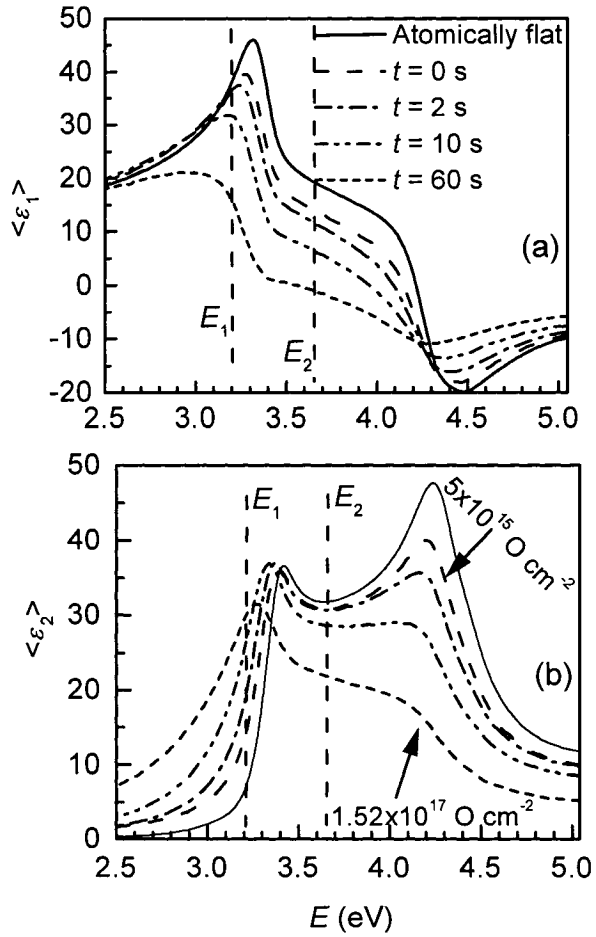

Figure 5.2. *In situ real-time spectroscopic ellipsometry data in terms of (a) real* $\langle\varepsilon_1\rangle$ *and (b) imaginary* $\langle\varepsilon_2\rangle$ *parts of the pseudo-dielectric function showing evidence of time-dependent modifications of the c-Si (001) optical response in an* O_2 *RF plasma at* V_B = -600 *V. Data for clean, atomically flat Si(001) is taken from [115].*

we show that model 3 can also capture the essence of the substrate modifications *as they occur*, by analyzing ellipsometric trajectories obtained at E_1 and E_2. Experimental and simulated $\langle\varepsilon_2\rangle$ vs. $\langle\varepsilon_1\rangle$ trajectories are plotted in Figs. 5.3b and 5.3c for a c-Si(001) sample exposed to V_B = -600 V at the RF-powered electrode.

As expected, all three models adequately reproduce the t = 0 s spectra corresponding to the HF-cleaned Si(001) substrate. After plasma ignition (t > 0 s), model 1 completely fails to

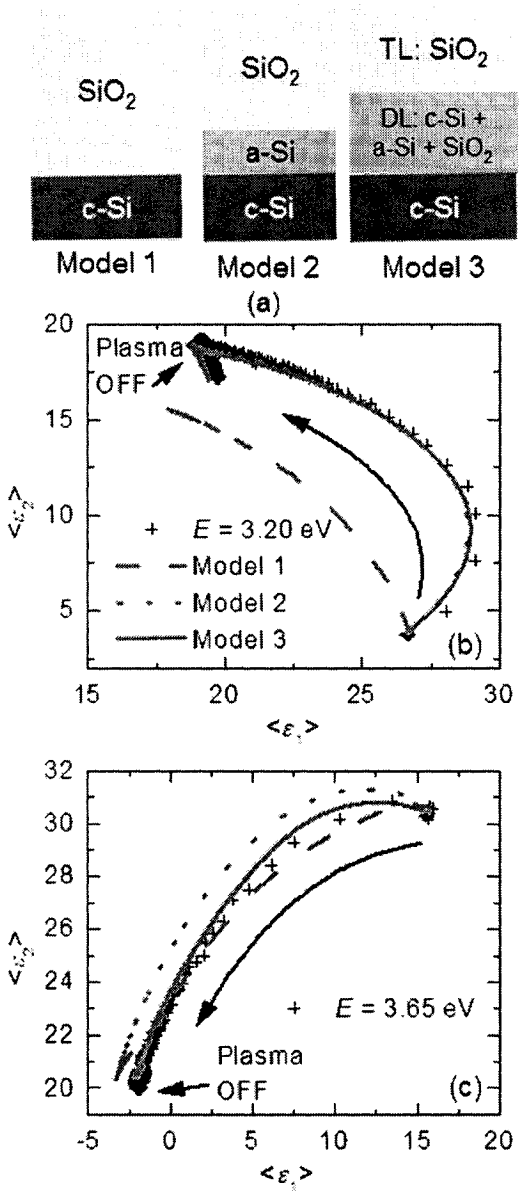

Figure 5.3. *Ellipsometric analysis of plasma-oxidation of c-Si(001) at V_B = -600 V: (a) single- and double-layer models 1, 2 and 3 used to calculate ellipsometric trajectories at (b) E_1 = 3.20 eV and (c) E_2 = 3.65 eV. Measured trajectories are plotted as well. T_s was fitted in models 2 and 3.*

describe the E_1 trajectory. In contrast, models 2 and 3 – significantly more flexible owing to the presence of a DL – follow the trajectory more closely, suggesting that initial modifications are dominated by DL formation. Model 3 has the ability to vary the

composition of the DL, which enables to fit the E_2 trajectory better. This capability permits model 3 to fit the SE data almost perfectly over the entire measurement spectrum (see reference [195]). Model 3 has undergone additional testing (by varying the starting solutions of the model) to verify the uniqueness of the fit (see previous work [195]). E_1 thus allows to discriminate between the single layer and two-layer models, and also has the characteristic of being sensitive to T_s [204], while E_2 is known to be essentially insensitive to T_s in the case of pure c-Si.

In the description of the target modifications, the ellipsometric model should account for substrate heating and cooling effects during plasma exposure. Both E_1 and E_2 trajectories show evidence of cooling after plasma extinction, as the $<\varepsilon_1>$ vs. $<\varepsilon_2>$ trajectory returns towards pre-exposure values. As indicated above, we allow temperature-dependent optical materials properties in models 2 and 3 to account for variations in T_s during the plasma treatment process under investigation. It is essential, however, to ensure that fitted values are physically meaningful and to discriminate between these two models. T_s values fitted using model 2 appear abnormally high (in excess of 200°C) and do not return to room temperature at the end of the cooling period, suggesting that the fitting process might lead to erroneous values for other parameters as well. In contrast, model 3 shows that T_s increases to ~130°C over a period of ~200 s at V_B = -600 V and remains stable for the remainder of plasma exposure; the fit also correctly reproduces sample cooling at the end of the surface treatment.

The behavior of the fitted values for the layer thicknesses and composition during the cooling cycle following plasma extinction provides clear indications of the quality of the modeling procedure (Fig. 5.4). Indeed, one should expect the surface layers to remain unchanged after the end of the treatment. Any departure should be analyzed carefully against the assumptions of the model. It is clear that totally ignoring sample heating effects results in physically unacceptable behavior as the total thickness in the two-layer model

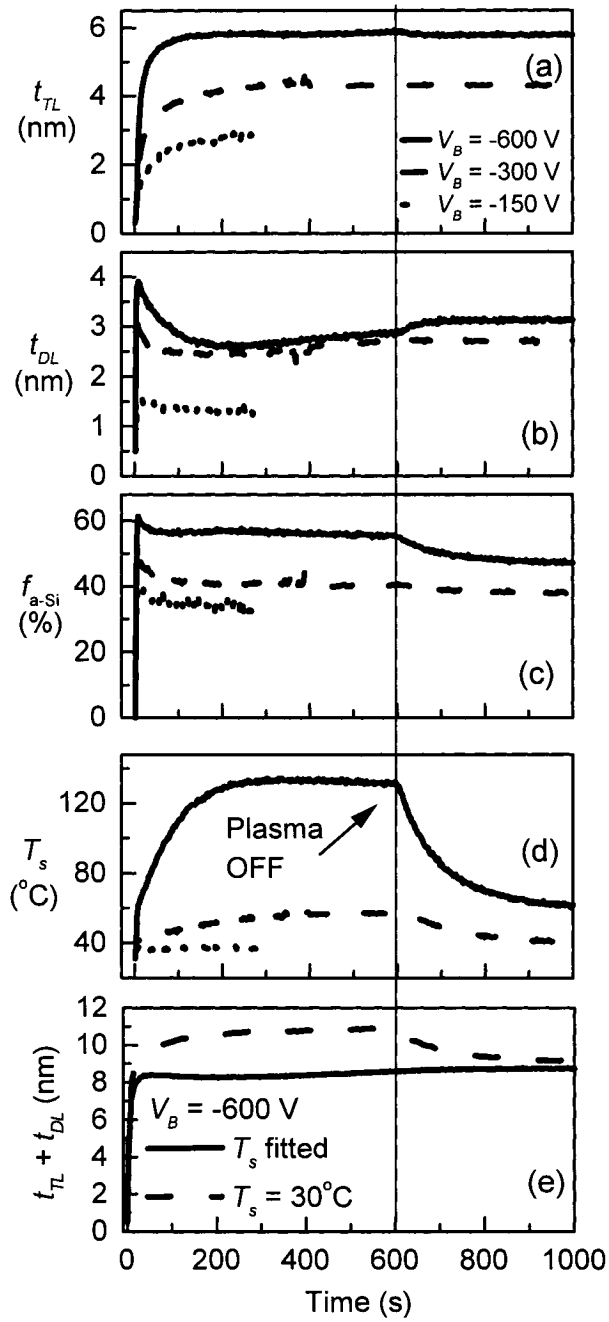

Figure 5.4. *Evolution of the model 3 parameters after fitting with RTSE data at V_B = -150, -300 and -600 V: (a) top layer (TL) oxide thickness, t_{TL}, (b) damage layer (DL) thickness, t_{DL}, (c) a-Si fraction, $f_{a\text{-}Si}$, (d) substrate temperature, T_s, and (e) total thickness (t_{TL} + t_{DL}).*

decreases during cooling whereas the T_s-dependent fit yields more reasonable results (Fig. 5.4e).

Detailed results obtained using the T_s-dependent model 3 are presented in Figs. 5.4a-d for three substrate biases. Again, a careful scrutiny of the stability of the individual fitted values as the plasma is turned off allows to gauge the effect of T_S on the fitting process. Following plasma extinction (t > 600 s) at V_B = -600 V, we note small and unexpected variations in t_{DL} (+0.2 nm) and $f_{a\text{-}Si}$ (-7%). No such variations are detectable at V_B = -300 V or below (not shown), where changes in T_s are small compared to those for higher $|V_B|$ experiments [T_s increases by ~100°C (up to ~130°C) at -600 V, by ~30°C (up to ~60°C) at -300 V, and remains unchanged at -150 V or below]. Such small variations are not surprising since we have chosen to neglect changes in the optical properties of a-Si because we are considering here a mixture rather than an homogeneous a-Si film (see section 5.3 for the detailed justification). In all cases, however, the compositional changes in fitted values following substrate cooling are rather small compared to absolute figures. Despite its inherent limitations, we are confident that model 3 can be reliably used to extract accurate results from RTSE measurements of the plasma treatment. In addition, it is possible to account for the changes described above in post-deposition analyses whenever required.

5.5.1.2 Dynamical Evolution of Plasma-Induced Modifications

The time evolutions of t_{TL}, t_{DL} and $f_{a\text{-}Si}$ reveal the dynamics of plasma-induced modifications in c-Si at the RF-powered electrode. t_{TL} initially increases until saturation at a V_B-dependent value on a time scale of ~100 s (Fig. 5.4a). In contrast, the DL is formed almost immediately upon plasma ignition, growing very rapidly to its maximum thickness, then shrinking slightly to a V_B-dependent steady-state thickness (Fig. 5.4b). $f_{a\text{-}Si}$ in the DL follows suite with t_{DL}, decreasing toward a steady-state value very shortly after peaking immediately after plasma ignition (Fig. 5.4c). The opposite growth behaviors of the TL and DL during the initial ~200 s (after the spike) suggest that the TL is growing into the DL by gradually oxidizing Si just below the TL. We will further discuss TL and DL growth dynamics in sections 5.5.1.5 and 5.5.2.2, but first, we investigate damage and oxide

formation in c-Si as a result of ion-surface interactions during plasma pre-treatment.

5.5.1.3 Damage Formation and Amorphization Dynamics

Ion-surface interactions in the case of hyperthermal ions are dominated by nuclear collisions. These lead to atomic relocations, including unstable IV pair formation, which, when given the opportunity to accumulate, tend to form thermodynamically stable nanoclusters of amorphous material in a crystalline matrix, and eventually lead to complete amorphization. The loss of long range crystalline order that results from damage and amorphization smoothes out the characteristic peaks in the dielectric function (see Fig. 5.2b). Consequently, it is possible to extract information about the depth, the extent, and the rate of damage formation from quantitative RTSE analysis, as we have done in Fig. 5.4. In this section, we monitor damage evolution over time and ion fluence, and how damage formation depends on V_B.

Considering that the damage study is performed in the presence of oxygen ions, the target will inevitably oxidize, thereby decreasing the apparent a-Si signal from damage clusters. We accommodate this factor by defining *damage* as the process leading to a-Si formation, as detected by SE, and we define the damage fraction (DF) with respect to total modifications according to the following expression:

$$\mathrm{DF}\,(\%) = \frac{t_{DL}}{\Delta t_{TL} + t_{DL}} f_{\text{a-Si}}, \tag{5.6}$$

where $\Delta t_{TL} = t_{TL} - t_{TL}(0\ \text{s})$ is the change in TL thickness with reference to the residual native oxide at $t = 0$ s. The DF allows to assess the importance of damage formation in relation with other modifications (i.e. oxidation) during the plasma treatment process. According to eq. (6), oxide formation in the target [e.g. increase of t_{TL} and/or f_{SiO2} ($f_{\text{a-Si}}$ decreases if f_{SiO2} increases, because $f_{\text{SiO2}} + f_{\text{a-Si}} + f_{\text{c-Si}} = 100\%$)] effectively reduces the calculated DF.

We have presented the DF [eq. (6)] in Fig. 5.5a as a function of O fluence and V_B. The DF, plotted on a semi-logarithmic scale for V_B between -60 and -600 V, indicates that damage formation is V_B-dependent at all times/fluences. Some damage is observed at very low fluence (<10^{15} O cm^{-2}, equivalent to ~0.1 s and 2 s in our plasma conditions at V_B = -600 V and -60 V, respectively), and is most significant between 10^{15} and 10^{16} O cm^{-2} (e.g. DF > 50% at V_B = -600 V). The DF decreases when $\Phi_O > 1\times10^{15}$ and > 5×10^{15} O cm^{-2}, at V_B = -60 and -600 V, respectively, and approaches steady state when $\Phi_O > 10^{17}$ O cm^{-2}. The steady-state is characterized by permanent damage at all V_B, with the exception of V_B = -60 V where DF remains close to zero.

The shift of the DF peak (coinciding with the onset of TL growth into the DL) towards higher fluence with increasing V_B, can be explained by the fact that the ion penetration depth increases with V_B (due to the greater range of high E_i ions), requiring a greater O supply to oxidize.

We have plotted the evolution of DF at 3×10^{15} O cm^{-2} vs. V_B in Fig. 5.5b (3×10^{15} O cm^{-2} is the average fluence of DF peak position for all V_B data). The DF value increases with V_B in a sub-linear fashion: DF $\propto |V_B|^{1/2}$. Knowing that oxygen ions are initially implanted into room temperature c-Si (not SiO_2), the V_B-dependence of damage formation at the very early stages of the pre-treatment can be explained in terms of two simple arguments:

(1) The number of IV pairs increases approximately linearly with E_i (and V_B) according to the Kinchin-Pease (KP) approximation [175]:

$$N_{FP}(E_i) \approx \begin{cases} 0 & \text{if } E_i < E_D \\ \dfrac{E_i}{2E_D} & \end{cases}, \qquad (5.7)$$

where E_D is the bulk displacement threshold;

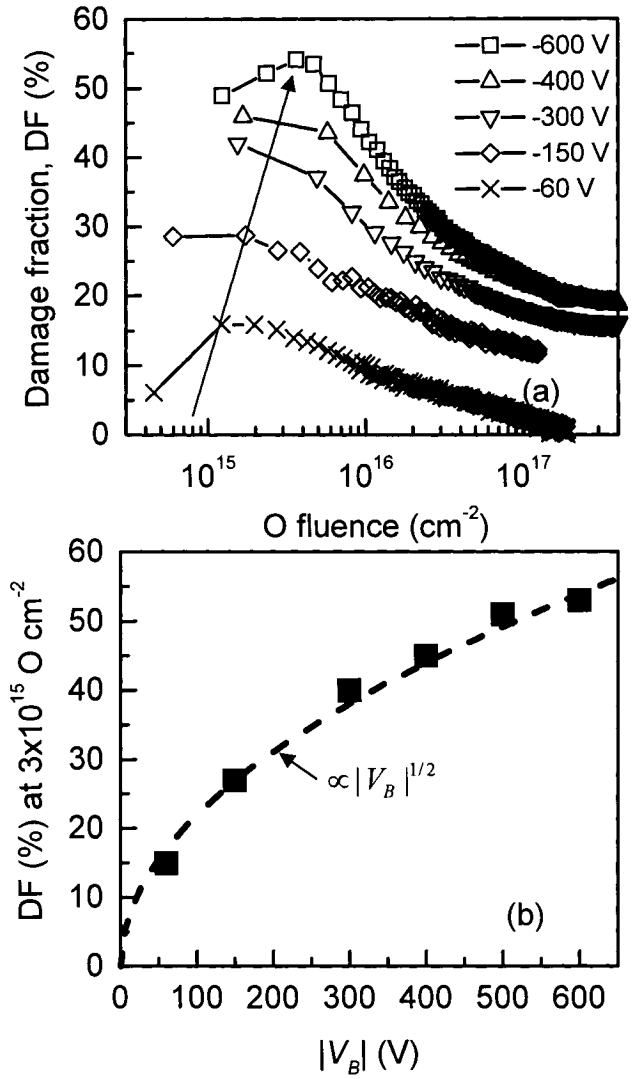

Figure 5.5. (a) *Damage fraction (DF) calculated from RTSE data using eq. (6) as a function of O fluence. (b) DF at 3×10^{15} O cm^{-2} plotted as a function of $|V_B|$.*

(2) the depth – and hence the volume – in which IV pairs are formed increases with $\sim E_i^{1/2}$ (see section 5.6.1 and Fig. 5.13b). Consequently, the DF at low fluence is expected to rise proportionally to $\sim|V_B|^{1/2}$, as confirmed in Fig. 5.5b.

5.5.1.4 Oxidation Dynamics

The dynamics of oxidation closely follow the damage formation described above. Indeed, damage results from IV-pair accumulation from O subplantation, and IV-pairs in c-Si can transform into SiO_2 in the presence of oxygen atoms. Several different oxygen-based species (besides ions) can potentially supply the c-Si target with oxygen in a low-pressure O_2 plasma environment. Wild and Koidl [37] have shown that some O_2 neutrals may acquire kinetic energy in the RF-sheath due to charge transfer collisions. In addition, highly active oxygen radicals, such as O^1D, are abundant in the gas phase and can penetrate up to 2-3 nm below the oxide surface [172]. So, while oxidation is expected to be supply-limited, it is *a priori* unclear if the oxygen is supplied exclusively by subplantation.

To determine if subplantation is the primary mechanism of O supply, we have calculated the oxidation efficiency (OE) from the RTSE data presented in Fig. 5.4. The OE is a measure of the fraction of oxygen atoms that are incorporated inside the target per unit oxygen ion fluence; it is calculated directly from changes in TL thickness and f_{SiO2} in the DL, assuming stoichiometric SiO_2.

OE plots in Fig. 5.6 show that oxygen incorporation is highly efficient at low fluence, where the target is c-Si only. The fact that OE > 1 suggests that some radicals and neutrals (not accounted for in the ion bombardment fluence) are likely participating in the early stages of oxidation. Since they can only supply the top 2 to 3 nm of the target, their contribution to new oxide formation at high depth is expected to subside as soon as the near-surface region gets saturated with oxygen (at intermediate fluence).

The OE declines with increasing fluence, as excess subplanted O is likely reemitted by the oxygen-saturated near-surface regions as suggested by observations made in ion beam

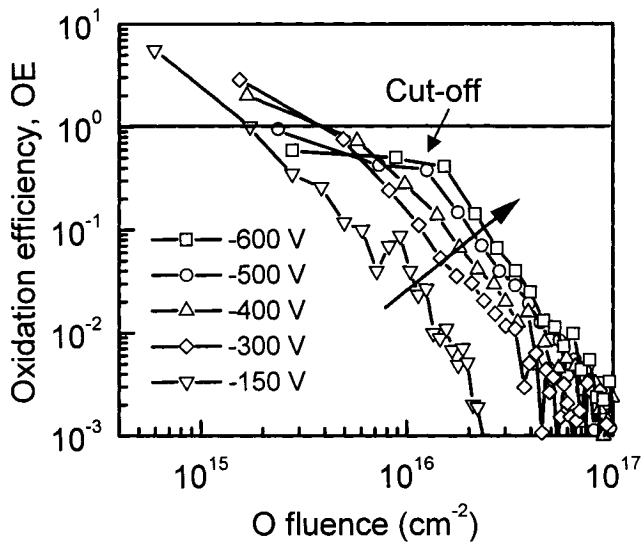

Figure 5.6. *Oxidation efficiency, i.e. fraction of O incorporated into the target and leading to SiO_2 formation (detected by in situ RTSE), vs. incident O fluence.*

oxidation studies [101]. O transport by subplantation also decays rapidly with depth, leading to a sharp decline of the OE above – what we will call – the cut-off fluence (see Fig. 5.6). This cut-off fluence is observed at intermediate fluence in mid- to high-$|V_B|$ treatments; it coincides with TL growth (see Fig. 5.5a), and is likely linked to the fact that the overwhelming majority of ions. This means that low-E_i ions (see Fig. 5.1b) cannot penetrate beyond a few nanometers of near-surface SiO_2 (formed at intermediate fluence) and they are hence reemitted in the vacuum chamber as they cannot be retained by the saturated target.

5.5.1.5 Surface Motion: Swelling and RF-Sputtering

The depth-dependent transport of oxygen and its accumulation can be affected during the plasma treatment by volume swelling (due to O incorporation) and surface recession (from sputtering). Surface swelling reduces the reach of ions in the bulk, while surface recession facilitates oxygen transport to greater depth in the bulk; these competitive processes are thus expected to alter the dynamics of IB-induced modifications until a steady-state regime is attained.

SiO_2 sputtering continuously removes both oxygen and silicon from the surface, however the sputtering rate of SiO_2 (R_S) is mostly dictated by the Si sputtering yield (Y_{Si}), since oxygen is replenished by low-energy subplantation. R_S was calculated using the SRIM program, assuming surface binding energies (E_s) taken as E_s = 2.0 eV and 4.7 eV, for O and Si, respectively [62, 72, 75]. Fig. 5.7 presents R_{Si} plots for V_B ranging between -60 and -600 V as calculated by the IEDF method and using two single-energy approximations, namely E_m and E_{max}. The sputtering rate varies by up to two orders of magnitude over the entire V_B range, owing to the increases of both Y_{Si} (not shown) and ϕ_i (section 5.4) with V_B. E_m appears to approximate the sputtering rate calculated by the IEDF source relatively well for $|V_B| > 100$ V, while E_{max} clearly overestimates it.

Swelling was calculated based on t_{TL}, t_{DL}, and f_{SiO2} data, and assuming a volume ratio of SiO_2 to Si of ~2.2. The calculated swelling and sputtering rates are used to present the RTSE analysis results (t_{TL} and t_{DL}) relative to the absolute surface position. The results are plotted on the left side of Fig. 5.8 for V_B = -150, -300, and -600 V (shown from top to bottom) in a format that focuses on the early stages of the formation of DL and TL during the plasma treatment.

The dynamical evolution of t_{DL} and DL composition ($f_{a\text{-}Si}$, $f_{c\text{-}Si}$ and f_{SiO2} are shown in the central column of Fig. 5.8) reveal that the DL composition and thickness evolve rapidly toward stabilization after a relatively low fluence of ~10^{15} –10^{16} O cm^{-2}. These results are in excellent agreement with previous reports [81] of ion-beam damage threshold (~5×10^{14} cm^{-2}) in a similar energy range (10^2 to 10^3 eV Ar^+).

Stabilization implies that the rate of damage accumulation declines considerably between ~10^{15} and 10^{16} O cm^{-2}. This coincides with the initial TL growth and swelling. Swelling affects ion implantation, as illustrated in Fig. 5.8, where special markers (crosses) identify

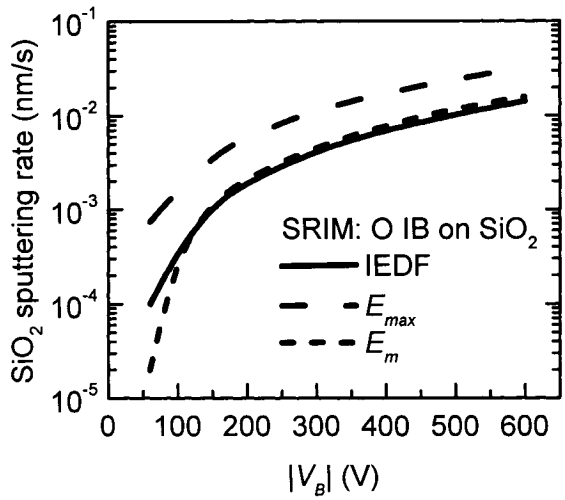

Figure 5.7. *Calculated sputtering rate (R_s) using SRIM for IEDF, and single energy E_m and E_{max} ion sources as a function of $|V_B|$.*

the evolution of the maximum ion penetration depth (calculated using SRIM with E_{max} O^+ ions; see section 5.6.1 for details) with respect to the surface position. The ion penetration front moves away from the bulk when the target swells up at intermediate fluence, and then moves into the bulk when oxide growth gradually subsides and recession sets in at high fluence (between 10^{16} to 10^{17} O cm^{-2}). This behavior underlines the self-limiting growth behavior of the oxide and damage layers, and is confirmed by the convergence of $t_{TL} + t_{DL}$ towards the maximum ion penetration depth.

5.5.2 Ion-Surface Interactions at the RF-Powered Electrode: Monte-Carlo TRIDYN Simulations

In order to analyze the contributions of various ion-beam processes to the surface modifications observed experimentally (see section 5.5.1), we have undertaken detailed TRIDYN simulations of the effects of IB at the RF-biased electrode in a RF-discharge. It is well established that a small number of higher-energy ions within a broadband distribution can drastically alter the dynamics of substrate modifications and film growth, and that using the average energy as a single parameter in simulations is usually not appropriate

[205]. Consequently, we have developed the procedure described in section 5.4 to account for the energy distribution of the plasma source in TRIDYN simulations. To highlight the effect of the low- and high-energy components of the distribution on surface modifications, we compare our broad-beam numerical results with monoenergetic simulations at the average E_m and maximum E_{max} energies when appropriate. TRIDYN simulations are then combined with analytical modeling of c-Si amorphization to investigate the transformation of c-Si into damaged Si and to study the DL formation dynamics.

5.5.2.1 Ballistic Transport of Ions and Atoms by a Broadband Ion Source

Our first goal is to evaluate the depth-dependent transport and accumulation of O in the Si(001) substrate being amorphized and oxidized by a broadband ion source. To illustrate the effect of the IEDF, and specifically the role of high-E_i ions, on the depth-dependent transport of O, we have plotted TRIM-calculated ion distributions in Fig. 5.9a for (1) an E_m ion source, an E_{max} ion source, (3) an IEDF ion source (full IEDF), and (4) an IEDF source missing the contribution of high-E_i O^+ ions (low IEDF), all calculated at V_B = -600 V. We observe a net increase of the ion penetration depth by ~3 nm between (2) and (3) at the tail-end of the ion distribution (10^{-5} a. u.), which is attributed to the greater penetration depth of energetic O^+ ions in the former case. The difference in O penetration depth between (2) and (3) also coincides perfectly with the width of the DL (see markers in left column of Fig. 5.8), confirming that higher-E_i ions are in fact responsible for oxygen and IV pair accumulation leading to DL formation.

As a representative example of O accumulation, we present in Fig. 5.9b the TRIDYN-calculated [O] depth profile in a Si target (coated with a 0.8 nm native oxide) exposed to 5×10^{15} O cm^{-2}. Simulations are performed at V_B = -600 V using the full IEDF method as well as two monoenergetic approximations of the plasma source (E_m = 175 eV and E_{max} = 690 eV), in order to evaluate the maximum penetration depth of ions. Examination of the simulation results for the two monoenergetic simulations clearly reveal, as expected,

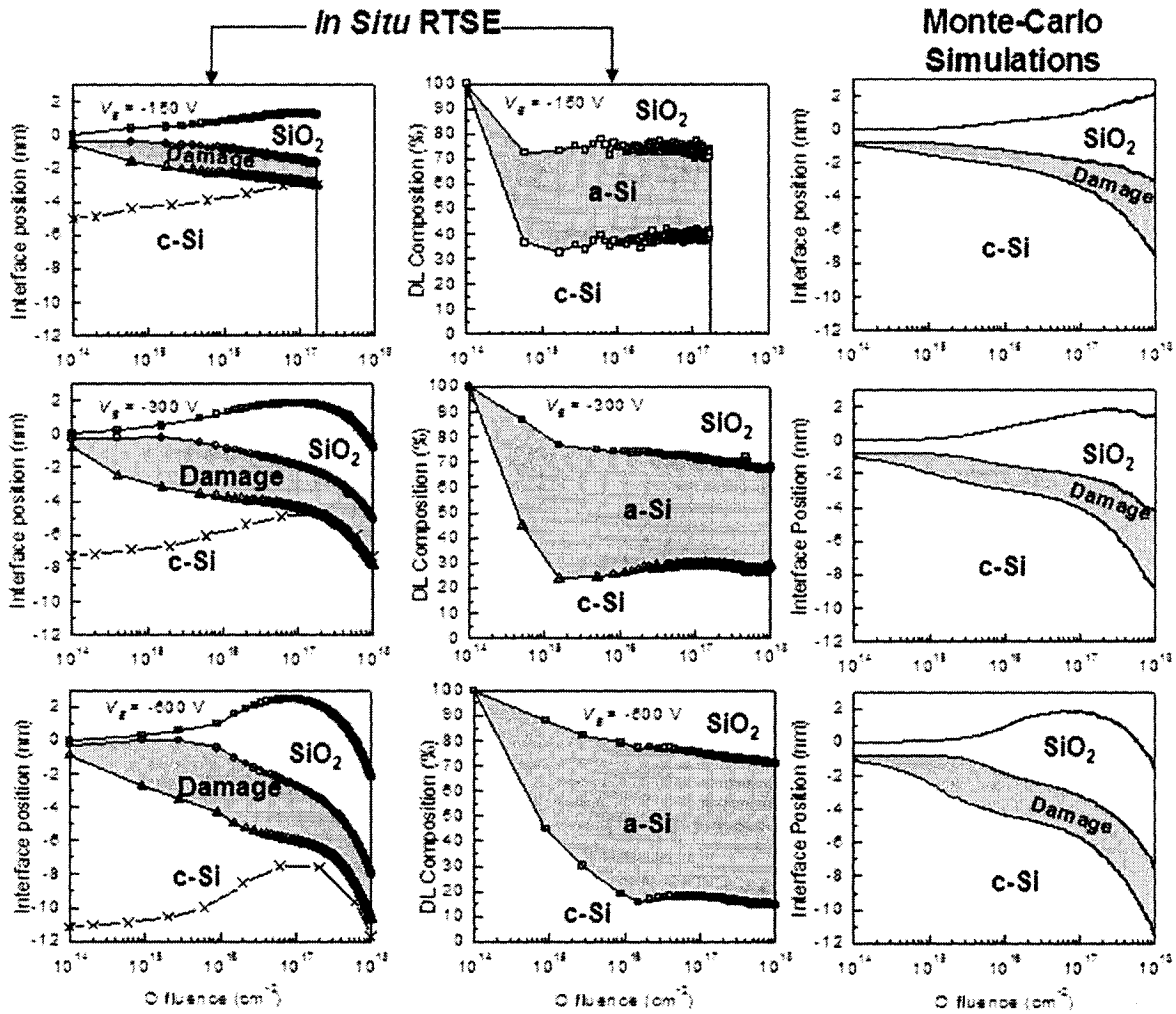

Figure 5.8. *Dynamics of c-Si (001) modifications, including oxide and damage layer formation, relative to the surface position in the presence of swelling and surface sputtering for V_B = -150 V (top row), V_B = -300 V (middle row), and V_B = -600 V (bottom row). In situ RTSE data are presented in the left and center panels; Monte-Carlo simulation results (see section 5.5.2.3) are plotted in the right panel for comparison.*

that the [O] profile extends to a much greater depth and causes more atomic relocations in the case corresponding to ions of higher energy (Fig. 5.9c). In comparison, the IEDF source (including energetic O^+) subplants oxygen at depths comparable to those obtained for the monoenergetic simulation with E_{max}. The effects of the IEDF source on the atomic displacement profile (Fig. 5.9c), however, are felt at an intermediate depth owing to the presence of a small fraction of high-energy ions in the distribution. We also note that the

IEDF causes very few atomic displacements in the near-surface region. Since the low-E_i ions of the IEDF continually replenish the near-surface region with oxygen, we expect the near-surface oxide to remain stoichiometric during plasma exposure. Simulations performed at lower $|V_B|$ values gave qualitatively similar results.

While the E_{max} ion source overestimates sub-surface modifications at low fluence, we argue that the maximum penetration depth of E_{max} ions should dictate the maximum depth of plasma-induced modifications ($t_{TL} + t_{DL}$) at steady-state for all V_B conditions. To verify this affirmation, we have plotted in Fig. 5.10a the experimental oxide thickness (t_{TL}) and maximum modifications depth ($t_{TL} + t_{DL}$) at high fluence (taken after cooling), along with the calculated maximum penetration depth of E_{max} ions in SiO_2 (not in Si, because the target is oxidized at high fluence). Calculations were made by the transport equation approach developed by Ziegler, Biersack and Littmark (ZBL) [62] (available in the SRIM simulation package [72]), which is orders of magnitude faster than Monte-Carlo TRIM calculations, and can accurately calculate the range (R_P) and straggle (ΔR_p) – defined as the half-width at half maximum – of the Gaussian-like ion distribution over a wide range of E_i (results are within 5% of TRIM results [61] for single energy beams). The calculated oxide thickness and maximum modification depth were approximated (see Fig. 5.10a) according as $t_{TL} \sim R_p + 2\Delta R_p$ and $t_{TL} + t_{DL} \sim R_p + 3\Delta R_p$ (note: R_p and ΔR_p are calculated at E_{max} for all V_B) by a method similar to what has been previously proposed by Williams et al. [74] to estimate oxide thickness in the case of ion-beam oxidation of c-Si by 3 to 40 keV O^+ beams at high fluence (10^{18} cm^{-2}).

The relative importance of the effects of low- and high-E_i components of a broad energy ion source can be estimated by considering the scaling of the ion penetration depth and IV pair formation in a target. We demonstrate in Fig. 5.10b that t_{TL} and $t_{TL} + t_{DL}$ scale as $\sim E_{max}^{1/2}$ (Fig. 5.10b), which is theoretically predicted in the case of sub-keV ion implantation in c-Si, because the stopping of hyperthermal ions in solids is dominated by elastic nuclear collisions [75], whereas IV pair production scales linearly with E_i [eq. (5.7)].

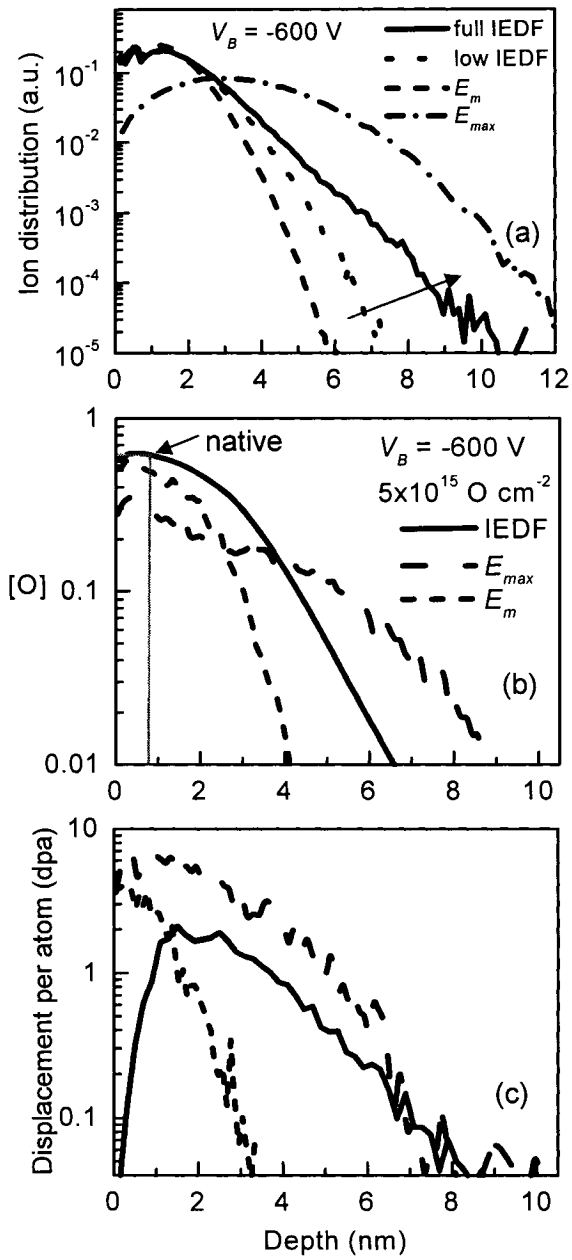

Figure 5.9. *(a) Simulated depth profiles of oxygen transport obtained by TRIM for the complete IEDF, for the low-E_i components of the IEDF, and for an E_m ion source. Depth profiles of (b) oxygen concentration [O] and (c) dpa at V_B = -600 V using TRIDYN for single energy (E_m and E_{max}) and IEDF sources.*

The two scaling laws were combined with the original IEDF (Fig. 1b) by multiplying it with $E_i^{3/2}$ and renormalizing it to unity (see Fig. 5.10c). The curve for IEDF × $E_i^{3/2}$ shows

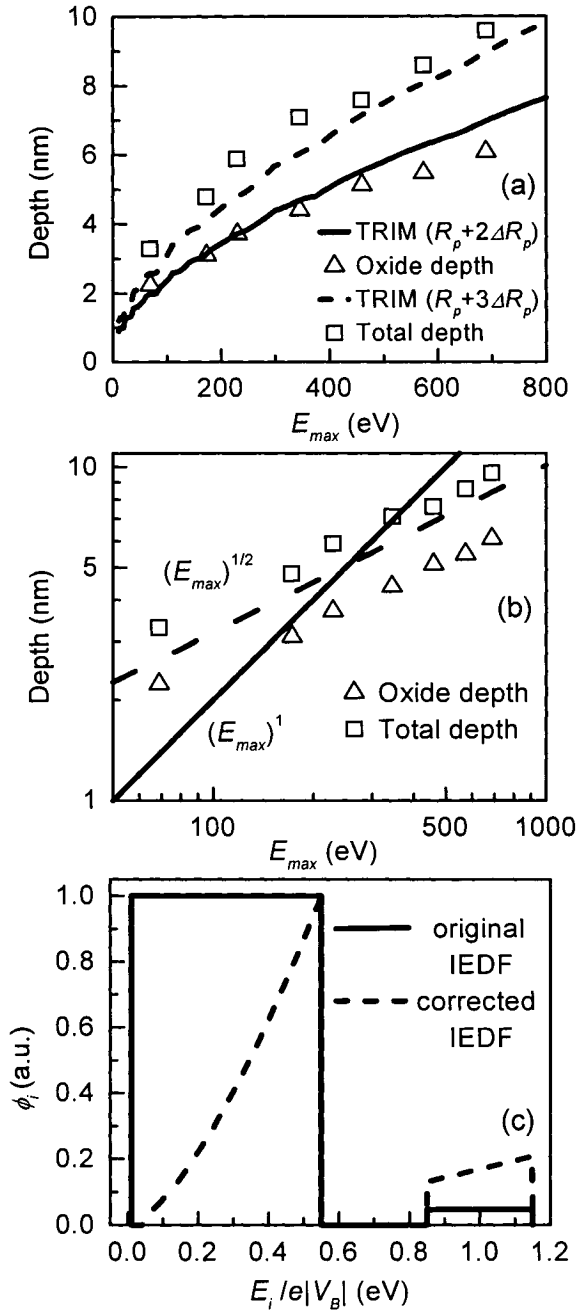

Figure 5.10. *Oxide and damage depth at saturation determined from in situ RTSE as a function of maximum ion energy E_{max} for -600 < V_B < -60 V plotted (a) on linear and (b) log-log scales; (c) IEDF showing the relative impact of ions in terms of penetration and defect formation in Si.*

that the relative impact of energetic O^+ ions – representing no more than 2.5% of all ions (after dissociation of O_2^+) – is as high as ~20%, while low-E_i ions account for up ~80% of

the overall impact of the IEDF, while they represent 97.5% of the overall distribution. Low-E_i ions are responsible for the rapid damage and oxidation of the target's surface early during the plasma treatment, and for continuously replacing oxygen atoms lost by displacement (to the bulk) and by sputtering (see Fig. 5.9a) at steady-state (high fluence), whereas high-E_i ions determine the maximum depth of modifications in the target, and contribute to DL formation.

The accumulation of oxygen resulting in target swelling and the sputtering rate also strongly depend on the energy distribution of the plasma source, hence surface motion dynamics can be expected to vary as well. We have calculated, using TRIDYN, the surface position of the target as a function of ion fluence again for the IEDF plasma source as well as for monoenergetic E_m and E_{max} ion sources (Fig. 5.11). The surface position obtained from experimental results (combining swelling and TRIM-based sputtering rate calculations) is also shown in the same figure for comparison. The data for V_B = -600 V has been selected here, because it exhibits the most significant swelling and sputtering of all conditions investigated. Keeping in mind that E_{max} overestimates the sputtering rate of the broadband ion source, which E_m describes well (Fig. 5.7), we conclude from Fig. 5.11 that E_{max} severely overestimates surface swelling, whereas E_m underestimates swelling. We obtain excellent agreement between the IEDF method and the RTSE results, which reinforces our confidence in the accuracy of our implementation of a broadband ion source in TRYDIN simulations without any fitting parameter. Similarly good agreement is obtained for other V_B conditions, as we will discuss in section 5.5.2.3.

5.5.2.2 Damage and Oxidation Depth-Profiles

Damage production and amorphization have been directly linked to the energy deposited per atom (E_a) by the ion source inside the target, and were modeled analytically as a combination of direct-impact and interface-stimulated amorphization processes [93]. The relationship between E_a and the amorphization fraction (f_a) is expressed as:

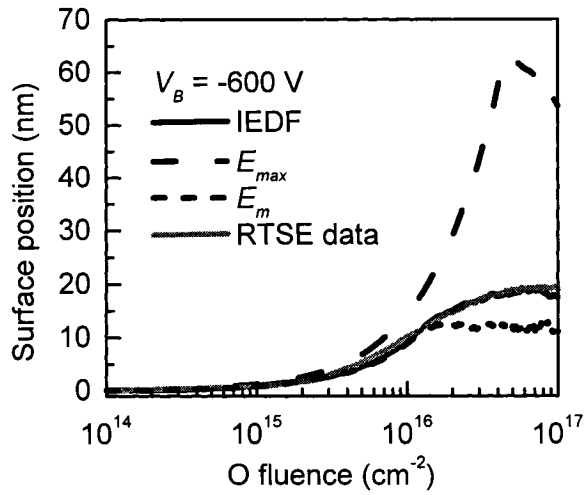

Figure 5.11. *TRIDYN simulation of an O_2 plasma treatment of Si showing the evolution of absolute surface position calculated from single energy (E_m and E_{max}) and IEDF ion sources. The surface position determined from RTSE accounting for swelling and sputtering (TRIM) calculations is also shown for comparison.*

$$f_a = 1 - \frac{\sigma_a + \sigma_s}{\sigma_a + \sigma_s e^{(\sigma_a + \sigma_s)E_a}}. \tag{5.8}$$

Here, σ_a and σ_s are the direct-impact and interface-stimulated amorphization cross-sections, respectively. A comprehensive MD study of ion-beam damage and amorphization of c-Si [65] by 3 eV to 2 keV recoils created by self-implanted Si has confirmed the validity of eq. (7). Values of $\sigma_a = 0.0553$ eV^{-1} and $\sigma_s = 0.447$ eV^{-1} were obtained by fitting the MD data to the analytical model. Being that E_a does not explicitly depend on the characteristics of the external ion source, its use is not restricted to any one type of ion source. Instead, the f_a depth-profile can be calculated from the simulated E_a depth-profiles obtained from TRIM or TRIDYN for any type of ion source, including one with a broadband energy distribution.

A direct relationship can be established between the E_a and – atomic displacements measured by units of – dpa by calculating their depth-profiles per unit fluence in a Si target by the IEDF method for V_B = -60 to -600 V. Simulations show that a single linear relationship links dpa to E_a for all V_B (not shown). Fig. 5.12 plots f_a as a function of E_a and dpa per unit fluence (unit fluence is taken as 10^{15} O cm^{-2}). Si is partially amorphized (f_a ~

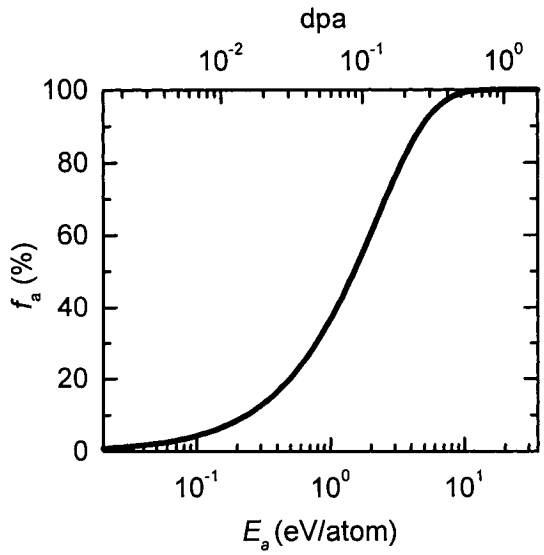

Figure 5.12. *Amorphization fraction vs. deposited energy, E_a, and displacement per atom (dpa) in c-Si determined according to equation (7).*

10 %) at a very low energy threshold (E_a > 0.23 eV/atom, > 0.017 dpa), while significant damage accumulation (f_a ~ 90 %) occurs for E_a ~ 5 eV/atom (0.25 dpa). Full amorphization requires nearly 10 to 11 eV/atom (0.55 to 0.65 dpa), in agreement with previously published experimental results of critical energy dose [196].

Now that we have the ability to calculate the f_a (in addition to [O]) depth-profile in Si, we combine this capability with TRIDYN simulations to obtain the evolution of f_a depth-profiles during plasma treatment. We have plotted the f_{SiO2} (from [O]) and f_a depth-profiles in Fig. 5.13 for four oxygen fluence values, ranging between 5×10^{14} and 5×10^{17} cm^{-2}. f_a depth-profiles reveal damage formation up to ~4-5 nm below the surface at very low fluence (5×10^{14} cm^{-2}), even though very little O is implanted to these depths. Near-surface oxygen accumulation is observed at a slightly higher fluence (5×10^{15} cm^{-2}), while significant oxide formation occurs at intermediate fluence (5×10^{16} cm^{-2}). We also observe the formation of a broad and O-deficient damage region between the oxide and the c-Si substrate, in effect forming a transition region between SiO_2 and c-Si. The width of this region remains virtually unchanged at intermediate to high fluence, where it reaches a steady state value. Similar results are obtained for lower $|V_B|$ simulations.

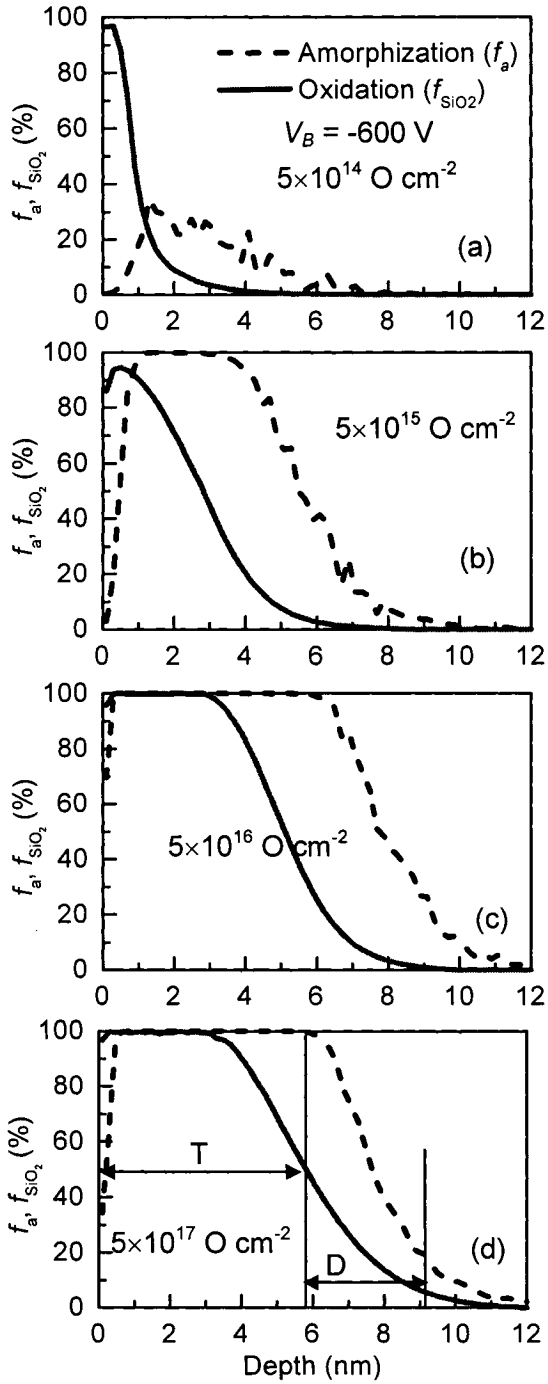

Figure 5.13. *TRIDYN simulation of SiO_2 fraction (solid line) and amorphization (dashed line) of the c-Si target at V_B = -600 V after exposure to O fluences of (a) 5×10^{14}, (b) 5×10^{15}, (c) 5×10^{16} cm^{-2}, and (d) 5×10^{17} cm^{-2}.*

5.5.2.3 Dynamical Evolution of Si Modifications

Comparing the overall dynamics of the modifications of the Si substrate determined experimentally with those obtained from TRIDYN simulations provides insights into the dynamics of the various processes involved in plasma-surface interactions at the RF-powered electrode. There are, however, inherent difficulties in making such comparisons. First, RTSE is unable to determine [O] and f_a gradients on such small depth scales (a few nanometers), and is limited to the two-layer assumption. Second, we do not perform post-cascade treatments of atomic transport in TRIDYN, such as by thermal or ion-enhanced diffusion. Hence simulated [O] depth-profiles tend to slightly underestimate the transport of O – which can be enhanced by thermal spike effects [206] – at high depths. Post-cascade treatments of TRIDYN simulations were previously performed by Todorov [101] and Vancauenbergh [100], but they required to fit the simulation parameters to obtain a good agreement with ion beam oxidation experiments, since diffusion parameters associated to the thermal-spike-enhanced transport of O and Si are not known in c-Si. The simulation results were thus partly trivialized by the inclusion of such a post-cascade treatment. Instead, we have opted here to take the simulated interface positions to agree well with the basic two-layer assumption of RTSE analysis at all V_B.

The dynamical simulation results are presented in the right column of Fig. 5.8 in a format similar to RTSE results (left column). The simulated surface position was taken from Fig. 5.11 (IEDF method) whereas the interfaces correspond to the marker positions illustrated in Fig. 5.13d, i.e. TL/DL (taken at 50% SiO_2) and DL/c-Si (20% a-Si), taken from experimental results. For all V_B values, we observe a good quantitative agreement between TRIDYN and RTSE results, from the initial damage formation to swelling, and to the recession-dominated steady-state regime proving that TRIDYN can be used to predict plasma-induced modifications over time and depth scales pertinent to real-life plasma processing experiments. The agreement at all fluence values also indicates that the broadband ion source at the RF-powered electrode is adequately modeled by the IEDF

method presented in section 5.4, and that plasma-surface interactions are in fact dominated by ion bombardment effects.

5.5.2.4 Surface Motion Dynamics and Sub-Surface Modifications

We showed in section 5.5.1.5 that sputtering leads to significant surface recession during plasma treatment. In the present section we demonstrate that such recession leads to a broadening of the [O] and f_a depth profiles, which in effect results in the formation of an O-deficient DL. To illustrate the effect of surface motion dynamics on the ability of O and IV pairs to accumulate in the target, we perform three nominally identical plasma treatment simulations, where we artificially vary the sputtering rate (low, normal and high values), and we look at its impact on the dynamics of surface position, O incorporation, as well as [O] and f_a depth profiles. Surface sputtering rates were controlled by varying E_S(Si) between 57 eV (low recession rate) to 0.57 eV (high recession rate).

The evolution of the surface position and O surface density as a function of fluence and E_s is shown in Figs. 5.14a and 5.14b. In general, the results show a dramatic effect of the surface recession rate on the ability of the target to incorporate O above 10^{16} O cm^{-2}. At high recession rate (E_s = 0.57 eV), O incorporation reaches a steady-state value very early during the plasma treatment (Fig. 5.14b). The resulting oxide layer is very thin (~3 nm-thick according to Fig. 5.14c) and does not grow any further, even at high fluence (Fig. 5.14d). This is due to the inability of oxygen to renew itself during surface recession at high depth, i.e. where O accumulation rate is low. At the other extreme of surface motion (E_s = 57 eV), surface recession is inhibited, leading to a swelling-dominated oxidation regime. Such a regime is characterized by net oxygen intake by the target (oxide growth) at all fluences, until a self-limiting regime is reached (at higher fluence than in normal conditions) as a result of O saturation throughout the implantation depth.

Oxidation and amorphization depth profiles are shown at intermediate [5×10^{16} cm^{-2}, (Figs.

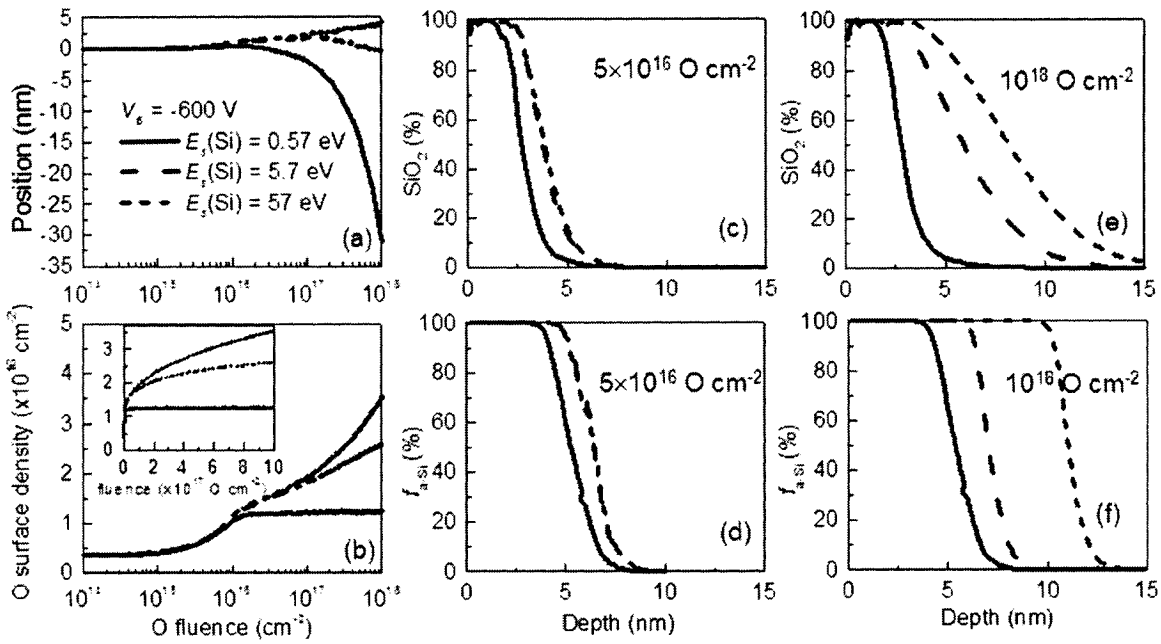

Figure 5.14. *Calculated dynamical evolution of (a) surface position and (b) O surface density in the case of sputter-dominated (E_s(Si) ~ 0.57 eV), realistic (5.7 eV), and implantation-dominated (57 eV) oxidation; SiO_2 and amorphization depth profiles are plotted in (c, d) for low fluence (5×10^{16} cm^{-2}) and (e, f) for high fluence (10^{18} cm^{-2}) for V_B = -600 V.*

5.14c and 5.14e)] and high fluence [10^{18} cm^{-2}, (Figs. 5.14d and 5.14f)], where they also reveal surprisingly strong effects of surface motion dynamics on the sub-surface modifications at high fluence, including [O] and f_a depth profiles, which in turn lead to broadening of both the TL and the DL.

5.6 Discussion

5.6.1 Factors Leading to Damage Layer Formation

The optical monitoring of a c-Si(001) substrate during an oxygen plasma treatment has provided us with considerable insight into the dynamical effects of plasma-surface interactions at the RF-powered electrode. TRIDYN simulations successfully predicted all of the effects observed by RTSE analysis (Fig 8), and suggested that O accumulation at

high depth is likely counterbalanced by surface recession, which inhibits O accumulation. Given that this is difficult to verify experimentally, because both oxygen transport and surface recession are inextricably linked to a single process parameter, V_B, we used TRIDYN simulations to decouple the O transport from the sputtering rate (Fig. 14), and demonstrated beyond a reasonable doubt that while the IEDF controls the depth-dependent O transport, the surface motion dynamics dictate the effective accumulation rate of IV-pairs and oxygen in the target. This led us to conclude that in normal surface motion conditions, the width of the DL is determined (1) by the IEDF, and more specifically by the presence of high-E_i O^+ ions, and (2) by the surface recession rate, which inhibits the accumulation of IV-pairs and oxygen in deep-lying regions of the target, hence leading to formation of an O-deficient damage layer.

Demonstrating the sensitivity of sub-surface modifications to surface motion dynamics has broader implications on the understanding of the mechanisms of ion- and plasma-etching of materials. For instance, the simulations in section 4.2.4 showed that modifying the sputtering rate has significant consequences on sub-surface modifications by O and IV-pair accumulation, although ion implantation and ballistic transport are not affected. Consequently, it is reasonable to assume that surface roughening which leads to a reduction of the sputtering yield can affect the sub-surface modifications (damage and oxide depth-profiles) as a result of enhanced surface recession rate. Similarly, one can envision that using a second beam at glancing angle in ion beam sputtering of a target can enhance the sputtering yield of surface atoms without causing sub-surface implantation by the second beam, but still change the sub-surface modification depth-profiles simply as a result of the changes in surface motion dynamics.

5.6.2 Plasma-Induced Modifications During Deposition at the RF-Powered Electrode

The results of this work, namely the observation of rapid and pronounced sub-surface modifications resulting from ion-surface interactions, are of direct and immediate relevance

for the fabrication of optical coatings by PECVD. Indeed, the plasma conditions selected here are identical to the ones perfected over the years to obtain dense optical films with relatively abrupt interfaces [22, 67]. Our work clearly reveals that interface broadening is impossible to avoid completely during PECVD at the RF-powered electrode and is intrinsically controlled by the ion bombardment conditions. Interface broadening being highly undesirable in most OIF applications, for which abrupt interfaces are essential to achieve the required spectral performance, we have used the methodology developed in this study to investigate and minimize interface broadening by controlling ϕ_i/ϕ_n during PECVD [178].

The interface profile is primarily determined by two key parameters: (1) the penetration depth of ions (determined by E_{max}), which causes ion mixing during film deposition to occur as long as the interface is within the ion range, and (2) the ion to neutral flux rate ratio (ϕ_i/ϕ_n) which essentially determines the growth rate. The nature and density of the bottom layer determines the true ion penetration depth, as the stopping mechanism of hyperthermal ions is dominated by nuclear interactions. In addition, since the growth surface is continually moving upwards during film growth therefore gradually burying the interfacial region, a high deposition rate can effectively limit the overall broadening profile. We estimate, based on the dynamics of oxide formation shown in Fig. 8 , that significant compositional changes can be likely minimized if the deposition rate is kept above ~1 nm/s.

Our results also indicate that the incorporation of oxygen by subplantation is quite significant, and it may contribute to improving the quality of transparent oxide coatings by enabling more O incorporation below the surface to enhance the stoichiometry and transparency of the film, as well as by contributing to thin film densification. High ϕ_i values ensure O incorporation even at high deposition rates, which then makes it possible to improve the turnaround time of PECVD processes, whilst keeping films dense and limiting interface broadening.

In the case of graded-index OIFs with continuously varying interfaces (e.g. composition [22] or density [23]), atomic mixing favors the broadening and smoothening of interfaces, which are highly desirable for such filters. We can argue here that for graded-index filters manufactured by PECVD, continuous atomic mixing below the growth surface ensures that incremental and discrete variations of the plasma chemistry (by variation of the precursors' flow) lead to continuous composition and refractive index gradients with depth and is also responsible for the growth of a single-phase mixture of materials, such as in the case of TiO_2/SiO_2 graded-index layers [22]. Other benefits have also been associated to graded index OIFs and the PECVD process, such as enhanced optical performance, chemical stability, as well as mechanical, and fracture properties superior to multilayer filters [207, 208].

5.7 Conclusion

This work is, to our knowledge, the first study in its kind to combine the advantages of *in situ* RTSE and Monte-Carlo TRIDYN simulations to investigate the effects of ion-surface interactions at the RF-powered electrode in a PECVD environment. Simulations are key to identifying the impact of the IEDF and surface motion on target damage and oxidation dynamics on time or fluence scales that are of interest to low-pressure plasma processes.

We have shown that sub-surface modifications occur on a very short time scale ranging from a fraction of a second for damage formation, up to few seconds (~1 – 2 s) for oxidation. Major modifications include significant damage accumulation in c-Si detected to a depth of up to ~3.5 to 9.5 nm for V_B = -60 and -600 V, respectively. We have identified oxygen subplantation as responsible for damage accumulation and oxidation, and shown that both of these occur at rates that strongly depend on the supply of O ions. As a result, the modifications are self-limiting in nature, as the transport of O decays with depth.

TRIDYN simulations revealed that damage formation and [O] depth-profile depend sensitively on the IEDF and on surface motion dynamics. The IEDF controls the ballistic O transport and the depth-dependent accumulation rate of O and IV pairs. Surface motion due to swelling and recession affects the ability of O to accumulate; in the presence of swelling, the ion implantation front moves away from the bulk, inhibiting O accumulation at high depth, whereas surface recession at high fluence and $|V_B|$ continuously removes SiO_2 from the surface and moves the ion penetration front into the bulk, thereby preventing oxygen accumulation especially at the tail of the implantation distribution. The combination of IEDF and surface recession are therefore responsible for the formation of a broad, O-deficient damage layer.

Since the experiments were carried out in process conditions identical to optical coatings deposition, the results of this work have clear implications on thin film growth by PECVD and related plasma- and ion-assisted processes. The initial film deposition is expected to be accompanied by significant subplantation into the underlying substrate or thin film, which means that damage accumulation is unavoidable over short time scales (< 1 s). Composition changes require more time (higher fluence) and may not occur in the substrate at high deposition rate. Furthermore, atomic relocations at film/substrate and film/film interfaces can lead to interface broadening, which may be highly undesired for multilayer optical interference filter applications.

5.8 Acknowledgements

The authors thank Dr. Matthias Posselt (Forschungszentrum Rossendorf, Germany) for providing a copy of the TRIDYN simulation code, and Dr. Oleg Zabeida for helpful discussions. This work was supported by the Natural Sciences and Engineering Council of Canada (NSERC). PD acknowledges support from the Canada Research Chair program. AA acknowledges the support from the NSERC Post-Graduate Scholarship program.

Chapter 6. Article 3: Interface Broadening Due to Ion Mixing During Thin Film Growth at the Radiofrequency-Powered Electrode in a Plasma-Enhanced Chemical Vapor Deposition Environment

A. Amassian[1], M. Svec[2], P. Desjardins[1], L. Martinu[1]

[1]Regroupement québécois sur les matériaux de pointe (RQMP) and Department of Engineering Physics, École Polytechnique de Montréal, P. O. Box 6079, Station Centre-ville, Montréal, Québec, H3C 3A7, Canada

[2]Department of Physics, Jan E. Purkyne University, Hoøení 13, 400 96, Ustinad Labem, Czech Republic

Submitted for publication: Journal of Vacuum Science and Technology A (November 2005)

6.1 Abstract

We show that ion bombardment in the range of a few hundreds of eV used in ion- and plasma-assisted deposition processes leads to significant interface broadening due to subplantation and ion mixing during the initial stages of film deposition. First, by studying the modifications of a c-Si(100) target exposed to an O_2 plasma at the radiofrequency-powered electrode using *in situ* real-time spectroscopic ellipsometry (RTSE), we detect important ion-surface interactions, such as implantation, damage, and oxidation to a depth of up to ~10 nm, which we confirm and validate with Monte-Carlo TRIDYN simulations assuming a broadband ion energy source. *In situ* RTSE was then used to monitor TiO_2 deposition on SiO_2 under similar ion bombardment conditions. We experimentally observed the formation of a 2 to 4 nm-thick interfacial layer, depending on deposition rate. TRIDYN simulations show that oxygen subplantation leads to mixing of Ti and Si atoms at the interface during TiO_2 growth. Simulations also show that at low deposition rate, ion mixing is allotted sufficient time to displace the majority of deposited Ti atoms below the growth surface, suggesting that the growth is dominated by sub-surface deposition. Increasing the deposition rate reduces interface broadening, and leads to thin film growth dominated by surface deposition.

6.2 Introduction

Ion bombardment (IB) assisted deposition has been used for the fabrication of high performance optical films and coatings – with dense and amorphous microstructure – that are essential for photonics and telecommunications applications [6]. This includes IB assisted evaporation, dual ion beam sputtering, unbalanced magnetron sputtering and other techniques described in numerous reviews [19, 20]. More recently, plasma enhanced chemical vapor deposition (PECVD) has emerged as a way to fabricate transparent thin films [28] with good optical and mechanical properties. This highly versatile process allows to sensitively control the film microstructure [23] as well as optical [22] and interfacial

properties [24]. In particular, a selective control of the ion-to-atom flux ratio (ϕ_i/ϕ_n) and the mean ion energy (E_m), such as in dual-mode microwave (MW)/radiofrequency (RF) discharges [37, 31, 32], has enabled to finely tune film porosity and density [23, 54].

The IB characteristics mentioned above depend indirectly on external process parameters, such as plasma power, substrate bias (V_B) and working pressure (p). Significant efforts have been devoted to study plasma chemistry and IB characteristics in terms of the external process parameters, in order to bridge the gap between the bulk properties of the plasma, ion-surface interactions and their effects in terms of surface-, interface- and thin film modifications. The effects of IB on thin film formation [209, 210] have been studied using many conventional techniques, including Rutherford backscattering spectroscopy (RBS) and transmission electron microscopy (TEM), which are highly invasive, destructive, and cannot be operated *in situ*. In addition, the low-pressure PECVD environment is incompatible with the use of ion and electron beams during processing, owing to the chemically and electrically active environment. Consequently, it appears that non-destructive and non-invasive *in situ* optical diagnostics can serve to investigate plasma-surface interactions *during-processing* in the PECVD environment.

Recently, we have used *ex situ* variable angle spectroscopic ellipsometry (VASE) [195] to analyze c-Si(001) samples pre-treated for 10 minutes at the RF-powered electrode in an O_2 RF discharge. For typical deposition conditions of oxide films, where V_B can vary anywhere between -60 and -600 V, modifications of c-Si were found to be quite dramatic, including damage layer formation and oxide growth down to a V_B-dependent depth of ~3 to ~10 nm. Monte-Carlo (MC) TRIM simulations [62] showed that the depth-dependent transport of implanted oxygen is responsible for damage formation at high depth, and near-surface oxidation.

These results raise an important question about the possible effects of ion-surface interactions during the early stages of thin film deposition: can ion bombardment in the

PECVD environment lead to significant interface broadening by mixing atoms at substrate/film or film/film interfaces? It was previously demonstrated that thin films prepared by ion-beam assisted deposition [192], sputtering [211], and pulsed cathodic arc deposition [199] processes are subject to interface broadening, which increases with ion energy (E_i) and ion mass, and decreases with deposition rate (r). Interface broadening in optical interference filters (OIFs) is highly undesirable, because it can reduce reflections at individual interfaces in the multilayer stack, and deteriorate the spectral performance of the OIF [6]. The research on interface broadening has also greatly benefited from MC TRIDYN simulations [63, 64, 197, 198, 199], which enable the depth-dependent transport of ions and atoms on time and fluence scales of interest for thin film deposition processes ($\sim 10^{-2} <$ time $< 10^{3}$ s).

In this work, we wish to demonstrate that ion-surface interactions act very rapidly (10^{-1} to 10^{1} s) in a PECVD environment to cause damage and significant composition changes in the c-Si(001) substrate by subplantation (shallow implantation) of hyperthermal ions (10^{0} to 10^{3} eV). Furthermore, we wish to investigate how ion bombardment leads to interface broadening during the deposition of TiO_2 on SiO_2 at the RF-powered electrode. We use *in situ* real-time spectroscopic ellipsometry (RTSE) to monitor both the O_2 plasma pretreatment of c-Si at the RF-powered electrode, and the subsequent TiO_2 deposition on SiO_2. TRIDYN simulations have been modified to account for a broad energy ion source, and will be used to simulate plasma pretreatment and interface broadening during thin film deposition.

6.3 Experimental Methodology

The experiments were performed in a parallel plate RF PECVD system (30 liters volume) [146] with a base pressure $< 10^{-5}$ torr. The c-Si(001) substrates were placed on a 15 cm-diameter RF-powered electrode, while being exposed to IB induced by the self-developed negative bias V_B.

The experiments involve two distinct parts: (1) plasma pre-treatment in an O_2 RF discharge of c-Si placed at the RF-powered electrode, and (2) subsequent PECVD deposition of TiO_2. The pre-treatment was performed at p = 20 mTorr. The substrates were first exposed during 10 minutes at V_B = -600 V (part 1), then V_B was reduced, without extinguishing the plasma, to -450 V in preparation for part 2. This bias condition is required to fabricate dense TiO_2 films of optical grade [212]. After ~1 minute at V_B = -450V, $TiCl_4$ was introduced into the reactor, thereby initiating TiO_2 growth. The partial pressure of $TiCl_4$ was kept low at around 0.1 mTorr in order to obtain $R < 0.1$ nm/s and was used to control the deposition rate.

The pre-treatment (part 1) and the deposition (part 2) were monitored *in situ* by RTSE (M-2000, J. A. Woollam Co.). The ellipsometer, equipped with a rotating compensator, was mounted at an angle of incidence near 65° from the substrate normal. Spectral range for data acquisition and analysis was limited to 477 photon energies (E) from 1.24 to 5.05 eV (245 nm to 1000 nm). RTSE spectra were acquired at 0.4 s intervals, ensuring that multiple spectra are recorded for each monolayer of TiO_2 (assuming 1 ML ~ 0.24 nm).

6.4 Dynamic Monte-Carlo Simulations with Broad-Band Ion Source

The TRIDYN simulations are based on the binary collision approximation (BCA); they take dynamic target modifications into consideration, enabling to simulate high fluence implantations. The TRIDYN code has been designed for single-energy ion sources, and has to be modified in order to simulate broadband ion energy sources such as at the RF-powered electrode [37].

Ignoring the resonance peaks, the IEDF at the RF-powered electrode (Fig. 6.1a) may be approximated by a rectangular function with E_i ranging from a few eV up to $E_{max} \sim 1.15e|V_B|$, while the O^+ distribution is a saddle-like structure, centered at around $E_i \sim e|V_B|$,

with energy ranging from ~$0.85e|V_B|$ to ~$1.15e|V_B|$. Working with the rectangular distribution, we first dissociate all molecular ions (≥95% of all ions [37]) into atomic species (dissociation energy of O_2^+ molecules is much smaller than E_i), then we split the IEDF into 10 discrete energy channels. Simulations are performed at each energy channel using 10 pseudoparticles (or packets) of 10^{11} O cm^{-2} fluence at each channel, for a total O fluence of 10^{12} cm^{-2}. The overall impact of the IEDF on the target is calculated by weighted averaging simulation results (such as elemental depth profiles, surface densities, sputtering yield, surface recession, etc.) from all energy channels. The results of the weighted averaging after a fluence increment of 10^{12} O cm^{-2} are taken as the starting point for the next incremental exposure to 10 pseudoparticles at each of the 10 channels. This procedure is repeated until a total fluence of 10^{18} O cm^{-2}, equivalent to a plasma exposure time of few minutes.

TRIDYN simulations were also performed to evaluate the effects of IB during deposition of up to 15 nm-thick TiO_2 film on SiO_2. TiO_2 plasma deposition was simulated by alternately adding a 0.1 nm-thick slice of TiO_2 film (3.4 g/cm^3 [22] for amorphous TiO_2 by PECVD), and irradiating it with an O fluence determined by the deposition rate. Simulations were performed for R = 0.04 to 4.00 nm/s, corresponding to ϕ_i/ϕ_n ~ 6.00 to 0.06, respectively.

6.5 Results and Discussion

6.5.1 Plasma pre-treatment

6.5.1.1 *In situ* RTSE monitoring of the O_2 plasma pre-treatment (part 1)

We have previously shown that modifications of the c-Si(001) substrate induced by an O_2 plasma pre-treatment at the RF-powered electrode can be optically modeled by a two-layer structure [167, 178, 195]: an SiO_2 overlayer on top of a mixed-phase interfacial layer [IL, modeled as a Bruggeman effective medium approximation (BEMA) mixture of c-Si, a-Si and SiO_2] on the c-Si substrate (see Fig. 6.1c, part 1).

The optical model was fitted to the RTSE spectra and the results are plotted in Fig. 6.2 (part 1). The dynamic evolution of oxide and IL thickness (t_{IL}) is reported relative to the initial surface position, so as to include the effects of oxidation-induced swelling and RF-sputtering. Swelling was calculated from the SiO_2 thickness and the SiO_2 fraction in the IL. The sputtering rate was obtained from TRIM simulations [62] and estimated to be ~0.014 nm/s for V_B = -600 V. The ion fluence scale shown at the top of part 1 in Fig. 6.2 was obtained from ϕ_i measurements performed earlier [32]. We estimate that ϕ_i ~1.0×10^{15} $cm^{-2}s^{-1}$ and ~1.3×10^{15} $cm^{-2}s^{-1}$ for V_B = -450 V and -600 V, respectively. Since more than 95% of ions are O_2^+ molecules, we consider that the total oxygen flux leading to ion bombardment is ~1.95 times larger than ϕ_i. In the remainder of this paper, we report results as a function of O fluence: $1.95\times\phi_i\times$time.

IL formation is observed after an exposure of ~5×10^{14} O cm^{-2}, corresponding to ~0.2 s of plasma exposure. This result is in agreement with the amorphization threshold of bare c-Si, which was found to be ~ 4×10^{14} cm^{-2} for a 500 eV Ar^+ beam [81].

Oxidation is detected a few seconds later, and saturates following 40 s of plasma exposure (~10^{17} O cm^{-2} in Fig. 6.2, part 1). Saturation of the oxide thickness is expected to occur as oxygen implantation decays rapidly with depth. As oxygen accumulation saturates near the surface, swelling slows down and is subsequently replaced by surface recession due to sputtering (see part 1 of Fig. 6.2 for the transition from swelling to recession). Oxide removal leads to a self-limiting steady-state regime, characterized by SiO_2 removal from the surface, and to damage and oxide formation in the IL as it moves into the target.

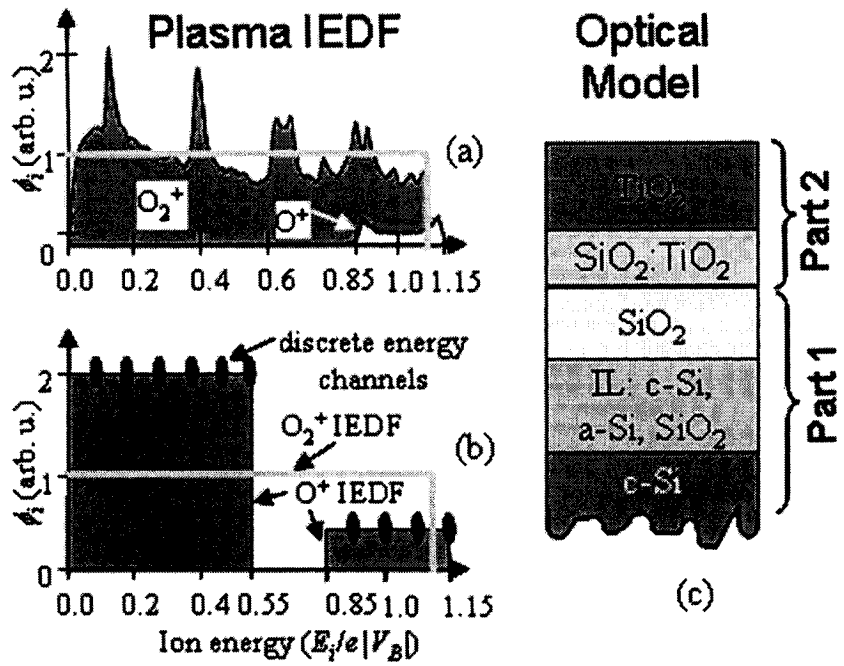

Figure 6.1. *(a) Ion energy distribution function (IEDF) of an O_2 RF discharge at the RF-powered electrode, including distributions of O_2^+ and O^+ ions, and (b) the resulting atomic oxygen energy distribution function used in TRIDYN simulations. (c) Optical model used for the analysis of in situ RTSE data (see text for more details).*

6.5.1.2 Monte-Carlo TRIDYN Simulations of Plasma Pre-Treatment (Part 1)

TRIDYN calculations of the compositional depth profile in the Si target are shown in Fig. 6.3a, following irradiation at two fluences (5×10^{14} and 5×10^{16} O cm^{-2}) by the IEDF method. The target's composition is expressed in terms of the stoichiometry of SiO_x. At low fluence (5×10^{14} cm^{-2}) oxygen is subplanted as deep as ~8 nm, but it is present in very low quantity (not detectable by optical means). At the same time, we observe significant atomic relocations, with values greater than 0.1 displacement per atom (dpa), at a depth of up to 4 nm. This dpa value is high enough to cause damage formation in room temperature Si [98], as evidenced by the early detection (by RTSE, see Fig. 6.2, part 1) of damage in c-Si (IL formation).

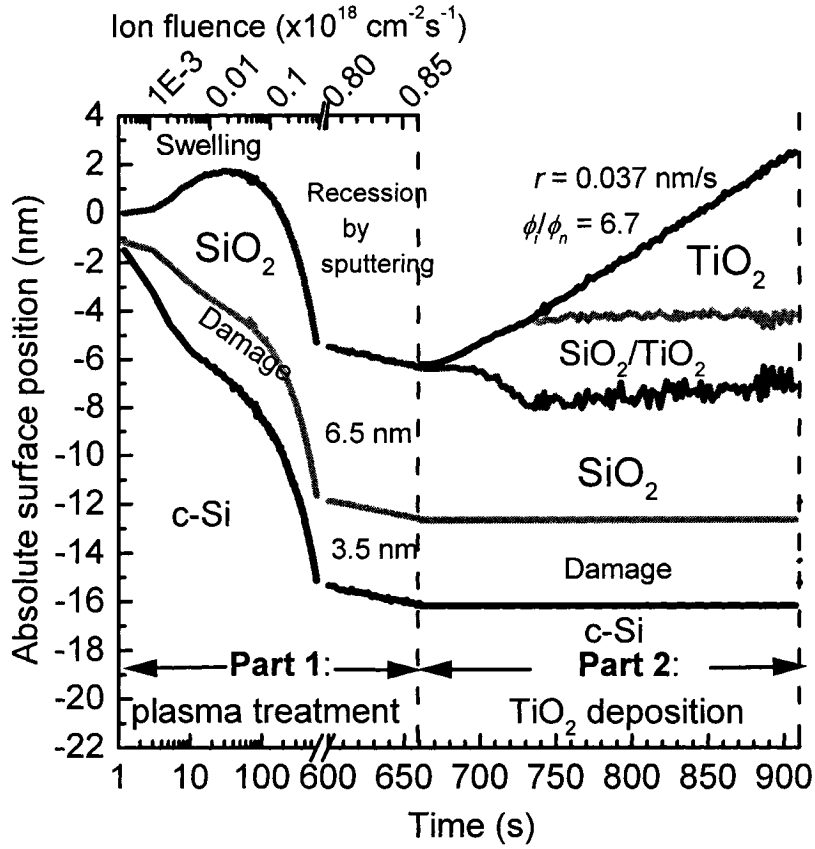

Figure 6.2. *In situ RTSE analysis results of O_2 plasma pre-treatment of c-Si(001) (part 1) and TiO_2 deposition (part 2) at the RF-powered electrode. All surface and interface positions are presented in reference to the initial surface position of the substrate.*

At higher fluence (5×10^{16} cm^{-2}) oxygen accumulation proceeds inward from the surface, and damage accumulation moves deeper. The fact that atomic relocations are observed beyond the reach of O ions is most probably due to the preferential displacement of Si in comparison to O; the bulk displacement energy (E_D) of Si is usually taken as $E_D \sim 12$ eV and $E_D \sim 28$ eV for O in SiO_2 [62]. Consequently, Si recoils have more kinetic energy than O recoils, and they are also more likely to move deeper.

Surface motion was obtained from TRIDYN simulations by using the IEDF method and in the single-energy E_{max} approximation. For comparison, we also calculated surface motion

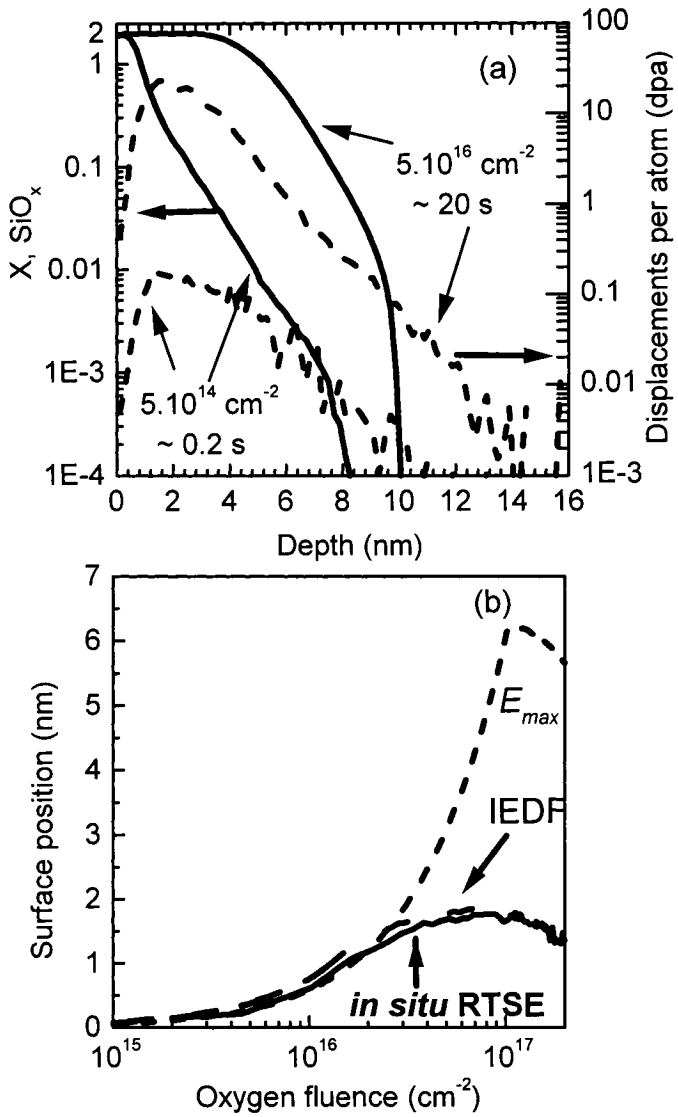

Figure 6.3. *TRIDYN simulation of the O_2 plasma pre-treatment process on a Si target. (a) Oxide composition and displacements per atom (dpa) after exposure to 5×10^{14} and 5×10^{16} O cm^{-2}, and (b) evolution of the absolute surface position of the target obtained by TRIDYN simulations (for a broad ion energy source and E_{max} ions), and calculated from a combination of RTSE and TRIM results.*

by combining the oxide thickness (RTSE results) with the sputtering rate (TRIM simulations). The results are plotted in Fig. 6.3b; they show that TRIDYN simulations with the IEDF method agree very well with surface motion data calculated from RTSE and TRIM results. The large discrepancy between the IEDF method and the E_{max} approximation

originates from the fact that E_{max} ions are much more energetic than E_m (mean ion energy of the IEDF), hence E_{max} ions form a thicker oxide, and sputter SiO_2 at a much higher rate than IEDF ions.

From these simulations, we conclude that the dynamics of surface modifications, such as damage formation, oxidation, and swelling are modeled with sufficient accuracy by BCA-based MC codes, without any fitting parameter.

6.5.2 Plasma Deposition of TiO_2 on SiO_2 at the RF-Powered Electrode (Part 2)

6.5.2.1 *In situ* RTSE During Plasma Deposition

TiO_2 deposition was initiated by introducing $TiCl_4$ in the reactor during O_2 plasma pre-treatment. TiO_2 growth was monitored by *in situ* RTSE; the optical model used to fit the RTSE spectra is shown in Fig. 6.1c (part 2). Parameters fitted in part 1 were fixed during the fitting process for part 2, except for SiO_2 thickness, which was allowed to change in order to account for potential Ti relocation into the SiO_2, leading to the formation of mixed-oxide interface. TiO_2 thickness (t_{TiO2}) and interface thickness ($t_{interface}$) were allowed to vary, while the TiO_2 optical constants were fixed during the fitting procedure. TiO_2 optical constants (n_{550} = 2.4) were obtained from Tauc-Lorentz [167, 170] parameterization of a 200 nm-thick TiO_2 film, which was deposited on glass under identical conditions. The interfacial layer was modeled as a 1:1 BEMA mixture of TiO_2 and SiO_2.

The results of the fitting procedure are presented in part 2 of Fig. 6.2. We initially detect formation of the TiO_2/SiO_2 mixed oxide layer ($660 < t < 730$ s) at the expense of the SiO_2 film, which is seen to shrink slightly. The thickness of the bulk TiO_2 layer starts to increase only after $t \sim 730$ s. TiO_2 deposition rate (r) is found to be $r \sim 0.037$ nm/s, and corresponds to $\phi_i/\phi_n \sim 6.7$ ($\phi_i \sim 1\times10^{15}$ $cm^{-2}s^{-1}$ at V_B = -450 V [32]; $\rho \sim 3.4$ g cm^{-3}).

It is quite notable that $t_{interface}$ remains constant between ~3 to 4 nm throughout the remainder of the deposition run and does not shrink with time, as would be expected for a nucleation layer. It is well known, for instance, in the case of evaporation processes, that TiO_2 growth starts with the formation of a low-*n* nucleation layer, which gradually disappears as coalescence sets in [213]. The results in Fig. 6.2 suggest that the growth proceeds differently. Early on, Ti atoms are pushed into the substrate and mixed with Si, forming a mixed-oxide layer. The film does not show evidence of nucleation, as islands are likely dissolved by IB [214], and the film is densified. As the film surface moves away from the interface, ion mixing decreases, because atomic displacements are mainly located near the surface. The IB continues to mix Ti and O atoms during subsequent growth, ensuring densification of the growing film. In the next section, we present simulations to support this interpretation, and explore ways to control/minimize interface broadening.

6.5.2.2 TRIDYN Simulations of TiO_2 Deposition by PECVD (Part 2)

TRIDYN simulations of ion bombardment at the RF-powered electrode during TiO_2 deposition at V_B = -450 V were performed for r ranging between 0.04 and 4 nm/s. This is equivalent to ϕ_i/ϕ_n in the range from ~6 to ~0.06. We neglect the effects of $TiCl_4$-based molecular ions in the IEDF, because their overall impact is negligible compared to O_2^+ and O^+ ions: (1) a very small fraction of Ti and Cl atoms and molecules are ionized compared to O_2, as suggested by the ratio of partial pressures: p_{TiCl4}/p_{O2} ~ 0.005; (2) Ti and Cl ions have a smaller kinetic energy than O atoms following molecular dissociation, hence their implantation is shallower. For example, assuming a $TiCl_3^+$ ion incident at E_{max} ~500eV, we calculate (using TRIM) the maximum penetration of Ti and Cl ions [E_i(Ti) ~190 eV and E_i(Cl) ~100 eV after dissociation] in TiO_2 and SiO_2 to be less than half the penetration depth of energetic O^+ ions.

TRIDYN calculations of Ti, Si, and O molar fraction depth-profiles are plotted in the inset of Fig. 6.4a for $\phi_i/\phi_n \sim 0.06$ and 6. The oxygen molar fraction is stable at 67% (maximum molar fraction allowed in the simulations), with the remainder (Si and Ti molar fractions) going from 0 to 33%. We can assume that a binary oxide of the form $Ti_xSi_{1-x}O_2$ is created, as previously observed during PECVD fabrication of mixed TiO_2/SiO_2 films [22]. The equivalent refractive index at 550 nm (n_{550}) of this mixed-phase oxide can be expressed according to the following expression:

$$n_{550} = n_{TiO2} \cdot x + n_{SiO2} \cdot (1-x), \qquad (6.1)$$

where $n_{TiO2} = 2.4$ and $n_{SiO2} = 1.45$ at 550 nm. We can use eq. (2) to express the O, Ti and Si molar fraction depth-profiles in terms of a single parameter (n_{550}) which simplifies the graphic representation, and enables a more direct comparison to RTSE results. The presentation of n_{550} depth profiles is also appealing from the perspective of OIF applications, where the interface width is usually expressed in terms of a n depth profile.

The simulated n_{550} depth-profiles of 8 nm-thick TiO_2 films with $\phi_i/\phi_n = 0.06$, 0.6 and 6 are plotted in Fig. 6.4a. We observe the following general trends: (1) n_{550} depth profiles (and molar fraction profiles) resemble an error function distribution (consistent with measured ion mixing profiles [59]); (2) interface broadening increases with ϕ_i/ϕ_n; (3) a slight profile asymmetry is formed as a result of preferential displacement of Si into TiO_2 than Ti into SiO_2 [E_D(Si) ≈ 12 eV and E_D(Ti) ≈ 25 eV].

The significant difference between interface broadening at $\phi_i/\phi_n = 0.06$ and 6 can be explained by the hundred-fold increase of ion-atom collisions per unit of film deposit. More collisions lead to more atomic relocations, and increases mixing of Ti and Si atoms about the interface.

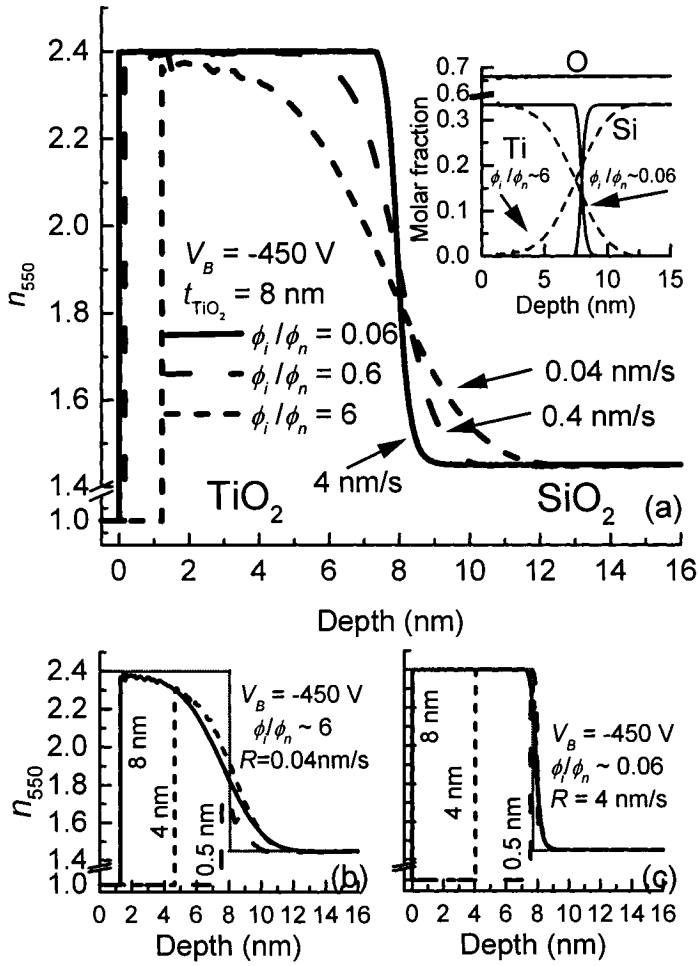

Figure 6.4. *TRIDYN simulation results of interface formation during TiO_2 deposition on SiO_2. (a) Refractive index (n_{550}) depth profiles of 8 nm-thick TiO_2 films (ϕ_i/ϕ_n = 0.06, 0.6 and 6) calculated from Ti, Si and O molar fractions shown in the inset. n_{550} depth profiles of a TiO_2 film growing at (b) ϕ_i/ϕ_n = 6 and (c) ϕ_i/ϕ_n = 0.6, after t_{TiO2} = 0.5, 4 and 8 nm.*

We now take a closer look at the effect of ϕ_i/ϕ_n at different stages of film growth. We have plotted the simulated n_{550} depth-profiles at various stages of TiO_2 growth at ϕ_i/ϕ_n ~ 6 (low r) and 0.06 (high r) in Figs. 6.4b and 6.4c, respectively. They show that the early growth of

TiO_2 (t_{TiO2} < 1 nm) at $\phi_i/\phi_n \sim 6$ is dominated by subplantation, as most Ti atoms end up deposited below the SiO_2 surface, and a large number of Si atoms are mixed into the growing film. Subplantation and ion mixing reduce n of the growing film by Si incorporation; for instance, we see that $n_{550} \sim 1.75$ near the growth surface of a 0.5 nm-thick TiO_2 film deposited at $\phi_i/\phi_n \sim 6$ (low r), corresponding to a TiO_2 fraction of only ~30%. After 4 nm of deposition, we still have $n_{550} < n_{TiO2}$, however n_{550} has increased substantially both near the growth surface and near the interface. Here, the deposition of Ti atoms leads to an increase of n_{550} near the surface, as well as in the bulk of the growing film, owing to sub-surface relocation of Ti atoms from the surface. In contrast, ion mixing is much lower at high r, as suggested by the abrupt n_{550} depth-profile shown in Fig. 6.4c. We therefore conclude that high ϕ_i/ϕ_n (low r) conditions ensure that IB is allotted sufficient time to mix many more Ti and Si atoms at the interface than at low ϕ_i/ϕ_n (high r). This is consistent with RTSE results shown in part 2 of Fig. 6.2, where the initial growth appears to take place mainly below the original SiO_2 surface position, giving birth to a mixed oxide layer which grows during the initial ~3 nm of TiO_2 deposition (Fig. 6.2, part 2).

Ion mixing and the resulting interface broadening are quantified by calculating the interfacial thickness ($t_{interface}$), taken as the distance between the 90% to 10% positions of the Ti molar fraction. We have plotted $t_{interface}$ in Fig. 6.5a as a function of t_{TiO2} for different ϕ_i/ϕ_n; a reference line corresponding to $t_{interface} = t_{TiO2}$ is also included to indicate whether surface deposition ($t_{TiO2} > t_{interface}$), or subplantation ($t_{TiO2} < t_{interface}$) is the dominant growth mechanism of TiO_2. For thin films deposited at $\phi_i/\phi_n \geq 0.6$, we observe that $t_{TiO2} < t_{linterface}$ during the initial ~2 nm of deposition, suggesting that the majority of Ti atoms are displaced below the growth surface, and that TiO_2 growth is dominated by subplantation. By increasing r ($\phi_i/\phi_n < 0.6$) we observe a faster saturation of $t_{interface}$, so that $t_{TiO2} > t_{interface}$, and fewer atoms are displaced into the bulk, meaning that surface deposition is likely to be the dominant growth process.

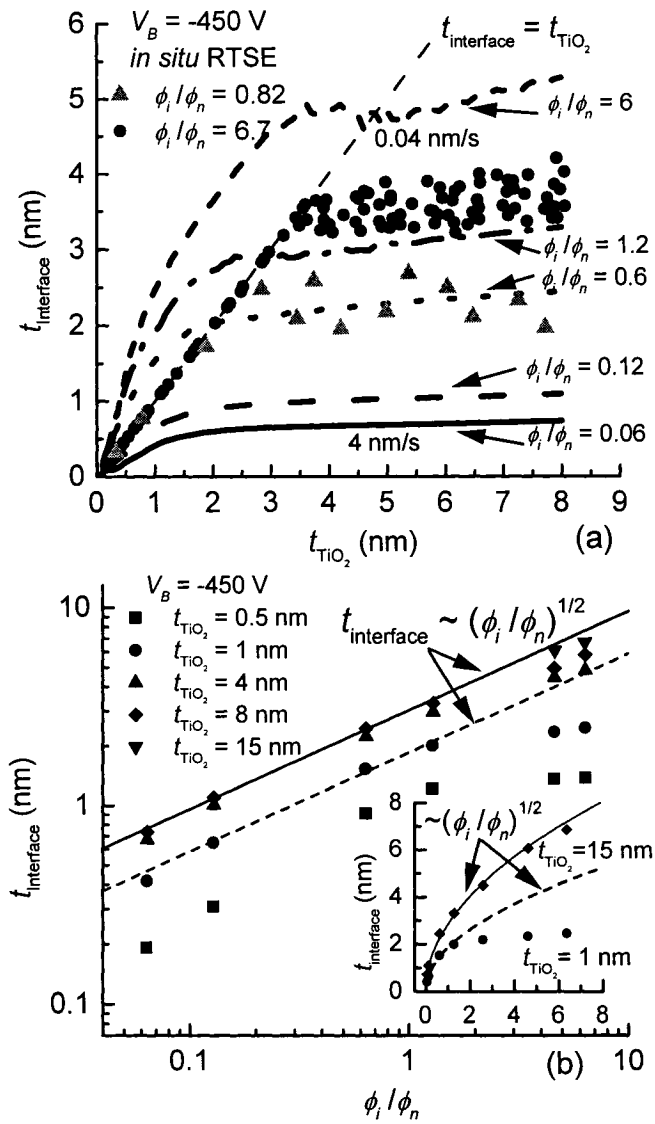

Figure 6.5. *(a) Evolution of $t_{interface}$ vs. t_{TiO2} for different r and ϕ_i/ϕ_n values during deposition of TiO_2 on SiO_2; (b) $t_{interface}$ as a function of ϕ_i/ϕ_n for different t_{TiO2} values (t_{TiO2} = 0.5, 1, 4, 8, and 15 nm) plotted on logarithmic scale; the inset shows the same data (t_{TiO2} = 1 and 15 nm, solid and dashed curves) plotted on a linear scale.*

Experimental results of the evolution of $t_{interface}$ at ϕ_i/ϕ_n = 0.82 and 6.7, obtained by *in situ* RTSE analysis, are shown in Fig. 6.5a (see solid symbols). The initial growth appears to be perfectly linear, followed by saturation at steady-state values of $t_{interface}$ ~3.5 ± 0.5 nm and ~2.3 ± 0.3 nm, for ϕ_i/ϕ_n ~ 6.7 and 0.82, respectively. The linear increase of $t_{interface}$ may be

the result of using a two-layer model with fixed optical constants. The comparison between RTSE and TRIDYN results of $t_{interface}$ shows a relatively good agreement between the two. Quantitatively, the experimental data points at $\phi_i/\phi_n = 0.82$ are situated between simulations at $\phi_i/\phi_n = 0.6$ and 1.2, while the data points for $\phi_i/\phi_n = 6.7$ are ~1 to 1.5 nm below the TRIDYN predictions for $\phi_i/\phi_n = 6$. This discrepancy may be linked to the restrictive nature of the two-layer optical model, where both layers' optical properties were kept constant.

The simulated $t_{interface}$ is also plotted on a logarithmic scale in Fig. 6.5b as a function of ϕ_i/ϕ_n for $t_{TiO2} = 0.5$, 1, 4, 8, and 15 nm. We observe that at steady-state (i.e. $t_{TiO2} \sim 15$ nm), $t_{interface}$ scales with $(\phi_i/\phi_n)^{1/2}$ for all ϕ_i/ϕ_n. This scaling law is similar to what has been observed during ion-beam mixing at the interface between two static thin films [59]. However, the situation is slightly more complicated here, because ion mixing occurs during thin film deposition; two important consequences are noted: (1) the growing film continually pushes the ion penetration front away from the interface, and (2) the film is a finite source of atoms, with very little Ti compared to Si during the early stages of growth. The first point is illustrated by the saturation behavior of $t_{interface}$ with t_{TiO2} (Fig. 6.5a). Given that the penetration depth of hyperthermal ions is less than ~10 nm in SiO_2 and ~6 nm in TiO_2, and that the ion implantation depth-profile decays with depth, it is clear that ion-interface interactions will decrease substantially during thin film growth.

The second point suggests that in some conditions (at high ϕ_i/ϕ_n), the ion fluence per unit film deposit can be sufficiently high to displace most, if not all deposited atoms, as well as many bulk atoms within range. This happens when there aren't sufficient quantities of one atom species to continue the mixing process and to further the interface broadening. From Fig. 6.4b, it appears that at least half of the Ti atoms deposited at $t_{TiO2} = 0.5$ nm are displaced into the SiO_2 and are replaced by Si atoms, thereby reducing the mixing potential. This is illustrated by the "premature" saturation of $t_{interface}$ at $\phi_i/\phi_n > 2$ for $t_{TiO2} = 0.5$, 1, 4 and 8 nm (Fig. 6.5b), also seen in the inset of Fig. 6.5b for $t_{TiO2} = 1$ nm. Not surprisingly,

the mixing law is gradually restored at $\phi_i/\phi_n > 2$ when more Ti is supplied to the target (see inset of Fig. 6.5b for $t_{TiO2} = 15$ nm).

We propose a simple rule of thumb to estimate interface broadening as a function of deposition conditions. We know that the number of incident ions for each incident atom is given by ϕ_i/ϕ_n, and the number of recoils (N_{IV}) created by each ion can be estimated from the Kinchin-Pease relation, given by $N_{IV} = E_m/2E_d$, where $E_m \sim 0.3e|V_B|$ [195] is the mean ion energy of the IEDF. Hence, by combining these relations in light of Fig. 6.5a, we estimate that when $\frac{\phi_i}{\phi_n} \times \frac{E_m}{2E_d} \leq 1$, the growth mechanism is dominated by surface deposition, and $t_{interface} \leq 1$ nm. For instance, when $V_B = -450$ V ($E_m \sim 135$ eV), N_{IV} is in the vicinity of ~5 to 6 for Si atoms in SiO_2 ($E_D = 12$ eV) and ~2 to 3 for Ti atoms in TiO_2 ($E_D = 25$ eV). Taking the average, i.e. $N_{IV} \sim 4$, we calculate that $t_{interface} \leq 1$ nm only if $\phi_i/\phi_n \leq 0.25$, or $r > 1$ nm/s. This rule can reveal the extent of ion mixing and interface broadening for given deposition conditions, and it can be very useful for optimizing the fabrication of OIFs that require abrupt interfaces.

6.6 Conclusion

We have demonstrated, using a combination of *in situ* RTSE and TRIDYN simulations, that ion-surface interactions at the RF-powered electrode in a low-pressure PECVD environment can lead to significant interface broadening during thin film growth. *In situ* RTSE has revealed the formation of a mixed-oxide interfacial layer with thicknesses of ~3.5 ± 0.5 nm and ~2.3 ± 0.3 nm for $\phi_i/\phi_n \sim 6.7$ ($r = 0.037$ nm/s) and 0.82 ($r = 0.3$ nm/s), respectively. TRIDYN simulations confirmed interface broadening very successfully, and they indicated that interface broadening is largely linked to ion bombardment. In addition, simulations also predicted that $t_{interface}$ scales with $(\phi_i/\phi_n)^{1/2}$, in agreement with ion mixing laws.

6.7 Acknowledgements

The authors acknowledge Dr. Matthias Posselt of Forschungszentrum Rossendorf (FZR) for providing a copy of the TRIDYN simulation code. The authors thank Dr. Oleg Zabeida for helpful discussions. This work was supported by the NSERC and CFI programs of Canada. P.D. acknowledges the support from the Canada Research Chair program. A.A. acknowledges the support from the NSERC Post-Graduate program.

Chapter 7. Article 4: Interface Engineering During Plasma-Enhanced Chemical Vapor Deposition of Porous/Dense $SiN_{1.3}$ Optical Multilayers

A. Amassian, R. Vernhes, J. E. Klemberg-Sapieha, P. Desjardins, and L. Martinu

Regroupement québécois sur les matériaux de pointe (RQMP) and Département de génie physique, École Polytechnique de Montréal, P.O. Box 6079, Station Centre-Ville, Montréal, Québec H3C 3A7 Canada

Article published: *Thin Solid Films* **469-470** (2004) 47-53.

7.1 Abstract

We investigate the growth of dense/porous $SiN_{1.3}$ multilayers by dual-mode radio-frequency/microwave plasma-enhanced chemical vapor deposition using *in situ* real-time spectroscopic ellipsometry (RTSE) and post-deposition atomic force microscopy. Dense $SiN_{1.3}$ films grown under high-energy ion bombardment on flat c-Si (001) substrates are very smooth (root mean square roughness R = 0.5 nm) and exhibit bulk-like optical properties (n = 2.0 at 550 nm). In contrast, porous $SiN_{1.3}$ films deposited at low ion energies are porous and columnar, with $n \sim 1.6$ and $R \sim 2$ nm. When $SiN_{1.3}$ layers are grown under high ion-energy bombardment conditions on porous films, RTSE analyses reveal a rapid filling of surface porosity, at a rate depending on the incident precursor flux, before the total film thickness starts to increase. Films prepared under these conditions exhibit a lower average n (~1.8), an ascending index depth profile, and a higher roughness ($R > 3$ nm) than the layers deposited under identical conditions on initially flat surfaces. We also demonstrate that the use of Ar ion bombardment, under RF plasma conditions, is an effective method for decreasing the roughness of porous films. $SiN_{1.3}$ layers deposited under RF-plasma conditions on such surface engineered substrates are dense with high and uniform n values. Such an approach has been successfully used to grow dense/porous multilayer optical interference filters. It efficiently stops roughness propagation through the multilayer stack and allows growing filters with optical characteristics essentially identical to those predicted from the design.

7.2 Introduction

Vast majority of advanced multilayer optical filter designs rely on the availability of materials with high optical contrast and the fabrication of multilayer structures with well defined and controlled interfaces. This is generally accomplished using deposition processes in which strong ion bombardment results in stœchiometic films with bulk-like densities, low optical absorption, and small surface roughness. Plasma-enhanced chemical

vapor deposition (PECVD) has been shown to produce such high quality optical coatings [28] owing to the high-energy ion bombardment in the radiofrequency (RF) regime [31]. This highly flexible technique enables, through the control of plasma chemistry and ion bombardment, the accurate tuning of the film optical and mechanical properties as demonstrated, for example, in our work on inhomogeneous optical filters with refractive index $n(z)$ varying continuously along the growth direction. [23 , 215]

By varying the layer composition, we have demonstrated the growth of single-phase amorphous TiO_2/SiO_2 mixtures with refractive index values varying smoothly between those of SiO_2 and TiO_2 [21]. New multilayer filter designs [5, 11] featuring quarterwave and non-quarterwave films with any intermediate index between SiO_2 and TiO_2 may also be fabricated using this approach.

Our group has demonstrated that refractive index control can also be achieved in a single-material system by varying the ion-bombardment characteristics to control film density and microstructure. Using a dual-mode radiofrequency (RF)/microwave (MW) PECVD system, we have obtained optically uniform $SiN_{1.3}$ films with refractive index, n, values ranging from 1.6 to 2.0, respectively, for wavelengths in the middle of the visible spectrum [23]. By modulating the plasma conditions during growth, we have fabricated multilayer and graded-index inhomogeneous optical interference filters solely based on the control of film porosity in $SiN_{1.3}$.

Low index porous films optimized to achieve a good balance between a low refractive index and adequate mechanical properties have been shown to exhibit a columnar microstructure [216]. Even though inhomogeneous filters with relatively good optical characteristics were obtained, process control is difficult to achieve since optical monitoring of inhomogeneous filters is at best a difficult task [217], and in most cases an unresolved issue. Moreover, the significant surface roughness resulting from the growth of

the porous layers greatly affects the transition from low to high index regions [23, 216] for both inhomogeneous and multilayer systems.

Further developments in the fabrication of such single-material porous/dense multilayer optical coatings rely on a detailed atomic-level understanding and control of surface morphological evolution under ion bombardment during interface formation. In this article, we show that dense (d-) $SiN_{1.3}$ films grown under high-energy ion bombardment on flat c-Si(001) substrates are smooth (root mean square roughness $R < 0.5$ nm) and exhibit bulk-like optical properties. In contrast, porous (p-) $SiN_{1.3}$ films deposited at low ion energies are porous and columnar, with $n \sim 1.6$ and $R \sim 2$ nm. We demonstrate that the use of Ar ion bombardment, under RF plasma conditions, is an effective method for decreasing the roughness of porous films. d-$SiN_{1.3}$ layers deposited under RF-plasma conditions on such surface engineered porous films have densities comparable to that of bulk and exhibit high and uniform n values. Such an approach has been successfully used to grow good quality dense/porous multilayer optical interference filters [218] as it efficiently stops roughness propagation through the multilayer stack.

7.3 Experimental Procedure

Dense and porous $SiN_{1.3}$ films were grown in a dual-mode MW/RF reactor described in detail elsewhere [23, 32]. The MW power was applied through a fused silica window using a slotted waveguide applicator. The RF-powered substrate holder was equipped with a rotatable carrousel, which allows one to sequentially deposit onto four samples that are introduced to the deposition chamber via a load lock system. The films were deposited on c-Si (001) using a mixture of SiH_4 (3 sccm), N_2 (20 sccm) and Ar (3 sccm) at a pressure of 40 mTorr.

RF and MW modes have very different ion energy distributions and fluxes, thus resulting in films with markedly different microstructures. Films deposited on the RF electrode at a

substrate self-bias, V_B, of -450 V are denser since they grow under intense ion bombardment (up to ~ 480 eV), while films deposited in 300 W MW plasma are porous due to the absence of energetic ions (< 10 eV) [31]. An RF Ar plasma (3 sccm and 40 mTorr), with V_B ranging from -100 V to -580 V, was used to modify the surface of porous layers prior to the growth of dense films. We found that plasma treatments with $|V_B|$ values near 700 V resulted in film etching.

The dynamics of film deposition and surface treatment was monitored *in situ* from 300 to 1600 nm by real-time spectroscopic ellipsometry (RTSE) using a rotating compensator ellipsometer (RCE, model M-2000, J.A. Woollam Co., Inc.) mounted at an angle of incidence of 65°. The capabilities of RCE and its advantages in the analysis of wide band-gap materials such as optical coatings have been demonstrated and explained [43]. The columnar porous layers are modeled as birefringent films with uniaxial anisotropy and the principle optical axis along the normal to the substrate. Both ordinary and extraordinary indices, $n_o(\lambda)$ and $n_e(\lambda)$, respectively, were parameterized independently using the classical three-term Cauchy dispersion equation. For the analysis of the porous and dense layers grown on the Si substrate, the surface over-layer (OL) was modeled as a Bruggeman effective medium approximation (BEMA) [119, 219] mixture of the underlying film (n_o) with void in a 1:1 ratio (see inset of Fig. 7.2b). In the analysis of the effect of the plasma treatment on the surface morphology and microstructure of the porous films, the OL layer was replaced by a two-term Cauchy dispersion. OL thickness, index and porous film thickness are fitted. Finally, during the growth of dense films on the plasma-treated surfaces, the OL index and thickness are considered as fitting parameters while the thickness of the porous film is fixed to its post-treatment value determined as described above.

Atomic force microscopy (AFM) operated in tapping mode, was used to determine the morphology of porous and dense films. The measurements were carried out in air using oxide-sharpened Si tips having average radii of 5-10 nm. Images were linearly planarized

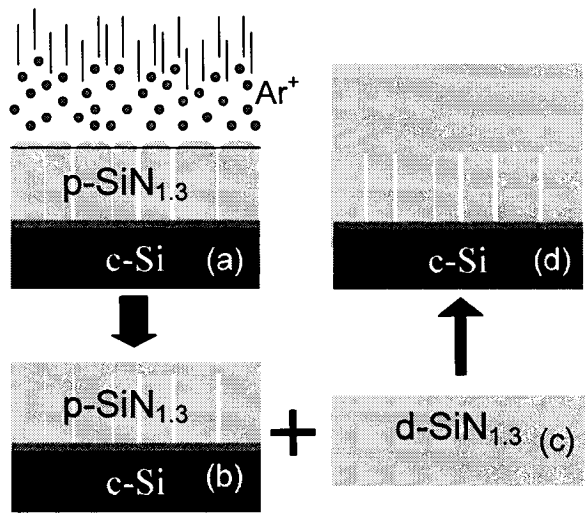

Figure 7.1 *Schematic illustration of the surface engineering approach for obtaining high quality dense/porous multilayer optical interference filters: The MW plasma deposited porous columnar film surface of p-$SiN_{1.3}$ is bombarded with high energy Ar ions in RF plasma (a) in order to produce a flat and dense surface region (b) on which d-$SiN_{1.3}$ is deposited in RF plasma (c, d).*

to remove sample tilting effects. The surface roughness was quantified by calculating the root mean squared (RMS) roughness, R, of the probed surface.

7.4 Results and Discussion

Our general approach for studying the evolution of the optical properties and the surface morphology during PECVD growth of $SiN_{1.3}$ thin films and dense/porous multilayers is presented schematically in Fig. 7.1. The growth study of porous and dense $SiN_{1.3}$ (p-$SiN_{1.3}$ and d-$SiN_{1.3}$) films on a flat c-Si surface (Section 7.4.1) is followed by surface engineering consisting of an Ar plasma treatment of the porous layers (Section 7.4.2). As the next step, we grow dense films with bulk-like characteristics on a plasma treated surface of p-$SiN_{1.3}$ (Section 7.4.3).

7.4.1 Dense and Porous $SiN_{1.3}$ Films on c-Si(001)

In the first part of this work we study the growth of single layer d-$SiN_{1.3}$ and p-$SiN_{1.3}$ on c-Si. The evolution of the refractive index at λ = 550 nm, n_{550}, as a function of thickness, t_p and t_d, for porous and dense films, respectively, is presented in Fig. 7.2a. For the d-$SiN_{1.3}$ film, n_{550} reaches saturation within the initial 5 nm of growth, at a value of $n_{550} \approx 1.93$, indicating a porosity of $p = 11.2 \pm 1.5$ %. This calculation is based on the averaging of linear ($i = 1$) and quadratic ($i = 2$) mixing laws:

$$n_{550}^{\,i} = n_{\text{void}}^{\,i} \times p + n_{\text{bulk}}^{\,i} \times (1 - p) \qquad (7.1)$$

Here i is the power of the mixing law, $n_{\text{void}} = 1$ and $n_{\text{bulk}} = 2.03$ for bulk-like $SiN_{1.3}$.

The overall behavior for the porous film is qualitatively similar, with n_o and n_e reaching 1.52 and 1.68, respectively, at a thickness of 7 nm. As the growth proceeds, n_o steadily increases to 1.59, while n_e decreases to 1.65 after 100 nm. This corresponds to a decrease of the overall birefringence of the film from its maximum value of nearly 0.13 down to 0.07, as shown in Fig. 7.2b. According to the expression of Bragg and Pippard [220] for the composite film index in the case of a columnar microstructure, the porosity in these films is in the order of ~30%, while a linear mixing law yields a porosity of ~40%.

AFM images from 100-nm thick d- and p-$SiN_{1.3}$ layers grown directly on Si(001) are presented in Figs. 7.2c-d. Both films are characterized by small rounded nanostructures with $R \approx 0.5$ nm for the dense film, and $R \approx 2.2$ nm for the porous layer. AFM data from a series of porous layers (not shown) with increasing thickness, t_p, reveal that R increases to 3.7 nm at $t_p = 200$ nm, and to 5.1 nm at $t_p = 500$ nm.

7.4.2 Ar RF-Plasma Treatment of Porous $SiN_{1.3}$ Films

We performed a series of RF-plasma treatments on porous layers in order to smoothen the surface and enable growth of d-$SiN_{1.3}$ layers in the subsequent step. In the analysis of the

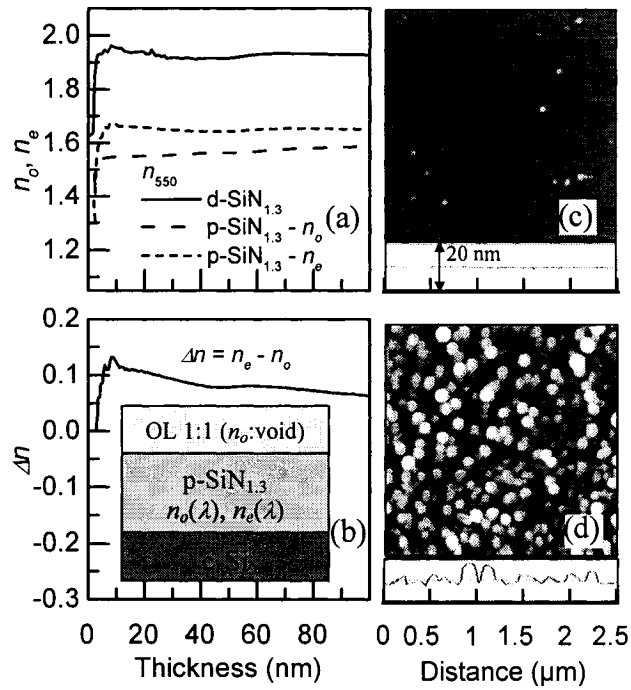

Figure 7.2 *Growth of d- and p-SiN$_{1.3}$ films in RF and MW plasmas: (a) Evolution of the refractive index (at λ = 550 nm), n_{550}, as a function of thickness, t_p and t_d, for porous and dense films, respectively, obtained from fitting ellipsometric model parameters to RTSE data (see model in the inset of (b)); (b) birefringence, $\Delta n = n_e - n_o$, of p-SiN$_{1.3}$ with uniaxial anisotropy as a function of t_p; (c) AFM surface images of as deposited d-SiN$_{1.3}$ (2.5x2.5 μm^2 area) and line profile; (d) AFM image of as deposited p-SiN$_{1.3}$. All vertical scales are 20 nm.*

RTSE data, the OL thickness, t_{OL}, the index at 550 nm, n_{OL}, as well as t_p are fitted, while the film optical constants are considered to remain unaltered since the plasma treatment is expected to affect only the near-surface region of the film.

Figs. 7.3a-c present the time-evolution of n_{OL}, t_{OL} and t_p of 100-nm-thick p-SiN$_{1.3}$ films during RF-plasma treatments with V_B ranging from -100 to -580 V. Experiments with V_B = -700 V (not shown) resulted in film sputter-etching. Initially between 1.35 and 1.45, n_{OL} increases with time of the plasma exposure at a rate that increases with the magnitude of $|V_B|$. Values of up to $n_{OL} \sim 1.9$ were obtained with treatments of approximately 100 s at V_B = -580 V. The behavior of t_{OL} is more complex as it initially increases up to 16-20 nm,

depending on V_B, before slowly decreasing (note the logarithmic time scale). Also, t_p appears to vary inversely with t_{OL} (Fig. 7.3c).

A detailed analysis reveals that the maximum in t_{OL} is measured when n_{OL} and n_{550} of the porous underlayer match each other ($n_{OL} \sim n_{550} \approx 1.6$). The complementary behavior of t_{OL} and t_p values is an optical artifact due to the n_{OL} approaching, matching, and then passing n_{550} of the underlying porous film. When $n_{OL} \sim n_{550}$, the film and the OL become optically indistinguishable, therefore highly correlated. While complete correlation is expected for $n_{film} = n_{OL}$, the fit still yields relatively stable thickness results since both layers have slightly different dispersion curves, and because the film exhibits optical uniaxial anisotropy. The matching condition is, therefore, met at different times for different wavelengths which explains the stability of the fit. As counterintuitive as it may seem, the n_{OL} determination improves near the matching condition. Indeed, n_{OL} is implicitly well determined at the matching condition since n_{550} is well known. The matching also results in distinct peaks seen in Fig. 7.3a, indicating that the n_{OL} data is not very reliable at all treatment times. The reliability of n_{OL} data is good at the matching, and far from it.

Since ellipsometry is primarily sensitive to the optical thickness (i.e. the product of physical thickness and refractive index), we expect this fitted quantity to behave very reliably even in the present situation where index matching conditions complicate the individual determination of n_{OL}, t_{OL} and t_p. Furthermore, since this quantity is the most significant parameter to control in optical interference filter fabrication, the ability of the model to determine the optical thickness compensates for its weakened ability to determine t_p and t_{OL}. The total (film and OL) optical thickness (OT), plotted as a function of time in Fig. 7.3d, decreases smoothly without any sign of correlation artifacts seen in Figs. 7.3a-c. As expected, a limited amount of OT decreases, which is due to densification and etching at elevated $|V_B|$. In some cases, we observe slow and monotonous OT increase after saturation, possibly due to slight loss of nitrogen and enrichment in silicon, or eventually due to

additional deposition occurring from Ar sputtering of $SiN_{1.3}$ coated cathode and reactor wall surfaces.

The results for t_p and t_{OL} obtained from the fit of the ellipsometric data before initiating the plasma treatment at different exposure times (see Fig. 7.3) are summarized in Table 7.1. As already observed in Fig. 7.3a, the plasma exposure time required for n_{OL} to match n_{550} for p-$SiN_{1.3}$ decreases rapidly with increasing $|V_B|$ values, from 1400 s at -100 V to approximately 6 s at -580 V. All plasma treatments resulted in n_{OL} well above n_{550} of p-$SiN_{1.3}$, reaching 1.93 for V_B = -580V. We attribute this significant increase to a considerable rearrangement and densification of the surface layer under ion bombardment.

The calculated decrease of total OT is smaller than the OT of the OL prior to plasma exposure. This indicates that the OL might not get densified or etched completely. If we assume that the decrease of OT due to densification and etching is restricted to the OL, then we can estimate what proportion of OT is lost due to etching. This estimate is based on the following reasoning: when a film of thickness t_{OL1}, porosity p_1, and index n_1 is densified (without addition or subtraction of material), it becomes a new film of thickness t_{OL2}, porosity p_2, and index n_2 (with $t_{OL2} < t_{OL1}$, $p_2 < p_1$, and $n_2 > n_1$), and its OT decreases due to the loss of physical thickness. If the ambient medium is air, and assuming a linear mixing law (eq. 1), we can demonstrate that the OT lost due to densification is simply equal to the $t_{OL1} - t_{OL2}$ difference. By definition, the rest of the OT change is due to etching. The contribution of etching to the loss of OT is reported in the last but one column of Table 7.1. We observe that the contribution of etching in the OT loss increases with $|V_B|$.

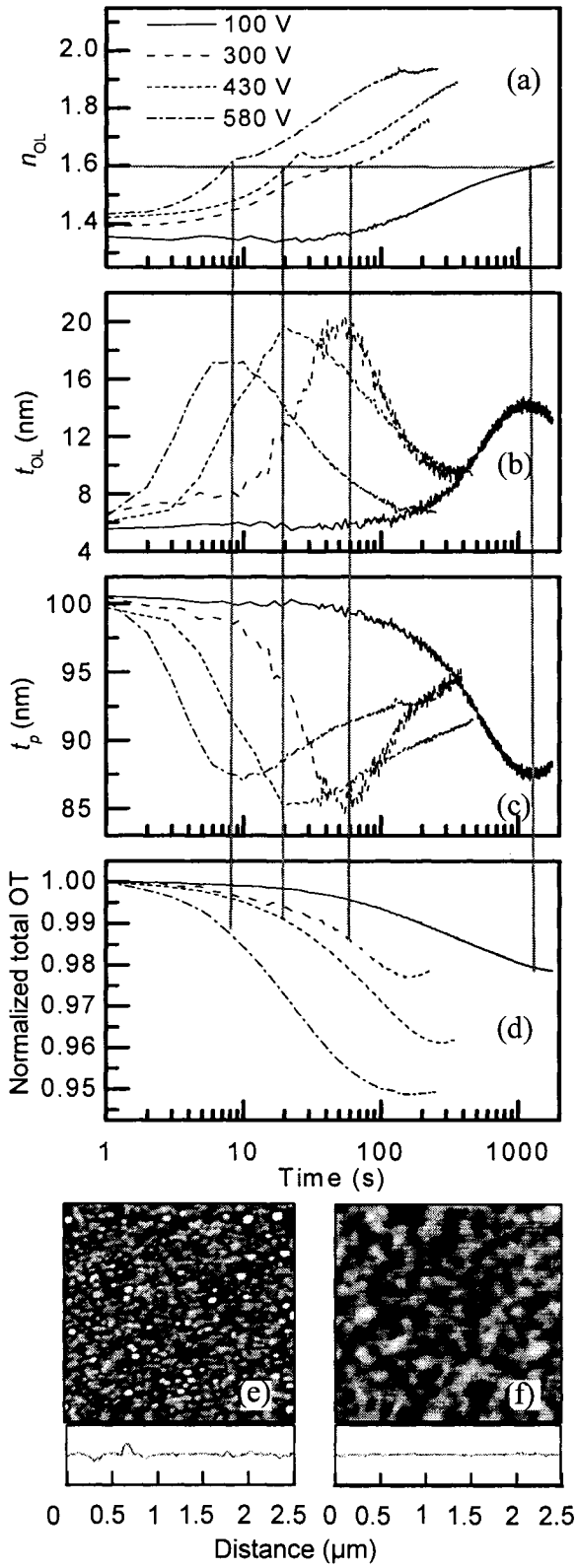

Figure 7.3 *Real-time evolution of ellipsometric fit parameters during Ar plasma treatment*

of p-$SiN_{1.3}$ film surface with increasing $|V_B|$ (the ellipsometric model is shown in the inset of Fig. 7.2b): (a) n_{OL}; (b) t_{OL}; (c) t_p; (d) overall normalized optical thickness change (vertical lines indicate correlation between t_{OL} and t_p at the matching of n_{OL} and n_{550}). AFM images of p-$SiN_{1.3}$ surfaces treated at (e) V_B = -300 V and (f) V_B = -580 V in Ar plasma.

Table 7.1 *Summary of p-$SiN_{1.3}$ thickness and index before and after Ar plasma treatment*

V_B (V)	Before treatment			After treatment				
	t_p (nm)	t_{OL} (nm)	n_{OL}	n_{OL}	Time to matching (s)	Time to optical thickness saturation (s)	Etch (%)	R (nm)
-100	100.6	5.5	1.36	1.61	1400	1800	25	3.4
-300	100.5	6.7	1.39	1.73	60	180	13	1.4
-430	99.7	6.0	1.42	1.88	20	300	46	1.0
-580	100.3	6.4	1.43	1.93	6	130	54	0.6

The effect of Ar plasma treatment on the surface morphology is seen in AFM images in Figs. 7.3e-f for V_B = -300 and -580 V. With the exception of the -100 V sample, the treated surfaces are considerably smoother than for the as-grown films (see Fig. 7.2d for comparison). The V_B = -100 V sample exhibits a large density of asperities compared to the untreated one, typical of ion bombardment induced roughening [221]. This trend is fully reversed for higher $|V_B|$ values as R systematically decreases from 1.4 to 0.6 nm when V_B varies from -300 to -580 V. AFM images from the -300 and -580 V samples show significantly different surface morphologies. While both surfaces are much smoother than before plasma treatment, the lower $|V_B|$ sample still exhibits some asperities, while the higher $|V_B|$ sample is characterized by an even smoother surface, but with few nanoholes

[222] (shown as black circles on AFM micrographs) revealing large porosity from the underlying film.

7.4.3 Growth of Dense $SiN_{1.3}$ on Untreated and Plasma-Treated Porous $SiN_{1.3}$ Layers

A series of nominally dense films were grown on untreated and plasma-treated porous $SiN_{1.3}$ layers. Immediately following the Ar plasma treatment, SiH_4 and N_2 are introduced in the chamber, and the RF plasma is ignited at V_B = -400 V. The nominal deposition rate is approximately 0.3 nm s^{-1}.

The time evolution of n_{550} for d-$SiN_{1.3}$ and of the physical film thickness, t_d, are plotted in Figs. 7.4a and 7.4b. The starting thickness is taken as the final t_{OL} value following the plasma treatment, and as the initial t_{OL} in the case of the non-treated sample.

Film growth on the untreated surface is characterized by a non-linear t_d evolution with time. During the initial 12 s of deposition, t_d increases only slightly, while the n_{OL} increases from 1.37 to 1.6. Since the OL porosity is 58 ± 6 % according to linear and quadratic mixing laws (eq. 1), we can attribute this initial behavior to pore filling before growth. In fact, during the 12 s period, approximately 4 nm of dense material is deposited (nominal rate of 0.3 nm s^{-1}), while only a change of 2 nm of t_d is measured at an average $n_{550} \sim 1.485$. Moreover, based on the results presented in section B, we can expect that the ion bombardment at V_B = -450 V leads to partial densification and possibly modifications of the near surface region of the untreated film. For comparison, a 10 s treatment at V_B = -430 V in Ar RF-plasma (Fig. 7.3a) led to an increase of n_{OL} from 1.42 to nearly 1.5.

Since the surface of the plasma-treated porous layers has already been densified, we expect that growth on such "engineered" surfaces will proceed linearly from the beginning. This is indeed confirmed in Fig. 7.4, which also reveals that initial n_{550} values for d-$SiN_{1.3}$ on p-$SiN_{1.3}$ are higher for larger $|V_B|$ treatments. From the data analysis in Fig. 7.4a, we conclude

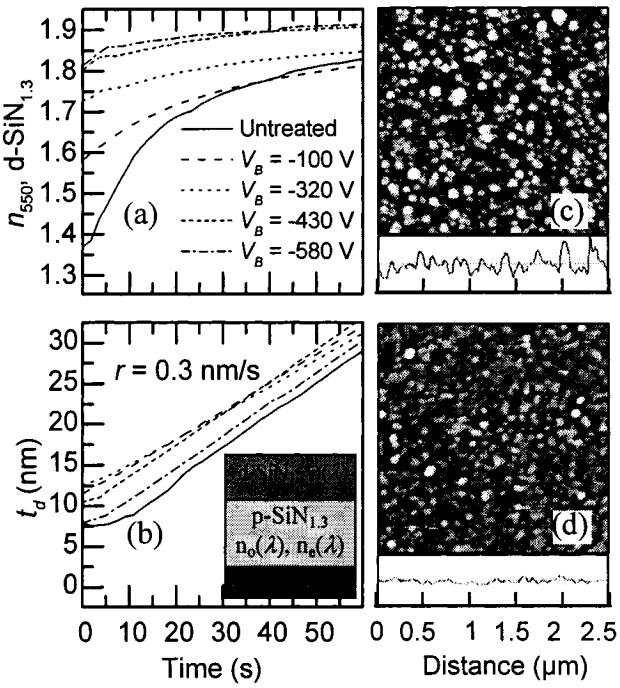

Figure 7.4 *Time evolution of (a) n_{550} and (b) t_d during the growth of d-SiN$_{1.3}$ on non-treated and plasma-treated p-SiN$_{1.3}$. AFM images (2.5x2.5 μm^2) from 100-nm-thick dense films deposited on non-treated (c) and plasma treated (d) (V_B = -580 V) p-SiN$_{1.3}$ surfaces.*

that even though d-SiN$_{1.3}$ with relatively large n_{550} can be deposited on untreated and -100 V treated samples, such films are highly inhomogeneous and unsuitable for the fabrication of multilayer coatings with sharp interfaces. In fact, n_{550} continues to increase after 60 s of growth and remains more than 0.1 below bulk values.

These results also show that films grown on surfaces with high $|V_B|$ treatment exhibit the least index variation (Fig. 7.5a), indicating a more homogeneous, denser film with possibly thinner interfacial regions. These films have a higher index after 100 nm deposition than the reference film (n_{550} ~ 1.93) deposited on c-Si with n_{550} = 1.97 for the d-SiN$_{1.3}$ film deposited on top of -580 V plasma-treated surface of p-SiN$_{1.3}$. We believe that these improvements are in large part due to a combination of different effects, including surface smoothening, chemical activation and local heating through ion bombardment.

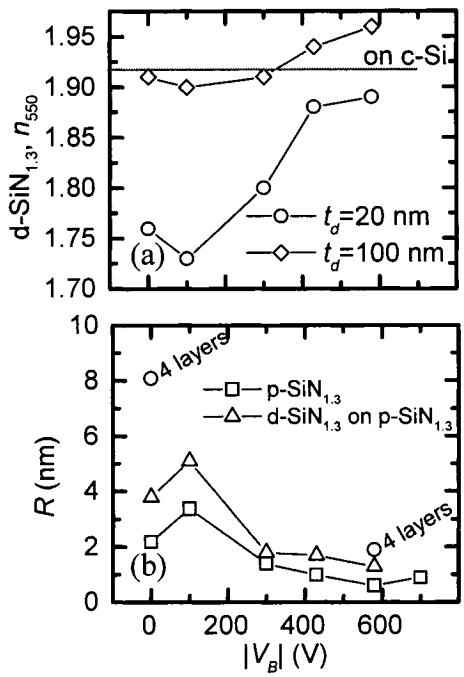

Figure 7.5. *Effect of interface engineering by Ar plasma treatment at different V_B values: (a) n_{550} of 20 nm and 100 nm thick d-$SiN_{1.3}$ films grown on c-Si and 100 nm thick p-$SiN_{1.3}$; (b) R of 100 nm thick p-$SiN_{1.3}$ film and of 100 nm thick d-$SiN_{1.3}$ film on top of a 100 nm thick p-$SiN_{1.3}$ layer. R for a 4 layer system is shown for comparison*

Examples of AFM images from the surfaces of nominally dense 100-nm thick d-$SiN_{1.3}$ films grown on non-treated and treated (V_B = -580 V) surfaces are presented in Figs. 7.4c and 7.4d. The plasma treatment has major impact on d-$SiN_{1.3}$ surface morphology and roughness (Fig. 7.5b). While d-$SiN_{1.3}$ films grown on c-Si are very smooth (see section 7.3.1), films prepared under identical conditions on as-deposited p-$SiN_{1.3}$ exhibit a larger roughness than that of p-$SiN_{1.3}$. The Ar RF plasma treatment at $|V_B| >> 100$ V thus enables the growth of much smoother surfaces as detailed in Fig. 7.5b. This is an important prerequisite for the fabrication of multilayer optical interference filters.

AFM measurements were also carried out on the surface of four-layer stacks of 100 nm porous/dense films fabricated with and without plasma-treatment (Fig. 7.5b). The untreated stack had an overall surface roughness of R = 8.1 nm, while the multilayer deposited using

the surface engineering procedure at -580 V was much smoother with R = 1.9 nm, a value close to that of a porous/dense double-layer.

The overall set of results underlines the importance and the potential of surface engineering approaches to control and improve the interface characteristics during the deposition on porous media. Our results also indicate that ion bombardment during the deposition is not sufficient for obtaining sharp interfaces and optically uniform layers; it is necessary to use an intermediate densifying step.

7.5 Conclusion

We showed, using *in situ* RTSE dynamic analysis, that interface engineering by RF Ar plasma treatment of porous film surfaces prior to deposition of a dense film in a multilayer stack is an essential process step for the fabrication of single-material porous/dense multilayer optical interference filters with good optical performance. Microstructural and optical properties of porous/dense multilayer filters fabricated with interface engineering are significantly improved by reduced surface roughness propagation throughout the multilayer stack. Dense $SiN_{1.3}$ films grown on top of surface treated p-$SiN_{1.3}$ grow similarly to d-$SiN_{1.3}$ on c-Si. They possess bulk-like optical properties (n_{550} ~ 2.0), and their refractive index inhomogeneity is largely eliminated. In contrast, d-$SiN_{1.3}$ films grown on untreated p-$SiN_{1.3}$ are far more porous (n_{550} ~ 1.8 after 40 nm deposition), inhomogeneous and rough. In addition, we have shown that the methodologies of *in situ* RTSE monitoring as well as of the interface engineering are generally valuable to develop processes of coating porous media with smooth and dense thin films.

Chapter 8. Conclusions, General Discussion, and Perspectives

8.1 Summary of the Results

The primary objective of this work was to gain an in-depth understanding of the role of ion-surface interactions in the PECVD environment, and more specifically to focus on plasma-surface interactions in conditions relevant to optical thin film deposition at the RF-powered electrode.

In order to achieve this goal, we have carried out a systematic investigation of the surface modifications resulting from the exposure of a model c-Si(001) substrate to an O_2 RF discharge, combining real-time spectroscopic ellipsometry and Monte-Carlo-based dynamical simulations (TRIDYN) of ion-surface interactions. As a result, the methodology developed during this work has significantly increased the understanding of such technologically relevant processes.

The use of c-Si increased our ability to detect and understand ion bombardment effects, since (1) there is excellent knowledge about ion beam oxidation and damage of c-Si, (2) the ion bombardment leaves permanent and optically detectable traces in this substrate, e.g. damage and oxide formation, and (3) the optical properties of Si are well documented for all its phases (crystalline, polycrystalline, damaged, amorphous, oxidized, etc.), and their temperature-dependence is also known. In addition, (4) we have benefited from extensive work in the literature on the optical modeling of ion-beam and plasma oxidation of c-Si [51, 99, 107, 110, 120, 121, 122, 124, 128, 129], which have demonstrated SE to be highly sensitive, robust and quantitatively accurate tool to depth-profile the near-surface damage and oxide formation in c-Si.

To help understand and interpret the *in situ* RTSE results, we have performed extensive simulations of ion-surface interactions with the TRIDYN code, which we modified to take

into account a broadband ion source, such as at the RF-powered electrode in a RF discharge. Here too, we included previous knowledge of ion bombardment characteristics, such as flux and energy of ions (IEDF, E_{max}, and E_m) as a function of external process parameters [37, 31, 32], permitting precise modeling of the ion source. This certainly contributed to the accurate prediction by TRIDYN simulations of *all* experimental observations (Chapters 4 and 5) pertaining to sub-surface modifications (quasi-instantaneous damage formation, followed by oxidation) observed on time-scales in the range from 10^{-1} to 10^{2} s, and depth-scales of up to ~10 nm.

Simulations also revealed which mechanisms are responsible for the dynamical evolution of damage and oxide formation, and explained the sub-surface modifications entirely in terms of well-known IB-related processes, which we summarize as follows:

(1) *Ion implantation*, responsible for the ballistic and depth-dependent transport and accumulation of oxygen in the target until a self-limiting regime is established at high fluence;
(2) *atomic relocations*, leading to IV-pair formation and damage accumulation in c-Si;
(3) *volume swelling* due to oxide formation, leading to a reduction of the damage accumulation rate at the onset of oxidation;
(4) *surface recession* due to sputtering, responsible for the formation of an O-deficient interfacial layer at high ion fluence.

These processes are all directly related to the IEDF and the incident ion flux, and are inextricably linked to external process parameters, V_B and p. Since TRIDYN simulations allow to predict the dynamic evolution of sub-surface modifications for given process parameters using well known ion bombardment characteristics, we therefore believe that our work has bridged the gap between the external process parameters and the sub-surface modifications resulting from plasma-surface interactions.

From the understanding developed in Chapters 4 and 5, and using the same methodology (*in situ* RTSE monitoring and TRIDYN simulations), we extended our investigation to the studies of interface mixing and subplantation during the initial stages of TiO_2 deposition on SiO_2 at the RF-powered electrode (Chapter 6) as a model system for investigating interface formation in amorphous oxide multilayers. The study reveals that TiO_2 growth at the RF-powered electrode is dominated by sub-surface deposition (more so at low deposition rate) of Ti and O as a result of O subplantation and relocation of near-surface Ti atoms (probably adsorbed or chemisorbed) into the bulk. In addition, the early stages of film deposition are dominated by ion mixing of interfacial atoms, leading to interface broadening, which mainly depends on the ion-to-neutral arrival rate ratio (ϕ_i/ϕ_n, inversely proportional to the deposition rate). TRIDYN simulations predicted a scaling of the interfacial width proportional to $(\phi_i/\phi_n)^{1/2}$. In practical terms, we found that an increased deposition rate (for constant IB conditions, i.e. IEDF and ϕ_i) leads to thinner interfaces. As a general rule, we proposed that interface thickness remains below 1 nm when $\frac{\phi_i}{\phi_n} \times \frac{E_m}{2E_d} \leq 1$, where $E_m \sim 0.3e|V_B|$. This translates to a necessity to keep the deposition rate of TiO_2 above 1 nm/s at V_B = -450 V. Interestingly, interface broadening was found to remain active even after the deposition of a few nanometers of TiO_2 (up to ~4 nm), because the maximum ion penetration depth (O^+) is ~8.5 nm in SiO_2 and ~5 nm in TiO_2 in normal deposition conditions (V_B = -450 V).

Finally, we have used ion bombardment to tailor the bulk microstructure and surface morphology of model Si_3N_4 thin films by depositing them in microwave (MW) and RF discharges (Chapter 7). The mean ion energy (E_m) in a MW plasma is very low (< 10 eV), unable to displace thin film atoms, and leads to the formation of underdense films with columnar microstructure and high surface roughness at room temperature, whereas RF-deposited films are bombarded at E_m > 100 eV, and are very dense as a result of multiple displacements per ion. To enable the controlled deposition of dense films on porous layers, we proposed a plasma-based interface engineering procedure, where an Ar plasma

treatment at the RF-powered electrode smoothened and densified the surface of the porous Si_3N_4 film within a few minutes of exposure. This in turn enabled the growth of dense, homogeneous and smooth Si_3N_4 films on the surface of porous films. Interface engineering is therefore shown to be an interesting and simple-to-implement process step, which enables the manufacture of single-material multilayer OIFs with controlled microstructure and interfaces.

8.2 Discussion of the Main Contributions

This thesis has drawn attention to the fact that *very much is going on below the surface* of a target, a substrate or a growing thin film at the RF-powered electrode of a PECVD reactor. We will now discuss the role of **ion bombardment**-related processes below surfaces at the RF-powered electrode, which is in fact a point of similarity between PECVD and plasma- or ion-assisted PVD processes. We will also emphasise the role played by the **methodology** in detecting and quantifying sub-surface effects of ion-surface interactions on time scales pertinent to plasma treatment and thin film deposition processes. Finally, we discuss the implications of a new capability to **tailor interface morphology** by plasma treating porous films at the RF electrode, and its benefits to the fabrication of technologically promising microstructured film stacks.

8.2.1 The Importance of Ion Bombardment

While ion bombardment effects are well understood by the scientific and the thin film communities for PVD processes, unfortunately, they have not been the focus of intense research in PECVD processes, owing to the complexity of the chemistry and plasma-surface interactions. As such, many textbooks and publications in this field tend to emphasise and tackle the complex – and important – surface chemical reactions typical to all CVD-based processes. Relatively few authors have, however, noted the role of ion bombardment in the PECVD environment, and qualitatively described its sub-surface effect

during thin film growth, while calling for more research effort by either *in situ* monitoring or computational studies [33, 41].

The Functional Coatings and Surface Engineering Laboratory (FCSEL) has shared this vision for many years, and has paid particular attention to this subject [30, 28, 31, 32, 54, 55, 67]. In keeping with this, we have opted to continue in this direction and to study the PECVD process from the perspective of a physical problem, rather than from the chemistry point of view, focusing on ion bombardment effects. In hindsight, our judgment seems to have been correct, as we have consistently shown that IB-related processes at the RF-powered electrode of a PECVD reactor will *inevitably* lead (1) to significant sub-surface modifications of any substrate on very short time scales (< 1 s to 2 s), (2) to changes in the thin film's growth mechanism and microstructure by continuous ballistic mixing of deposited atoms via nuclear interactions, and (3) to interface broadening in multilayers as a result of the mixing of atoms at the interface.

The above findings primarily based on an indirect ellipsometric analysis and MC simulations are now strongly supported by experimental evidence in a parallel study [223, 224]. Using the methodology developed in this thesis, in combination with XTEM analyses of the growth of ternary TiN/Si_3N_4 and quaternary $TiC_xN_y/SiCN$ nanocomposite superhard coatings on c-Si(001) at the RF-powered electrode by PECVD, we have visually confirmed the existence of a ~7 to 8 nm-thick heavily damaged interfacial region. This region is formed at the interface between the monocrystalline substrate and the polycrystalline thin film, in full agreement with *in situ* RTSE and TRIDYN simulation studies.

It is the hope of this candidate, that this thesis will lead to ion bombardment effects being given more serious consideration in future studies of thin film growth by PECVD or similar plasma-assisted processes.

8.2.2 The Importance of the Experimental and Simulation Methodologies

The IB-related modifications under investigation are detectable on time and lengths scales (and in locations just below the surface) that are difficult to access experimentally. The PECVD environment is also not compatible with most *in situ* probes, which made *in situ* RTSE an ideal candidate for process monitoring, especially in light of new and recent developments in instrumentation, calibration, data acquisition and optical modeling.

The SE signal is very rich, but, unfortunately, also highly convoluted. In order to extract relevant information, we needed to develop robust optical modeling tools, which, when combined with well-known model materials such as c-Si, can yield a wealth of information about the origin and dynamics of the modifications (see for example Fig. 5.4).

We also benefited from extensive characterization work on the "ion source" at the RF-powered electrode in a RF discharge carried out in our laboratory [31, 32] and elsewhere [37]. This enabled us to simulate ion-surface interactions by the MC-based TRIM and TRIDYN codes on time and length scales similar to RTSE results. These simulation tools were developed by the ion-beam processing and sputtering communities and were quite helpful to us, but still needed to be adapted to the broadband ion distribution.

In this respect, this thesis represents, to our knowledge, the first study in its kind to quantitatively and accurately simulate such a wide range of sub-surface effects resulting from ion bombardment by a complex broadband energy ion source. This capability is potentially significant for industrial applications, because it can simulate processes simply based on knowledge about the external process parameters (if IB characteristics are previously studied). This capability also constitutes a step in the general shift by the thin film community away from 'recipe' approaches to process development, and towards a more atomistic understanding of the thin film growth (including IB effects) [53].

8.2.3 Interface Engineering to Control the Transfer of Thin Film Morphology in Dense/Porous Stacks

The effects of ion bombardment on thin film microstructure and surface morphology were clearly illustrated in Chapter 7. The most interesting result was that plasma-surface and ion-surface interactions at the RF-powered electrode can effectively smooth and densify the rough surface of a porous thin film. When combined with *in situ* RTSE monitoring, the plasma process can be controlled and tailored to obtain the desired level of densification and smoothing. Hence, the transfer and propagation of the underdense morphology in a dense/porous stack can also be controlled. In optimal smoothing conditions (see Chapter 7), we deposited dense films with bulk-like properties on porous films, which was not possible without plasma treatment, suggesting that interface engineering inhibits the propagation of the underdense morphology throughout the multilayer stack.

8.3 Perspectives and Future Work

PECVD is being used for a variety of materials and applications in the broad field of functional coatings, ranging from plasma surface treatments, to the deposition of multilayer and compositionally- or microstructurally-graded coatings, to nanocomposites and hard/superhard coatings, to barrier coatings, etc. The development and understanding of PECVD processes is important for the optical coatings community in its effort to broaden the gamut of materials and optical properties available to fabricate advanced OIF-based devices. Current limitations concerning the optical coatings include the control of interfaces and film density, and require new approaches to unravel the multiple processes simultaneously involved in a PECVD environment, including *in situ* process monitoring, and – equally important – the development of working and well-proven simulation tools, which can be used to predict thin film and interfacial properties based on external process parameters.

This work contributed to the detailed observation and understanding of the role of ion-surface interactions, a key component among the multiple plasma-surface interactions (neutrals, radicals, electrons and photons) in a PECVD environment. The development of a simulation tool capable of predicting these effects during film growth and on time scales of seconds to hours will enable PECVD process development and optimization, such as in the case of PVD processes, where MC-based simulations have allowed to predict the entire process from the sputtering of the solid-state target [197, 225] to the thin film growth [226, 227].

This work has not focused on thin film formation per se, nor its subsequent growth; and so many problems still call for future studies; chief among these are gradients of the optical properties, which are problematic for OIFs, because they constitute non-idealities, capable of deteriorating the optical performance of devices. We need to unravel the origin of these gradients, which are presumably linked to the microstructural and morphological evolution during the growth of thin films, and to stress accumulation and release via relaxation mechanisms [228], as well as to the drift in plasma conditions, to involuntary substrate heating or impurities, and other possible sources. Overcoming these challenges will allow us to achieve better control of thin film microstructure and properties so important for the optical coatings community.

It will be interesting to extend this work, performed exclusively on amorphous materials, to the case of polycrystalline and single-crystal coatings. Here too, the *in situ* damage and amorphization study of c-Si has opened up new horizons, because the study could be extended to other materials, leading to a better understanding of the damage accumulation and thresholds for microstructural changes. This would require complicated MD simulation studies to gain an atomistic understanding of such effects as nanocluster formation or phase segregation.

From the perspective of polycrystalline thin film growth, *in situ* RTSE can reveal some details about the nucleation and coalescence processes [229, 230, 231, 232], and TRIDYN is mainly limited to atomic transport in the direction normal to the sample surface, so it will be necessary to use other approaches, such as a combination of high resolution TEM [53] and atomistic 3D kinetic Monte-Carlo simulations [226, 227] to study the nucleation process, texturing, as well as grain coarsening, re-nucleation and reduction of surface roughness in the presence of ion bombardment [53, 233]. This work is currently underway in the case of model polycrystalline films deposited in ultra-high vacuum (UHV) by PVD techniques [53], but would pose enormous challenges in the case of high vacuum and so-called "dirty" processes, such as PECVD, and will possibly require a worldwide concerted effort to perform both computational and experimental studies to build viable 3D growth models.

References

[1] J. A. Dobrowolski, in *Optical Society of America's Handbook of Optics*, edited by M. Bass (McGraw-Hill, New York, 1995), Chap. 42.

[2] *Thin Films for Optical Systems*, edited by F. R. Flory, (Marcel Dekker, New York, 1995).

[3] J. A. Dobrowolski, "Optical interference filters for the adjustment of spectral response and spectral power distribution", *Appl. Opt.* **9** (1970) 1396-1402.

[4] N. A. O'Brien, M. J. Cumbo, K. D. Hendrix, R. B. Sargent, and M. K. Tilsch, "Recent advances in thin film interference filters for telecommunications", in *Proceedings of the 44th Annual Tech. Conf.* (2001) 255-261.

[5] P. G. Verly, "Design of a robust thin-film interference filter for erbium-doped fibre amplifier gain equalization", *Appl. Opt.* **41** (2002) 3092-3096.

[6] *Optical Interference Coatings*, edited by N. Kaiser and H. K. Pulker, Springer, 2003.

[7] W.H. Southwell, "Coating design using very thin high- and low-index layers" *Appl. Opt.* **24** (1985) 457-460.

[8] B.T. Sullivan and J.A. Dobrowolski, " Implementation of a numerical needle method for thin-film design", *Appl. Opt.* **35** (1996) 5484-5492.

[9] A. V. Tikhonravov, M. K. Trubetskov and G. W. DeBell, "Application of the needle optimization technique to the design of optical coatings", *Appl. Opt.* **35** (1996) 5498-5508.

[10] J. A. Dobrowolski, D. Poitras, P. Ma, H. Vakil and M. Acree, "Toward perfect antireflection coatings : numerical investigation" *Appl. Opt.* **41** (2002) 3075-3083.

[11] P. G. Verly, "Modified needle method with simultaneous thickness and refractive-index refinement for the synthesis of inhomogeneous and multilayer optical thin films", *Appl. Opt.* **40** (2001) 5718-5725.

[12] A. Macleod, "Future of optical coatings", Optical Interference Coatings Topical Meeting, invited talk MA1, June 28 2004.

[13] P. J. Leurgans, "The impedance concept in thin film optics", *J. Opt. Soc. Am.* **41** (1951) 714-717.

[14] W. H. Southwell, "Spectral response calculations of rugate filters using coupled-wave theory", *J. Opt. Soc. Am.* **A5** (1988) 1558-1564.

[15] K. Kaminska, T. Brown, G. Beydaghyan, and K. Robbie, "Vacuum evaporated porous silicon photonic interference filters", *Appl. Opt.* **42** (2003) 4212-4219.

[16] D. Poitras and L. Martinu, "Simple method for determining slowly varying refractive-index profiles from *in situ* spectrophotometric measurements", *Appl. Opt.* **37** (1998) 4160-4167.

[17] B. Johs, J. Hale, N. J. Ianno, C. M. Herzinger, T. Tiwald and J. A. Woollam, "Recent developments in spectroscopic ellipsometry for *in situ* applications" in *Optical Metrology Roadmap for Semiconductor, Optical and Data Storage Industries II, Proc. SPIE* **4449** (2001) 41-57.

[18] E. G. Berasategui, S. J. Bull and T. F. Page, "Mechanical modelling of multilayer optical coatings", *Thin Solid Films* **447-448** (2004) 26-32.

[19] *Handbook of Deposition Technologies for Films and Coatings*, edited by R. F. Bunshah (Noyes, Park Ridge, NJ, 1994).

[20] *Thin Films Processes II*, edited by J. L. Vossen and W. Kern, (Academic Press, New York, 1991).

[21] A. Mahdjoub and L. Zighed, "New designs for graded refractive index antireflection coatings", *Thin Solid Films* **478** (2005) 299-304.

[22] S. Larouche, H. Szymanowski, J. E. Klemberg-Sapieha, and L. Martinu, "Microstructure of plasma-deposited SiO_2/TiO_2 optical films" *J. Vac. Sci. Technol.* **A22** (2004) 1200-1207.

[23] R. Vernhes, O. Zabeida, J.E. Klemberg-Sapieha, and L. Martinu, "Single-material inhomogeneous optical filters based on microstructural gradients in plasma-deposited silicon nitride", *Appl. Opt.* **45** (2004) 97-103.

[24] A. Amassian, R. Vernhes, J. E. Klemberg-Sapieha, P. Desjardins, and L. Martinu, "Interface engineering during plasma-enhanced chemical vapor deposition of porous/dense $SiN_{1.3}$ optical multilayers", *Thin Solid Films,* **469-470** (2004) 47-53.

[25] D. Dalacu and L. Martinu, "Spectroellipsometric characterization of plasma-deposited Au/SiO_2 nanocomposite films", *J. Appl. Phys.* **87**, (2000) 228-235.

[26] P. Jedrzejowski, B. Baloukas, J. E. Klemberg-Sapieha and L. Martinu, "Optical characterization of $TiN/SiN_{1.3}$ nanocomposite coatings", *J. Vac. Sci. Technol.* **A22** (2004) 725-733.

[27] P. Jedrzejowski, J. E. Klemberg-Sapieha, and L. Martinu, "Optical properties and color of hard quaternary nanocomposite TiC_xN_y/SiCN coatings prepared by plasma-enhanced chemical vapour deposition", *Surf. Coat. Technol.* **188-189** (2004) 371-375.

[28] L. Martinu and D. Poitras, "Plasma deposition of optical films and coatings: a review", *J. Vac. Sci. Technol.* **A18** (2000) 2619-2645.

[29] Invited talks given by Macleod and Dobrowolski at the Optical Society of America's 8^{th} topical meeting on Optical Interference Coatings, July 2004, Tucson, Az.

[30] L. Martinu, J. E. Klemberg-Sapieha, and M. R. Wertheimer, "Dual-mode microwave/radio frequency plasma deposition of dielectric thin films" *Appl. Phys. Lett.* **54** (1989) 2645-2647.

[31] A. Hallil, O. Zabeida, M. R. Wertheimer, and L. Martinu, "Mass-resolved ion energy distributions in continuous dual mode microwave/radio frequency plasmas in argon and nitrogen" *J. Vac. Sci. technol.* **A18** (2000) 882-890.

[32] O. M. Küttel, J. E. Klemberg-Sapieha, L. Martinu, and M. R. Wertheimer, "Energy Fluxes in Mixed Microwave-R.F. Plasma", *Thin Solid Films*, **193/194** (1990) 155-163.

[33] A. von Keudell, "Surface Processes during thin-film growth", *Plasma Sources Sci. Technol.* **9** (2000) 455-467.

[34] A. Raveh, J. E. Klemberg-Sapieha, L. Martinu, and M. R. Wertheimer, "Deposition and properties of diamondlike carbon films produced in microwave and radio-frequency plasma", *J. Vac. Sci. Technol.* **A10** (1992) 1723-1727.

[35] J. Vlcek, K. Rusnak, V. Hejek, and L. Martinu, "Reactive magnetron sputtering of CN_x films: Ion bombardment effects and process characterization using optical emission spectroscopy", *J. Appl. Phys.* **86** (1999) 3646-3654.

[36] E. M. Liston, L. Martinu, and M. R. Wertheimer, "Plasma surface modification of polymers for improved adhesion: a critical review" *J. Adh. Sci. Technol.* **7** (1993) 1091-1127.

[37] C. Wild and P. Koidl, "Ion and electron dynamics in the sheath of radio-frequency glow discharges", *J. Appl. Phys.* **69** (1991) 2909-2922.

[38] J. Segner in *Thin Films for Optical Systems*, edited by F. R. Flory (Marcel Dekker, New York, 1995), Chap. 7, p. 209.

[39] *Thin Films on Glass, Schott Series on Glass and Glass Ceramics*, edited by H. Bach and D. Krause (Springer, Berlin, 1997).

[40] J. C. Angus, P. Koidl, and S. Domitz, *Plasma Deposited Thin Films*, edited by J. Mort and F. Jansen, Chemical Rubber Company , Boca Raton, Fl., 1986.

[41] Y. Lifshitz, S. R. Kasi, and J. W. Rabalais, "Subplantation model for film growth from hyperthermal species: application to diamond" *Phys. Rev. Lett.* **62** (1989) 1290-1293.

[42] Y. Lifshitz, S. R. Kasi, and J. W. Rabalais, "Subplantation model for film growth from hyperthermal species" *Phys. Rev.* ***B*****62** (1990) 10468-10480.

[43] J. Opsal, J. Fanton, J. Chen, J. Leng, L. Wei, C. Uhrich, M. Senko, C. Zaiser, and D. E. Aspnes, "Broadband spectral operation of a rotating-compensator ellipsometer", *Thin Solid Films* **313-314** (1998) 58-61.

[44] D. E. Aspnes, "Expanding horizons: new developments in ellipsometry and polarimetry", *Thin Solid Films* **455-456** (2004) 3-13.

[45] Y. Cong, I. An, K. Vedam, and R. W. Collins, "Optical characterization of a four-medium thin film structure by real-time spectroscopic ellipsometry: amorphous carbon on tantalum", *Appl. Opt.* **30** (1991) 2692-2703.

[46] P. J. Van Den Oever, M. C. M. Van de Sanden, and W. M. M. Kessels, "Roughness evolution of high-rate deposited a-SiN_x:H films studied by atomic force microscopy and

real-time spectroscopic ellipsometry", in *Amorphous and Nanocrystalline Silicon Science and Tehcnology, Mat. Res. Soc. Symp. Proc.* **808** (2004) 233-238.

[47] R. W. Collins, and J. M. Cavese, "Effect of deposition conditions on the nucleation and growth of glow-discharge a-Si:H" J. *Appl. Phys.* **61** (1987) 1869-1881.

[48] A. M. Antoine, and B. Drevillon, "Influence of the substrate on the early stage of the growth of hydrogenated amorphous silicon evidenced by kinetic ellipsometry", *J. Appl. Phys.* **63** (1988) 360-367.

[49] R. M. A. Azzam, and N. M. Bashara, *Ellipsometry and Polarized Light* (North-Holland, Amsterdam, 1977).

[50] K. Fock, "The simultaneous determination of n, k, and t from polarimetric data", *Thin Solid Films* **455-456** (2004) 349-355.

[51] P. J. McMarr, K. Vedam, and J. Narayan, "Spectroscopic ellipsometry: a new tool for non-destructive depth profiling and characterization of interfaces", *J. Appl. Phys.* **59** (1986) 694-701.

[52] D. W. Hoffman, and R. C. McCurne, "Microstructural control of plasma-sputtered refractory coatings", in *Handbook of Plasma Processing Technology*, edited by S. M. Rossnagel, J. J. Cuomo, and W. D. Westwood, Noyes Publications, Park Ridge, 1990, p. 483-517.

[53] I. Petrov, P. B. Barna, L. Huttman, and J. E. Greene, "Microstructural evolution during film growth", *J. Vac. Sci. Technol.* **A21** (2003) S117-S128.

[54] L. Martinu, J. E. Klemberg-Sapieha, O. M. Küttel, A. Raveh, and M. R. Wertheimer, "Critical ion energy and ion flux in the growth of films by plasma-enhanced chemical vapour deposition", *J. Vac. Sci. Technol.* **A12** (1994) 1360-1364.

[55] L. Martinu, J. E. Klemberg-Sapieha, and M. R. Wertheimer, "Dual-frequency deposition of high quality insulating thin films", in *Proc. 4th Int. Conf, Prop. Appl. Diel. Mat.* (1994) 227-230.

[56] D. Poitras, "Admittance diagrams of accidental and premeditated optical inhomogeneities in coatings", *Appl. Opt.* **41** (2002) 4671-4679.

[57] K. C. Cadien, M. A. Ray, S. M. Shin, J. M. Rigsbee, S. A. Barnett, and J. E. Greene, "Ion mixing during film deposition: Growth of metastable semiconducting and metallic alloys", *J. Vac. Sci. Technol.* **20** (1982) 370-371.

[58] J. E. Greene, T. Motooka, J.-E. Sundgren, D. Lubben, S. Gorbatkin, and S. A. Barnett, "The role of ion/surface interactions and photo-induced reactions during film growth from the vapor phase", *Nucl. Intr. Meth.* **B27** (1987) 226-242.

[59] W. Bolse, "Mechanisms of ion beam induced atomic mixing in solids", *Mat. Sci. Eng.* **A233** (1998) 194-201.

[60] N. D. Telling, S. J. Guilfoyle, D. R. Lovett, C. C. Tang, M. D. Crapper, and M. Petty, "Evidence of roughness distributions and interface smoothing in Co/Cu multilayers deposited under energetic particle bombardment", *J. Phys.* **D31** (1998) 472-481.

[61] W. Eckstein, *Computer Simulation of Ion Solid Interactions* (Springer, Berlin, 1991).

[62] J. F. Ziegler, J. P. Biersack, and U. Littmark, *The Stopping and Range of Ions in Matter*, vol. 1 (Pergamon, New York, 1985).

[63] W. Möller, and W. Eckstein, "TRIDYN-a TRIM simulation code including dynamic composition changes", *Nucl. Instr. Meth.* **B2** (1984) 814-818.

[64] W. Möller, W. Eckstein, and J. P. Biersack, "TRIDYN-binary collision simulation of atomic collisions and dynamic composition changes in solids", *Comput. Phys. Commun.* **51** (1988) 355-368.

[65] J. Nord, K. Nordlund, and J. Keinonen, "Amorphization mechanism and defect structures in ion-beam-amorphized Si, Ge, and GaAs", *Phys. Rev.* **B65** (2002) 165329-165343.

[66] L. Hanley, and S. B. Sinnott, "The growth and modification of materials via ion-surface processing", *Surf. Sci.* **500** (2002) 500-522.

[67] L. Martinu, O.M. Küttel, A. Raveh, J.E. Klemberg-Sapieha, and M.R. Wertheimer, "Critical ion energies and ion fluxes", *J, Vac. Sci. Technol.* **A12** (1994) 1360-1364.

[68] J. A. Brinkman, "On the nature of radiation damage in metals", *J. Appl. Phys.* 25 (1954) 961-970.

[69] P. Sigmund in *Sputtering by Particle Bombardment I*, edited by R. Behrish (Springer, Berlin, 1981), p. 9.

[70] P. Sigmund, "Collision theory of displacement damage, ion ranges, and sputtering", *Rev. Roum. Phys.* **17** (1972) 823-870.

[71] J. Lindhard and M. Scharff, "Energy dissipation by ions in the keV region", *Phys. Rev.* **124** (1961) 128-130.

[72] J. F. Ziegler, 'SRIM 2003', computer simulation software available for download via internet http://www.SRIM.org.

[73] H. Gnaser, H. L. Bay, and W. O. Hofer, "Depth distribution of low-energy ^{4}He implanted in solids", *Nucl. Instrum. Meth.* **B15** (1986) 49-53.

[74] J. S. Williams, M. Petravic, B. G. Svensson, and M. Conway, "Oxidation of silicon by low energy oxygen bombardment", *J. Appl. Phys.* **76** (1994) 1840-1846.

[75] J. F. Ziegler, *Handbook of Stopping Cross Sections for Energetic Ions in all Elements* (Pergmon, New York, 1980).

[76] L. Pelaz, L. A. Marqués, M. Aboy, J. Barbolla, and G. H. Gilmer, "Atomistic modeling of amorphization and recrystallization in silicon", *Appl. Phys. Lett.* **82** (2003) 2038-2040.

[77] L. A. Marqués, L. Pelaz, M. Aboy, L. Enríquez, and J. Barbolla, "Microscopic description of the irradiation-indiced amorphization in silicon", *Phys. Rev. Lett.* **91** (2003) 135504-135507.

[78] L. Csepregi, E. F. Kennedy, J. W. Mayer, and T. W. Sigmon, "Substrate-orientation dependence of the epitaxial regrowth rate from Si-implanted amorphous Si", *J. Appl. Phys.* **49** (1978) 3906-3911.

[79] Y. Masaki, P. G. LeComber, and A. G. Fitzgerald, "Solid phase crystallization of thin films of Si prepared by plasma-enhanced chemical vapor deposition", *J. Appl. Phys.* **74** (1993) 129-134.

[80] J. S. Williams, "Ion implantation of semiconductors", *Materials Science and Engineering* **A253** (1998) 8-15.

[81] W. Bock, H. Gnaser, and H. Oechsner, "Modification of crystalline semiconductor surfaces by low-energy Ar^+ bombardment: Si(111) and Ge(100)", *Surf. Sci.* **282** (1993) 333-341.

[82] D. K. Brice, J. Y. Tsao, and S. T. Picraux, "Partitioning of ion-induced surface and bulk displacements", *Nucl. Instrum. Meth.* **B44** (1989) 68-78.

[83] A. Claverie, C. Vieu, J. Fauré, and J. Beauvillain, "Cross-sectional high-resolution electron microscopy investigation of argon-ion implantation-induced amorphization of silicon", *J. Appl. Phys.* **64** (1988) 4415-4423.

[84] F. L. Vook in *Proc. Conf. On Radiation damage and defects in semiconductors, Reading*, 19-21 July 1972, edited by J. E. Whitehouse (Institute of Physics, London, 1973) pp. 60-71.

[85] K.-W. Wang, W. G. Spitzer, G. K. Hubler, and D. K. Sadana, "Ion implantation of Si by ^{12}C, ^{29}Si, and ^{120}Sn: amorphization and annealing effects" *J. Appl. Phys.* **58** (1985) 4553-4564.

[86] M. J. Caturla, T. Diaz de la Rubia, and G. H. Gilmer, "Disordering and defect production in silicon by keV ion irradiation studied by molecular dynamics", *Nucl. Instrum. Meth.* **B106** (1995) 1-4.

[87] H. Hensel and H. Urbassek, "Implantation and damage under low-energy Si self-bombardment", *Phys. Rev.* **B57** (1998) 4756-4763.

[88] T. Diaz de la Rubia and G. H. Gilmer, "Structural transformation and defect production in ion implanted silicon : a molecular dynamics simulation study", *Phys. Rev. Lett.* **74** (1995) 2507-2510.

[89] M. R. Pascucci, J. L. Hutchison, and L. W. Hobbs, "The metamict transformation in alpha-quartz", *Radiat. Eff.* **74** (1983) 219-226.

[90] S. U. Campisano, S. Coffa, V. Rainieri, F. Priolo, and E. Rimini, "Mechanisms of amorphization in ion implantated crystalline silicon", *Nucl. Instrum. Meth.* **B80-81** (1993) 514-518.

[91] W. Bolse, "Formation and development of disordered networks in Si-based ceramics under ion bombardment", *Nucl. Instrum. Meth.* **B141** (1998) 133-139.

[92] J. F. Gibbons, "Ion implantation in semiconductors. II. Damage production and annealing", *Proceedings of the IEEE* **60** (1972) 1062-1096.

[93] N. Hecking, K. F. Heidemann, and E. T. Kaat, "Model of temperature dependent defect interaction and amorphization in crystalline silicon during ion irradiation", *Nucl. Instrum. Meth.* **B15** (1986) 760-764.

[94] J. K. N. Lindner, K. F. Heidemann, and E. T. Kaat, "Radiation damage and amorphization of silicon by 6 MeV Ni ion implantation", *Nucl. Instrum. Meth.* **B39** (1989) 306-310.

[95] J. K. N. Lindner, R. Zuschlag, and E. T. Kaat, "Radiation damage and amorphization of silicon by 2 MeV nitrogen ion implantation", *Mat. Sci. Eng.* **B12** (1992) 7-11.

[96] J. K. N. Lindner, "Radiation damage of 2 MeV Si ions in $Si_{0.75}Ge_{0.25}$: Optical measurements and damage modelling", *Nucl. Instrum. Meth.* **B112** (1996) 316-320.

[97] W. J. Weber and L. M. Wang, "The temperature dependence of ion-beam-induced amorphization in beta –SiC", *Nucl. Instrum. Meth.* **B106** (1995) 298-302.

[98] W. J. Weber, "Models and mechanisms of irradiation-induced amorphization in ceramics", *Nucl. Instrum. Meth.* **B166-167** (2000) 98-106.

[99] O. Vancauwenberghe, O. C. Hellman, N. Herbots, and W. J. Tan, "New SiGe dielectrics grown at room temperature by low-energy ion beam oxidation and nitridation", *Appl. Phys. Lett.* **59** (1991) 2031-2033.

[100] O. Vancauwenberghe, N. Herbots, and O. C. Hellman, "Role of ion energy in ion beam oxidation of semiconductors: Experimental study and model", *J. Vac. Sci. Technol.* **A10** (1992) 713-718.

[101] S. S. Todorov, I. R. Chakarov and D. S. Karpuzov, "Low energy ion beam oxidation of silicon surfaces: ballistics, diffusion and chemistry", *Nucl. Instr. Meth.* **B65** (1992) 79-83.

[102] D. L. Pulfrey, F. G. M. Hathorn, and L. Young, "The anodization of Si in an RF plasma", *J. Electrochem. Soc.* **120** (1973) 1529-1535.

[103] D. W. Hess, "Plasma-assisted oxidation, anodization and nitridation of silicon", *IBM. J. Res. Develop.* 43 (1999) 127-145.

[104] J. R. Ligenza, "Silicon oxidation in an oxygen plasma excited by microwaves" *J. Appl. Phys.* **36** (1965) 4323-4330.

[105] J. Kraitchman, "Silicon oxide films grown in a microwave discharge", *J. Appl. Phys.* **38** (1967) 4323-4330.

[106] N. Cabrera and N. Mott, "Theory of the oxidation of metals", *Rept. Prog. Phys.* **12** (1948) 163-184.

[107] Y. Z. Hu, J. Joseph, and E. A. Irene, "*In situ* spectroscopic ellipsometry study of the electron cyclotron resonance plasma oxidation of silicon and interfacial damage", *Appl. Phys. Lett.* **59** (1991) 1353-1355.

[108] J. Joseph, Y. Z. Hu, and E. A. Irene, "A kinetic study of the electron cyclotron resonance plasma oxidation of silicon", *J. Vac. Sci. technol.* **B10** (1992) 611-617.

[109] P. R. Levebvre, and E. A. Irene, "Comparison of Si and GaAs/interfaces resulting from thermal and plasma oxidation", *J. Vac. Sci. Technol.* **B15** (1997) 1173-1181.

[110] Y. Z. Hu, Y. O. Wang, M. Li, J. Joseph, and E. A. Irene, "*In situ* investigation of temperature and bias dependent effects on the oxide growth of Si and Ge in an electron cyclotron resonance", *J. Vac. Sci. Technol.* **A11** (1993) 900-904.

[111] A. T. Fromhold, Jr. and M. Baker, "Oxide growth in an RF plasma", *J. Appl. Phys.* **51** (1980) 6377-6392.

[112] S. A. Nelson and R. A. Buhrman, "Thin silicon oxides growth by low-temperature RF plasma anodization and deposition", *Appl. Phys. Lett.* **50** (1987) 1095-1097.

[113] S. A. Nelson, H. D. Hallen, and R. A. Buhrman, "A structural and electrical comparison of thin SiO_2 films grown on silicon by plasma anodization and rapid thermal processing to furnace oxidation", *J. Appl. Phys.* **63** (1988) 5027-5035.

[114] R. A. Street, *Hydrogenated Amorphous Silicon* (Cambridge University Press, Cambridge, 1991).

[115] C. H. Herzinger, B. Johs, W. A. McGahan, J. A. Woollam, and W. Paulson, "Ellipsometric determination of optical constants for silicon and thermally grown silicon dioxide via a multi-sample, multi-wavelength, multi-angle investigation", *Appl. Opt.* **83** (1998) 3323-3236.

[116] H. Piller, in *Handbook of Optical Constants of Solids: Part II*, edited by E. D. Palik (Academic Press, New York, 1991), p. 571.

[117] H. R. Philipp, in *Handbook of Optical Constants of Solids*, edited by E. D. Palik (Academic Press, New York, 1985), p. 765.

[118] H. R. Philipp, in *Handbook of Optical Constants of Solids*, edited by E. D. Palik (Academic Press, New York, 1985), p. 749.

[119] D. E. Aspnes, "Optical properties of thin films", *Thin Solid Films* **89** (1982) 249-262.

[120] Y. Z. Hu, M. Li, K. Conrad, J. W. Andrews, E. A. Irene, M. Denker, M. Ray, and G. McGuire, "*In situ* spectroscopic ellipsometry studies of hydrogen ion bombardment of crystalline silicon", *J. Vac. Sci. Technol.* **B10** (1992) 1111-1117.

[121] Y. Z. Hu, J. Joseph, and E. A. Irene, "*In situ* spectroscopic ellipsometry study of the electron cyclotron resonance plasma oxidation of silicon and interfacial damage", *Appl. Phys. Lett.* **59** (1991) 1353-1355.

[122] E. A. Irene, "Applications of spectroscopic ellipsometry in microelectronics", *Thin Solid Films* **233** (1993) 96-111.

[123] D. E. Aspnes, and A. A. Studna, "An investigation of ion-bombarded and annealed <111> surfaces of Ge by spectroscopic ellipsometry", *Surf. Sci.* **96** (1980) 294-306.

[124] R. W. Collins, "Structural studies of hydrogen-bombarded silicon using ellipsometry and transmission electron microscopy", *J. Vac. Sci. Technol.* **A4** (1986) 153-158.

[125] A. H. M. Holtslag, U. C. Slager, and A. van Silfhout, "The interpretation of ellipsometric measurements of ion bombardmenent of noble gases on semiconductor surfaces", *Surf. Sci.* **152/153** (1985) 1079-1085.

[126] J. L. Buckner, D. J. Vitkavage, and E. A. Irene, "Ellipsometric and Rutherford backscattering characterization of low-energy hydrogen-, helium-, neon-, and argon-bombarded silicon" *J. Appl. Phys.* **63** (1988) 5788-5794.

[127] M. Fried, T. Lohner, W. A. M. Aarnink, L. J. Hanekamp, and A. van Silfhout, "Non-destructive determination of damage depth profiles in ion-implanted semiconductors by spectroscopic ellipsometry using different optical models", *J. Appl. Phys.* **71** (1992) 2835.

[128] P. K. Giri, S. Tripurasundari, G. Raghavan, B. K. Panigrahi, P. Magudapathy, K. G. M. Nair, and A. K. Tyagi, "Crystalline to amorphous transition and band structure evolution in ion-damaged silicon studied by spectroscopic ellipsometry", *J. Appl. Phys.* **90** (2001) 659-669.

[129] D. E. Aspnes, S. M. Kelso, C. G. Olson, and D. Y. Lynch, "Direct determination of sizes of excitations from optical measurements on ion-implanted GaAs", *Phys. Rev. Lett.* **48** (1982) 1863-1866.

[130] P. B. Barna and M. Adamik, "Fundamental structure forming phenomena of polycrystalline films and the structure zone models", *Thin Solid Films* **317** (1998) 64-68.

[131] H. Lewis, "Considerations of telescopic field of view in the prescribing of low vision lenses", *Thin Solid Films* **48** (1971) 953-960.

[132] J. F. Pocza, A. Barna, and P. B. Barna, "Formation processes of vacuum-deposited indium films and thermodynamical properties of submicroscopic particles observed by *in situ* electron microscopy", *J. Vac. Sci. Technol.* **6** (1969) 472-475.

[133] B. A. Movchan and A. V. Demishin, "Investigation of the structure and properties of thick vacuum- deposited films of nickel, titanium, tungsten, alumina and zirconium dioxide", *Fiz. Met. Metallov.* **28** (1969) 653-660.

[134] R. Messier, "Toward quantification of thin film morphology", *J. Vac. Sci. Technol.* **A4** (1986) 490-495.

[135] A. L. Barabasi and H. E. Stanley, *Fractal Concepts in Surface Growth* (Cambridge University Press, Cambridge, UK, 1995).

[136] I. Petrov, L. Hultman, U. Helmersson, J.-E. Sundgren, and J. E. Greene, "Microstructure modification of TiN by ion bombardment during reactive sputter deposition", *Thin Solid Films* **169** (1989) 299-314.

[137] N. Kaiser, "Review of fundamentals of thin-film growth", *Appl. Opt.* **41** (2002) 3053-3060.

[138] D. Dobrev, "Ion-beam-induced texture formation in vacuum-condensed thin metal films", *Thin Solid Films* **92** (1982) 41-53.

[139] K. H. Muller, "Dependence of thin-film microstructure on deposition rate by means of a computer simulation", *J. Appl. Phys.* **58** (1985) 2573-2576.

[140] J. M. E. Harper, J. J. Cuomo, and H. T. G. Hentzel, "Synthesis of compound thin films by dual ion beam deposition. I. Experimental approach", *J. Appl. Phys.* **58** (1985) 550-555.

[141] J. E. Greene, S. A. Barnett, J.-E. Sundgren, and A. Rockett, in *Ion Beam Assisted Film Growth*, edited by T. Itoh (Elsevier, Amsterdam, 1988), Chap. 5.

[142] J. A. Thornton, "The microstructure of sputter-deposited coatings", *J. Vac. Sci. Technol.* **A4** (1986) 3059-3065.

[143] R. Messier, A. P. Giri, and R. A. Roy, "Revised structure zone model for thin film physical structure", *J. Vac. Sci. Technol.* **A2** (1984) 500-503.

[144] C. R. M. Grovenor, H. T. G. Hentzel, and D. A. Smith, "The development of grain structure during growth of metallic films", *Acta Metall.* **32** (1984) 773-781.

[145] K.-H. Muller, "Stress and microstructure of sputter-deposited thin films: Molecular dynamics investigations", *J. Appl. Phys.* **62** (1987) 1796-1799.

[146] J. E. Klemberg-Sapieha, O. M. Küttel, L. Martinu, M. R. Wertheimer, "Dual microwave-RF plasma deposition of functional coatings", *Thin Solid Films* **193/194** (1990) 965-972.

[147] S. Larouche, *Étude de mélanges de SiO_2/TiO_2 déposés par PECVD et fabrication de filtres à gradient d'indice*, Master's thesis, Départment de génie physique, École Polytechnique de Montréal, 2003.

[148] C. Lavoie, M. Meunier, R. Izquierdo, S. Boivin, and P. Desjardins, " Large area excimer laser induced deposition of titanium from titanium tetrachloride", *Appl. Phys.* **A53** (1991) 339-342.

[149] D. Poitras, P. Leroux, J. E. Klemberg-Sapieha, S. C. Gujrathi, and L. Martinu, "Characterization of homogeneous and inhomogeneous Si-based optical coatings deposited in dual-frequency plasma", *Opt. Eng.* **35** (1996) 2693-2699.

[150] F. Abelès, "Recherches sur la propagation des ondes électromagnétiques sinusoïdales dans les milieux stratifiés. Application aux couches minces", *Annales de la Physique* **5** (1950) 596-640.

[151] H. A. Macleod, *Thin-Film Optical Filters*, 3rd edition (Institute of Physics Publishing, Bristol, UK, 2001).

[152] K. Levenberg, "A method for the solution of certain nonlinear problems in least squares", *Quarterly Appl. Math.* **2** (1944) 164-168.

[153] D. W. Marquardt, "Solution of nonlinear chemical engineering models", *Chem. Eng. Progress* **55** (1959) 65-70.

[154] R. Fletcher, *Practical Methods of Optimization*, 2nd edition, Wiley, New York, 1987.

[155] J. A. Woollam, B. Johs, C. M. Herzinger, J. N. Hilfiker, R. Synowicki, and C. Bunguay, "Overview of variable angle spectroscopic ellipsometry (VASE), part I: basic theory and typical applications", in *SPIE proceedings* **CR72** (1999) 29-58.

[156] US Patent #5,757,494 "System and method or improving data acquisition capability in spectroscopic ellipsometers".

[157] WVASE32, version 3.445, J. A. Woollam Co. Inc.

[158] T. Mori and D. E. Aspnes, "Comparison of the capabilities of rotating-analyzer and rotating-compensator ellipsometers by measurements on a single system", *Thin Solid Films* **455-456** (2004) 33-38.

[159] D. E. Aspnes, "Optimizing precision of rotating-analyzer and rotating-compensator ellipsometers", *J. Opt. Soc. America* **A21** (2004) 403-410.

[160] B. Johs and C. M. Herzinger, "Precision in ellipsometrically determined sample parameters: simulation and experiment", *Thin Solid Films* **455-456** (2004) 66-71.

[161] R. Kleim, L. Kuntzler, and A. El Ghemmaz, "Systematic errors in rotating-compensator ellipsometry", *J. Opt. Soc. America* **A11** (1994) 2550-2559.

[162] B. Johs, J. A. Woollam, C. M. Herzinger, J. N. Hilfiker, R. Synowicki, and C. Bungay, "Overview of variable angle spectroscopic ellipsometry (VASE), part II: advanced applications", in *SPIE proceedings* **CR72** (1999) 59-72.

[163] EASE software, version 1.39, J. A. Woollam Co. Inc.

[164] W. Eckstein, C. Garcia-Rosales, J. Roth, and J. Laszlo, "Threshold energy for sputtering and its dependence on angle of incidence", *Nucl. Instrum. Meth.* **B83** (1993) 95-109.

[165] M. T. Robinson and I. M. Torrens, "Computer simulation of atomic-displacement cascades in solids in the binary collision approximation", *Phys. Rev.* **B9** (1974) 5008-5024.

[166] S. Tachi and K. Miyake, "Plasma etching mechanism of silicon studied by mass-selected ion beam irradiation", *Semicond. Technol.* **1984** (1984) 343-357.

[167] A. Amassian, P. Desjardins, and L. Martinu, "Study of TiO_2 film growth mechanisms in low-pressure plasma by *in situ* real-time spectroscopic ellipsometry" *Thin Solid Films* **447-448** (2004) 40-45.

[168] D. A. Cole, J. R. Shallenberger, S. W. Novak, R. L. Moore, M. J. Edgell, S. P. Smith, C. J. Hitzman, J. F. Kirchhoff, E. Principe, W. Nieveen, F. K. Huang, S. Biswas, R. J. Bleiler, and K. Jones, "SiO_2 thickness determination by x-ray photoelectron spectroscopy, Auger electron spectroscopy, secondary ion mass spectrometry, Rutherford backscattering, transmission electron microscopy, and ellipsometry" *J. Vac. Sci. Technol.* **B18** (2000) 440-444.

[169] Y. Z. Hu, M. Li, K. Conrad, J. W. Andrews, E. A. Irene, M. Denker, M. Ray, and G. McGuire, "*In situ* spectroscopic ellipsometry studies of hydrogen ion bombardment of crystalline silicon", *J. Vac. Sci. Technol.* **B10** (1992) 1111-1117.

[170] G. E. Jellison Jr, and F. A. Modine, "Parameterization of the optical functions of amorphous materials in the interband region", *Appl. Phys. Lett.* **69** (1996) 371-373.

[171] H. Jenett, and V.-D. Hodoroaba, "Energy spectra of secondary neutrals obtained by means of the electrostatic energy filter of a commercial low-pressure HF-plasma secondary neutral mass spectrometer" *J. Vac. Sci. Technol.* **A15** (1997) 3158-62.

[172] T. Ueno, T. Akiyama, K. Kuroiwa, and Y. Tarui, "Highly efficient generation of high-energy photons and low-temperature oxidation of a crystal silicon surface with O^1D Radicals", *Appl. Surf. Sci.* **79/80** (1994) 502-506.

[173] W. J. Weber, F. Gao, R. Devanathan, W. Jiang, and C. M. Wang, "Ion-beam induced defects and nanoscale amorphous clusters in silicon carbide", *Nucl. Instrum. Meth.* **B216** (2004) 25-35.

[174] Y. Yao, Z. Hargitai, M. Albert, R. G. Albridge, A. V. Barnes, J. M. Gilligan, B. Pratt Ferguson, G. Lüpke, V. D. Gordon, N. H. Tolk, J. C. Tully, G. Betz, and W. Husinsky, "New molecular collisional interaction effect in low-energy sputtering", *Phys. Rev. Lett.* **81** (1998) 550-553.

[175] G. H. Kinchin, and R. S. Pease, "The displacement of atoms in solids by radiation", *Rep. Prog. Phys.* **18** (1955) 1-51.

[176] S. Reinke, R. Freudenstein, and W. Kulisher, "On the role of ion bombardment in cubic boron nitride deposition", *Surf. Coat. Technol.* **97** (1999) 263-269.

[177] C. Fitz, A. Kolistsh, W. Moller, and W. Fukarek, "Growth of low-stress cubic boron nitride films by simultaneous medium-energy ion implantation", *Appl. Phys. Lett.* **80** (2002) 55-57.

[178] A. Amassian, M. Svec, P. Desjardins, and L. Martinu, "Interface broadening due to ion mixing during thin film growth in plasma-enhanced chemical vapor deposition environment", *J. Vac. Sci. Technol. A* (submitted).

[179] E. M. Liston, L. Martinu, and M. R. Wertheimer, "Plasma surface modifications of polymers for improved adhesion: a critical review", *J. Adhesion Sc. Technol.* **7** (1993) 1091-1127.

[180] O. Zabeida, J. E. Klemberg-Sapieha, L. Martinu, and D. Morton, "Effect of ion bombardment in polymer surface modification: comparison of pulsed high frequency plasma and ion beam", in *Mat. Res. Soc. Proc.* **544** (1999) 233-238.

[181] S. Vallon, A. Hofrichter, L. Guyot, B. Drevillon, J. E. Klemberg-Sapieha, L. Martinu, and F. Poncin-Epaillard, "Adhesion mechanisms of silica layers on plasma-treated polymers. I. Polycarbonate", *J. Adhesion Sci. Technol.* **10** (1996) 1287-1311.

[182] F. Sanchette, E. Damond, M. Buvron, L. Henry, P. Jacquot, N. Randall, and P. Alers, "Single cycle plasma nitriding and hard coating deposition in a cathodic arc evaporation device", *Surf. Coat. Technol.* **94-95** (1997) 261-267.

[183] W. Liang, G. Yuzhou, and X. Bin, "Plasma vapor deposition of hard coatings on pre-nitrided low alloy steel", *Surf. Coat. Technol.* **131** (2000) 452-456.

[184] P.J. Revell and G. F. Goldspink, "A review of reactive ion beam etching for production", *Vacuum* **34** (1984) 455-462.

[185] A. A. Orlikovskii, "Plasma processes in micro- and nanoelectronics. I. Reactive ion etching", *Mikroelektronika* **28** (1999) 344-362.

[186] N. Layadi, J. I. Colonell, and J. T.-C. Lee, "An introduction to plasma etching for VLSI circuit technology", *Bell Labs Tech. J.* **4** (1999) 155-171.

[187] G. S. Oehrlein, M. F. Doemling, B. E. E. Kastenmeier, P. J. Matsuo, N. R. Rueger, M. Schaepkens, and T. E. F. M. Standaert, "Surface science in plasma etching", *IBM J. Res. Devel.* **43** (1999) 181-197.

[188] P. K. Chu, "Recent developments and applications of plasma immersion ion implantation", *J. Vac. Sci. Technol.* **B22** (2004) 289-296.

[189] P. K. Chu, "Semiconductor applications of plasma immersion ion implantation", *Plasma Phys. Controlled Fusion* **45** (2003) 555-570.

[190] Z. Zeng, R. K. Y. Fu, X. Tian, and P. K. Chu, "Plasma immersion ion implantation of industrial gears", *Surf. Coat. Technol.* **186** (2004) 260-264.

[191] M. Bruel, "Silicon on insulator material technology", *Electron. Lett.* **31** (1995) 1201-1202.

[192] W. Moeller, and S. Mukherjee, "Plasma-based ion implantation", *Current Sci.* **83** (2002) 237-253.

[193] K. Tanaka and A. Matsuda, "Glow-discharge amorphous silicon: growth process and structure", *Mater. Sci. Rep.* **2** (1987) 139-184.

[194] R. Vernhes, A. Amassian, J. E. Klemberg-Sapieha, and L. Martinu, "Plasma treatment of porous SiN_x:H films for the fabrication of porous-dense multilayer optical filters with tailored interfaces" (in preparation).

[195] A. Amassian, P. Desjardins, and L. Martinu, "Ion-Surface Interactions on c-Si (001) at the Radiofrequency-Powered Electrode in Low-Pressure Plasmas: *Ex Situ* Spectroscopic Ellipsometry and Monte-Carlo Simulation Study", *J. Vac. Sci. Technol.* **A** (in press).

[196] T. Motooka, "The role of defects during amorphization and crystallization processes in ion implanted Si", *Mat. Sci. Eng.* **A253** (1998) 42-49.

[197] E. B. Svedberg, J. Birch, I. Ivanov, E. P. Münger, and J.-E. Sundgren, "Asymmetric interface broadening in epitaxial Mo/W (001) superlattices grown by magnetron sputtering", *J. Vac. Sci. Technol.* **A16** (1998) 633-638.

[198] D. Depla, Z. Y. Chen, A. Bogaerts, V. Ignatova, R. De Gryse, and R. Gijbels, "Modeling of the target surface modification by reactive ion implantation during magnetron sputtering", *J. Vac. Sci. Technol.* **A22** (2004) 1524-1529.

[199] S.-Y. Chun, "TEM-examination and computer simulation of nano-scale multilayers by pulsed cathodic arc deposition", *J. Ceramic Processing Res.* **4** (2003) 115-117.

[200] J. Sik, J. Hora, and J. Humlicek, "Optical functions of silicon at high temperature", *J. Appl. Phys.* **84** (1998) 6291-6298.

[201] G. E. Jellison, Jr and F. A. Modine, "Optical functions of silicon between 1.7 and 4.7 eV at elevated temperatures", *Phys. Rev.* **B27** (1983) 7466-7472.

[202] D. Daineka, V. Suendo, and P. Roca i Cabarrocas, "Temperature dependence of the optical function of amorphous silicon-based materials: application to *in situ* temperature measurements by spectroscopic ellipsometry", *Thin Solid Films* **468** (2004) 298-302.

[203] K. Kaminska, A. Amassian, N. Davis, L. Martinu, and K. Robbie, "Ellipsometric analysis of high temperature glancing angle deposited amorphous silicon films", *Thin Solid Films* (submitted).

[204] E. A. Irene, "Applications of spectroscopic ellipsometry to microelectronics", *Thin Solid Films* **223** (1993) 96-111.

[205] J. D'Arcy-Gall, D. Gall, P. Desjardins, I. Petrov, and J. E. Greene, "Role of fast sputtered particles during sputter deposition: Growth of epitaxial $Ge_{0.99}C_{0.01}$/Ge(001)", *Phys. Rev.* **B62** (2000) 11203-11208.

[206] H. D. Mieskes, W. Assmann, F. Gruner, Z. G. Wang, and M. Toulemonde, "Electronic and nuclear thermal spike effects in sputtering of metals with energetic heavy ions", *Phys. Rev.* **B67** (2003) 155414-155415.

[207] D. Rats, D. Poitras, J. M. Soro, L. Martinu, and J. von Stebut, "Mechanical Properties of plasma-deposited silicon-based inhomogeneous optical coatings", *Surf. Coat. Technol.* **111** (1999) 220-228.

[208] S. Larouche, H. Szymanowski, A. Amassian, J. E. Klemberg-Sapieha, and L. Martinu, "Microstructure of SiO_2/TiO_2 Coatings and Their Use in Graded-Index Optical Filters", *Proc. 46th Ann. Tech. Conf., Society of Vacuum Coaters* (2003) 334-338.

[209] C. R. Ottermann and K. Bange, "Correlation between the density of TiO_2 films and their properties", *Thin Solid Films* **286** (1996) 32-34.

[210] M. Ishimaru, S. Harada, and T. Motooka, "Transmission electron microscopy studies of crystal-to-amorphous transition in ion implanted silicon", *J. Appl. Phys.* **81** (1997) 1126-1130.

[211] A. Barna, M. Menyhard, G. Zsolt, A. Koos, A. Zalar, and P. Panjan, "Interface broadening due to Ar^+ ion bombardment measured on Co/Cu multilayer at grazing angle of incidence", *J. Vac. Sci. Technol.* **A21** (2003) 553-557.

[212] S. Larouche, A. Amassian, S.C. Gujrathi, J.E. Klemberg-Sapieha, and L. Martinu, "Multilayer and Inhomogeneous Optical Filters Deposited by PECVD Using Titanium

Dioxide and Silicon Dioxide" in *Proc. of the Society of Vacuum Coaters 44th Ann. Tech. Conf.* (2001) 277-281.

[213] Y. Leprince-Wang, and K. Yu-Zhang, "Study of the growth morphology of TiO_2 thin films by AFM and TEM and correlation with optical properties", *Surf. Coatings Technol.* **140** (2001) 155-160.

[214] L. Hanley and S. B. Sinnott, "The growth and modification of materials via ion-surface processing", *Surf. Sci.* **500** (2002) 500-522.

[215] D. Poitras, S. Larouche, and L. Martinu, "Design and plasma-deposition of dispersion-corrected multiband rugate filters", *App. Opt.* **41** (2002) 5249-5255.

[216] A. Amassian, S. Larouche, R. Vernhes, J. E. Paultre, J. E. Klemberg-Sapieha, P. Desjardins, and L. Martinu, "Analysis and control of film growth by *in situ* real-time spectroscopic ellipsometry", in *Opto-Canada: SPIE Regional Meeting on Optoelectronics, Photonics, and Imaging*, **SPIE TD01** (2002) 493-495.

[217] B. Johs, "General virtual interface algorithm for *in situ* spectroscopic ellipsometric data analysis", *Thin Solid Films* **455-456** (2004) 632-638.

[218] R. Vernhes, A. Amassian, J. E. Klemberg-Sapieha, P. Desjardins, and L. Martinu, "Fabrication of Fabry-Pérot filters using porous-dense silicon nitride stacks with optimized interfaces" in *Optical Interference Coatings on CD-ROM* (The Optical Society of America, Washington, DC, 2004), MF3.

[219] T. C. Choy, *Effective Medium Theory: Principles and Applications* (Oxford University Press, Oxford, 1999), pp. 7-9.

[220] W. L. Bragg and A. B. Pippard, "The form birefringence of macromolecules", *Acta Crystallographia* **6** (1953) 865-867.

[221] Z. W. Kowalski, "Ion bombardment-induced surface roughness of solids", *J. Mat. Sci. Lett.* **12** (1993) 1204-1205.

[222] N. Ozaki, "Observation of silicon surface nanoholes by scanning tunneling microscopy", *Surface Science* **493** (2001) 547-545.

[223] P. Jedrzejowski, A. Amassian, E. Bousser, J. E. Klemberg-Sapieha, and L. Martinu, "Real-Time *In Situ* Growth Study of TiN- and TiC_xN_y- Based Superhard Nanocomposite Coatings Using Spectroscopic Ellipsometry", *Appl. Phys. Lett.* (in press).

[224] P. Jedrzejowski, A. Amassian, E. Bousser, L. Martinu, J. E. Klemberg-Sapieha, "Real-Time *In Situ* Growth Study of TiN–, TiC_xN_y–, and $TiSiC_xN_y$ –Based Superhard Nanocomposite Coatings Using Spectroscopic Ellipsometry" (in preparation).

[225] D. Gattler, B. Abendroth, R. Grotzschel, W. Moller, and D. Depla, "Mechanisms of target poisoning during magnetron sputtering as investigated by real-time *in situ* analysis and collisional computer simulation", *Appl. Phys. Lett.* **85** (2004) 6134-6136.

[226] F. H. Baumann, D. L. Chopp, T. Diaz de la Rubia, G. H. Gilmer, J. E. Greene, H. Huang, S. Kodambaka, P. O'Sullivan, and I. Petrov, "Multiscale modeling of thin-film deposition: Applications to Si device processing", *MRS Bull.* **26** (2001) 182-189.

[227] G. H. Gilmer, H. Huang, T. Diaz de la Rubia, J. Dalla Torre, and F. Baumann, "Lattice Monte Carlo models of thin film deposition", *Thin Solid Films* **365** (2000) 189-200.

[228] B. Abendroth, R. Gago, F. Eichhorn, and W. Moller, "X-ray diffraction study of stress relaxation in cubic boron niride films grown with simultaneous medium-energy ion bombardment" *Appl. Phys. Lett.* **85** (2004) 5905-5907.

[229] J. Lee and R. W. Collins, "Real-time characterization of film growth on transparent substrates by rotating-compensator multichannel ellipsometry", *Appl. Opt.* **37** (1998) 4230-4238.

[230] C. Basa, Y. Z. Hu, and E. A. Irene, "*In situ* ellipsometry for monitoring nucleation and growth of silicon on silicon dioxide", *Thin Solid Films* **313-314** (1998) 424-429.

[231] T. Heitz, B. Drevillon, J. E. Bouree, and C. Godet, "Early stages of the growth of hydrogenated amorphous carbon investigated by *in situ* infrared ellipsometry", *J. non-crystalline solids* **227-230** (1998) 636-640.

[232] M. Ebert, K. A. Bell, S. D. Yoo, K. Flock, and D. E. Aspnes, "*In situ* monitoring of MOVPE growth by combined spectroscopic ellipsometry and reflectance-difference spectroscopy", *Thin Solid Films* **364** (2000) 22-27.

[233] K. H. Heinig, T. Muller, B. Schmidt, M. Strobel, and W. Moller, "Interfaces under ion irradiation: growth and taming of nanostructures", *Appl. Phys.* **A77** (2003) 17-25.

Rx MEDICATION

A Caution About Breast feeding While Using Codeine

Researchers recently described a healthy breast-feeding newborn who, at the age of one week, developed difficulties breast feeding and was lethargic, and by 13 days of age he died from what was found to be extremely high levels of morphine in his blood. Because of episiotomy pain, the baby's mother has been prescribed a pain medication containing codeine, which she had taken as directed; on the second day she developed sleepiness and constipation, so she reduced the dose.

The authors point out that codeine itself is not an active drug in humans; it only becomes active when it is converted to morphine by enzymes in the body. In this tragic case, the mother had an unusual genetic variation in the enzyme that changes codeine to morphine and the enzyme produced extremely large amounts of morphine, which made her constipated and sleepy but also got to her infant via breastmilk. Because newborns have difficulty getting rid of morphine in their blood, an amount that might have been only bothersome to its mother proved fatal to the infant. ***(Koren G et al: Lancet, August 19, 2006, p. 704)***

. . . . . .

COMMENT: At first it may seem strange that taking codeine could cause toxic effects from another drug, morphine, but in fact codeine itself doesn't have pharmacologic effects until it is converted to morphine by specific enzymes in the body. Until this report, doctors were unaware that a genetic variation in a mother's codeine-converting enzymes could lead to blood levels of morphine that could be highly toxic to a breastfeeding infant.

How often might this kind of problem take place? Despite the fact that codeine is frequently used to treat episiotomy pain in new mothers, and despite the fact that these mothers often breastfeed, this is the first report of this problem that we can recall, so clearly this is not an everyday occurrence.

On the other hand, this case demonstrates that in rare circumstances, codeine taken by a breast-feeding mother can pose serious harm to her infant. For this reason, it's critically important that breast-feeding mothers who are taking codeine in the weeks after delivery make sure they are alert to possible early signs of morphine toxicity, such as constipation, lethargy, or poor feeding. CHA

...And A New Treatment For Ear Infections?

Growing concerns about widespread use of antibiotics has focused attention on the treatment of ear infections (acute otitis media) in children, both because these are the most common reason for using antibiotics in children and because it's been shown repeatedly that most ear infections will get better without antibiotics.

Previous studies have evaluated a "wait and see" approach, where parents are given an antibiotic prescription when the doctor first diagnoses an ear infection but are asked not to fill it unless the child is either not better or gets worse in the following 48 hours. This method has worked successfully in doctors' offices, but it wasn't clear whether it might also work in a pediatric emergency department.

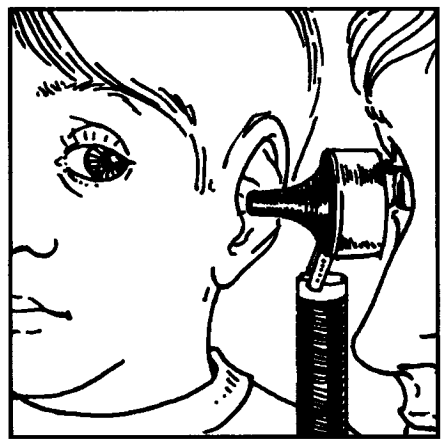

Researchers from Yale University studied children, ages 6 months to 12 years, who came to their emergency room with an acute ear infection. On a random basis, they either got a standard prescription for antibiotics or they were given a prescription but asked not to fill it in the next 48 hours unless the child didn't get better or got worse. All the children were also given ibuprofen and ear drops to manage their pain at home.

The researchers report that fewer children in the watch-and-wait group used antibiotics compared to those who got antibiotics right away, yet they didn't have higher complication rates or more frequent problems with fever, ear pain, or the need for further medical visits. The authors note that ear pain, when it occurred, lasted less than half a day longer in the watch-and-wait group: on the other hand, because fewer children in the watch-and-wait group got antibiotics, only 8% of them had diarrhea (typically caused by the antibiotics), whereas in the group prescribed antibiotics right away, 23% had diarrhea.

The authors conclude that using a wait-and-see prescription approach substantially reduced unnecessary use of antibiotics in children with acute ear infections who are seen in the emergency department "and may be an alternative to routine use of anti-microbials for treatment of such children." ***(Spiro DM et al: Journal of the American Medical Association, September 13, 2006, pp. 1235-1241)***

. . . . . .

COMMENT: The results of this study, conducted in a pediatric emergency department, are similar to those conducted in doctors' offices, and show that antibiotics are not immediately necessary in the treatment of most ear infections. In some countries, such as the Netherlands, children with ear infections are rarely treated with antibiotics at all.

Since it is well proven that most ear infections will go away without antibiotics, and we know that reducing use of antibiotics will help reduce the growing problem of bacteria becoming resistant to antibiotics, anything that we can do to avoid unnecessary use of antibiotics is a good idea.

Most ear infections will begin to resolve on their own within a couple days, and during this time the child's symptoms can be minimized by using pain relieving ear drops along with ibuprofen or acetaminophen. If symptoms continue or get worse after a couple days, the antibiotic prescription can be filled, and there appears to be no serious complications resulting from waiting a couple days.

As doctors in the U.S. become more comfortable with the idea of not using antibiotics right away for acute ear infections, parents can expect to see this approach becoming more common; we think it is a welcome development that can help reduce the use of antibiotics and eliminate the side effects they might have caused, all without significantly affecting the child's symptoms or recovery. CHA